Developing photonic, microfluidic and electrical systems to study the antibiotic susceptibility of individual *Escherichia coli*

Giampaolo Pitruzzello

Doctor of Philosophy

University of York

Physics

April 2019

Abstract

Antimicrobial Resistance (AMR) is an important societal and medical burden being faced by every healthcare system in the world. The large overuse of antibiotics favours bacterial resistance, thereby causing drugs to become ineffective. While traditional susceptibility tests are well established, they are slow at informing prescriptions, which means that many antibiotics are prescribed without proper diagnostics. This inefficacy stems from the detection of bacterial growth at the bulk colony level. In addition, averaging over bulk colonies masks any cell-to-cell difference even though it is well known that bacterial populations and their response to antibiotics are heterogenous. These differences need to be considered to correctly assess the efficacy of any microbial agent in a timely manner.

This thesis presents a multiparameter approach for profiling the susceptibility of individual bacteria to antibiotics. Hydrodynamic trapping provides the mechanism for retaining and examining hundreds of single *E. coli* in a microfluidic channel. The multiparameter aspect consists of the simultaneous assessment of bacterial motility and morphology upon exposure to antibiotics. This combined approach allows us to detect susceptibility and resistance of *E. coli* MG1655 in as little as 1 hour from spiking the culture. Standard microdilution assays and bacteria counts confirmed the validity of the classification. Additionally, the richness of single-cell data enables us to study the dynamics of population killing and the mode of action of the antibiotics.

The methodological approach presented here has the potential to complement traditional susceptibility tests by providing a deeper understanding of the drugs' action and a more rapid way of assessing the bacterial response to antimicrobial agents. More generally, the assay provides a platform for monitoring the behaviour of hundreds of single bacteria over time, while preserving the individuality of each microorganism.

Contents

List of figures

Acknowledgements

I would like to express my sincerest gratitude to all the people I have had the fortune to share the last few years with. This thesis would have not seen the light without them and would not be the piece of work I am now so proud of.

My deepest gratitude certainly goes to my supervisor, Prof. Thomas Krauss, for the countless opportunities of scientific and personal growth he provided me with. His relentless optimism, lively enthusiasm and invaluable comments (including the honest but constructive ones!) have been essential ingredients for the completion of this PhD. It has been my utmost privilege to work with him and surrounded by the inspiring multidisciplinary atmosphere he manages to cultivate in the group. I could never have imagined the large set of transversal knowledge that I have been exposed to and how much I have benefitted from it, both personally and scientifically.

The gratitude also extends to Dr. Steve Johnson (Department of Electronic Engineering), Dr. Hermes Gadêlha (Department of Mathematics), Dr. Adrian Evans and Dr. Neil Todd (York Hospital) for the useful advice and guidance throughout the entire project. They have been critical throughout this work and introduced me to topics and mindsets that I used to be entirely unfamiliar with.

I would like to thank all the members of the Photonics and Bio-Inspired Technologies research groups in York, both present and past ones: Dr. Donato Conteduca and Dr. Jose Juan-Colás, for always being there for me, Isabel Barth, Dr. Kezheng Li, Dr. Christopher Reardon, Dr. Yue Wang, Alexander Drayton, George Duffett, Manuel Deckart, Lewis Reeves, Dr. Ben Coulson, Dr. Ahmed Kenaan, Josh Male, Joe McKeown, Steve Thorpe for being a guide into the microbial world, Callum Silver, Dr. Lisa Miller, Dr. Matt Simmons, Dr. Casper Kuntsmann, Dr. Mark Scullion, Dr. Matthias Fischer, Dr. Amna Safdar, Dr. Bryan O' Regan, Dr. Daan Stellinga and Dr. Graham Triggs. Thanks for the numerous discussions, advices, laughs, meals and coffee breaks. You have all contributed in one way or another, maybe intangibly, to what this work is. My only hope is that I have been somewhat able to return the gratitude.

A heartfelt appreciation goes to Mark Carey, Emily Johnsen, Caleb Coleman, Ben Williams and Taryn Mackey for often going through my endless rants about the **random offensive adjective here** sausages (a.k.a. bacteria) not getting trapped, some mysterious equipment not working or the joyful British weather.

Special thanks go to Yehan Wang, who has been by my side in the process of writing up and tolerated my ups and downs with her unconditional support, kindness and warmth.

I would also like to acknowledge my friends back in the deep south for their never-ending support, even though we are 3000 km apart. The biggest thanks are definitely due to Giuseppe, Marco A., Marco M., Damiano, Giulia, Maria and Miriam.

Last, but very far from least, an immense thanks to my parents and my sister, to whom this entire thesis is dedicated. Your unceasing support through occasional flights, video calls and even simple texts has been crucial for everything I have achieved in my life, including the completion of this PhD. I owe you (way more than) one. Thank you.

Author's declaration

I, Giampaolo Pitruzzello, declare that this thesis entitled "Developing photonic, microfluidic and electrical systems to study the antibiotic susceptibility of individual Escherichia coli" is a presentation of original work and I am the sole author. This work has not previously been presented for an award at this, or any other, University. All sources are acknowledged as References. I also confirm that:

- This work was done wholly or mainly while in candidature for a research degree at this University.
- Part of the experimental work presented in section 12 of chapter III was conducted by Stephen Thorpe (PhD student) from the Department of Biology at this University. In particular in sub-sections 12.3.1 (resistant bacteria transformation and selection in appropriate antibiotics) and 12.4 (resazurin microdilution assays).
- Where I have consulted the published work of others, this is always clearly attributed as References.
- Where I have quoted from the work of others, the source is always given as References. With the exception of such quotations, this thesis is entirely my own work.
- I have acknowledged all main sources of help as References.
- Where the thesis is based on work done by myself jointly with others, I have made clear exactly what was done by others and what I have contributed myself.

The following lists provide details of publications that have had contributions from the work undertaken for this thesis (1,2), publications from side projects (3-5), past publications (6,7), conference and summer school attendances and a list of awards earned during the course of my doctorate.

Journal articles

1. Pitruzzello, G., Thorpe, S., Johnson, S., Evans, A., Gadêlha, H., & Krauss, T. F. (2019). Multiparameter antibiotic resistance detection based on hydrodynamic trapping of individual *E. coli*. *Lab on a Chip*, 19, 1417-1426.
2. Pitruzzello, G., & Krauss, T. F. (2018). Photonic crystal resonances for sensing and imaging. *Journal of Optics*, *20*(7), 073004. Invited Topical Review - **paper of the week in mid-June 2018**.

3. Hoffmann, J., Schulz, K. M., Pitruzzello, G., Fohrmann, L. S., Petrov, A. Y., & Eich, M. (2018). Backscattering design for a focusing grating coupler with fully etched slots for transverse magnetic modes. *Scientific Reports*, *8*.
4. Fohrmann, L. S., Pitruzzello, G., Petrov, A. Y., & Eich, M. (2018). Coupling between multimode fibers and slab waveguides. *Optics Express*, *26*(23), 30255-30266.
5. Fohrmann, L. S., Sommer, G., Pitruzzello, G., Krauss, T. F., Petrov, A. Y., & Eich, M. (2017). Integrating cell on chip - Novel waveguide platform employing ultra-long optical paths. *APL photonics*, *2*(9), 096102.
6. Pitruzzello, G. (2015). Inspiration is all around you. *Nature Nanotechnology*, *10*(7), 652.
7. Ruffino, F., Romano, L., Pitruzzello, G., & Grimaldi, M. G. (2012). High-temperature annealing of thin Au films on Si: Growth of SiO2 nanowires or Au dendritic nanostructures? *Applied Physics Letters*, *100*(5), 053102.

Conferences attendance

1. Pitruzzello, G., Thorpe, S., Johnson, S., Evans, A., Gadêlha, H., Krauss, T.F., Multiparameter susceptibility test based on hydrodynamic trapping of single bacteria. **poster presentation** at *MicroTAS 2018*, Kaohsiung, November 2018.
2. Pitruzzello, G., Thorpe, S., Johnson, S., Gadêlha, H., Krauss, T.F. Multiparameter susceptibility test based on hydrodynamic trapping of individual *E. coli* – **poster presentation** at *Microfluidics 2018*, Heidelberg, May 2018.
3. Pitruzzello, G., Thorpe, S., Gadêlha, H., Krauss, T.F., Fast Antimicrobial Susceptiblity test based on hydrodyanamic trapping of single bacteria – **oral presentation** at *Europtrode XIV*, Naples, March 2018.
4. Pitruzzello, G., Thorpe, S., Gadêlha, H., Krauss, T.F. Multiparameter antimicrobial susceptibility test based on hydrodyanamic trapping of individual bacteria – **poster presentation** at *Photonics West*, San Francisco, January 2018 – **runner up at a 3-minute poster pitch competition**
5. Wang, Y., Reardon, C.P., Pitruzzello, G., Krauss, T.F., Guided Mode Resonance imaging – a novel sensing technique to study bacterial biofilm antibiotic resistance – **oral presentation** at *Photonics West*, San Francisco, January 2018.
6. Pitruzzello, G., Wang., Y., Krauss, T.F., Antimicrobial Resistance: from biofilm to single bacteria **– poster presentation** at *IBST*, Riva del Garda, May 2017 – **best poster award**.

Summer Schools

1. 10th Advanced Study Course on Optical Chemical Sensors – *ASCOS 2017* – Třešt (Czech Republic) – July 2017.
2. Photonic systems for Sensing and Metrology summer school - University of St. Andrews – June 2016.

Awards

1. 1st place at the Doctoral Researcher Awards (200+ applicants) given by the Association of British Turkish Academics (ABTA), UCL, London, May 2019.
2. Runner up at the University of York 3 Minute Thesis competition 2018, June 2018.
3. Finalist at the STEM for Britain poster competition, House of Commons, London, March 2018.
4. Runner up at a 3-minute poster pitch at Photonics West 2018, San Francisco, February 2018.
5. Best diploma thesis award ("Resonant Photonic Structures for Biosensing") at Scuola Superiore di Catania (10 contestants), December 2017.
6. K.M. Scott poster prize (~30 posters), University of York, October 2017
7. Best oral presentation (~30 speakers) at the Postgraduate Conference, University of York, September 2017
8. Best poster presentation at IBST conference (350+ posters), May 2017

To my parents and sister

Where there's a will, there's a way

I. Introduction and aims

Miniaturising technologies and pushing our understanding of the micro- and nano-worlds have often proven to be winning strategies. The first computer ever built in 1946, the ENIAC, covered an area of ~170 m^2. Three average-sized 1-bedroom apartments in the UK would be just enough to accommodate it. Nowadays, thanks to the miniaturisation of electronic components, a common laptop is thousands of times smaller than the ENIAC, yet thousands of times more powerful. It would now take about 2000 MacBook Pro machines to cover the previous three apartments' floors.

In this thesis, I will examine the behaviour of small biological entities: bacteria. Importantly, like in any other domain of physics or engineering, it is crucial to match the scale of a probing technique to that of the object to be examined: we would not try to detect a single cell with a floodlight nor use a handheld laser to observe a distant galaxy. Hence, the need for miniaturisation to study the biological world. This thesis attempts to address this scale-matching necessity by involving three domains: photonics, microfluidics and electrical techniques. They correspond to chapter II, III and IV of the thesis, respectively. The aim is to make these domains interact synergistically for studying single bacteria and their response to antibiotics.

While photonics allows us to mould light at the nanoscale, microfluidics affords the same for fluids at the microscale. In the context of biosensing, photonics can make light interact with biological matter. For a judicious design, this interaction modifies the properties of the radiation in a detectable and quantifiable way. On the other hand, since most biology happens in liquids, microfluidics arose as the natural candidate to manipulate solutions and aid detection. Furthermore, the same advances in microfabrication that drove the success of photonics and microfluidics have also allowed electrical contacting to be matched to the size of single cells and bacteria. Since the life cycle of microorganisms heavily relies on the exchange of ionic compounds, it is reasonable to assume that an electrical technique will provide useful insights into the microbial world.

Hence, while photonics sees the bacteria as phase objects and measures their refractive index, electrical techniques incorporate microorganisms as components of an electrical circuit and probe their conductive properties. Microfluidics aids to manipulate cells and position them within the photonics or electrical sensing areas.

1. The need for novel antimicrobial susceptibility tests

"When I woke up just after dawn on September 28, 1928, I certainly didn't plan to revolutionise all medicine by discovering the world's first antibiotic". Fleming would later say: "But I suppose that was exactly what I did". Indeed, since the serendipitous discovery of penicillin by Alexander Fleming, antibiotics have been regarded as a cornerstone discovery of the 20th century. They have saved countless lives and still continue to do so. However, the use of any therapeutic agent is always compromised by the development of possible tolerance by the target microorganisms. After all, bacteria are living organisms subjected to the natural selection rule, whereby the survival of the fittest is usually guaranteed. Therefore, once resistance to an antimicrobial is developed, resistant strains survive and thrive.

The problem has become increasingly serious in recent years because the rate of development of new antimicrobials has not been able to keep up with the pace at which bacteria develop resistance. Hence, there is a clear need for a more targeted use of existing antibiotics. A more tailored approach would favour the use of narrow-band, specific antibiotics instead of the broadband drugs that are currently being prescribed as a result of educated guesswork; it would also reduce unnecessary courses of antibiotics if, e.g., the infection is not bacterial at all. Consequently, chances for bacteria to develop resistance would be reduced. However, current diagnostic techniques are not rapid enough to inform targeted prescriptions. In addition, these traditional tests examine billions of microorganisms at once, thereby washing out any cell-to-cell differences. The outcome of such bulk experiments is a single value with its confidence interval, which then disregards any underlying distribution of quantities of interest. Contrarily, single cell techniques can produce histograms of relevant values, which are extremely valuable for understanding population dynamics and heterogeneity.

Therefore, there is an urgent need for alternative ways of characterising susceptibility to antibiotics at the single bacteria level, with the twofold aim of speeding up detection while probing the heterogeneity of bacterial populations.

2. Goals of this thesis

Having recognised the need for new susceptibility tests, the main challenges that my work attempts to address are:

- Is there a measurable bacterial property that is affected by antibiotics on a shorter timescale compared to growth?
- If there was such a property, could its response to drug exposure be used as a signature of susceptibility? In other words, would susceptible and resistant strains respond differently?
- If the previous points hold true, are these signatures in agreement with the standard definition of susceptibility?

We started by hypothesising that bacterial motility and morphology are valuable alternative signatures to test for. Indeed, there is evidence in the literature suggesting that antibiotics affect both properties. However, the vast majority of tests only examines morphology, while motility has been largely overlooked. In addition, while current motility assays afforded short detection times (~1h), a true single cell level has not yet been reliably achieved, as I will comment in the relevant section (section 4 of chapter III). Hence, we identified the need for a retention mechanism that allowed us to hold a single bacterium in place while allowing some degree of movement to be measured. At the same time, a significant number of bacteria was needed to ensure statistical relevance. To this end, we decided to employ the hydrodynamic trapping platform illustrated in Figure 1.

The main body of this thesis is divided into three chapter marked by roman numerals and corresponding to a different domain, as detailed below. Each chapter consists of a variable number of chapters.

- **Chapter II**. The initial design envisaged to exploit trapping arrays fabricated onto a photonic resonant surface, specifically a sub-wavelength grating supporting guided mode resonances (GMRs). The original idea was to exploit the surface sensitivity of the optical mode to image single bacteria and to monitor their movements upon trapping. However, the fundamental spatial resolution limit of this measurement scheme (stemming from the very nature of the GMR mode) prevented single-bacteria resolution to be achieved. Chapter II of the thesis presents

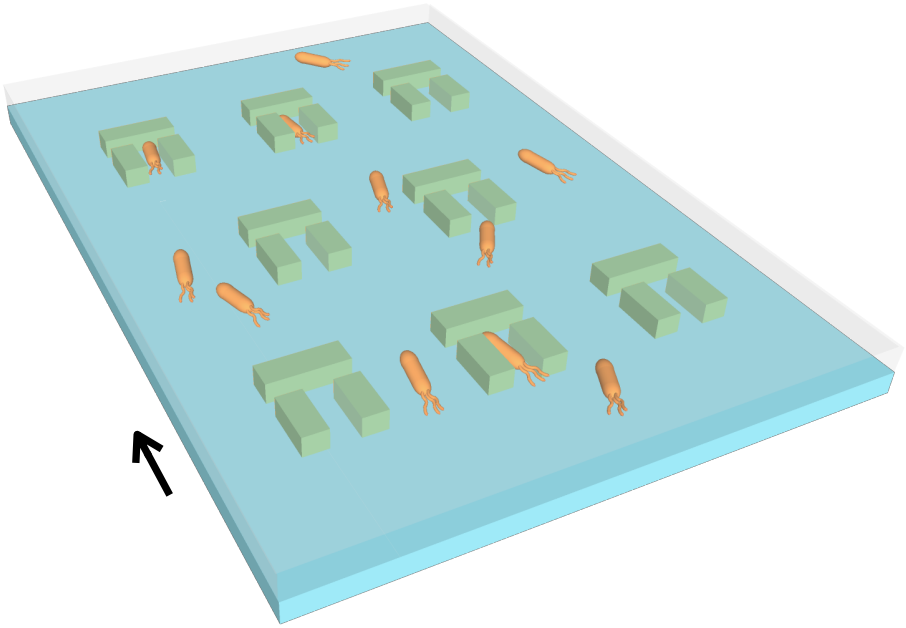

Figure 1. 3D diagram of the hydrodynamic trapping assay. Single bacteria, with a typical length of the order of 3 µm, are trapped in U-shaped microwells inside a microfluidic channel. The black arrow indicates the direction of the fluid flow.

the design, simulation, fabrication, experimental validation and limitations of the photonic platform.

- **Chapter III**. A different strategy was thus implemented to monitor individual bacteria. I chose to employ a standard phase contrast microscope to measure bacterial motility. The increased imaging resolution also allowed me to monitor bacterial morphology as a second signature of the antibiotic action. The combined assessment of the two properties at the single cell level resulted in rich data sets that not only led to the detection of susceptibility in as little as 1 hour, but also provided insights into the dynamics of the drug actions. These aspects are discussed in chapter III of the thesis.

- **Chapter IV**. As a further addition, we envisaged to integrate electrical impedance spectroscopy into the assay with the aim of providing an electrical signature of susceptibility. Its integration would also allow to electrically monitor an individual bacterium over time, a scheme that has not yet been presented in the relevant literature. This third task was not brought to conclusion due to time constraints. Nevertheless, I managed to design the assay by simulating it with COMSOL, optimised its fabrication and performed some proof of concept experiments. I present these points and comment on their potential future development in chapter IV.

II. Photonic resonances for biosensing

This chapter of the thesis focuses on the use of photonic crystal resonant surfaces as optical biosensors. In particular, structures based on guided mode resonances (GMRs) are discussed theoretically, simulated, fabricated and characterised in terms of optical properties, refractive index sensitivity and imaging capabilities. Specifically:

- A general introduction is given in section 1 which highlights the importance of optical biosensors, their general purpose and basic working principles.
- Sections 2 and 3 contain a summary of the main findings of a literature review [1]. They focus on the definition of figures of merit of an optical (bio)sensor and they present some of the latest advances in sensing and imaging.
- Section 4 presents the theory of light propagation in periodic structures, i.e. Maxwell's equations in periodic media. The particular case of one-dimensional gratings is examined to understand the origin of GMRs. The S4 code, a rigorous coupled wave analysis (RCWA) simulation package is presented and employed to simulate the optical response of gratings supporting GMRs.
- The microfabrication and measurement techniques for GMR gratings are described in Section 5.
- Section 6 contains experimental results obtained for TiO_2 gratings. Their performance is assessed, in particular the sensitivity to refractive index changes, the limit of detection and the spatial resolution for imaging.
- Section 7 highlights the limitations of the GMR approach for imagining small biological entities, i.e. individual bacteria. The need for an alternative solution is highlighted.
- A summary and conclusive remarks are given in section 8.

1. Introduction

A deeper understanding of the properties of materials has often been the driving force behind many of the historical technological breakthroughs. We have learned to control the mechanical and electrical properties of materials, especially through advances in fabrication techniques and improvements in basic understanding. These have led, for example, to the microelectronics revolution, a field which is still a main driver of technological innovation today.

In the last few decades, a new frontier has opened up, i.e. the control of optical properties of materials and, in particular, the emergence of micro- and nanostructured materials. The aim of these technologies is to control the interaction of electromagnetic radiation with materials and to tailor this interaction according to our needs. Indeed, photonic sensors continue to be high on the agenda because of the ever-increasing demand for sensing applications in areas such as healthcare, defence, security, environment and food quality control, with a particular emphasis on miniaturised and personalised technologies [2–4]. Lab-on-a-chip systems represent the State-of-the-Art of photonic sensing since they exhibit high sensitivity and selectivity, small footprint and allow for on-field operation [5]. With the commercialization of this type of devices, the next generation of sensors is expected to be reliable, portable and able to be fabricated with mass production techniques, therefore leading to a significant reduction of cost.

According to a market analysis performed by Allied Market Research, the global photonic sensor market is expected to reach a $15.2bn total market revenue by 2020, with Europe being a very strong contributor. A significant slice of this market is represented by photonic biosensors [6]. Correspondingly, research into photonic biosensors has steadily increased over the years because of the many exciting research challenges they offer. This trend is also reflected by the ISI Web of Science, which shows how the number of publications in the area has more than doubled in the last 10 years, with 2.2k papers containing the keyword ‘biosensor’ published in 2007 and 4.8k in 2017, compared to an annual growth rate in the total number of papers of approximately 3%[7]. A similar trend is observed for ‘optical biosensor’ papers [8].

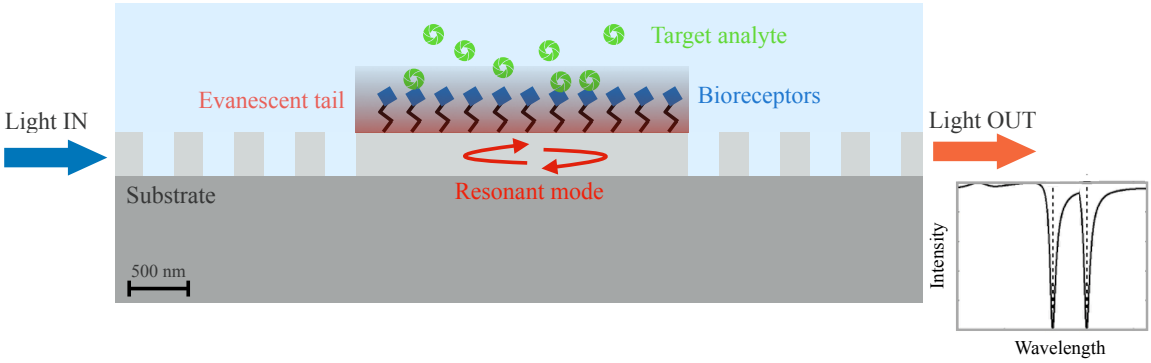

Figure 2. Scheme of a photonic crystal cavity for biosensing. The resonant mode is confined via the photonic band gap, i.e. because the nearby holes act as reflectors. The mode is sensitive to the cover medium because of the overlap with the evanescent tail. The surface is functionalised with bioreceptors (in blue) showing high affinity to a specific analyte in solution (in green). Any binding event modulates the effective index of the optical mode, thereby causing a shift of its resonant wavelength, as depicted in the transmission spectrum on the right-hand side.

The purpose of a biosensor is the detection of biologically-relevant targets such as proteins, DNA, pathogens, cells, bacteria, pollutants, hormones and enzymes. In most cases, their presence and/or concentration in samples such as blood, urine, saliva, sweat or tears can be an early indicator of disease, so that the sensor can be used as a valuable diagnostic tool. In its general form, a biosensor is a transducer that reports a molecular or biochemical binding event as a physical quantity. In the case of a surface affinity biosensor, the sensing element is a surface covered in a biorecognition molecule such as DNA, proteins, antibodies or particular cell receptors that can selectively bind to targets in the analyte under examination. Depending on the transduction mechanism, devices are classified into electrical, electrochemical, piezoelectric, nano-mechanical, acoustic, magnetic or optical biosensors.

This chapter of this thesis concerns optical biosensors, meaning that the presence of the analyte or organism of interest in the vicinity of the sensor's surface modulates the interaction with optical radiation in a detectable way. In particular, such sensors rely on guided-wave optics, whereby light propagates in a waveguide or in other wave-guiding structures, and the evanescent tail of the guided mode interacts with the analyte. Upon binding or attachment of biological targets, the refractive index (RI) at the surface changes, which modulates the phase of the guided mode via the effective index. This change in phase is picked up interferometrically or by placing the mode in a resonant structure and recording the change in resonant wavelength. The latter configuration is schematically depicted in Figure 2, where the resonant cavity is realised via a Bragg mirror. Optical absorption may also be used instead, but since most biological targets are phase objects, RI sensing tends to be the preferred option [3,9].

A particular photonic structure that can be used for sensing is a photonic crystal (PhC). PhCs consist of a periodic arrangement of dielectric materials [10,11]. Their operation can be easily understood by analogy with electrons in a crystalline structure: a PhC does to photons what a semiconductor crystal does to electrons. The analogue of the periodicity of the Coulombic potential in a semiconductor is the periodicity of the dielectric constant.

The key characteristic, for a judicious choice of materials and geometry, is the presence of a photonic band gap, namely a range of frequencies that are not allowed to propagate in the structure. The origin of this band gap is the constructive interference of waves reflected at the different dielectric material interfaces. The easiest way to picture this is a distributed Bragg reflector (DBR), namely a periodic stack of alternating dielectric materials of different RI. Such a stack exhibits a band gap when half the wavelength in the material corresponds to the period of the stack. The presence of a band gap can be exploited to create waveguides and cavities, whereby the light is guided along specific paths or localised at specific locations. It is also possible to tailor the interference between leaky modes in order to obtain the desired spectral behaviour: PhCs exquisitely allow us to mould and adapt the flow of light to our needs.

2. PhC structures for biosensing

Two main classes of PhC-based sensors can be identified, namely devices based on PhC cavities and those based on guided mode resonances (GMRs). This distinction perfectly reflects the versatility of PhCs and captures all their relevant aspects and advantages.

On the one hand, PhC cavities offer a high degree of spatial confinement, resulting in a very small footprint and in the possibility of extreme miniaturisation. This strong localisation comes with a high degree of wavelength selectivity: ultrahigh Q factors of up to 10^7 have been measured [12]. Note that the combination of high spatial and high spectral confinement is unusual in photonics; typically, one thinks of high Q cavities as being large objects and not wavelength-scale. These characteristics make PhC cavities suitable for multiplexing and very localised sensing of biomarkers, cells and bacteria. In terms of sensing properties, the high Q translates into a low limit of detection (LOD), while the small volume translates into very small analyte volumes and the possibility to even measure inside cells. Indeed, research has affirmed PhC cavities to show the highest performance in the field of PhC biosensors [1].

The second model system, i.e. GMR-based devices, operates in the regime of quasi-guided or leaky modes [13,14]. Similar to strictly guided modes, GMRs confine energy in the slab, but unlike them, energy can readily couple to external radiation. This ease of interfacing provides an efficient way of coupling power into and out of the slab to facilitate the sensing function, especially in the context of point-of-care (POC) devices. Furthermore, they are inherently able to spatially resolve the resonance information, so they are also suitable for imaging, as I will detail later on. However, this ease of interfacing comes at the cost of reduced Q factor and sensitivity compared to the cavity approach.

2.1. Figures of merit of a biosensor

The performance of a biosensor depends on a number of different factors. Firstly, the optical properties of the transducer need to be considered, such us the Q factor, the mode distribution, the reflection or transmission spectrum and the active sensing area. Secondly, even for the same optical characteristic, the biological protocols for surface functionalisation can affect the outcome depending on the quality of the bioreceptor layer and its binding affinity to the surface. Finally, the specific setup influences the accuracy of the measurement, especially in terms of adding sources of noise. Doing all of these effects justice would be well outside the scope of this work, so we mainly focus on the photonic aspects.

2.1.1. Wavelength sensitivity and limit of detection (LOD)

A key contributor to the performance of a (bio)sensor is its sensitivity. Sensitivity is defined as the ratio between the change in sensor response, typically the wavelength change dλ, and the change in the value of the measurand, typically the RI change dn. Hence, for an optical sensor, the sensitivity S_λ represents the shift in wavelength per unit change of RI and it thus quoted in nm/refractive index unit (RIU):

$$S_\lambda = \frac{d\lambda}{dn} \tag{1}$$

The value of S_λ it is obtained by plotting the position of the resonance for different known values of the RI and by calculating the slope of such a curve. In general, changes in refractive index due to binding events are such that the behaviour of the calibration curve

$S_\lambda(n)$ can be approximated as linear. In fact, the evaluation is usually performed by employing water:ethanol or glucose solutions at different concentrations, which provide index variations of the order of 10^{-2} RIU. The combination of S_λ with the smallest detectable wavelength shift yield the limit of detection (LOD). The LOD is the smallest change in the measurand that produces a detectable change in the sensor response. The smallest measurable response R_{LOD} is defined as [15,16]:

$$R_{LOD} = R_{blank} + 3\sigma_{blank} \quad (2)$$

where R_{blank} is the mean response in the absence of the measurand and σ_{blank} the associated noise (i.e. the resonance wavelength and the associated fluctuations prior to any binding event). The LOD is calculated by dividing $3\sigma_{blank}$ by the sensitivity S_λ, so it is expressed as the minimum change in RI that would produce a response equal to $3\sigma_{blank}$. The assumption behind this definition is that the values of the measured sensor response are normally distributed [17,18]. Therefore, the $3\sigma_{blank}$ rule implies a confidence of 99.7% that a change in response is caused by an actual binding event. While the sensitivity strictly depends on the physical mechanisms involved in the interaction between the radiation and the biolayer, the noise level (σ_{blank}, and the LOD as a consequence) depends on the measurement configuration and the data analysis procedures. This means that the same sensor system can show very different values of LOD.

The measurement in resonant systems then involves determining the spectral position of the resonant peak and how much it shifts. Two main sources of noise can be identified, namely intensity and wavelength noise [17,19]. Sources of intensity noise are typically related to photodetector noise and to fluctuations of the light source intensity, while wavelength noise comes from instability in the wavelength emitted by the source and temperature fluctuations that influence the resonator by slightly modifying its resonance condition; both effects deteriorate the signal to noise ratio (SNR) of the system.

2.1.2. Minimum detectable wavelength shift

The second contributor to the LOD is the smallest wavelength shift that can be detected, which is directly proportional to the Q factor; the Q factor measures the sharpness of the resonant peak as the ratio between its centre frequency and its full width at half maximum

(FWHM). Sharper peaks (higher Q) are easier to track and it has been demonstrated that in the intensity noise-limited regime, $3\sigma_{blank}$ depends linearly on the linewidth $\Delta\lambda$ of the peak. This means that the minimum detectable shift is inversely proportional to the Q factor [17]. However, the matter is not trivial. For very high Q factors, the peak becomes more sensitive to wavelength noise, which affects narrow peaks more significantly. In this regime, which holds for resonators with a $Q \sim 10^5$ or higher, temperature variations become the main sources of noise and the smallest detectable shift only increases with $\sqrt{Q}$ [19]. Furthermore, it becomes impractical to measure very sharp peaks because of the need for very precise spectrometers or very fine-tuneable narrow-bandwidth sources to probe the response of the resonator. Also, high Q values typically imply that the optical mode is more strongly confined to the cavity material, meaning that the overlap with the analyte is reduced and so is the sensitivity.

2.1.3. Surface sensitivity

The above figures refer to what is known as the bulk sensitivity, which describes the sensor response to changes in the entire cover medium. The bulk sensitivity is certainly useful for calibrating the performance of the sensor against media of known refractive index. It is also meaningful when considering the detection of large targets, such as cells and bacteria, which represent a bulk RI change due to their size being typically larger than the evanescent tail of the optical mode. In most cases, however, the sensor is designed to detect molecular binding events, which occur very close to the surface. Hence, we need to define the surface sensitivity as the wavelength shift upon surface molecular binding.

A general relation between the bulk and the surface sensitivity has been derived in Zhu *et al.* [20] for ring resonators. A similar procedure for converting bulk sensitivity to surface sensitivity can be applied to all resonant-based RI sensors [17,20]. Several parameters contribute to determining the surface sensitivity, such as the polarizability and the surface density of the biomolecule layer. Nevertheless, as demonstrated in [21,22] for GMR-based devices, it is difficult to produce a general rule, since results strongly depend on the nature of the mode. In particular, the position of the modal symmetry axis has to be taken into account (that is the centreline through the resonant mode along the structure) as well as the effective index (n_{eff}) and the penetration depth into the medium.

The effective index n_{eff} can be considered as an average refractive index weighted by the field distribution of the mode and, together with the index of the cover medium (n_c), it determines the decay length of the evanescent tail. For instance, for a guided mode, the field at the boundary between the guiding structure and the surrounding medium can be expressed as:

$$E(z) = E(0)\, e^{-\gamma z} \quad with \quad \gamma = \frac{2\pi}{\lambda}\sqrt{n_{eff}^2 - n_c^2} \tag{3}$$

where the decay constant γ dictates how rapidly the mode tails off into the medium. The larger γ, the shorter the decay length, which means that the overlap between the evanescent wave and the biolayer is increased. This concept leads to the definition of a detection zone as the fractional field intensity integrated over the spatial regions occupied by the biomolecules [23]. The overlap should be maximised as those parts of the field that do not overlap with the biolayer do not contribute to the sensitivity.

3. GMRs for sensing and imaging: a review

A guided mode resonance (GMR) is a leaky or quasi-guided mode that is supported by a periodically patterned slab [13,14], or by multiperiodic or aperiodically ordered supercells [24,25]. The field of sensing with GMRs has been pioneered by Magnusson [13] and Cunningham [26,27], who highlighted the possibility of using GMRs for sensing applications and then showed the possibility of detecting the protein streptavidin down to ng/ml levels. Cunningham *et al.* also demonstrated the detection of DNA-protein, sequence-dependent binding and highlighted the inhibition mechanisms of these interactions [28]. However, one of the main limitations of GMR-based sensors is their modest sensitivity (usually of the order of 100 nm/RIU) and Q factor (of the order of 100), limiting the LOD to the range of 10^{-4} RIU, as opposed to the popular surface plasmon resonance (SPR) sensors. Plasmonic sensors manage to afford sensitivities of several thousands of nm/RIU and LODs of the order of 10^{-7} RIU [1,29–31]. The reason for this high sensitivity is intrinsic to the mode-coupling physics exploited by SPRs which is very well discussed in [1]. Therefore, a number of strategies have been proposed to improve the limitations inherent to GMR devices and increase their sensitivity towards that of SPR devices.

3.1. Suspended symmetric membranes

El Beheiry *et al.* [21] simulated a variety of silicon nitride slabs suspended in free-space and patterned with square arrays of holes, assuming that the analyte completely encompassed the slab. Their main finding was that the suspended geometry, due to its inherent symmetry, can exhibit Q values as high as $1.6*10^5$, sensitivities approaching 800 nm/RIU, and an impressive LOD of 10^{-7} RIU. The reason for this high sensitivity is that the bottom half-plane also contributes to sensing action, thereby increasing the effective sensing area. In fact, this approach had already been tested experimentally by measuring a very similar configuration in [32]. Indeed, for a judicious choice of hole radius and period, a bulk sensitivity of 510 nm/RIU had been measured, even though the Q factor was only about 100. The drawback of the suspended design is the added fabrication step and the increased fragility, which may also make the structure more susceptible to noise. Nevertheless, membranes of a relatively large area of (200×200) μm^2 have been observed to withstand several hours of operation under flow pressure.

Another solution pointing in a similar direction consists of using a low refractive index substrate, which helps to push the centre of the mode up towards the cover medium. This method was demonstrated by fabricating the grating out of a low-index porous glass with an index of 1.17 and subsequently covering it with 165 nm of high-index TiO_2 to provide the necessary index contrast for confining the GMR. The sensitivity increased four-fold as a result for the detection of the protein A binding to IgG antibodies [33]. The performance can also be enhanced by adding a thin layer of porous TiO_2 to increase the number of sites available for molecular binding. This approach led to a maximum ~4x enhancement of the sensitivity compared to a standard design for the detection of an amine polymer film. The properties of the resonance were not affected significantly by the modified porous surface of the grating [34].

3.2. Sensing with different polarisation

An attractive feature of a GMR is that both TE and TM polarisations are supported, i.e. modes with the electric field vector being oriented parallel or perpendicular to the grating lines [14]. The two modes show different modal distributions and Q factors. In particular, the TM mode is more strongly confined, and it has a smaller decay length, making it suitable for proteins and the detection of small biomolecules. The TE mode, on the other hand, extends further into the analyte and is therefore more suitable for the detection of larger objects such as cells [1,21].

This polarisation duality was exploited by Magnusson [35] for the detection of tumour necrosis factor alpha (TNFα) (a cell signalling protein) with an LOD of 156 ng/ml (3.7 nM) and cancer biomarkers such as calreticulin, an early indicator of ovarian carcinoma. For the latter, the lowest measured concentration was 390 ng/ml (8.5 nM), but with a high SNR, meaning that even lower concentrations could have been detected. In these experiments, both TE and TM resonance peaks were tracked. The two sets of data allowed to distinguish any background index or density fluctuations from the binding events, providing a self-referencing mechanism. Additionally, two measured uncorrelated variables enable to determine two unknowns. This is because tracking the shift of a single resonance enables one to measure changes in the optical density, *i.e.* the product of the refractive index and the thickness of the layer, and the two quantities cannot be discerned. In contrast, by back fitting collected data from two independent resonances with simulation results, both the thickness and the refractive index of the adsorbed layer can be estimated from a single experiment. This approach is very powerful as it allows characterising different layers of surface-bound molecules and to monitor changes in molecular conformation [36], as demonstrated by Juan-Colás *et al.* with ring resonators [37]. Furthermore, if combined with electrochemical measurements, this approach enables direct and precise measurement of the molecular density on a surface [36,38]. Even though it holds remarkable promise, the polarisation duality has not been extensively exploited for GMR-based devices.

3.3. GMR as feedback element

GMRs, if appropriately designed, can reflect 100% of the radiation on resonance. This feature has been exploited by using a GMR grating as the reflector of an external cavity laser (ECL) [39]. The grating acts both as the transducer and as the wavelength selective element of the ECL. In particular, the grating was used to feed the back-reflected GMR mode into an external semiconductor optical amplifier which provides gain and sharpens the peak. Binding of biomolecules causes the effective cavity length to change and thereby the lasing wavelength shifts. The GMR grating itself shows a modest Q in the high 10^2, but its interaction with the amplifier increases the Q significantly to a value of the order of 10^7, while the sensitivity is unchanged (212 nm/RIU). This enhanced the performance of the assay led to a LOD of 10^{-7} RIU. A further upgrade was provided by mounting two gratings on the opposite sides of a flow chamber frame [40]. In this fashion, both gratings are exposed simultaneously to the same analyte which provides a self-referencing capability by only functionalising one of the two [41].

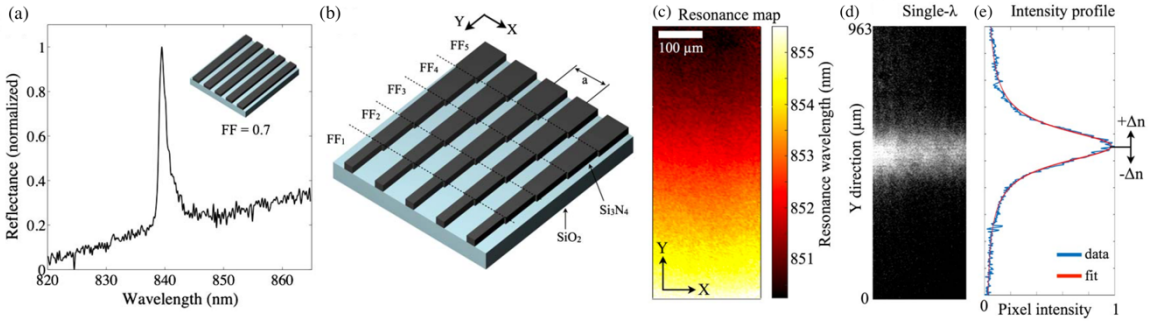

Figure 3. Sensing with a chirped grating. (a) Typical reflectance of a single filling fraction (FF) grating. (b) Schematic of the chirped grating proposed in [46]. The FF is tapered continuously along the direction of the grating lines. (c) Hyperspectral resonance map showing how the resonance changes spatially along the grating. (d) Brightfield image of the narrow transverse strip lighting up for a specific single wavelength at a specific position along the grating. (e) Fitted intensity profile used to retrieve the pixel position of the resonant line.

3.4. Phase shift detection

An alternative possibility for boosting sensitivity and improving performance is phase detection, whereby the aim is to exploit the large phase jump that occurs at resonance. The original idea dates back to 2004, with first experiments showing an LOD of the order of 10^{-7} RIU [42]. However, complex equipment and elaborate phase reconstruction algorithms were needed then [43,44]. More recently, Sahoo *et al.* have combined GMR detection with a relatively simple Mach-Zehnder interferometer [45]. Any change in refractive index on the sensor modifies the accumulated phase and consequently shift the fringe pattern. The sensor showed improved performances compared to a standard GMR configuration since phase detection is known to be more sensitive than wavelength tracking. These developments could competitively place GMR sensors close to plasmonic devices and promise further improvement to be forthcoming.

3.5. Chirped GMR

Most of the resonant methods mentioned so far require wavelength tracking. Hence, the ability of discerning very small wavelength shifts is crucial. Resolving minute changes in wavelength requires the use of sensitive, often bulky and expensive spectrometers and adds complexity to the measurement setup. An original solution has recently been introduced by our group which relies on chirping the geometrical parameters of the grating [46]. In particular, the filling fraction (i.e. the width of the grooves) is tapered spatially, as illustrated in Figure 3(a) and (b) which makes the resonance wavelength a function of the

position along the grating. An example of the spatial dependence of the resonance is shown in Figure 3(c).

In this configuration, when a monochromatic source illuminates the structure, only a narrow transverse region resonates, which results in a high reflectivity strip lighting up (Figure 3(d)). Any change in refractive index will cause the line to shift spatially as the resonance condition is now met for a slightly different filling fraction. Binding events can then be detected with a simple camera in the form of a moving bright line, whose position can be tracked by fitting the intensity profile directly from the acquired image, as seen in Figure 3(e). In other words, chirping gives the grating the dual function of transducer and spectrometer. The performance is similar to that of a standard grating sensor, with a sensitivity of 137 nm/RIU, an LOD of ~10^{-4} RIU and a minimum detectable concentration of 38 ng/ml (267 pM) for IgG protein. Additionally, by operating with a monochromatic source, all wavelength-related issues do not come into play, such as the spectral response of the camera or variable SNR, which can be minimised by choosing the wavelength that best suits the camera response.

3.6. Intensity detection

Another way of eliminating the need for a spectrometer is to use an intensity detection scheme. Such a method uses a monochromatic source to illuminate the grating, usually a relatively broad LED [47–49]. The input wavelength (or the grating parameters) is chosen such that the GMR resonance peak stands close to the rising edge of the illumination spectrum. In these conditions, the reflectance is low, because illumination and resonance are detuned. Binding events will shift the resonance to longer wavelengths along the rising edge of the LED, causing the resonance and the illumination to overlap and reflectance to increase. A schematic illustration is depicted in Figure 4.

The readout can simply be performed with a camera. The sensing surface can be spotted with several bioreceptors at different points for different types of molecules to be detected. The simplicity of the configuration has been exploited to make handheld sensors suitable for on-field use and smartphone-based readout. In [50], the authors fabricated such a device and proved it to able to detect three analytes at the same time. Different areas of the gratings are funcionalised drop-wise to detect the CD40 ligand antibody (13.5 µg/ml, 90 nM), EGF antibody (13.5 µg/ml, 90 nM) and streptavidin (30 µg/ml, 500 nM). While these values are

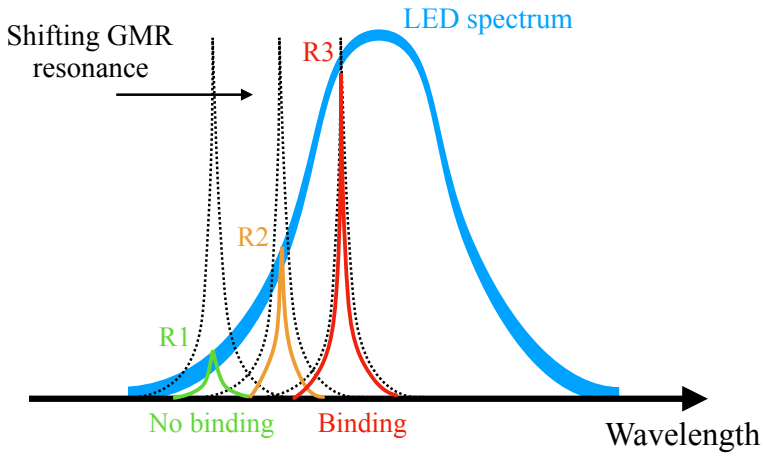

Figure 4. Schematic of the working principle of the intensity interrogation scheme. The reflectance R increases from R1 to R3 upon binding or change in refractive index because of the increased overlap between the GMR resonance line (changing from the green spectrum to the orange and the red one) and the LED illumination spectrum (in light blue).

certainly too high for a diagnostic tool, the authors estimated a LOD of 24 ng/ml (0.16 pM) for the CD40 and EGF.

One intrinsic limitation with such a method is that the accessible dynamic range is limited by the combination of the linewidth of the source with that of the GMR resonance. As illustrated in Figure 4, there needs to be spectral overlap between the rising/falling edge of the illumination and the resonance peak. Conversely, in wavelength-tracking method the dynamic range is decoupled from the resonance linewidth.

3.7. Imaging with GMRs

As already mentioned, GMRs on resonance take the form of a standing wave propagating in the plane of the grating, with a finite penetration depth. If we imagine a point-like perturbation on the surface of the grating, then its influence will extend laterally as far as this penetration depth. This feature allows for the mapping of refractive index distributions over the surface and it can be used for the surface-sensitive imaging of, for example, cells and their adhesion to the sensor.

Probing the mechanisms of cell adhesion to a surface is indeed of great importance for different reasons, such as the monitoring of biofilm formation and growth or the study of the interactions of cell membranes with a surface which are fundamental for growth, division, communications or tumour metastasis [51,52]. Traditional methods for investigating these processes have involved fluorescent dyes or proteins and mainly rely on autofluorescence. Although this scheme can be sufficiently sensitive to detect single

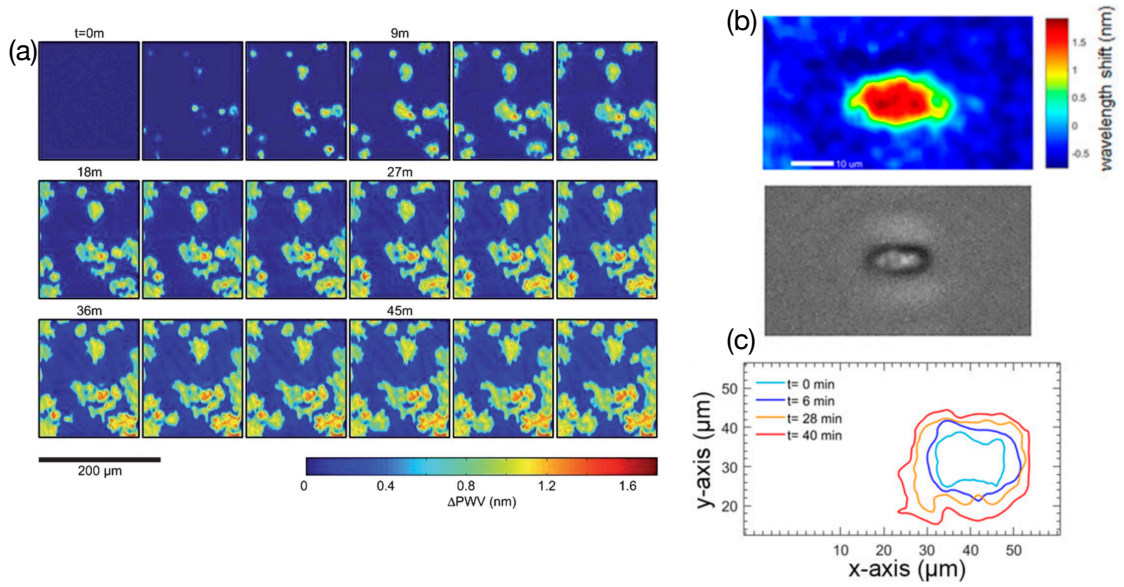

Figure 5. Examples of hyperspectral imaging with a GMR grating. (a) Hyperspectral imagining of mHAT9a cells attaching onto the grating surface over time. The process starts as a small and rounded area and then progresses toward larger areas as the cells spread. The outer boundaries appear irregular, consistently with small thin filopodia protruding from the cell body to explore the environment [53]. (b) Single HBK cell imaged on a grating compared to a phase contrast image. (c) Resonance wavelength contour plots showing an increase of resonance wavelength as cell secretions spread over time from the cell body [56].

molecules, the requirement for fluorescent labelling complicates the procedure, it may distort the measurement and it can interfere with the function of the biomolecules. Furthermore, monitoring a cell's activity over hours, or even days, is particularly challenging because of the photobleaching effect on fluorophores.

Atomic force microscopy (AFM) can also be used for studying cell morphology and mechanical properties. However, AFM does not provide much information about the interaction with the surface as it cannot probe the very interface.

As an alternative, PhC surfaces based on GMRs are completely label-free, since they rely on the refractive index sensing mechanism. This feature makes GMR surfaces unspecific, unless a targeted surface functionalisation is created on the surface. The sensing area can be as large as several cm^2 making the imaging region limited by the field of view of the camera and the magnification. Tens of cells can be monitored at the same time, increasing throughput. Furthermore, the optical mode penetrates only few hundreds of nanometres into the medium, making it very sensitive to the cellular membrane and its interaction with the surface.

This method of resonant imaging with GMRs or PhCs is also known as photonic crystal enhanced microscopy (PCEM) [53–55] and data is collected by hyperspectral imaging,

which will be described in the following sections. PCEM has been developed and widely explored by Cunningham *et al.* For example, in [53], they monitored the geometry of cell attachment, which is crucial in stem cell differentiation and cancer cell metastasis, as illustrated in Figure 5(a) over the course of about 1 hour. The group was able to follow drug-induced apoptosis over several hours and cell chemotaxis over a few days, which would be impossible with normal staining and fluorescence techniques. While the spatial resolution is inferior to fluorescence, subcellular details are nevertheless resolved, which may be indicative of a variation of the strength of attachment due to formation of actin bundles and lamellipodia [55]. More recently, Juan-Colàs *et al.* [56] proved the method to be able to follow the dynamics and heterogeneity of cytokines secreted by HepG2 cells (Figure 5(b) and (c)). Cytokines are critical molecules involved in cellular communication whose anomalies in secretion are often indicative of physiological disorder. More comprehensive reviews of PCEM can be found in [1,57].

3.7.1. Spatial resolution

Spatial resolution is clearly an important parameter for imaging. Various studies have investigated the resolution limit of resonant GMR imaging, i.e. the minimum separation that can be resolved and the minimum feature size that can be reliably reproduced. The limiting factor is the decay length of the mode in the grating plane (L_p), blurring any features smaller than this length.

Typically, the decay length is of the order of a few microns for a standard GMR, even though it depends on the choice of materials, geometrical parameters and the index contrast induced by the object(s) to be imaged. A careful design is also required because resolution and linewidth of the resonance are inversely related.

For instance, Triggs and co-workers [58] fabricated a standard resolution test pattern in Fox (a negative electron beam resist) on a 150 nm thin silicon nitride grating. This pattern provides a known distribution of refractive index in the form of different sized and shaped blocks distributed over the surface. Hyperspectral images were recorded in order to determine the minimum feature size and separation that can be resolved. The experiments demonstrated a resolution of 6 μm in the direction perpendicular to the grating grooves (i.e. along the grating vector) and 2 μm along the grooves. This anisotropy arises from the nature of the GMR, which induces oscillations in the direction of the grating vector, that is by adding the grating vector to the incoming light. In the perpendicular direction, no such addition of k-vector occurs, and the resolution can be diffraction-limited. 2D-periodic

structures, such as an array of air holes etched in a slab, showed instead the same limit along both directions, since the periodic structure imparts momentum in both directions.

These values are supported by Zhuo *et al.* in [54], where they imaged single TiO_2 and gold nanoparticles (NPs) deposited on the resonant grating. By analysing the hyperspectral scan, the authors were able inspect how far a single NP influences the resonance wavelength of neighbouring pixels. Pixels within the decay length of the mode were able to see the particle and show a corresponding shift in resonance. The final image resulted in a maximum wavelength shift centred on the NP and decaying within 3 μm on each side.

4. Theory of light propagation in periodic structures

In order to understand the nature and the optical behaviour of guided mode resonances (and, more generally, of photonic crystals), it is instructive to analyse the theory behind light propagation and interaction with periodic structures.

4.1. The master equation

Photonic crystals were first conceived in the early 90s and later realised in a guided mode format [11,59]. They are structures featuring a periodic modulation of the refractive index in one, two or three dimensions and their working principle is analogous to that of electrons in crystalline structures. The solution of Schrödinger's equation for such electrons is a Bloch wave, whose wave vector has to meet certain criteria to be able to travel in the periodic lattice. The restricted nature of Bloch waves is the origin of the electronic band gap in materials such as semiconductors or insulators, the term band gap referring to a range of energies and directions in which electrons are not allowed to propagate. The reason for a bandgap opening up is the mismatch between the electron wave vector and the lattice periodicity causing destructive interference at specific energies and/or directions [10].

A PhC is the optical analogue of such a periodic system. While electrons see coulombic potentials, photons see refractive indices. The periodicity of the atoms in the crystalline structures is replaced by a modulation of the refractive index arising from the alternation of different materials. Mathematically, while Schrödinger's equation describes the behaviour of electrons, Maxwell's equations describe the propagation of light:

$$\begin{aligned} \nabla \cdot \boldsymbol{B}(\boldsymbol{r},t) &= 0 \\ \nabla \times \boldsymbol{E}(\boldsymbol{r},t) + \frac{\partial}{\partial t}\boldsymbol{B}(\boldsymbol{r},t) &= 0 \\ \nabla \cdot \boldsymbol{D}(\boldsymbol{r},t) &= \rho(\boldsymbol{r},t) \\ \nabla \times \boldsymbol{H}(\boldsymbol{r},t) - \frac{\partial}{\partial t}\boldsymbol{D}(\boldsymbol{r},t) &= \boldsymbol{J}(\boldsymbol{r},t) \end{aligned} \tag{4}$$

where **E**, **B** are the electric and magnetic field vectors, respectively. Sources are represented by ρ and **J**, which are the external charge and current density. Information about the material is embedded in the displacement field **D** and the magnetizing field **H** and in their relations with the **E** and **B**, which are known as constitutive relations. In the case of non-polar and non-magnetic materials, the constitutive relations are:

$$\begin{aligned} \boldsymbol{D}(\boldsymbol{r},t) &= \varepsilon(\boldsymbol{r})\boldsymbol{E}(\boldsymbol{r},t) \\ \boldsymbol{H}(\boldsymbol{r},t) &= \frac{1}{\mu(\boldsymbol{r})}\boldsymbol{B}(\boldsymbol{r},t) \end{aligned} \tag{5}$$

The properties of the material appear in the electrical permittivity $\varepsilon(\boldsymbol{r})$ and in the magnetic permeability $\mu(\boldsymbol{r})$. Under the assumptions of anisotropy and transparency of the medium and upon expanding the field in Fourier series, Maxwell's equations can be combined into the so-called master equation. For the **H** field, the master equation is [10]:

$$\nabla \times \left[\frac{1}{\varepsilon(\boldsymbol{r})}\nabla \times \boldsymbol{H}(\boldsymbol{r})\right] = \left(\frac{\omega}{c}\right)^2 \boldsymbol{H}(\boldsymbol{r}) \tag{6}$$

This shows that the problem of finding the field profiles **H**(**r**) is equivalent to an eigenvalue problem of the form:

$$\widehat{\Theta}\boldsymbol{H}(\boldsymbol{r}) = \lambda \boldsymbol{H}(\boldsymbol{r}) \tag{7}$$

Where the operator $\widehat{\Theta}$ acting on the magnetic field is defined as $\widehat{\Theta} \equiv \nabla \times \left[\frac{1}{\varepsilon(\boldsymbol{r})}\nabla \times\right]$ and contains information about the spatial distribution of the dielectric constant ε(**r**). The eigenvectors are the spatial field profiles **H**(**r**) allowed to propagate in the medium, while the eigenvalues are $\lambda \equiv \left(\frac{\omega}{c}\right)^2$, where ω is the frequency of the corresponding modes.

Finally, we need to consider the periodicity of the photonic crystal, i.e. a function $\varepsilon(\mathbf{r})$ such that $\varepsilon(\mathbf{r} + \mathbf{R}) = \varepsilon(\mathbf{r})$, where $\mathbf{R}$ is the lattice periodicity vector. The Bloch theorem holds, and the master equation needs to be solved only in the unit cell of the dielectric lattice. This means that the solutions take the form of Bloch waves and can be labelled by a set of wave vectors $\mathbf{k}$ lying in the Brillouin zone. Each wave vector identifies an eigenstate of $\widehat{\Theta}$ with frequency $\omega(\mathrm{k})$ and an eigenvector $\boldsymbol{H}_k(\boldsymbol{r})$ representing the field distribution:

$$\boldsymbol{H}_k(\boldsymbol{r}) = e^{i\boldsymbol{k}\cdot\boldsymbol{r}}\boldsymbol{u}_k(\boldsymbol{r}) \tag{8}$$

$\boldsymbol{u}_k(\boldsymbol{r})$ is a periodic function with period $\mathbf{R}$ and can be represented in reciprocal space by introducing the lattice vector $\boldsymbol{G} = \frac{2\pi}{\boldsymbol{R}}$ as:

$$\boldsymbol{u}_k(\boldsymbol{r}) = \sum_{m=-\infty}^{+\infty} E_m e^{-im\boldsymbol{G}\cdot\boldsymbol{r}} \tag{9}$$

Furthermore, the operator $\widehat{\Theta}$ acting on $\boldsymbol{H}_k(\boldsymbol{r})$ can be shown to be Hermitian (i.e. equivalent to its conjugate transpose) and restricting a Hermitian eigenvalue problem to a finite volume leads to a discrete spectrum of eigenvalues. Therefore, for a fixed $\mathbf{k}$, the master equation admits an infinite set of modes with discretely spaced frequencies ω, which are usually labelled with a band index n. The frequencies of each band, that is fixing n, vary continuously as $\mathbf{k}$ varies. This family of functions $\omega_n(k)$ constitutes the band structure of the photonic crystal, which supplies us with most of the information needed to understand how the light interacts with the structure.

Clearly, the previous considerations and the master equation are also valid for the electric field $\mathbf{E}_k(\mathbf{r})$ such that it takes the form:

$$E_k(\boldsymbol{r}) = e^{i\boldsymbol{k}\cdot\boldsymbol{r}}\boldsymbol{u}_k(\boldsymbol{r}) = \sum_{m=-\infty}^{+\infty} E_m e^{-i(\boldsymbol{k}+m\boldsymbol{G})\cdot\boldsymbol{r}} \tag{10}$$

4.2. Guided mode resonances (GMRs) in 1D gratings

We now apply the previous findings to the case of a one-dimensional grating, namely a periodic arrangement of ridges of high refractive index material with a given period a and filling fraction FF, as schematically depicted in Figure 6. In this case, the previous

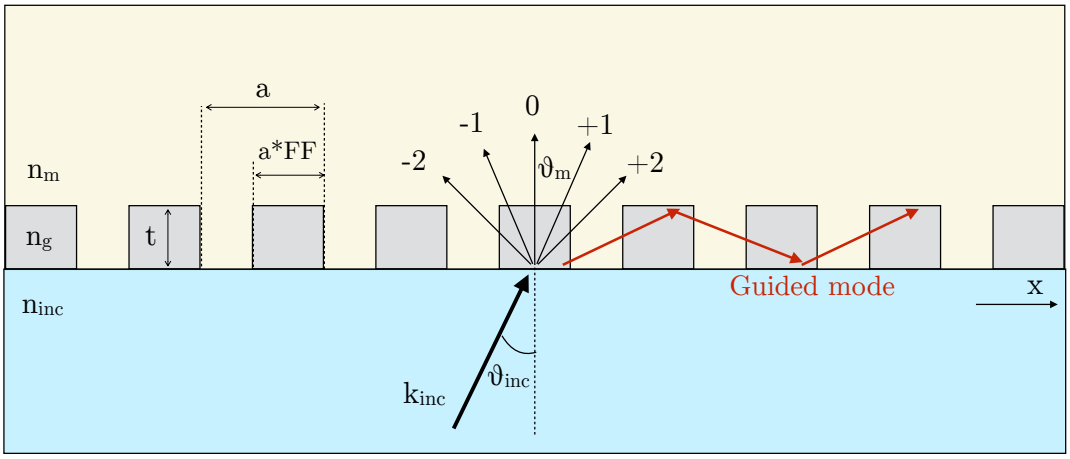

Figure 6. Diagram of a grating's behaviour in different regimes. The grating has thickness t, period a, filling fraction FF and it is made of a material of refractive index n_g. The grating is periodic along the x direction. A plane wave with k vector k_{inc} is incident at an angle θ_{inc} from the medium below (in light blue), which has an index n_{inc}. The wave is diffracted into the cover medium (refractive index n_m and in light yellow) at different angles θ_m. The various diffracted orders are indexed by the value of m (-2,-1,0,1,2). In specific conditions, (quasi) guided modes can be excited on the grating plane as depicted by the red arrows.

expression for the electric field is restricted to the periodicity direction (say x) with the lattice vector **G** simply taking the form $G = \frac{2\pi}{a}$. Thus:

$$E_k(x) = \sum_{m=-\infty}^{+\infty} E_m e^{i(k+mG)x} \tag{11}$$

The physical meaning of such an expansion becomes apparent when considering an incoming plane wave with wavevector k incident on the grating (i.e. a wave e^{ikx}). The electric field is represented by an infinite superposition of plane waves with integer multiples (m) of the grating vector G being added to the impinging k. In other words, the incident wave splits into diffraction orders with different wavevectors. Figure 6 shows a diagram of a plane wave incident at an angle θ_{inc} with respect to the vertical from a medium with refractive index n_{inc}.

The grating is covered by a medium with refractive index n_m. Field boundary conditions and conservation of momentum dictate the phase-matching condition to be satisfied along the direction of periodicity, namely that the x component of the wavevector must be constant:

$$k_{x,m} = k_{x,inc} + mG \qquad with\ \ m = \ldots, -2, -1, 0, 1, 2, \ldots \tag{12}$$

The subscripts *inc* and *m* refer to the incident wave and to the field propagating in the structure, respectively. Upon substitution of $G = \frac{2\pi}{a}$, $k_{x,inc} = n_{inc}\frac{2\pi}{\lambda_0}\sin\theta_{inc}$ and $k_{x,m} = n_{eff}\frac{2\pi}{\lambda_0}\sin\theta_m$, we obtain the grating equation:

$$\sin\theta_m = \frac{n_{inc}}{n_{eff}}\sin\theta_{inc} - m\frac{\lambda_0}{n_{eff}a} \tag{13}$$

where n_{eff} is the effective index of the mode and θ_m the diffraction angle of the mth order. The effective index can be imagined as the average refractive index of the grating weighted by the electric field intensity at every point of the unit cell. This leads to the definition of the wavelength of the mode in the grating as $\lambda_g = \frac{\lambda_0}{n_{eff}}$.

The behaviour of the structure then depends on the relative magnitude between the wavelength in the medium λ_g and the grating period a, since their ratio determines the solutions admitted by the grating equation. Tuning these parameters results in radically different behaviours in terms of diffraction and reflectivity. This versatility in tailoring a grating's spectral response is a highly desirable feature that makes such a simple structure ideal for a wide range of applications. Three operational regimes can be identified, as illustrated in Figure 7, which shows a reflectance plot for a SiN.

- Diffractive regime; $\lambda_g/a < 1 \leftrightarrow \lambda_0/a \lesssim 1.6$. In this regime, the grating behaves as purely diffractive, i.e. there exist non-zero orders (m≠0) carrying energy away from the grating into different angles, according to the grating equation. There are no high-reflectance regions, as illustrated by the absence of yellow areas in the reflectance plot in Figure 7.

- Near wavelength regime; $\lambda_g/a \approx 1 \leftrightarrow \lambda_0/a \approx 1.6$. Guided mode resonances can be excited in this regime. Assuming normal incidence for simplicity (so that $\sin\theta_{inc}$=0) and noting that $\frac{\lambda_g}{a} \approx 1$, the grating equation reduces to:

$$\sin\theta_m = m \tag{14}$$

  which clearly admits solutions only for m = 0, ± 1 and implies that the corresponding diffraction angles θ_m are 0° and ±90°: all other diffraction orders

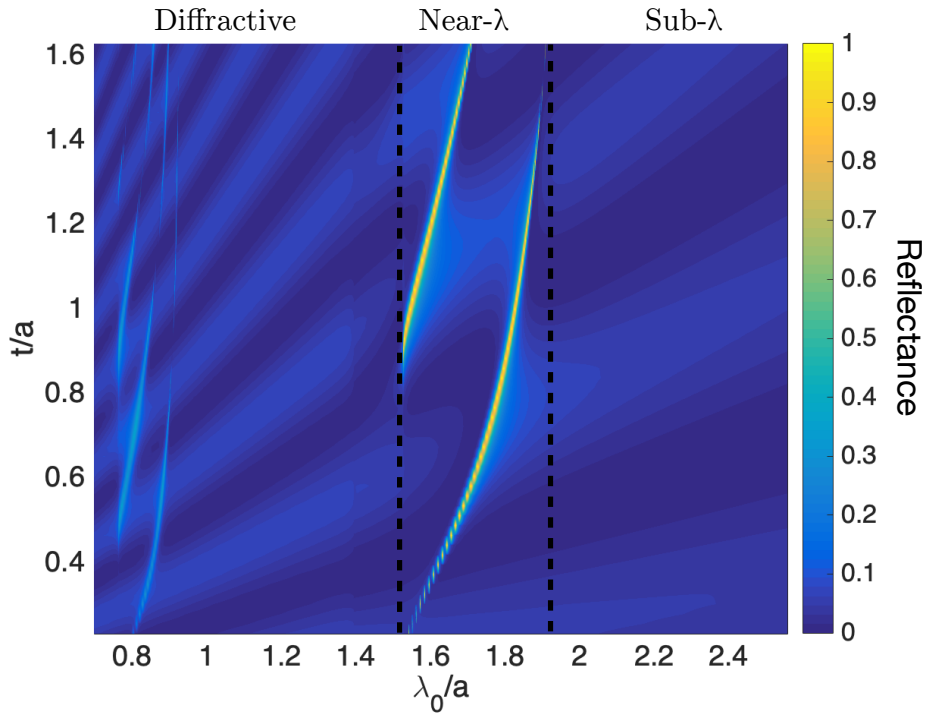

Figure 7. Colour plot of simulated reflectance as a function of the incident wavelength λ and thickness of the grating t. Both quantities are normalised to the period a. A plane wave is assumed to illuminate the grating at normal incidence. The grating has a refractive index n_g=2 and a filling fraction FF = 0.7. The three operational regimes are separated by the black vertical dashed lines.

are suppressed, apart from the 0th and the 1st, which is diffracted at 90°. Basically, the incident wavevector has no component in the *x* direction, so that the wavevector of the mode in the grating has to be equal to *G*, both in magnitude and direction. In this scenario, the mode propagates laterally with the grating acting as a waveguiding layer, as shown by the red arrows in Figure 8.

However, since the grating/waveguide is periodic and not homogeneous, the guided mode scatters at each ridge/groove interface causing energy loss into the substrate and the medium above. This scattering effect makes the modes leaky, or quasi-guided. For a specific set of grating thickness, period, filling fraction, angle of incidence, polarisation and refractive indexes, the phase of the leaky mode can be tuned in order to have complete destructive (or constructive) interference with the incoming beam and the 0th transmitted order. This results in a high reflection (or transmission) at the specific resonant frequency, making the grating a perfect mirror, as can be seen by the yellow regions in Figure 7. The behaviour on resonance is schematically depicted in Figure 8, where the inset shows the electric field distribution on resonance.

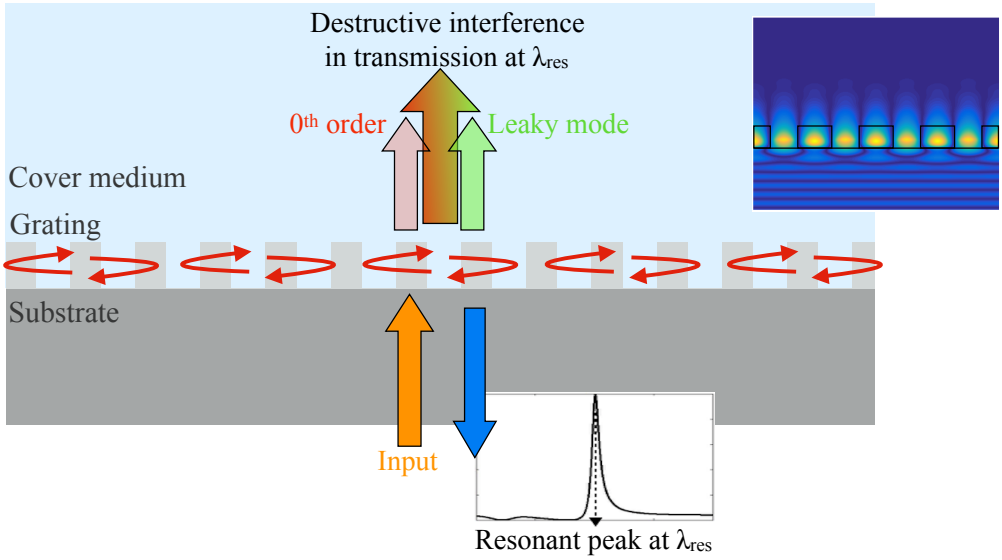

Figure 8. Diagram of a GMR excited in a wavelength-scale grating. At normal incidence (orange arrow), the 1st diffracted order couples into the grating plane and excites the quasi-guided mode which takes the form of a standing wave oscillating in the plane, as depicted by the red arrows along the grating. Since this is a leaky mode, it also scatters power upwards. Upon careful design of the structure, the transmitted 0th order (translucent red arrow) and the upward scattered leaky mode (translucent green arrow) interfere destructively for a specific incident wavelength λ_{res}, resulting in a strong reflection peak. The inset shows the field at resonance.

- Deep sub-wavelength regime - $\lambda_g / a > 1 \leftrightarrow \lambda_0/a \gtrsim 1.6$. The wave does not see the periodicity of grating. Mathematically, the ratio λ/a is too large for any solution of the grating equation to exist for any value of m other than 0. The equation reduces to the familiar Snell's law of refraction with the second medium being represented by a medium with the effective index of the mode:

$$n_{eff} \sin \theta_m = n_{inc} \sin \theta_{inc} \tag{15}$$

  In this regime, rather than acting as a diffraction or waveguiding element, the grating behaves as a homogeneous layer with index n_{eff} and simply refracts light according to Snell's law. The presence of such a fictitious layer being sandwiched between the substrate and cover medium generates a typical thin film interference pattern, manifested as the alternating fringes in the reflectivity plot in Figure 7.

Here, we are interested in the near-wavelength regime, where the high-reflectance GMRs are excited. The key characteristic at resonance is that the mode takes the form of a standing wave along the grating, with a fraction of the field exponentially decaying in the medium above the grating (see inset in Figure 8). It is the exponential tail that provides the

mechanisms for refractive index sensing. For a fixed grating geometry, angle of incidence and polarisation, the resonance wavelength is highly sensitive to the refractive index of the cover medium. Furthermore, as the mode is laterally confined within the grating itself due to the in-plane Bragg reflections at each interface, neighbouring regions on the grating display different resonance condition as determined only by the optical density of the material sitting at any precise location. Hence, by measuring the resonance wavelength on a pixel-by-pixel basis over the surface, it is also possible to image distributions of refractive index on the surface.

4.3. Propagation length of the GMR

A crucial characteristic of any photonic resonant device, particularly in the context of (bio)sensing, is its Q-factor. For a GMR excited in a one-dimensional grating, the Q factor plays a double role in relation to both operational regimes of the grating, i.e. the RI sensing and the imaging modality. For RI sensing, the value of Q is intrinsically linked to the ability of following spectral shifts and discerning the smallest wavelength shift possible, as discussed in section 2.1. In the context of imaging, the Q-factor is also strictly linked to the performance of the structure since Q is connected to the propagation length of the GMR mode.

The ability to distinguish differences in refractive index of neighbouring regions depends on the lateral penetration of the quasi-guided mode, i.e. on the number of grating elements the mode probes or "sees" before being coupled back out and detected. The main parameter controlling the penetration depth is the refractive index contrast between the grating material and the cover medium. A large index contrast causes strong reflections at each ridge/groove interface, both laterally and vertically, thereby resulting in a tighter confinement of the field and an inhibition of lateral propagation. Since the spatial distribution of the electric field and frequency domain are linked by a Fourier transform, a high degree of spatial confinement entails a broad range of frequency content, i.e. a larger linewidth of the resonant peak.

Figure 9(a) shows examples of simulated reflection spectra for different refractive indexes of the grating, where this effect is evident. The cover medium is the same (water, index 1.33) and I assumed normal incidence in all cases. As the index of the grating increases, the resonant peak becomes wider and shifts to longer wavelengths. The broadening effect is quantified in Figure 9(b), where the Q factor is plotted as a function of the grating index.

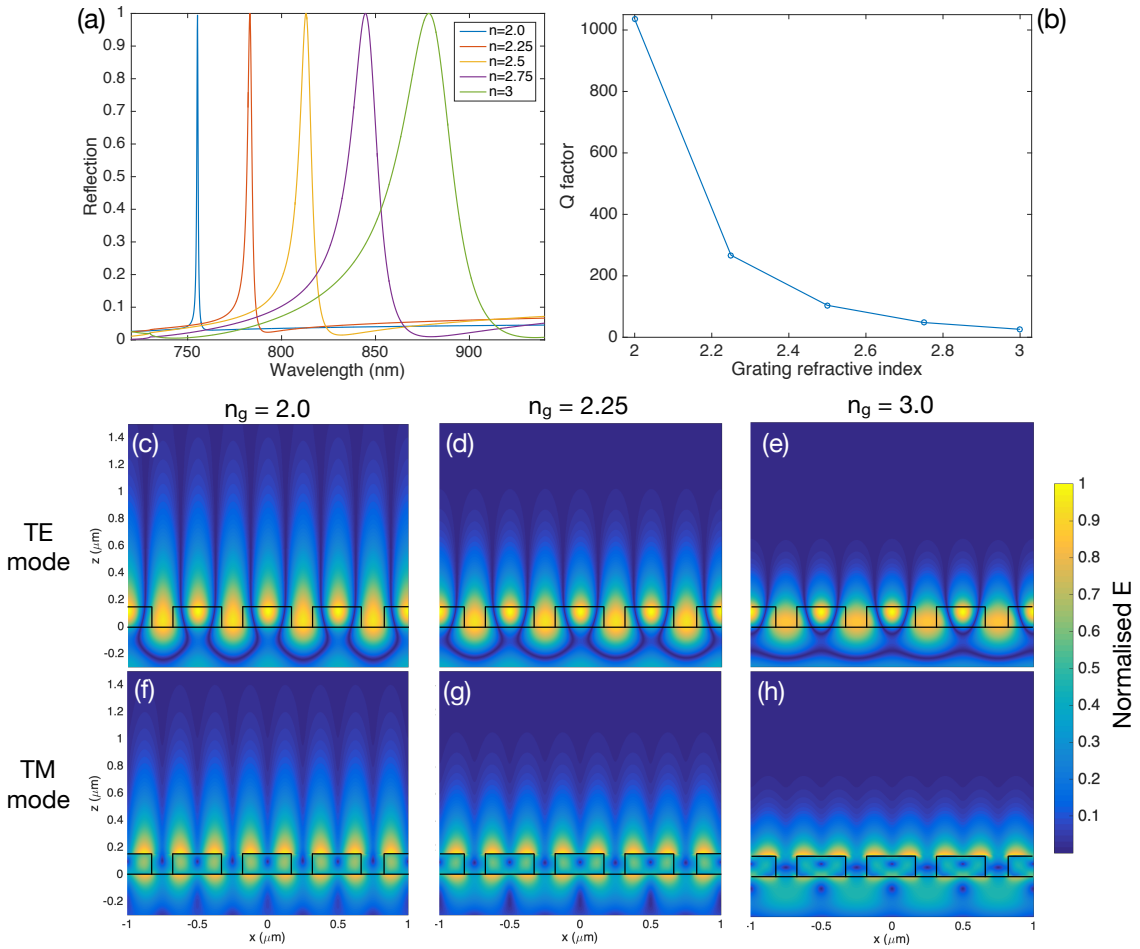

Figure 9. Spectral linewidth and field distributions for gratings of different refractive index. (a) shows how the reflectance spectrum changes for different refractive indexes of the grating material. The grating thickness and filling fraction are assumed to be 150 nm and 0.7, respectively. The grating is placed on a glass substrate (index 1.46) and covered with water (index 1.33). As the index increases, the linewidth becomes larger as a result of the stronger modal confinement. (b) quantifies the line broadening effect by showing the value of the Q factor as a function on the grating index. (c-e) illustrate how the field confinement for the TM mode strengthens, as evidenced by the decreasing penetration depth into the cover medium. (f-h) show the same effect for the TE mode.

Panels (c-h) illustrate the connection to the confinement of the mode, where the distribution of the electric field on resonance is shown for three different values of the index and for the two modes supported by the structure (TE and TM, where the incident electric field is oriented parallel or perpendicular to the grating lines, respectively). Note that the exponential tail of the mode decreases as the grating index increases for both modes.

This argument points out a more general trade-off typical of any physical system, namely the inverse relation between spatial and spectral resolution: the more spatially confined is a mode, the more frequencies are needed to "produce" the final resonance line, leading to larger linewidths but improved spatial resolution.

A simple relation between the propagation length L_p and the linewidth $\Delta\lambda$, or the Q factor, can easily be derived. The photon lifetime τ_p in a resonator is defined as the time at which the probability that a resonant photon has yet to be diffracted into the far field is 1/e. The fact that the Q factor is linked to the lifetime of the resonant mode can be used to quantify the lifetime τ_p. This lifetime is equivalent to Q/ω_0, where ω_0 is the resonant angular frequency. The propagation length L_p is thus the distance at which a fraction 1/e of the resonant photons remains in the mode and can be calculated as [22]:

$$L_p = \frac{c}{n_{eff}}\tau_p = \frac{c}{n_{eff}}\frac{Q}{\omega_0} = \frac{c}{n_{eff}}\frac{\lambda}{\Delta\lambda}\frac{1}{2\pi\nu} = \frac{\lambda^2}{2\pi\Delta\lambda} \tag{16}$$

This expression will be useful when we will discuss the imaging capabilities of such a structure. For instance, typical experimental values for a SiN grating ($\lambda\sim850$ nm and $Q\sim300$ [58]) result in $L_p \sim 40\mu m$, while the case of TiO_2 ($\lambda\sim650$ nm and $Q\sim80$, from section 6.2) gives $L_p \sim 8\mu m$. However, we note that these values do not directly correspond to the real spatial resolution, as we will show in section 6.3. The main reason is that the fabricated gratings deviate from the ideal resonator condition due to fabrication imperfections and sidewalls roughness. Therefore, photons are scattered and coupled out more efficiently than predicted by the simple previous model.

4.4. S4: a RCWA simulation toolbox

All the optics simulations presented here were performed using S4, an open-source code for the rigorous coupled wave analysis (RCWA) method implemented at Stanford University in 2012 [60]. The RCWA algorithm was first proposed by Moharam and Gaylord in the 80's [61]. The method is commonly employed for the simulation of electromagnetic waves propagating in layered 3D structures. The main requirement for its applicability is the spatial periodicity in either two directions, such as in photonic crystal slabs, or in a single direction, such as in one-dimensional gratings. The algorithm relies on numerically solving the semi-analytical form of Maxwell equations, whereby the fields and dielectric constants in the equations are expanded in a Fourier series over the periodicity direction(s), while the third coordinate is left analytical. The typical geometry of a RCWA simulation is reported in Figure 10 [62].

The structure of interest is decomposed in *M* layers along the z axis, which is defined as the direction of propagation. Each layer is assumed to be uniform along *z*, while it can be inhomogeneous in *xy*, as long as it is periodic over the entire plane. Two semi-infinite

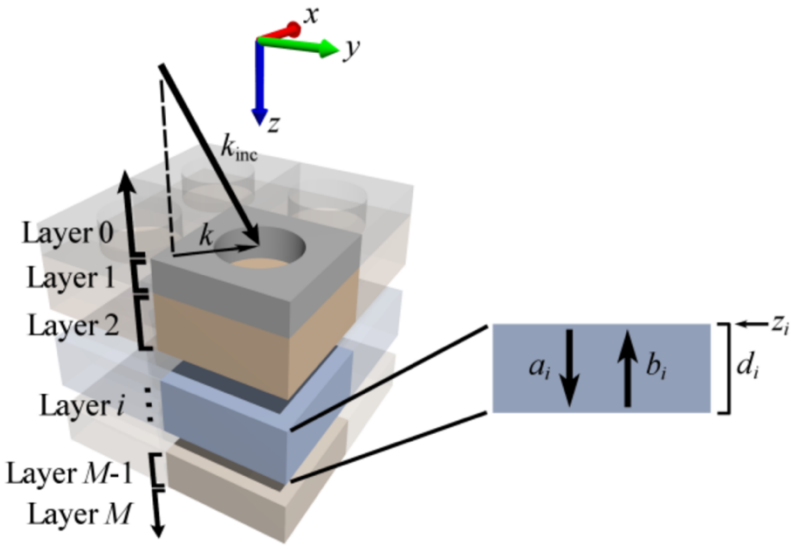

Figure 10. Schematic of a typical simulation domain in S4. M layers are stacked along the z direction, which is the propagation direction. Each layer is assumed to be uniform along z and periodic over the xy plane. A plane wave with wavevector k_{inc} is assumed to illuminate the structure from layer 0 [62].

planes are placed above and below the stack (layers 0 and M in Figure 10) and a plane wave is incident from layer 0 at a certain angle and with a given polarisation.

It is instructive to briefly look at some of the maths behind the method, as it provides useful insights into the propagation of light in such a periodic structure. Maxwell's equations are first written in a normalised form [63]:

$$\begin{aligned} \frac{\partial}{\partial y}E_z(\boldsymbol{r}) - \frac{\partial}{\partial z}E_y(\boldsymbol{r}) &= k_0\mu_r(x,y)\tilde{H}_x(\boldsymbol{r}) \\ \frac{\partial}{\partial y}\tilde{H}_z(\boldsymbol{r}) - \frac{\partial}{\partial z}\tilde{H}_y(\boldsymbol{r}) &= k_0\varepsilon_r(x,y)\tilde{E}_x(\boldsymbol{r}) \\ &\vdots \end{aligned} \tag{17}$$

where the magnetic field is normalised according to:

$$\tilde{\boldsymbol{H}}(\boldsymbol{r}) = -i\sqrt{\frac{\mu_0}{\varepsilon_0}}\boldsymbol{H}(\boldsymbol{r}) \tag{18}$$

Note that the fields are a function of the position vector **r**, while the properties of the material(s) $\mu_r(x,y)$ and $\varepsilon_r(x,y)$ are only functions of the *x* and *y* coordinates because of the uniformity assumption along *z*. Given the periodicity in the *xy* plane, a unit cell can be

identified, with spatial periods Λ_x and Λ_y. Hence, we can expand the fields and the material constants in Fourier series along the periodicity directions:

$$\begin{aligned} \varepsilon_r(x,y) &= \sum_{m=-\infty}^{+\infty}\sum_{n=-\infty}^{+\infty} a_{m,n} e^{-i\left(m\frac{2\pi}{\Lambda_x}x + n\frac{2\pi}{\Lambda_y}y\right)} \\ E_x(x,y,z) &= \sum_{m=-\infty}^{+\infty}\sum_{n=-\infty}^{+\infty} S_{x;m,n}(z) e^{-i\left(k_x(m)+k_y(n)\right)} \\ &\vdots \end{aligned} \tag{19}$$

The wavevectors $k_x(m)$ and $k_y(n)$ are given by the incident k vector plus the different orders contribution from the periodic structure, similarly to the simpler grating equation previously derived and discussed:

$$\begin{aligned} k_x(m) &= k_{x,inc} - m\frac{2\pi}{\Lambda_x}, \quad m = \ldots, -2, -1, 0, 1, 2, \ldots \\ k_y(m) &= k_{y,inc} - n\frac{2\pi}{\Lambda_y}, \quad n = \ldots, -2, -1, 0, 1, 2, \ldots \end{aligned} \tag{20}$$

The same expansions hold for all the components of each field and for the magnetic permittivity but are not reported here in the interest of clarity. The key quantities in the field expansions are the Fourier amplitudes of the fields, i.e. $S_{x,y;m,n}(z)$ for each field component (E_x, E_y, E_z and H_x, H_y, H_z). Clearly, the expansions need to be truncated to a finite number of harmonics, say M and N, which define the number of variables $S_{m,n}(x)$ to solve for, namely NM. Solving for these amplitudes allows one to reconstruct the fields in the structure. The equations are derived by inserting the Fourier expansions in the normalised form of Maxwell's equations. The results are rather complicated and are not shown here in the interest of simplicity. However, the beauty of this method emerges after a few mathematical steps, with the equations for $S_{m,n}(x)$ taking the (block matrix) form:

$$\frac{d}{dz}\begin{bmatrix}\boldsymbol{s_x}(z)\\ \boldsymbol{s_y}(z)\end{bmatrix} - \boldsymbol{\Omega}^2\begin{bmatrix}\boldsymbol{s_x}(z)\\ \boldsymbol{s_y}(z)\end{bmatrix} = \mathbf{0} \tag{21}$$

$\mathbf{s_x}(z)$ and $\mathbf{s_y}(z)$ are rather intricate functions of the initial Fourier amplitudes $S_{m,n}(x)$, while the matrix $\boldsymbol{\Omega}$ contains information about the wavevectors in the layer. This is a 2*(MN) set of ordinary differential equations which can be solved analytically. After a few more steps, the solution can be shown to take the form:

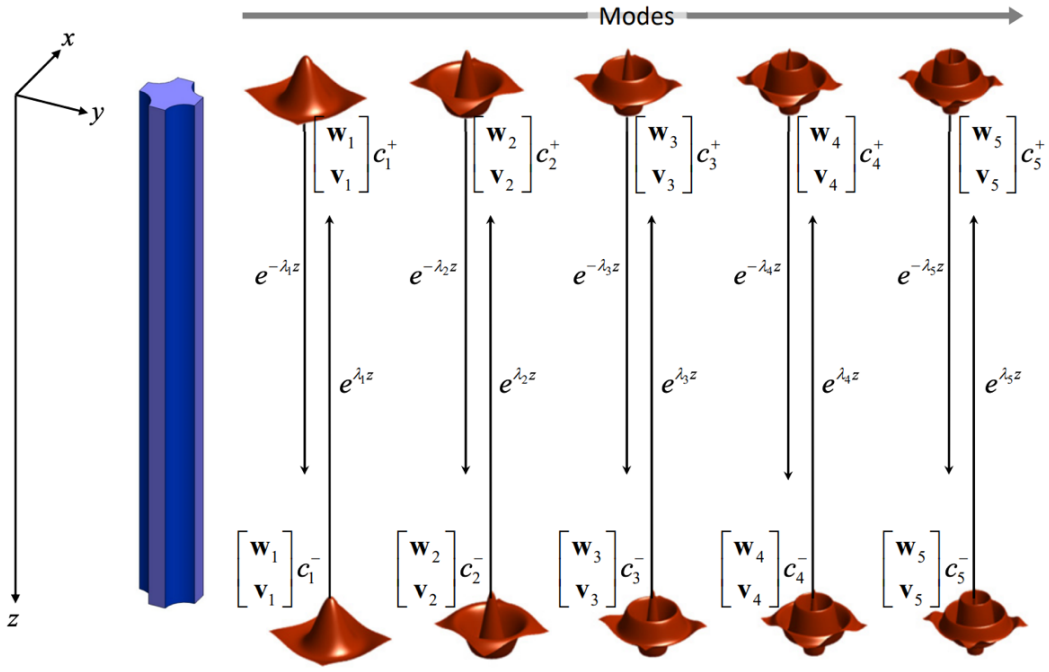

Figure 11. Graphical interpretation of the RCWA solution. The power within each layer is distributed across M modes described by the coefficients w and v. Each mode is weighted according to the coefficients c^+ (propagating forward) and c^- (propagating backwards). The propagation in each layer is regulated by the corresponding eigenvalues λ, which describe how the modes evolve [63].

$$\boldsymbol{\psi}(z) = \boldsymbol{W} e^{\boldsymbol{\lambda} z} \boldsymbol{c} \tag{22}$$

Here, $\boldsymbol{\psi}$ is a column vector containing all the field components, while **W** is the eigenvector matrix of $\boldsymbol{\Omega}^2$, **λ** its (diagonal) eigenvalue matrix and **c** a column vector of proportionality constants. The physical interpretation of a solution of this form is highly insightful. It shows that the propagating wave $\boldsymbol{\psi}$(z) can be thought of as the sum of multiple modes propagating in the layer. The modal distributions are described by the matrix **W**, which embeds information about the material and the layer periodicity. In particular, **W** contains the Fourier coefficients $a_{m,n}$ of the expansion of the dielectric permittivity ε(x,y). These coefficients are computed with no prior knowledge of the fields by a Fast Fourier Transform (FFT). ε(x,y) can be totally arbitrary, as long as it satisfies the condition of periodicity and a sufficient number of harmonics are employed to perform an accurate Fourier transform.

The matrix $e^{\lambda z}$ describes how the modes propagate along *z*, including any accumulation of phase (for real values of λ) and either gain or loss (for imaginary values of λ). Being **λ** the eigenvalue matrix of **Ω**, it carries information about the material and its periodicity, while **c** dictates the relative weight of each of the modes supported in the layer. It basically

quantifies how energy is distributed across the modes. Figure 11 provides an instructive visualisation of the solution [63].

Once the field amplitudes are known, we can calculate the reflection and transmission coefficients for each mode and finally sum them over all the modes to retrieve the total reflection, transmission or absorption. It is possible to include an arbitrary number of layers in the previous calculations, as long as proper boundary conditions are imposed at each layer's interface.

The number of harmonics employed to truncate the Fourier expansion is the sole parameter that dictates the accuracy of a RCWA simulation. It is critical in defining the goodness of the Fourier transform of $\varepsilon(x,y)$ and the number of modes needed to describe the propagation in each layer. The optimum number strongly depends on the unit cell, since any geometrical feature within the cell needs to be Fourier transformed correctly in order to avoid artefacts in the final results.

4.5. TiO_2 grating design

I used S4 to simulate sub-wavelength gratings and study dependencies and characteristics of the resonant modes as a function of the geometry and the surrounding refractive indices. A convenient way of illustrating results is to use colour plots, whereby a set of reflectance spectra (i.e. reflection vs wavelength) is plotted as a function of a third parameter, as shown in Figure 12.

The first column of graphs (a, c, e) illustrates reflectance plots for an incident TM-polarised plane wave, whereas (b, d, f) refer to TE polarisation. Rows report different parameters: grating thickness (a, b), filling fraction (c, d) and cover refractive index (e, f). The dashed black arrows point to the values chosen for subsequent fabrication and reported in the table in panel (h). A number of interesting features can be deduced from these graphs:

- For the same set of parameters, the TM mode is always spectrally narrower than the TE mode. This effect stems from the different modal distribution. In particular, the field of the TM mode is asymmetric with respect to the grating grooves, so the sign of the field on one side of the groove is the opposite to the sign on the other. This means that the two scattered components cancel each other out and cannot excite a radiating plane wave [14]. An easier way to visualise the broadening is provided in panel (g), which features both spectra in the same graph. The spectra

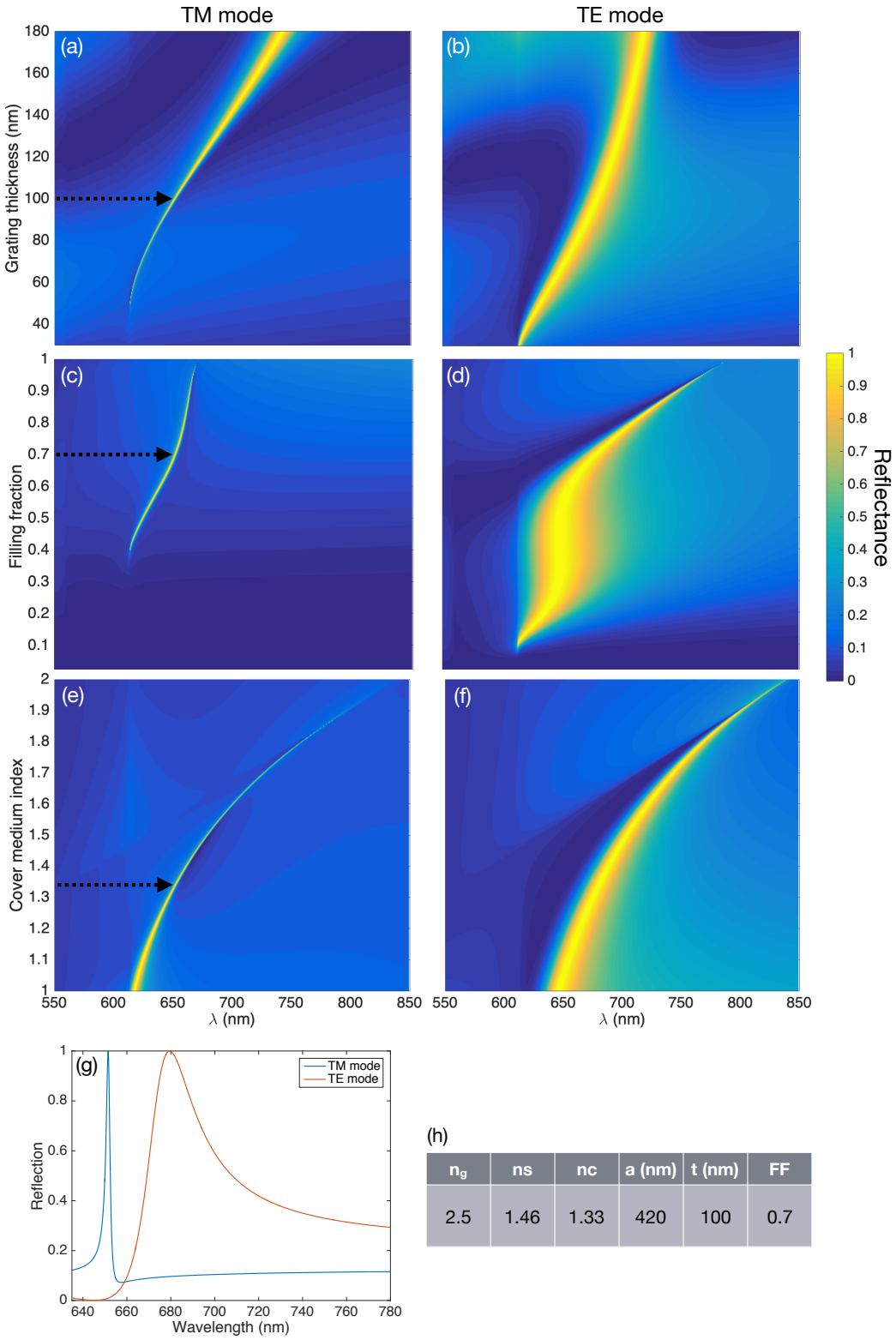

Figure 12. Reflectance plots for a TiO_2 grating as a function of different parameters and for the TE and TM mode. Plots display the dependence on the grating thickness ((a)-(b)), the filling fraction ((c)-(d)) and the refractive index of the cover medium ((e)-(f)). Black dotted arrows panels (a), (c) and (e) point to the selected design parameters. (g) Reflectance spectra for the parameters reported in (h) for the TE and TM mode.

were obtained for the set of parameters shown in the table in panel (h) and were used for subsequent fabrication and characterisation.

- The resonance condition shifts to larger wavelengths as both the thickness and the FF are increased, since they both contribute to increasing the effective index. If the thickness increases further, the system becomes multimodal, and multiple reflectance maxima will occur (not shown here).

- A minimum threshold on the thickness of the grating and the filling fraction is necessary for exciting the modes. This is more evident for the TM mode. A minimum FF of about 0.35 is needed to excite a TM, whereas the TE can be excited for FF as small as about 0.10. This difference in the excitation threshold stems from waveguide theory for asymmetric waveguides [64]. The analogy holds because the grating layer acts as a waveguiding layer for the guided mode resonance oscillating on the plane, as previously examined. Interestingly, this effect would not be observed if the system was symmetric (i.e. same substrate and cover medium).

- Panels (e) and (f) illustrate the ability of the grating to sense the RI of the cover medium. Both modes show non-linear behaviour. For a high cover index, both resonances narrow significantly before disappearing. This is due to the index contrast between the ridges and the grooves not being sufficient to sustain the in-plane Bragg reflection typical of the GMR mode. It should be noted that a rather wide range of indices ($1<n<2$) has been simulated for completeness. In reality, the grating is always operated within a very narrow range of values, in which the response can be considered linear. This linear response in the range 1.3-1.4 was found to have a slope of 120 nm/RIU for the TM mode and 105 nm/RIU for the TE mode, in accordance with the former extending further into the cover medium.

5. Fabrication and measurements

This chapter presents the fabrication methods for a 1D grating supporting GMRs and the subsequent setup employed for optical measurements and characterisation.

5.1. Fabrication of subwavelength gratings

The following points summarise the steps needed for fabricating sub-wavelength gratings in TiO_2. Figure 13 illustrates an overview of the key steps:

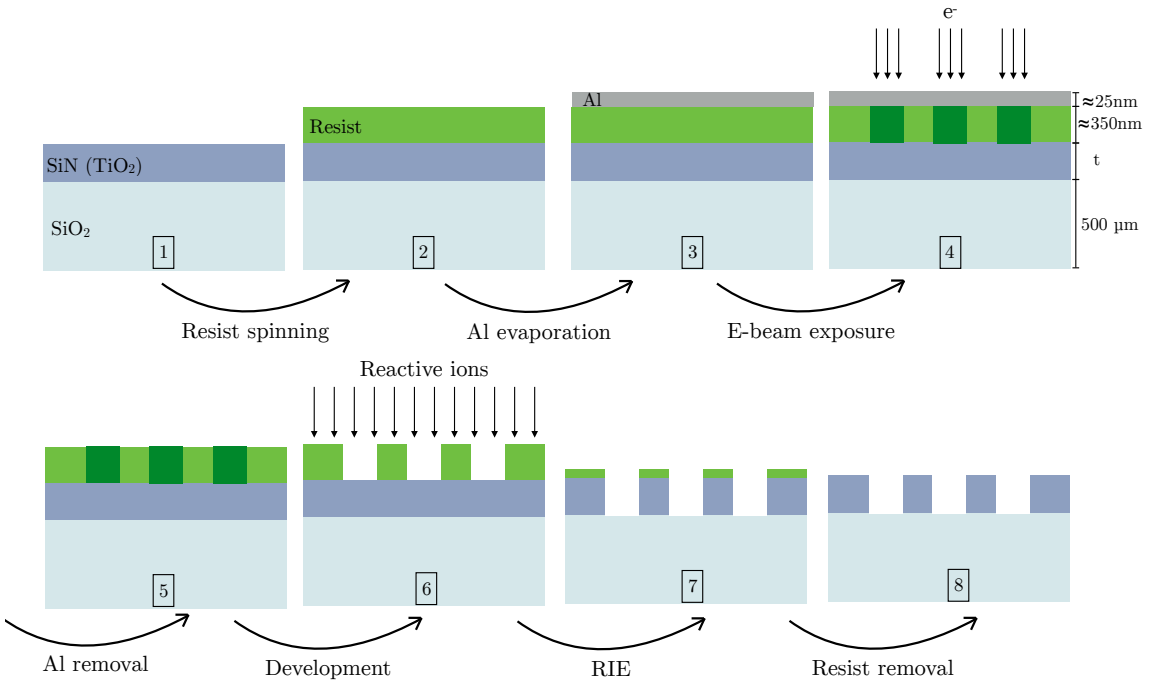

Figure 13. Sequence of steps necessary for the fabrication of the grating. The dielectric TiO_2 film is sputtered onto a glass substrate (1). The electron beam resist is spun onto the sample (2) and a thin layer of aluminium (25 nm) is evaporated on top (3). The electron beam exposure is carried out (4) and the aluminium is subsequently removed by a phosphoric acid dip (5). The sample is then developed (6) in order to dissolve the resist from the exposed areas, then a reactive ion etching (RIE) is performed to transfer the pattern to the dielectric layer (7) and finally any residual resist is removed (8).

- Dielectric material sputtering – A 100nm-thin layer of TiO_2 is sputtered onto microscope slides (25mm x 75mm).
- Resist spinning and covering – I use ARP electron beam resist (from Allresist), then evaporate a thin layer of aluminium to provide a charge dissipation layer given that the substrate is electrically insulating.
- Electron beam exposure – Gratings are exposed using electron beam lithography, before the aluminium being removed and the resist developed.
- Reactive Ion Etching (RIE) - The RIE step transfers the exposed pattern into the TiO_2 layer. The remaining resist is removed, and the sample cleaned.

5.1.1. Substrate cleaning and sputtering

The microscope slides are cleaned by immersing them in a 3:1 solution of sulfuric acid (H_2SO_4) and hydrogen peroxide (H_2O_2), known as piranha solution. The mixing is an exothermic reaction producing a new acid (H_2SO_5) which leads to the carbonization of organics on the surface. The carbon allotropes which are automatically formed are removed by a second slower reaction producing elemental oxygen, which is highly reactive and able to remove carbonized compounds from the surface. The slides are then sonicated

in acetone (ACE) and isopropylalchol (IPA) for a few minutes. A 100 nm film of TiO_2 is then reactively sputtered. First, the reaction chamber is flushed with 20 standard cubic centimetres (sccm) of argon at a pressure of ~$7*10^{-3}$ mbar; then a plasma is lit up at a DC voltage of ∼400 V. The aim of this first step is to clean the titanium target for 5 minutes by removing contaminants and the native oxide layer that naturally grows on its surface. During this process, the microscope slides are covered by a mechanical shutter to avoid contamination. For the deposition, 6.8 sccm of O_2 are added into the chamber to provide the oxygen to form TiO_2 on the substrate. The film is deposited at a typical rate of ∼0.2 Å/s.

5.1.2. Electron beam resist spinning and charge dissipation

The resist is deposited on the samples by spin coating, which produces a uniform thin film of controllable thickness on the substrate. A few drops of resist are applied on the sample, which is then rotated at high speed in order to spread the coating material by the centrifugal force. During rotation, the fluid spins off the edges of the substrate until the desired thickness achieved. I used ARP 6200.13 at 3000 rpm for 60 seconds to achieve a ~350 nm thin film according to the supplier's datasheet [65]. Afterwards, the remaining solvent is removed by baking the sample on a hot plate at a temperature of 180 °C for 10 minutes.

Since the substrate is glass and non-conducting, the sample exhibits significant charging during electron beam exposure. Charging leads to uncontrolled deflection of the beam and distortion of the shape to be written. To prevent charging, a thin layer (~25 nm) of aluminium is thermally evaporated on the sample prior to exposure. Thermal evaporation is a simple method of depositing thin films which is achieved through resistive heating of the material to be deposited. A small piece of aluminium is placed inside a tungsten boat. Electrical current is supplied to the boat, leading to the formation of a pool of melted metal, which then evaporates above the source and condenses onto the sample placed above the boat. The evaporation takes place in vacuum so that any vapour other than the source material is removed before the process begins. Since the pressure is rather low (of the order of $3*10^{-6}$ mbar), the atoms of the vapour can travel across the chamber in a straight line without hitting any background gas molecule (that is the mean free path is macroscopic) until they strike the sample surface, where they accumulate as a film. The deposition rate and the film thickness are monitored by a Quartz Crystal Microbalance (QCM).

5.1.3. Exposure and development

Upon electron beam irradiation, inelastic collisions of electrons within the resist result in the production of secondary electrons and physical and/or chemical changes in the resist. Positive-tone resists undergo a conversion from low to high solubility upon exposure, while the opposite happens to negative-tone ones.

During exposure, the electrons are slightly forward-scattered in the resist, which transfers energy and leads to exposure. Simultaneously, scattering causes deflections which contribute to broadening the electron beam. Most of the electrons pass through the resist and then continue scattering. Now, only the backscattered electrons are relevant, as they return from the substrate into the resist. The backscattered electrons have lower energy, which is, in fact, more effective at exposing the resist. This leads to the "proximity effect", whereby scattered electrons from neighbouring target points expose each other, thereby leading to non-uniform area exposure, especially close to features' edges. Another consequence is the enlargement of exposed areas, so that one must design structures with dimensions smaller than the target values. The amount of reduction required strongly depends on the exposure dose, the shape of the feature, the thickness of the resist and the acceleration voltage. Once these parameters are chosen, the enlargement is determined experimentally by comparing developed features to the designed ones. As an example, exposing grating grooves with a width of 70-100 nm results in final widths in the range 85-130 nm obtained by increasing the exposure dose (see results in section 6.2).

For the gratings fabricated here, I optimised the lithography process for a base exposure dose of 130 $\mu C/cm^2$, even though I always included a range of doses in each sample to consider fabrication variability and fabricate a range of filling fractions. Once the electron beam exposure is completed, I remove the charge dissipation layer in a solution of warm phosphoric acid (H_3PO_4 at 40 °C), which is a very fast etchant of aluminium, for around 2 minutes. No degradation of the ARP resist layer was noticed during this process. The resist is subsequently developed in Xylene for 2 minutes at room temperature.

5.1.4. Reactive ion etching (RIE) and resist removal

The sample is placed in the RIE chamber and pumped down to a base pressure of $3*10^{-6}$ mbar in order to remove water vapour and other gaseous contaminants. The chamber is flushed with the etching gases and stabilised for five minutes. RF power is then applied

between two capacitor plates to light up a plasma, thereby accelerating reactive ions towards the sample surface.

Three main processes occur during a RIE: physical etching, chemical etching and passivation. A proper balance between the three is necessary for achieving vertical side walls and transfer of the exposed patterns. The gas mixture and pressure and the DV voltage are the parameters that largely control the relative contributions of the three processes. Typical values are given below.

The acceleration of heavy ions (usually CF_x) towards the sample surface is mostly responsible for the physical etching. These high-energy ions hit the surface atoms of the sample, literally blasting them away, similarly to a sputtering system. The process is of physical nature since it relies on the physical mechanism of momentum transfer. This type of etching is anisotropic since the electric field accelerating the ions is nearly perpendicular to the surface, so that the sidewalls are less affected than the bottom surfaces. The amount and efficiency of physical etching is mostly controlled by the DC voltage, since a higher the voltage confers higher energy to the accelerated ions, so that the erosion process is more effective. On the other hand, the accelerating voltage impacts negatively on the resist mask. Hence, a suitable balance between the resist thickness and the acceleration voltage must be determined in order for the mask to suffer collisions until the underlying film etching is terminated.

Chemical reactions are responsible for chemical etching. This form of etching involves transport of the reactive gas species and their adsorption on the sample's surface, the chemical reaction and the final diffusion of the reaction products away from the surface. Chemical etching is isotropic, while the etch rate is mainly controlled by the pressure and the applied power. For instance, if either of these parameters is increased, a larger fraction of molecules undergoes ionisation and the rate of chemical reactions increases.

Finally, passivation is caused by ions that do not possess enough kinetic energy to physically etch the surface. Hence, they bond with atoms in the film and lead to the formation of a thin film. This passivation layer acts as an inhibitor that slows the etching process and may even arrest it. On the other hand, passivation brings the important advantage of protecting the side walls, thereby contributing to straight vertical erosion.

The etching of TiO_2 is achieved with CHF_3 and SF_6 gases in a 3:1 ratio (30 and 10 sccm, respectively) at a voltage of 180 V for 1 minute and 10 seconds. After etching, the sample

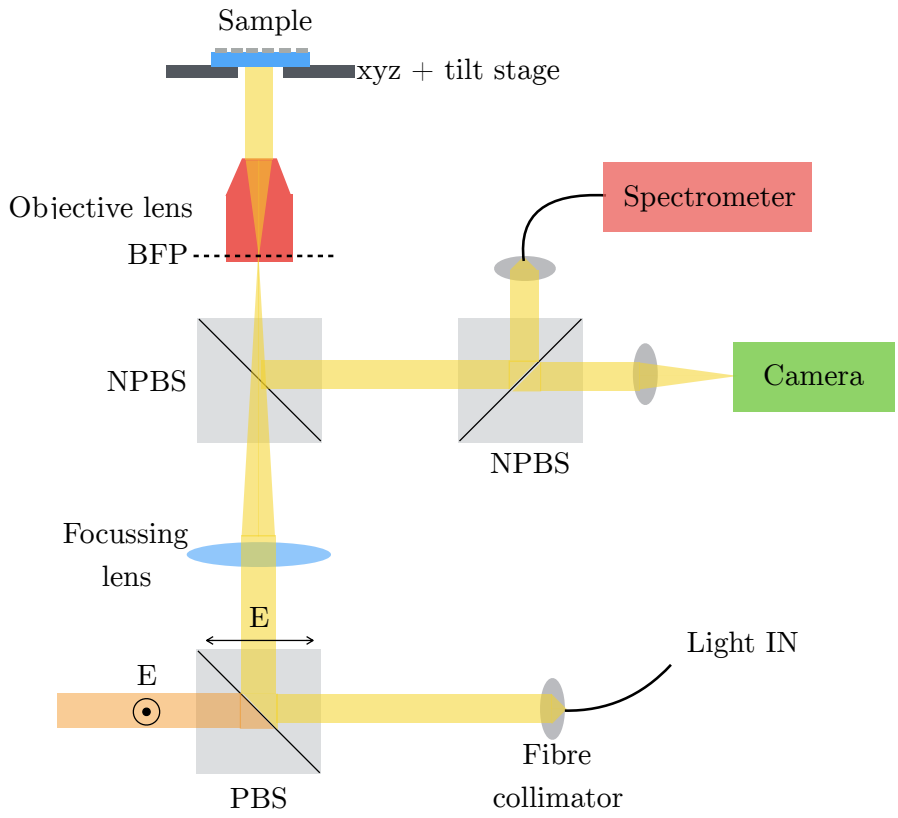

Figure 14. Setup used for the optical characterisation of the gratings. Light from a fibre is injected in the system via a fibre collimator. The polarisation of the beam is selected by a polarising beam splitter (PBS) and only one polarisation is directed upwards, where it is focused on the back focal plane (BFP) of an objective lens. Collimated light emerges from the objective lens and illuminates the sample, which is positioned on a moving and tilting stage. The back-reflected light is directed to a non-polarising beam splitter (NPBS) in order to image the sample with a camera (in green) and to collect the reflectance spectrum with a spectrometer (in red).

is cleaned with a resist remover (1165) followed by an ultrasonic bath in ACE and IPA to ensure that all the remaining resist is removed.

5.2. Optical measurement setup and techniques

The grating is able to operate in two distinct sensing modalities: as an averaging transducer sensing refractive index over its entire surface or by resolving the resonant information spatially, i.e. for imaging. We employed the same optical setup for both schemes. The apparatus works similarly to an inverted microscope including a spectrometer, a camera and a monochromatic source. Unlike a standard microscope, however, the GMR setup provides collimated illumination to the sample. Figure 14 shows a schematic of the system.

Light is injected from a fibre and directed to a polarising beam splitter (PBS). The PBS reflects a single polarisation, while the other one is not used. In the vertical arm, a lens focuses the light in the back focal plane (BFP) of an objective in order to collimate the beam illuminating the sample. The sample is placed on a translation stage to ensure proper

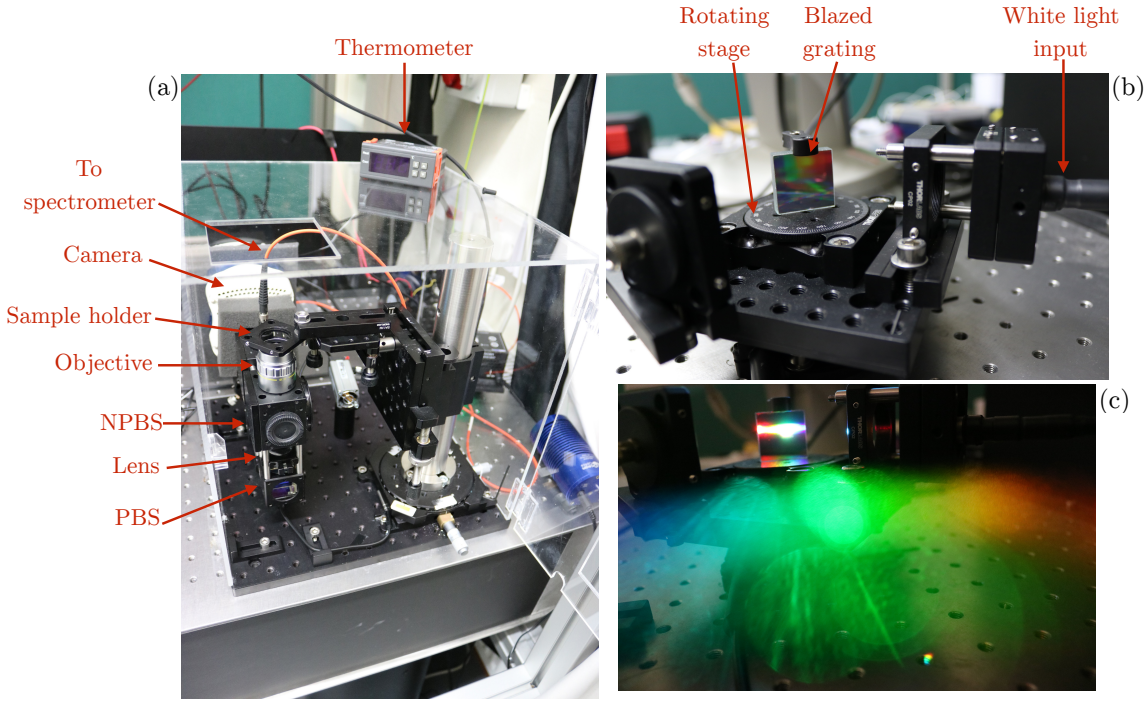

Figure 15. Pictures of the optical setup. The components are bolted onto an optical breadboard for stability and enclosed in a plastic box in order to maintain a constant temperature, should a specific experiment require it. (b) Free-space monochromator used to generate single wavelength from a white light source. A blazed grating diffracts the incoming light at different angles (as illustrated in panel (c)) and the diffracted light is collected by a fibre.

positioning and focussing. Modes with different polarisation are excited by rotating the sample on the stage, given that the polarisation of the incident beam is fixed by the orientation of the PBS.

The back-reflected light is subsequently directed to a horizontal arm by means of a non-polarising beam splitter (NPBS). A second NPBS in the horizontal arm splits the signal again between a spectrometer and a camera. Splitting the signal allows simultaneous recording of the reflection spectrum and imaging the sample. The objective lens can be replaced in order to use different magnifications if required, along with the focussing lens according to the position of the objective's BFP. All the mechanical and optical components are sourced from Thorlabs. The objectives are Olympus NeoDPlan (5x (NA = 0.13), 10x (NA = 0.25), 20x (NA = 0.46)). The camera is a CoolSnap Myo from Photometrics, while the spectrometer is a Thorlabs CCS175. Figure 15 shows pictures of the actual setup.

When operating in sensing modality, we measure the spectrum of the back-reflected light. The camera is needed only to ensure that the grating is centred in the field of view and illuminated by the incident beam. A standard halogen lamp is used to provide a broad

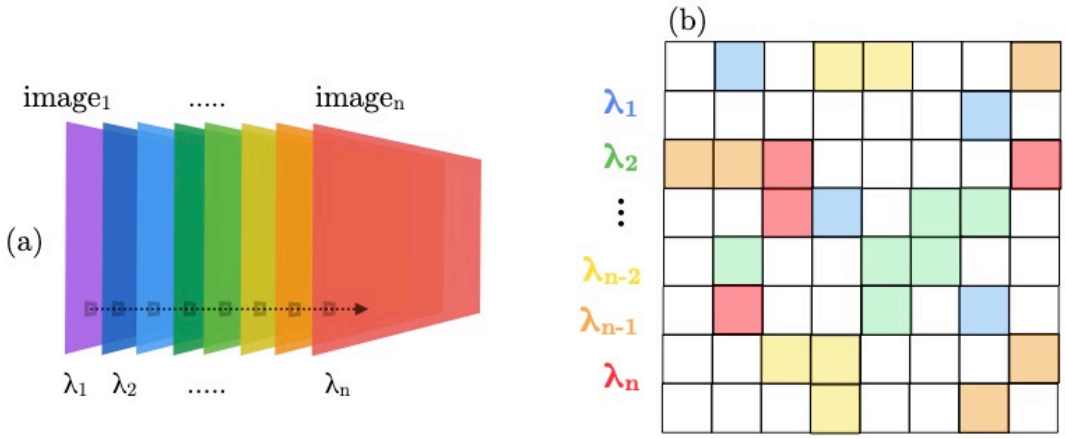

Figure 16. Working principle of hyperspectral imaging. (a) shows a schematic of the hyperspectral cube obtained by illuminating the sample with n different wavelengths (λ_1 to λ_n) and recording a brightfield image at each wavelength. The brightness of each pixel is plotted as a function of the excitation wavelength in order to associate the pixel with the wavelength of maximum brightness. (b) illustrates how the grating surface can be considered as made up of different pixels lighting up at the corresponding resonance wavelength.

wavelength excitation range and spectra are continuously taken for monitoring the spectral position of the peak.

The imaging modality, in contrast, represents the real advantage of using the grating as a biosensor, since most optical biosensors lack the possibility of spatially resolved measurements. To realise the imaging modality, I use the camera and a tuneable light source. A brightfield image is taken at each illumination wavelength, which is scanned in small wavelength steps. This measurement results in a hyperspectral cube where each slice represents an image (see Figure 16(a)) The information content of the cube is analysed with a custom-written MATLAB script. For each pixel, the script identifies the picture at which the pixel is brighter, thereby associating a resonance wavelength to each pixel. The information is then converted into a false colour map, as illustrated in Figure 16(b).

6. Results and discussion

I characterised the gratings to highlight the tunability and versatility in designing their spectral characteristics. I evaluated the refractive index sensitivity and the limit of detection. Finally, I tested the imaging capabilities and assessed the spatial resolution.

6.1. AFM and SEM characterisation

I spent a considerable amount of time on the optimisation of the experimental parameters for the correct fabrication of TiO_2 gratings. In particular, the dry etching needed to be

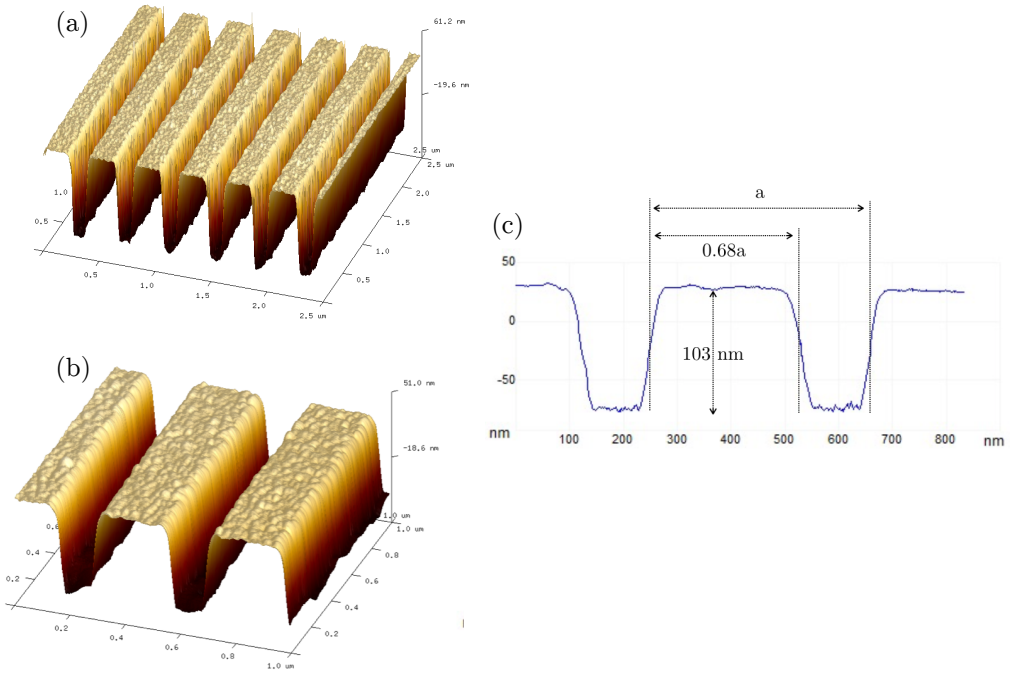

Figure 17. AFM characterisation of a TiO_2 grating. (a-b)3D reconstructions of the grating with different field of view. (c) A slice taken perpendicularly to the grating ridges in (b) for measuring relevant dimensions of the structure. A thickness of (103 ± 2) nm is measured, which compares well to the expected 100 nm from sputtering. The error is obtained by measuring at different locations over the surface.

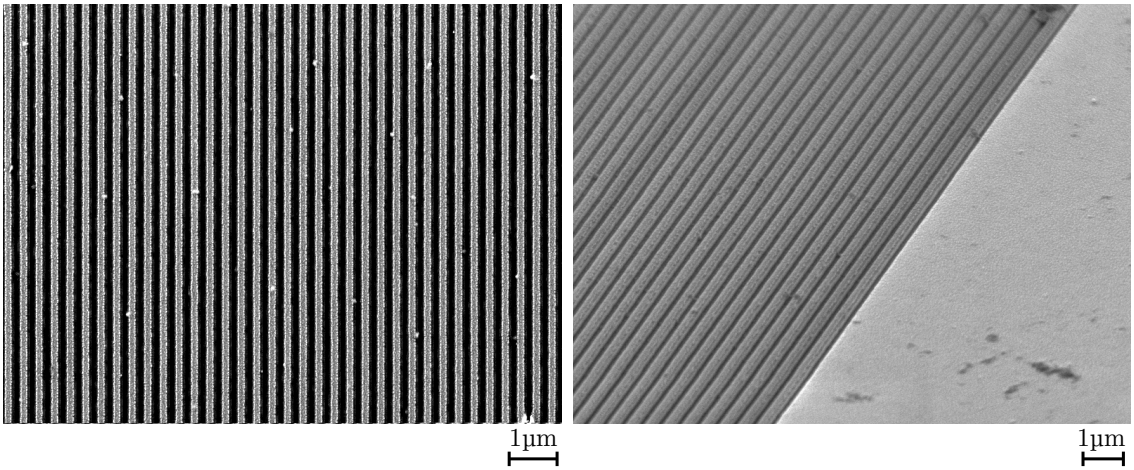

Figure 18. SEM pictures of a TiO_2 grating fabricated on a glass slide. A thin layer of titanium (~5 nm) was sputtered to avoid charging during imaging, which partly explains the observed surface roughness of the ridges.

optimised, with the aim of obtaining vertical side walls of the correct etching depth and with low sidewall roughness. Figure 17(a) and (b) show two AFM micrographs of an optimised grating, while Figure 17(c) is a height profile taken from a slice of (b). The filling fraction, period and etch depth are measured. In particular, the measured etch depth agrees well with the sputtered thickness of the TiO_2 film, suggesting that the film was completely etched. The reported height of (103 ± 2) nm is an average value calculated over different locations across the sample. The sidewalls look reasonably vertical. The small

angle is likely due to the shape of the AFM tip which is inevitably convoluted with the real shape of the edges. The AFM scans were acquired in tapping mode on a BioScope Resolve AFM (Bruker) using a R-TESPA 300 probe (Bruker, resonant frequency of 300 kHz, nominal spring constant of 40 N/m) and a scan frequency of 1 Hz.

Figure 18 shows two pictures taken with a Scanning Electron Microscope (SEM). Given that a thin dielectric grating on a glass substrate has a poor electrical conductivity, I evaporated a thin layer of metal (10 nm of aluminium) to avoid charging during image acquisition.

6.2. Reflectance spectra, sensitivity and limit of detection (LOD)

I characterised the optical properties of the grating using the optical setup described previously. Figure 19 shows reflectance spectra of gratings with different geometrical parameters in order to prove the possibility of tuning the spectral properties of the peak. The reflectance is always referenced against a silver mirror.

Figure 19 (a) shows the response of different gratings as a function of fill factor (FF). The fill factor was modified via the electron beam dose. A shift in the resonance wavelength is clearly visible; in particular, larger FFs result in longer resonance wavelengths, in agreement with RCWA simulations. However, the absolute values of the wavelength do not exactly reproduce the simulated ones. The reason is likely a mismatch between the refractive index of TiO_2 used in simulation and the real value. For the simulation, a rutile crystalline phase with a refractive index of 2.5 was assumed [66]. However, the sputtered film is not crystalline and the sputtering parameters (pressure, power and amount of oxygen) affect the stoichiometry and the quality of the film. These parameters were not fully tuned to optimise the process. Nonetheless, is it worth noting that the absolute resonance wavelength is not critical as we are interested in monitoring its shift upon changes of the local environment.

Figure 19(b) shows instead the reflection spectra acquired for different polarisations of the incident light. Recall that the TM polarisation features the electric field vector perpendicular to the grating grooves (that is parallel to the grating vector **G**), whereas the electric field is oriented along the grooves for TE. Given that the grating is periodic along one direction only, the planar *xy* symmetry is broken. A different behaviour of the two modes is thus expected. Indeed, the resonance wavelength is shifted by about 20 nm and a remarkable broadening of the line is observed. While the linewidth of the TM mode is

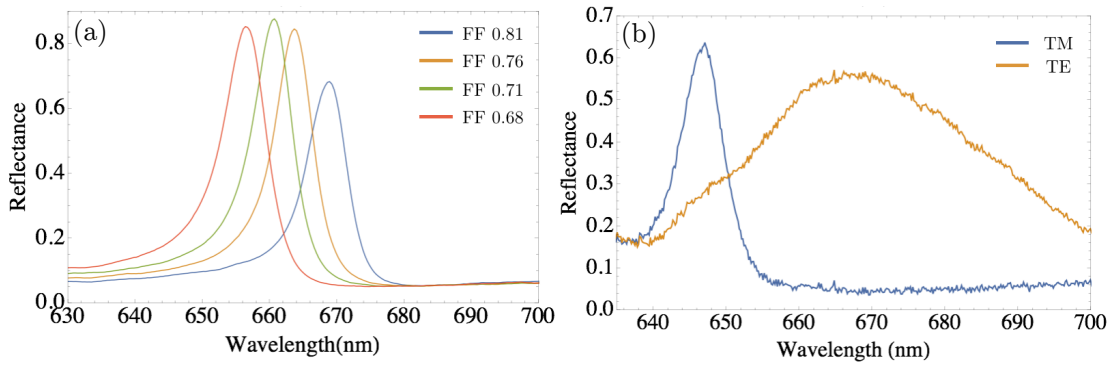

Figure 19. Reflectance spectra of TiO_2 gratings for different FFs and polarisations of incident light. (a) Reflectance spectra of TiO_2 gratings with different fill factors (FF). The reflectance is normalised to a silver mirror. The resonance condition is clearly modulated by the FF because of the different effective index of the mode. (b) Spectra for the two different polarisations of the incident light. The two modes feature different resonance wavelengths and linewidth due to the different effective index and modal distribution. Specifically, the TM mode is narrower, because it couples less into the out-of-plane direction.

about 6 nm, the TE is over 30 nm broad, leading to a factor ~5 between the two Q factors, as predicted in the simulation section (section 4.5).

A good way of measuring the refractive index sensitivity is to expose the grating to solutions with slightly different refractive indexes while continuously monitoring the spectral position of the resonance. Figure 20(a) shows four reflectance spectra obtained by covering the grating with the four solutions indicated in the legend. I used the TM mode and I flushed the solutions through a simple PDMS microfluidic channel bonded onto the sample.

The spectra in Figure 20(a) show a distinct red-shift as the refractive index is increased, as expected from simulations. It is also evident that the shape of the resonance is asymmetric, which is typical of physical phenomena where interference between two different scattering processes occurs, known as a Fano resonance [67,68]. In particular, a Fano resonance occurs when a given input state can scatter via two different processes, which then interfere. In this specific case, the first non-resonant process corresponds to the thin-film response of the grating, which features a low Q factor, while the second high-Q resonance is represented by the light coupled to the in-plane GMR mode. The corresponding spectral response is governed by a Fano lineshape of the form:

$$R(\lambda; a, f, q, \Gamma, \lambda_r) = a + f\frac{\left[q + 2\left(\frac{\lambda - \lambda_r}{\Gamma}\right)\right]^2}{1 + \left[2\left(\frac{\lambda - \lambda_r}{\Gamma}\right)\right]^2} \tag{23}$$

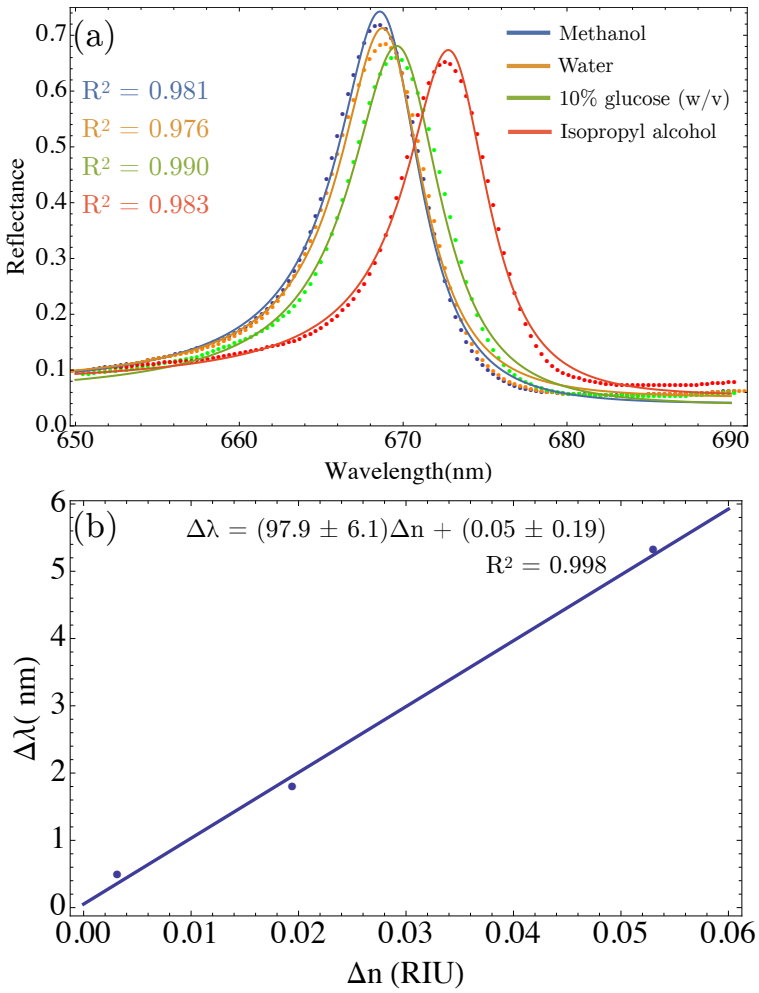

Figure 20. Measured resonant wavelength shift for different refractive indexes of the cover medium (a) Measured reflectance spectra for different cover media with increasing refractive index. A larger refractive index results in a redshift of the resonance wavelength. Spectra are fitted to a Fano lineshape, as shown by the continuous lines. The goodness of the fits is quantified by the R^2 values in the inset. (b) Shift of resonance wavelength $\Delta\lambda$ calculated from the previous fits as a function of the index contrast Δn. Each point refers to a single spectrum taken for the corresponding cover medium. The behaviour is linear, with the slope representing the bulk wavelength sensitivity of the grating.

where λ_r is the resonance wavelength, Γ is the spectral linewidth, *a* is an offset considering any background reflection and *f* is an amplitude factor. The dimensionless parameter *q* accounts for the asymmetry of the spectrum by describing the ratio between the resonant and non-resonant transition amplitudes in the scattering process. q can either take positive or negative values. For |q| values of the order of unity, which imply that the resonant and non-resonant amplitudes are comparable, the lineshape is strongly asymmetric; if |q| is large, the resonant pathway prevails, the lineshape tends towards a symmetric Lorentzian shape, while for small |q| values (|q|<1), it becomes a reversed Lorentzian [68].

After fitting the curves in Figure 20(a) to a Fano lineshape, the corresponding resonance wavelengths λ_r were plotted as a function of the refractive index. Figure 20(b) shows the

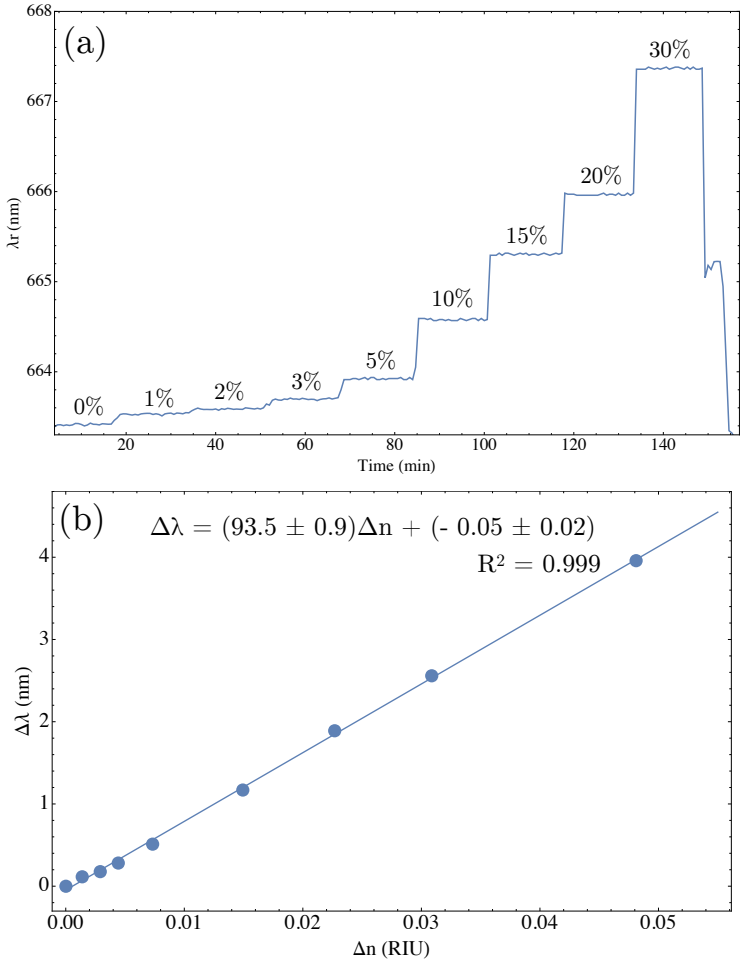

Figure 21. Measured wavelength shift for solutions with increasing glucose content. (a) Resonance wavelength as a function of time, for different concentrations of glucose solution, with concentrations shown above each step. Increasing the glucose content results in an increase of the refractive index of the solution, hence a shift of the resonance towards higher wavelengths. (b) Shift of the resonance wavelength Δλ as a function of the index contrast. Each data point is the average wavelength shift over the plateau value at each glucose concentration. Error bars are comparable to the size of the markers, hence not visible. The linear fit allows us to calculate the bulk wavelength sensitivity of the grating.

magnitude of the wavelength shift ($\Delta\lambda_r$) as a function of the refractive index change (Δn, with respect to methanol). A linear fit gave a value of the gradient of (97.9 ± 6.1) nm/RIU.

I later performed a similar measurement on a different sample by using glucose solutions, whereby a serial dilution of glucose in DI water produces slightly different refractive indexes to be tested. The solutions were withdrawn from different cuvettes with a syringe connected to a microfluidic pump at a flow rate of 20 µl/min. The grating surface was exposed to each solution for 15 minutes, with a spectrum being recorded every 30 seconds. The corresponding resonance wavelengths λ_r are shown as a function of Figure 21(a). Each step represents the injection of a solution with increasing glucose content (reported as a percentage above each plateau).

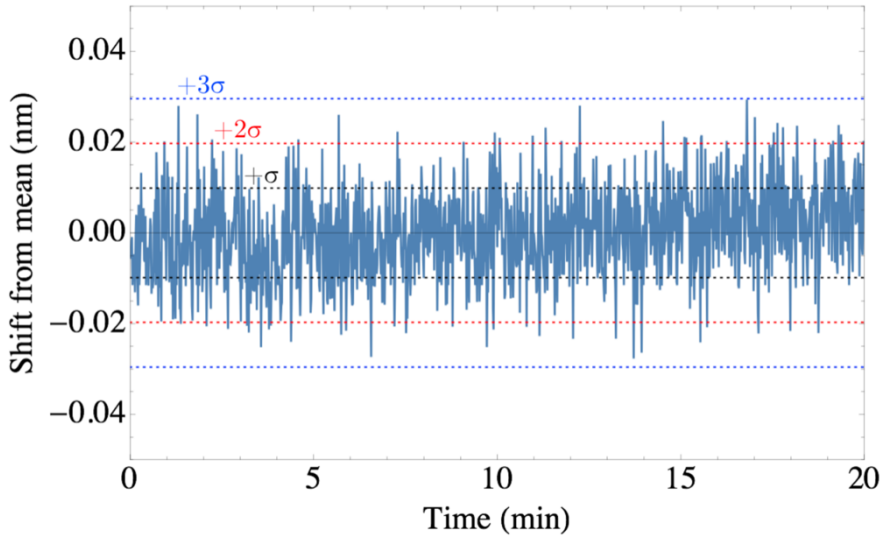

Figure 22. Deviation of resonance wavelength over 20 minutes for a grating exposed to DI water. The deviation is calculated with respect to the average value over the duration of the experiment. Increasing multiples of the standard deviation are shown as dotted lines. 3σ is taken as a threshold for the limit of detection.

Figure 21(b) illustrates $\Delta\lambda$ as a function of Δn, with respect to simple DI water (initial 0% solution). Each value of λ_r is calculated by averaging the values over each plateau at constant concentration of glucose. 30 values were recorded at each concentration. The linear fit gives a gradient of (93.5 ± 0.9) nm/RIU, which is compatible to the value obtained in the previous experiment (Figure 20(b)). These values also agree satisfactorily with typical sensitivities reported for other gratings, in particular with similar devices reported by Cunningham's group [1–3].

Another important figure of merit for a (bio)sensor is the LOD, namely the smallest detectable change in refractive index. The value of the LOD is strictly related to the experimental sources of noise resulting in an inevitable distribution of λ_r about a mean value. The main causes are inhomogeneities in the solution, thermal fluctuations, noise due to the light source and camera and mechanical vibrations of the measurement setup.

In order to evaluate the LOD, I monitored the spectral position of the peak while exposing the grating to the same solution for a certain period of time. Spectra were recorded each second for about 20 minutes with DI water being continuously flushed on the surface. Each spectrum was fitted to a Fano lineshape and the shift from the average resonance wavelength value over time is plotted in Figure 22.

The mean value over the entire range was $\lambda_{rm} = 663.11$ nm with an associated standard deviation $\sigma_r = 9.90$ pm, as shown by the horizontal dotted lines in Figure 22. The smallest

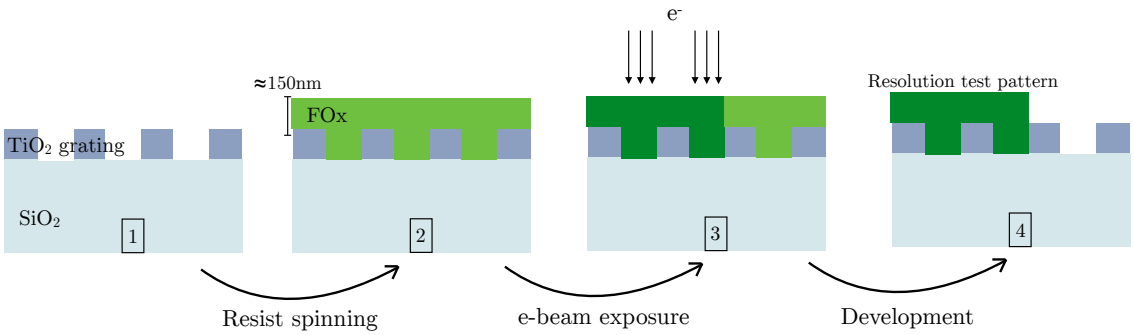

Figure 23. Steps for the fabrication of a resolution test pattern onto a grating. The grating was previously fabricated on glass (1), then 150 nm of FoX is spun onto it (2). The resolution pattern is defined with electron beam lithography by exposing the areas of interest (3). Upon development, the exposed areas remain on the sample because of FOx being a negative-tone resist (4).

detectable shift above the noise is commonly assumed to be above three times the standard deviation $3\sigma_r$ = 29.6 pm. The LOD is thus calculated by dividing this number by the measured sensitivity. A value of $(3.1 \pm 0.2)*10^{-4}$ RIU was obtained.

6.3. Spatial resolution for imaging

The imagining capability of the grating stems from the finite lateral penetration depth of the GMR mode, which results in neighbouring regions resonating at different wavelengths depending on the local refractive index. The method is extremely useful in providing significantly higher contrast than a standard brightfield image, in which phase objects such as cells are hardly recognizable. Like for any imaging system, the resolution is an important parameter.

Most of the existing literature focuses on imaging eukaryotic cells, whose size is in the order of tens of microns. These relatively large dimensions make the GMR grating able to fully resolve such cells and provide well-defined mapping. Our aim, instead, is to monitor bacteria, which are significantly smaller than eukaryotic cells. For example, an *Escherichia coli* bacterium is typically 2-3 μm long and 0.5-0.8 μm wide [69].

I tested the spatial resolution following the method introduced by Triggs *et al.* [58]. I fabricated a test pattern onto the grating with the aim of providing a known distribution of refractive index to be imaged. In particular, I realised a pattern using a negative electron-beam resist (FOx, Flowable Oxide) by exposing blocks of different sizes and reciprocal distances. The fabrication procedure is summarized in Figure 23. FOx (Dow-Corning) was diluted with MIBK (Methyl Isobutyl ketone) at a ratio 1:1 in order to achieve a thickness

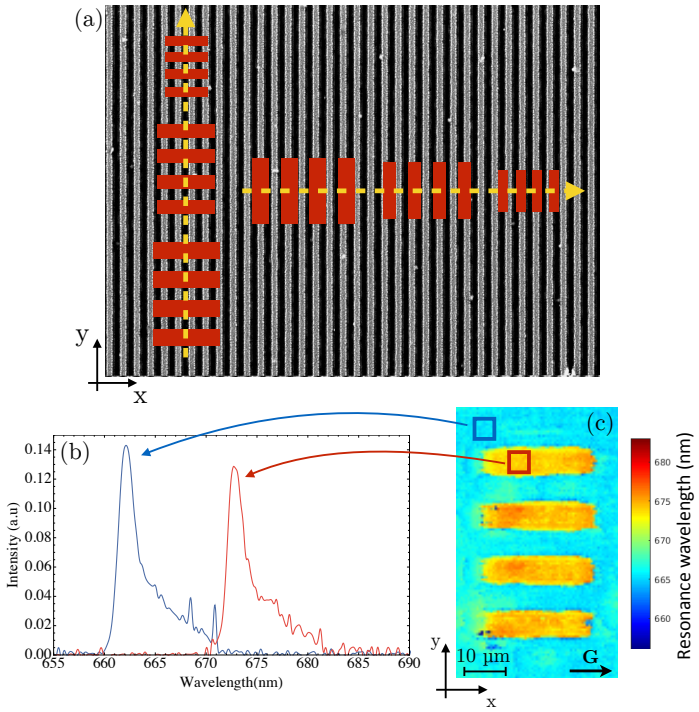

Figure 24. (a) Schematic of the blocks fabricated in FOx onto the grating. Two sets are exposed: along the grating direction and perpendicular to it, respectively. The yellow arrows indicate the direction along which the resonance wavelength will be plotted. (b) and (c). Hyperspectral image of a set of blocks (25µm wide and 25µm apart), whereby (b) illustrates the intensity spectra of the areas highlighted by the corresponding boxes on the image. Different pixels show maximum brightness at different wavelengths.

of around 150 nm at a spin speed of 2000 rpm. The thickness of the FOx layer was measured by spin coating a silicon substrate under the same conditions and measuring it with a bespoke ellipsometer. The resist was exposed with a base dose of 500 µC/cm^2. The structures were then developed in MF-319 for 10 minutes at room temperature in order to dissolve the unexposed resist.

A first criterion to determine the resolution could be defined by looking at the resonance image and locating the smallest/closest blocks that are clearly distinguished from the background. This method can be improved by plotting a profile of the values of λ_r across the series of blocks. A schematic is shown in Figure 24(a) (not to scale). I fabricated a variety of sizes, orientations and relative distances between the blocks in order to test the imaging capability for progressively smaller and closer blocks and in both spatial directions. Each group of blocks contains four units with a spacing equal to their size along the yellow dashed arrows. The sample was covered in DI water to mimic the typical scenario of an aqueous analyte. Four blocks are shown as an example in Figure 24(b). I chose to test the imaging ability of the TM mode as a compromise between the spatial

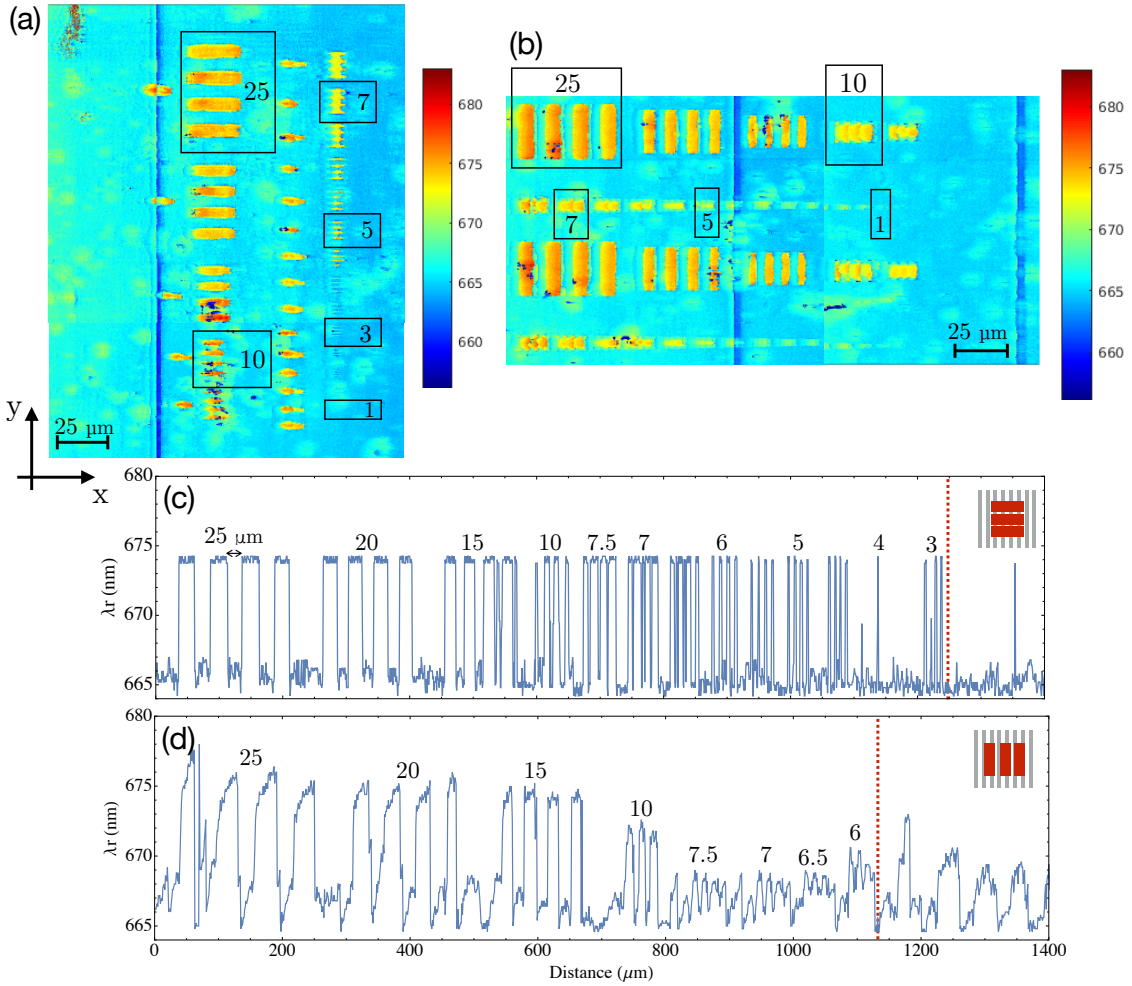

Figure 25. Hyperspectral images of the resolution test pattern. (a) and (b) show hyperspectral images of the grating with the resolution pattern oriented perpendicular and parallel to the grating lines, respectively. The blocks appear orange/red because of the associated higher resonance wavelength, as indicated in the colourbars. The dimensions of the blocks are indicated by the labels next to each group. (c) and (d). Resonance wavelength profiles across differently seized and spaced blocks being oriented perpendicular and parallel to the grating grooves, respectively. The vertical red dashed lines in each plot indicate the resolution limit beyond which individual blocks become indistinguishable.

resolution, which is poorer compared to that of the TE mode, and the refractive index sensitivity, which is instead superior to that of the TM mode, as discussed in section 4.5.

The full hyperspectral images are shown in Figure 25, which includes colour maps showing the sets of blocks ((a) and (b)) and the resonance wavelength profiles across the bars in (c) and (d). λ_r displays periodic plateaus due to the alternation between resist blocks and DI water. The widths and distances between the plateaus decrease as smaller blocks are met. The labels above each step are expressed in µm and refer to the size and distance between the blocks within each group of four. The two small insets depict a diagram of the orientation with respect to the grating grooves underneath.

The vertical red dashed lines in Figure 25(c) and (d) represent the limits beyond which the plateaus are no longer separable, meaning that the resolution limit is reached. Beyond these values, the blocks are of the order of, or smaller, than the lateral penetration depth of the optical mode. This threshold was found to be around 3 μm for the direction parallel to the grooves and around 6 μm for the perpendicular one. Note that the resolution is poorer along the *x* direction. This is expected since the standing mode oscillates along the grating vector direction. This lateral propagation blurs out the resonance information only in the *x* direction. This effect is also apparent from the colour maps: the smallest blocks in Figure 25(b) look less defined than those in panel (a).

7. Inadequacy of GMR for single bacteria imaging and alternatives

As mentioned in the introduction, the original aim of this work was to exploit the photonic resonant surface provided by a 1D grating for imaging and monitoring individual bacteria. However, in light of the findings revealed here, it is clear that guided mode resonances do not represent the most viable solution for single bacteria detection and/or imaging. The main reason being, clearly, the spatial resolution limit. The typical dimensions of a bacterium are smaller than the lateral extent of the mode (L_p), meaning that an individual bacterium is below the resolution limit. Note that a bacterium would be approximately of the same size of one of the 1 μm blocks fabricated in the previous resolution test, none of which was clearly distinguishable in the previous analysis (Figure 25(a) and (b)). Further insight is provided by Figure 26, where I imaged the same area on a grating with a standard brightfield microscope (panels (a) and (b)), SEM (panel (c)) and hyperspectral imaging (panels (d) and (e)). The imaged features are trapping wells made of PDMS, integrated with a microfluidic channel and bonded onto the grating. The relevant aspect is that different sizes of wells are fabricated (channels numbered 1,2,3 in panel (a); see the microfluidic chip design A in Appendix A1). In particular, the blocks in the close-up frame (b) are measured by SEM imaging (see panel (c)). The dimensions of the blocks, reported in μm, place them approximately at the resolution limit of the grating. Indeed, the hyperspectral picture in Figure 26(d) shows blurred features and poorly defined edges. The characteristic U-shape of the traps is more or less identified in the magnified frame in panel (e), even though details are very poor. Note the scale bar in Figure 26(e) and recall the typical length of a bacterium of about 2-3 μm.

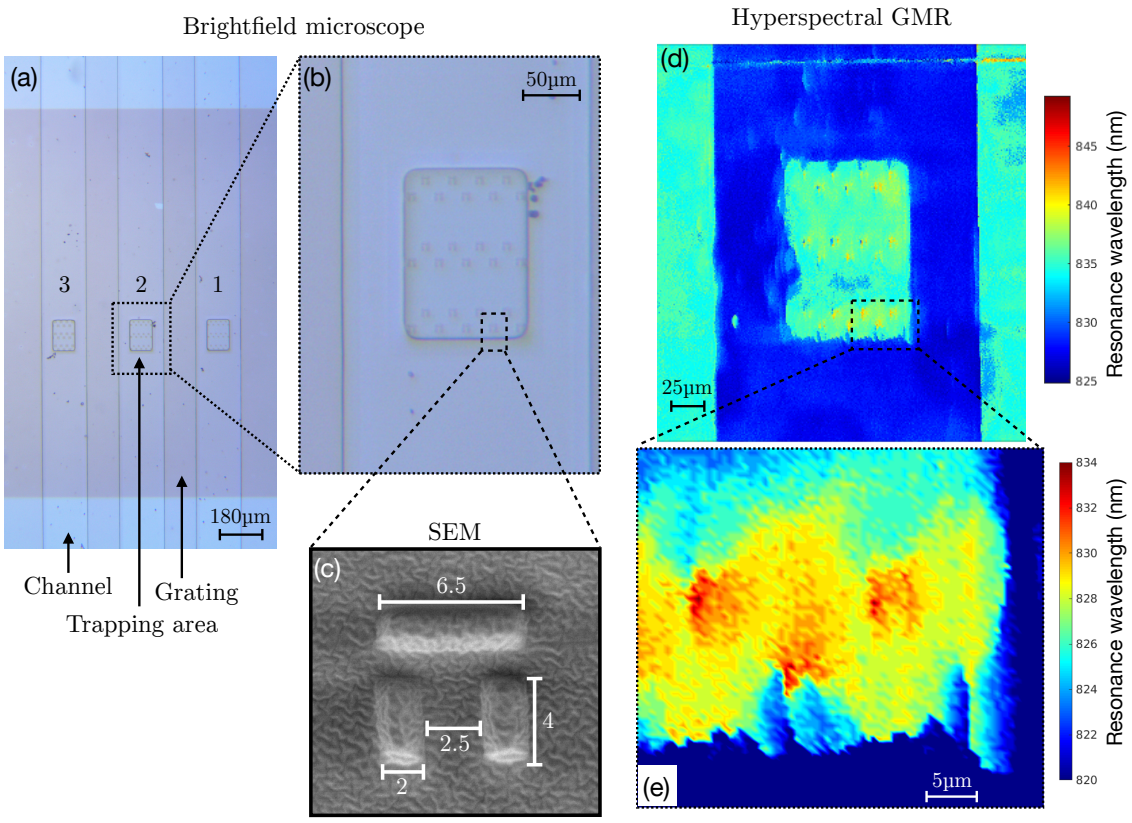

Figure 26. Comparison of imaging methods for micron-sized features. (a) Brightfield microscope image of three PDMS microfluidic channels permanently bonded onto a grating. The trapping regions are located in the central areas of each channel. Traps of three different sizes are fabricated, as indicated by the labels (1,2,3). (b) Close-up image of the middle channel, which contains three horizontal arrays of PDMS trap. (c) SEM image of a single trap from the middle channel with dimensions being reported in microns. (d) Hyperspectral image of the middle channel. While the channel and the central trapping area are clearly identified, the arrays of traps are barely visible. (e) Close-up of the previous hyperspectral scan. Three individual traps appear rather blurry and scarcely identifiable. Note the difference in the colorbar values, necessary to enhance the contrast.

These arguments imply that an individual bacterium would cause a shift in resonance and could be imaged, provided that a sufficient magnification is used. However, the sensitivity would be significantly reduced since the mode would probe an entity smaller than its extent, thereby resulting in the signal being washed out. In other words, the entire available power in the mode could not be used to probe a single bacterium. This would make it particularly challenging to study a single organism with sufficiently high resolution to gain any significant information on bacterial viability.

Overall, a guided mode resonance excited in a 1D grating cannot provide sufficient spatial resolution to clearly image features as small as a single bacterium. In order for the pixel size to be smaller, or at least comparable to the size of a single bacterium, the grating should excite and extinguish the quasi-guided mode within a lateral size of the order of the grating period, i.e. relying almost on a single ridge/groove interface. Given the dielectric

Bragg-reflection nature of the mode, this scenario is clearly not possible. Conversely, this capability has been demonstrated with plasmonic sensors, in particular for SPRi (Surface Plasmon Resonance imaging). The operational principle is analogous: the plasmon resonance is tracked on a pixel by pixel basis. However, a surface plasmon wave can be tuned to decay within a very short distance, depending on the film thickness and excitation wavelength. For instance, a 47 nm thin layer of gold at a wavelength of 532 nm reduces the lateral propagation of the plasmon to 200 nm [70]. Basically, it is physically possible to extinguish the SPR within very short lengths (up to very close to the diffraction limits) because of the extreme confinement allowed by metals and their lossy nature. The possibility of tailoring the SPR extinction length to sub-micron dimensions has indeed enabled imaging of single bacteria tethered to the surface via antibodies [71] and even single influenza viruses (about 100 nm in size) [72]. Mapping of proteins within cell membranes and of secretions in the vicinity of the cell body has also been demonstrated [73,74].

At this point, a different solution was needed to define quantities and methods to assess the response of individual trapped bacteria to antibiotics. Hence, I decided to focus mainly on the hydrodynamic optimisation of the trapping assay (chapter III of the thesis) and to conduct the bacteria analysis by employing a simple phase contrast microscope. Such a microscope is commonly used for cell imaging as it provides sufficient contrast for imaging biological entities. Moreover, it is diffraction limited, meaning that it also provides sufficient resolution to allow single bacteria imaging and monitoring.

Nevertheless, it is worth noting that the photonics strand presented in this chapter II has laid foundations for current developments as a viable sensing platform. A few examples are briefly described below:

- 1D gratings are being employed for the sensing of biofilm growth and its response to antibiotics. The motivation here being the importance of the bottom layer of a biofilm, which is difficult to access with drugs and is responsible for recurring infections. Optical biosensors, in particular GMR gratings, are particularly suited to this scope. One of the reasons being the short penetration depth of the optical mode which allows one to monitor a nascent biofilm by probing its very first layer and its evolution upon antibiotic treatments. The lateral propagation does not represent a limitation in this case, since biofilm forming colonies typically extend over tens of microns.

- TiO_2 is being developed as a material of choice for use with different geometries, in particular as an extension to 2D GMR surfaces, i.e. a surface featuring periodicity in both the x and y direction. The geometry in this case is a 2D array of holes instead of ridges/squares, since they have been shown to provide higher surface sensitivity and a stronger mode confinement. These improvements will allow for better biosensing performances as well as better spatial resolution for imaging. The findings presented in this work have been a fundamental starting point for the 2D GMR, especially in terms of the optimisation of fabrication steps and measurement techniques.

- The introduction of S4 is also representing a valuable addition to the photonics research strand as a powerful and versatile simulation toolbox with vast applicability to the class of structures we aim to employ for biosensing in our group.

8. Conclusions and future perspectives

The work presented in this chapter of the thesis does not fully support the scope of the project because the stated goal, namely monitoring the response of individual bacteria to antibiotics using photonic resonances, was not met. Nevertheless, the work has been particularly useful and insightful for gaining a deeper understanding of the optical properties and sensing capabilities of resonant photonic structures using guided mode resonances. It has also allowed us to point out strengths of this approach as well as weaknesses and limitations. Finally, the process has represented a valuable lesson of scientific development and research by exposing the most fundamental aspect of the scientific method: initial hypotheses may not be correct and may be invalidated, therefore new strategies are required to move forward.

The main outcomes of this chapter can thus be summarised as follows:

- Optics and Photonics offer powerful tools for (bio)sensing. Optical biosensors have the important advantages of being able to afford parallel and non-contact readout, being non-corrosive, and not suffering from electromagnetic interference. The evanescent tail sensing mechanisms also allows for label-free sensing, whereby the

use of photobleaching, lengthy-to-process and potentially interfering fluorescent labels is avoided.

- Guided mode resonance (GMR) sensors represent a viable solution for low-cost, easy to operate and in-field biosensing solutions. While their performance in terms of sensitivity and limit of detection is not record-high, research in the field is remarkably active and exciting improvements can be expected. GMRs promise an unprecedented easiness of interfacing and measuring, due to the intrinsic leaky nature of the optical mode.

- GMRs offer imaging capabilities, which are not a common feature among optical biosensors. They are suitable for studying biological objects of the order of tens of microns, such as eukaryotic cells, tissues and biofilms. However, GMRs are less suitable for single bacterial cell imaging and monitoring that requires a higher spatial resolution, the limitation being intrinsic to the decay/propagation length of the quasi-guided resonance. A certain number of grating periods, i.e. ridge/groove interfaces, is needed to excite, propagate and couple the mode out.

- A more viable solution for single bacteria imaging is represented either by SPR-based imaging devices or, more simply, by a standard phase contrast microscope, which allows for higher spatial resolution and sufficient contrast to clearly image biological entities. New exciting development might also be expected from the aforementioned 2D GMR structures in high-index materials (i.e. TiO_2 or amorphous silicon), whose tight mode confinement will allow for better spatial resolution.

III. Microfluidics for single bacteria trapping

This chapter of the thesis focusses on the use of microfluidics and hydrodynamic trapping for susceptibility testing. I start by discussing some examples from the recent literature that highlight the significant advantages of microfluidics to biologically relevant questions. I will devote particular attention to applications aimed at testing bacterial susceptibility to antibiotics in the context of antimicrobial resistance (AMR). Secondly, the theoretical framework behind the fluid flow in a microfluidic channel is presented, with a particular emphasis on the trapping geometry. Some preliminary experimental results are presented to support the theoretical analysis and the optimisation of the device. Then, I introduce the concepts of fluid shear and trapping efficiency, discuss their connection to the flow rate and bacterial motility and support this connection with preliminary experiments. The geometry of the trap is first optimised in simulations and then in fabrication. Finally, I will show how the assay was validated by using bacteria of different motility and by investigating the effects of different antibiotic on the motility and morphology of single *Escherichia coli* (*E. coli*). More specifically:

- A general introduction to microfluidics is given in section 1, while section 2 focusses on three relevant historical applications on single bacteria studies that I chose to highlight the possibilities offered by microfluidics.
- Section 3 presents a general overview of AMR by discussing its main causes, its spread and predictions of its societal impact over the next few decades.
- Section 4 discusses some examples from the recent literature on the applications of microfluidics to antimicrobial susceptibility testing. I will focus on recent efforts devoted to the quest for signatures alternative to bulk bacterial growth, with the aim of minimising detection time;
- Hydrodynamic trapping techniques for single cells are reviewed in section 5;
- The Navier-Stokes equation that governs the behaviour of fluids is presented and solved for simple geometries in section 6;
- Section 7 includes COMSOL simulations of the flow for various dimensions of the channel and of the fluid flow around and inside the trapping arrays. The geometry of the trap is also optimised to guide the subsequent fabrication.

- I will analyse the link between the trapping efficiency of the device and the velocity of the fluid in section 8 and support it with preliminary experimental results.
- Section 9 tracks bacteria swimming inside the microfluidic channel, providing a useful tool to sum up and prove the findings of chapter 8.
- In section 10, I will focus on the methodologies employed chapter III of the thesis by covering all aspects: samples fabrication, characterisation and trapping experiments with bacteria;
- Section 11 describes the custom MATLAB script that I designed and used for post-processing of the data to retrieve the quantities of interest to this thesis;
- The main experimental results are presented in section 12, including findings on the size and shape selectivity of the assay, control experiments with bacteria of different motility and the effects of three antibiotics of very different nature (kanamycin, ampicillin and trimethoprim) on susceptible and resistant strains. Additionally, a comparison with standard definitions of susceptibility is presented, i.e. growth curves measured within the channel and standard microdilution assays.
- Finally, section 13 provides a summary of the findings, potential future development and concluding remarks.

1. Introduction

Microfluidics is the science of manipulating and controlling the flow of fluids at the microscale. This typically happens inside microchannels with dimensions of the order of tens to hundreds of micrometres, with the aim of performing a number of different tasks. These tasks include, but are not limited to, mixing reagents for chemical reactions, separating particles such as cells, bacteria and even proteins from the main fluid flow or sorting them, focusing and defocussing flows, generating microdroplets to create isolated environments and many more [75–77]. A micron-sized device that performs all of the steps commonly conducted in an analytical chemistry lab is known as a Micro Total Analysis System (μ-TAS), or lab-on-a-chip platform [78,79].

Why would one want to shrink lab procedures down to this scale? A few practical reasons are obvious: equipment becomes small, thereby occupying less space in a lab; less sample, analytes and reagent volumes are needed, and devices are portable and easy to store. However, there is also a more fundamental reason that goes beyond mere practicality. One of the seminal papers in the field of μ-TAS [5] beautifully pointed out how scaling the length of an analysis platform results in a power law decrease of the typical time scale needed for diffusion, reaction and common lab routines. Microsystems are intrinsically faster and more efficient than their macro counterpart.

This approach is not novel in science, since it was the same motive that drove the microelectronics industry towards miniaturisation. However, there is a fundamental scale difference between the two worlds. The physics of fluids scales more rapidly with the dimensions of the system. While modern nanoscale electronic devices operate in a regime where electrons behave in a similar way as in the macroscopic world, microfluidic devices deal with fluidic behaviour that is profoundly different from the macroscale. In the realm of microfluidics, classical effects such as buoyancy, sinking, and common swimming action are meaningless. In fact, the flow is governed by viscous forces and damping, i.e. inertia does not play any role. A swimmer that was to stop stroking inside a microfluidic channel would come to rest immediately [80]. Additionally, fluid mixing in the classical sense is not relevant since flows are laminar, fluid sheets move in an orderly manner and faithfully follow streamlines, with intermixing happening only through diffusion. Finally,

heat and mass transfer times are greatly reduced compared to the macro-scale because of the enhanced surface-to-volume ratio.

Some of these features have made microfluidics a highly desirable tool in the field of microbiology, where precise fluid handling, control over the cells' environment and multiplexing have suddenly opened a completely new world of possibilities. Microfluidics is enabling microbiology to overcome several of its traditional limitations by providing an unprecedented spectrum of techniques and platforms to tackle unanswered problems. It is not an overstatement to say that microfluidics is revolutionising microbiology and our understanding of many biological processes. The reasons for this are illustrated in the next chapter by examining three "historical" experiments that enabled us to gain insight into the bacterial world.

2. Microfluidics for single bacteria

Traditionally, microbiology has been concerned with tubes and plates. Despite being well-established techniques, this approach does not allow targeted long-term monitoring of single bacteria while controlling their environment. Traditional microscopy techniques are not compatible with this requirement either. Because of the exponential growth of bacteria, environmental resources are consumed rapidly, thereby creating gradients within the population and creating inhomogeneity over the colony. Furthermore, the growth to billions of units makes it challenging to follow the behaviour of a single bacterium over time.

Why do we care about single bacteria in the first place? The first reason is that seemingly simple questions about bacterial life and behaviour, such as "How long does a bacterium live?" or "Can bacteria squeeze through narrow passages?" have long been answered since we have had access to single cell techniques, often enabled by microfluidics [81]. Part of this information is impossible to retrieve from an entire colony level experiment because of insufficient resolution. Moreover, just like it is often unfair to tar everyone with the same brush, bacterial colonies are deeply heterogeneous. Since traditional microbiology operates at the bulk level, any cell-to-cell difference is shadowed by the process of bulk averaging over a large number of cells. Contrarily, single cell techniques allow us to probe this heterogeneity and to reveal underlying distributions [82–84].

Three significant studies enabled by microfluidics represent valuable examples to highlight how single cell analysis has allowed unveiling mechanisms that would have remained obscure otherwise.

One of the most popular platforms that allows single bacteria studies is the so-called mother machine introduced by Wang *et al.* in 2010 [85]. In this device, a single bacterium (the pole mother cell) is localised in a narrow dead-end channel with dimensions matched to the cell body. By doing so, the growth of *E. coli* is constricted to the channel direction, thereby allowing one to follow bacterial division for more than 200 generations. Monitoring successive generations revealed that while the division rate was strikingly constant during the entire observation, the death rate increased after ~50 generations. These findings represented the first evidence that growth and death might be uncoupled processes, a possibility that had not been contemplated before. Specifically, the authors ascribed cell death to a growth-independent accumulation of a lethal factor. Furthermore, the mother machine design has fuelled several further applications to a variety of contexts, some of which will be described later on (chapter 4).

My second example is related to the phenomenon of drug persistence. In the 1940's, it was observed that a small fraction of bacteria, named persisters, always survived penicillin treatment in staphylococcal infections [86]. Persister cells have since been observed for a broad variety of bacteria and antibiotics [87]. However, unlike genetically resistant mutants, cells regrown from the persister fraction showed susceptibility. It was not until 2004 that the mechanism behind persistence was revealed by a series of single-cell experiments enabled by microfluidics. By immobilising single *E. coli* in open-ended channels, Balaban *et al*. [88] discovered a link between persistence and a phenotypical switch in the growth rate. While the vast majority of bacteria grew at a normal rate, a minute fraction of the population was dormant. These dormant cells were resistant to antibiotics. Microfluidics later gave even deeper insights into the phenomenon by identifying an opportunity time window during which the persister cells are more vulnerable to the antibiotic's treatment [89]. Clearly, these insights are very valuable from a clinical point of view and they need to be considered when combating infections.

The third and final case refers to microfluidics at the single cell level and the mechanical properties of the bacterial cell wall. Mannik *et al*. [90,91] used micro and nano-channels of different width to probe the ability of bacteria to pass through them. They discovered

the previously unknown ability of *E. coli* to squeeze through channels as narrow as half their width, down to 300 nm. Cells emerging from the opposite end of the channel were deformed, even though successive generations recovered their normal shape and growth rate. Interestingly, this effect was not observed in gram-positive bacteria, thereby suggesting that the different composition and rigidity of the cell wall plays an important role in conferring this ability.

3. The threat of Antimicrobial Resistance (AMR)

Human beings co-exist with bacteria. Actually, we are more bacteria than human, since there are about 1.3 times as many microbial cells in our body as there are human cells [92]. This co-existence is generally harmonious and mutually advantageous, as in the case of commensal bacteria which fulfil beneficial functions as long as they outnumber pathogenic organisms. However, opportunistic bacteria can develop virulence and cause infections, which are traditionally treated with antibiotics. Antibiotics are molecules that interfere with the normal bacterial life cycle by either stopping cell division (bacteriostatic action) or killing cells (bactericidal action).

However, the use of any therapeutic agent is always compromised by the development of tolerance or resistance by the microorganism. Alexander Fleming, who discovered the world's first antibiotic (penicillin) in September 1928, had already acknowledged the threat during his lucid Nobel prize lecture in 1945 [93]:

> *"It is not difficult to make microbes resistant to penicillin in the laboratory by exposing them to concentrations not sufficient to kill them, and the same thing has occasionally happened in the body. The time may come when penicillin can be bought by anyone in the shops. Then there is the danger that the ignorant man may easily underdose himself and by exposing his microbes to non-lethal quantities of the drug make them resistant. Here is a hypothetical illustration. Mr. X. has a sore throat. He buys some penicillin and gives himself, not enough to kill the streptococci but enough to educate them to resist penicillin. He then infects his wife. Mrs. X gets pneumonia and is treated with penicillin. As the streptococci are now resistant to penicillin the treatment fails. Mrs. X dies".*

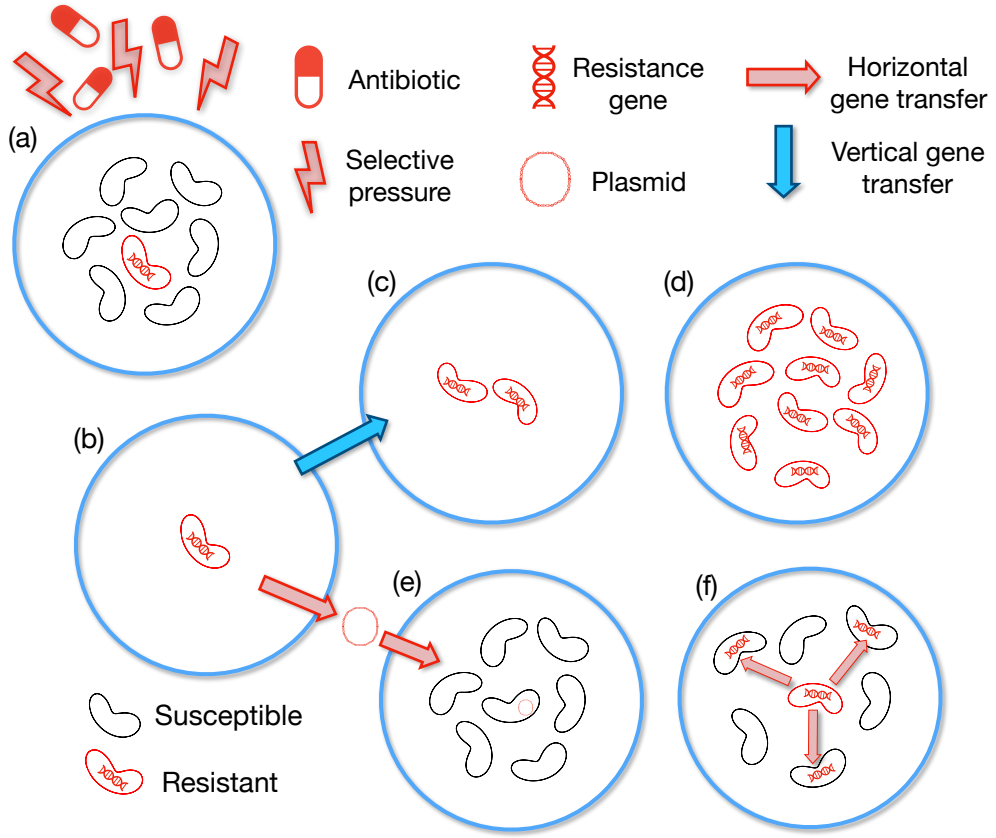

Figure 27. Illustration of the main AMR spreading mechanisms. (a) Upon exposure of a bacterial colony to antibiotics, susceptible organisms are killed (in black). Selective pressure is exerted on the entire population, thereby favouring individuals to genetically mutate and develop resistance (red bacterium in (a) and (b)). Resistance is transferred to daughter cells through vertical gene transfer, thereby leading to the formation of resistant colonies ((c) and (d)). Additionally, resistant bacteria can transfer resistance-encoding plasmids to sensitive bacteria via horizontal gene transfer ((e) and (f)).

What was the father of antibiotics trying to warn us about? While bacteria might be seemingly small and less evolved than eukaryotic cells, they are extraordinary evolutionary machines. Indeed, bacteria are able to develop resistance to antimicrobial agents on surprisingly short timescales. Amazingly, it has recently been reported [94] that *E. coli* and *P. aeruginosa* developed resistance to silver nanoparticles after repeated exposure by overproducing the protein flagellin, a natural component of the bacterial flagellum, which caused nanoparticles to aggregate and loose efficacy. This happened in as little as eight days.

Indeed, bacteria are living organisms and as such they follow the natural selection rule: what does not kill them, makes them stronger and more fit to survival. AMR is actually an exquisite example of natural selection at its best and a clear manifestation of the more general rule of evolutionary selective pressure. Figure 27 shows a diagram of the processes responsible for the development and transmission of AMR. Once a genetic mutation that

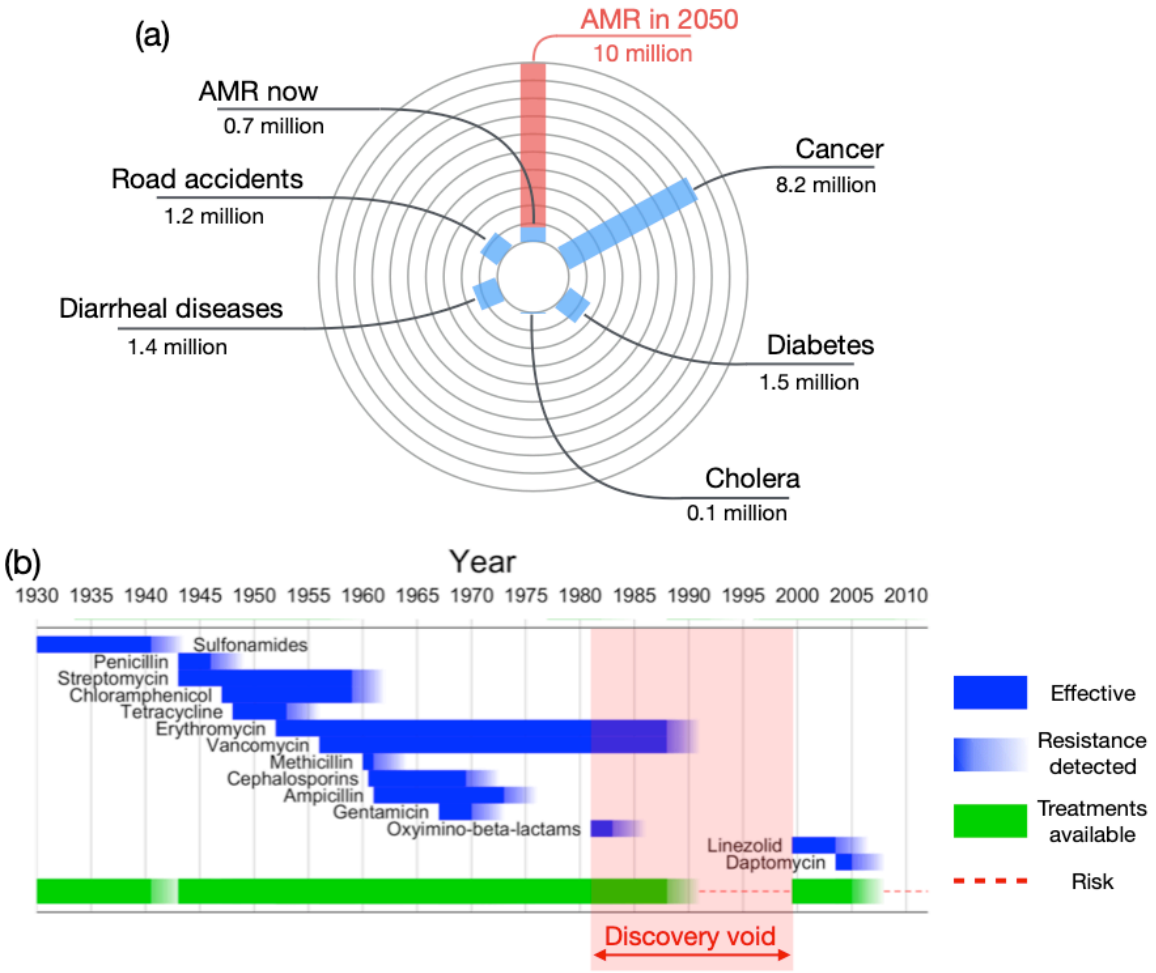

Figure 28. Significance of the AMR burden. (a) Bar plot showing the main causes of death per year worldwide (blue bars). Each ring corresponds to 1 million. AMR today is responsible for 700 000 deaths. This number could rise to 10 million by 2050 if current trends continue (red bars) [96]. (b) Timeline of antibiotic discovery and first detection of resistance, as indicated by the shaded blue bars. The discovery void is highlighted in red and the availability of effective drugs is indicated by the green bar at the bottom. The dashed red line refers to periods of time when there were not many effective drugs available [103].

confers resistance is developed by a single organism (panel (a) and (b) in Figure 27), the genetic trait is passed on to daughter cells (vertical gene transfer, panel (c)). Resistant cells will then thrive and establish a new population that will not respond to a future drug treatment (panel (d)). Resistance can also be transferred from one bacterium to another through the exchange of genetic material (horizontal gene transfer, panels (e) and (f)).

Hence, while the process occurs naturally, the ever-increasing quantities of antibiotics being improperly used worldwide can only contribute to its acceleration by exerting selective pressure. A plethora of studies have confirmed positive correlation between antibiotic use and the levels of resistance [95]. More recently, a very informative report commissioned by the UK Prime Minister quantified the AMR mortality rate and predicted its increase in the next decades up to levels comparable to the deaths caused by cancer (see

Figure 28(a), [96]), even though producing such estimates is not straightforward and should be critically considered [97].

In principle, the development of resistance to a particular antibiotic would not be a problem if we always had an alternative drug available. Therefore, the critical aspect is the rate at which drug resistance evolves compared to the rate at which new antibiotics are introduced into the market. Any strategy to combat the threat should deal with balancing these rates; i.e. we could either count on developing new antimicrobial agents more rapidly or work towards maintaining the effectiveness of current ones by managing bacterial evolution.

The first strategy has partly proven unsuccessful. Finding and introducing new antimicrobial agents is no trivial task for a number of reasons, including scientific challenges [98], but also because of the economic viability of antibiotic R&D. An insightful critical analysis can be found in [99]. These arguments have led to a stagnation in antibiotic development in the last 30 years, with the last discovery of a novel agent dating back to 1987 [98,100]. A few new agents have only been discovered in the last few years [101,102]. Furthermore, even if new drugs are being developed, AMR will remain a major threat if these drugs are not being used properly. This is clearly illustrated in Figure 28(b), which shows a timeline of antibiotics' introduction and subsequent detection of resistance. It is clear that resistance to most antibiotics was detected only a few years after their first introduction, as indicated by the light blue shaded areas.

Therefore, a more responsible management of antibiotics is the most effective and realistic strategy to pursue, as even verified by mathematical models [103]. However, this approach is not exempt from obstacles either. The main reason being a widespread overuse of antibiotics, not only in the healthcare context. In fact, approximately 80% of antibiotic consumption happens outside a hospital setting, meaning that professional guidance is limited, and many mistakes are being committed, such as taking antibiotics when the illness is not bacterial, not completing the entire prescribed course or not taking the correct drug. The clinical practice is not fault-free either, with the main problem being over-prescription. Shockingly, in the US alone, almost 70% of antibiotic prescriptions for respiratory issues in the period 2007-2009 were unnecessary [96,104]. Even though a decreasing trend was recently observed for respiratory tract infections [105], the level of avoidable prescriptions still stands at almost 25%, even in the UK [106].

One of the main reasons for this misuse has to do with the lack of rapid diagnostic tools. Current clinical assays are based on detecting bacteria growth (and its inhibition) from a patient's sample in the presence of antibiotics. Common methods include the agar disk-diffusion test (Kirby-Bauer method) and microdilution assays [107,108]. Despite being well understood and employed, these techniques have several drawbacks. Since they rely on detecting some visible signs of growth, they often require long incubation time and non-culturable organisms are extremely difficult to test. Furthermore, they are reagent-demanding and labour-intensive. The delayed diagnosis prevents a timely identification of the most suitable antibiotic for a specific infection, thereby resulting in empirical prescription [96].

Without knowing whether the infection is susceptible to a specific drug, the clinician has no choice but to initially use the antibiotic to which the fewest strains are resistant, or to use broad-spectrum antibiotics. The obvious consequences are the application of selective pressure to bacteria and the acceleration of AMR. Significant efforts have been made in recent years to improve diagnostics, with microfluidics playing an important role [109,110]. In fact, if a rapid and reliable microfluidic diagnostic tool was available, antibiotic prescription could be more effective and better tailored to the patient, thereby improving clinical outcomes whilst reducing the overall level of drug use.

4. Microfluidics for susceptibility testing: a review

There are two main approaches for profiling bacteria susceptibility: a phenotypic or a genotypic way. Genetic strategies imply sequencing the bacterial DNA to identify the presence of specific genetic markers (plasmids, genes or mutations) that confer resistance. However, there are two main drawbacks with genotyping. Such tests require prior knowledge of which resistance markers to test for, while the organisms might have acquired resistance through an unknown gene or mutation [111]. Furthermore, genotyping confirms resistance but does not inform susceptibility. It is surely valuable to know which drug not to prescribe, but it is arguably more important to determine the most suitable medication for healing the patient.

In contrast, phenotypic tests are based on detecting some phenotypical signature, typically bacterial growth. The definition is simple: an organism is susceptible if the antibiotic halts its division, either by a bacteriostatic or a bactericidal action. However, relying on growth according the classical definition requires time, as highlighted for the traditional methods.

Different phenotypical signatures need to be explored, such as single-cell growth, motility, morphology or metabolic activity. The goal is to identify some of these bacterial properties that are influenced by antibiotics on a shorter timescale compared to traditional tests. Microfluidics is arguably the best candidate to investigate such alternatives because of its ability to deal with small volumes and to isolate single cells over time while precisely controlling the environment bacteria are exposed to [109,110].

4.1. Growth at the single cell level

The main drawback of bulk growth-based assays is the time needed for the colony to reach a minimum detectable size. For instance, in a typical microdilution assay, turbidity is used as a signature for growth, whereby opaque solutions show increased optical density (OD) due to a higher concentration of bacteria. However, this method poses severe limitations dictated by the sensitivity of spectrometers and sets a lower boundary to the minimum detectable concentration of the order of 10^6 cfu/ml [112], which is higher than typical clinically relevant concentrations. For example, the threshold bacterial concentration for the diagnosis of urinary tract infections (UTIs) is of the order of 10^4-10^5 cfu/ml [113].

A better method was recently proposed by Baltekin *et al*. [114] who looked at the growth of single bacteria in a high-throughput format. The authors fabricated the modified version of the mother machine capturing assay shown in Figure 29(a), whereby single bacteria were captured in some of the channels.

Growth was monitored by tracking the position of the fore-most bacterium in each channel, since cell duplications cause the column to lengthen, as shown in Figure 29(b) and (c). The response from a single column was subsequently averaged over thousands of columns to measure the differential overall growth rate. The real advantage came from this averaging procedure being performed over the cells after the readout. This ensured that any noise and variations had less impact of the final measure and changes of the growth rate induced by drugs were picked up at the timescale of the antibiotic action. Consequently, this platform allowed one to profile susceptibility of *E. coli* in less than 30 minutes to nine different antibiotics administered at the minimum inhibitory concentration (MIC) level.

4.2. Morphology signatures

Antibiotics are known to significantly influence bacterial morphology in a variety of ways. This variety poses serious limitations on the extrapolation of general trends and on the

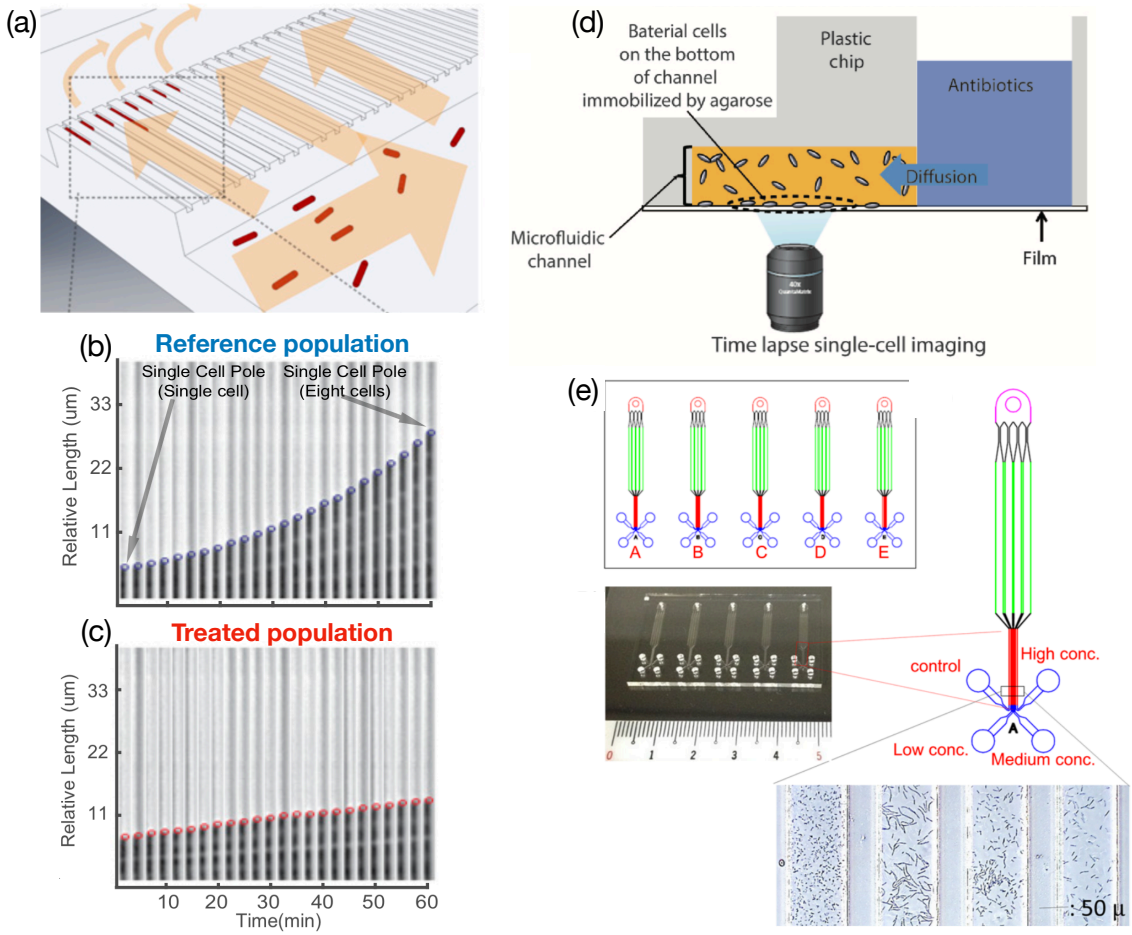

Figure 29. Examples of growth and morphology assays for susceptibility testing. (a) Illustration of the mother-like machine introduced by Baltekin et al. [114] Single bacteria are localised in narrow channels with openings at both ends to ensure medium recirculation. (b, c) Micrographs of one of the channels over time for a reference population (in blue) and an antibiotic-treated one (in red). The growth of the reference population is clearly identified by an exponential growth curve while the treated one only exhibits linear growth. (d) Schematic of the single cell morphological analysis (SCMA) platform [112]. Bacteria are sandwiched between an agarose pad and a glass substrate, while antibiotics diffuse from the side. Time-lapse imaging is performed from below. (e) Schematic of the device proposed by Matsumoto et al. [119] to follow bacterial growth and morphology in microfluidic channels. Multiplexing was achieved by fabricating multiple parallel channels with dried antimicrobials inserted prior to the injection of bacteria.

production of a universal rule. In fact, morphological responses depend on the concentration and incubation time of the drug as well as bacterial factors such as strain, growth phase, and, most importantly, their susceptibility to the test drug [115]. As an example, the two beta-lactam antibiotics cefuroxime and ceftazidime are known to induce filamentation, i.e. lengthening without division, on *E. coli* and *P. aeruginosa* at low antibiotic concentration (starting from 0.008xMIC). Conversely, spheroplast (i.e. spherical shapes) were observed at a concentration of approximately 0.5xMIC [115,116]. Moreover, this transition also depends on the duration of the exposure to the drug [117]. On the other hand, another common beta-lactam (ampicillin) produces filamentous *E. coli* followed by the formation of a bulge structure before cell lysis [115,118].

The dependence of morphology on the status of bacteria has been exploited in combination with growth at the single cell level by Choi *et al.* [112] in what they termed Single Cell Morphological Analysis (SCMA) test.

A simple microfluidic design was employed to immobilise a few bacteria between a glass slide and an agarose pad in a 96-well plate format, which ensured compatibility with standard microbiology protocols. Antibiotics diffuse through the agarose in order to expose the immobilised bacteria while the evolution of morphology was followed through time lapse imaging (see Figure 29(d) for a diagram of the device). An automatic algorithm was devised with the aim of detecting the number and morphology of bacteria within the field of view. These signatures were recorded for a wide variety of bacterial strains and antibiotics at different concentrations. However, given the broad range of responses to the treatment, a link to a standard susceptibility method was needed. In [112] the connection was provided by testing the same strains and concentrations with standard microdilution assays. The results allowed the authors to confirm the MIC values measured with the SCMA, which offered the advantage of a significant reduction in analysis time to a few hours in most of the considered cases.

A similar morphological approach was pursued by Matsumoto *et al.* [119], with the interesting addition of equipping the microfluidic channels with preloaded dried antimicrobial agents (see Figure 29(e)). Similarly to [112], the number and shape of *P. aeruginosa* colonies were monitored in control populations and treated ones. Semi-automatic analysis software was able to correctly inform susceptibility in a few hours and in agreement with outcomes obtained with microdilution assays.

4.3. Gradient microfluidics

The possibility of generating concentration gradients inside a chip is yet another powerful tool offered by microfluidics. The relative ease of producing concentration gradients stems from the laminar flow and the diffusive operational regime, together with the use of a porous material, such as agar. The diffusion time and length between different solutions can be precisely engineered in order to tailor gradients. Since cells are exposed to different concentrations of the compound of interest within restricted distances, multiple conditions can be tested in parallel, thereby increasing multiplexing capability and throughput [120].

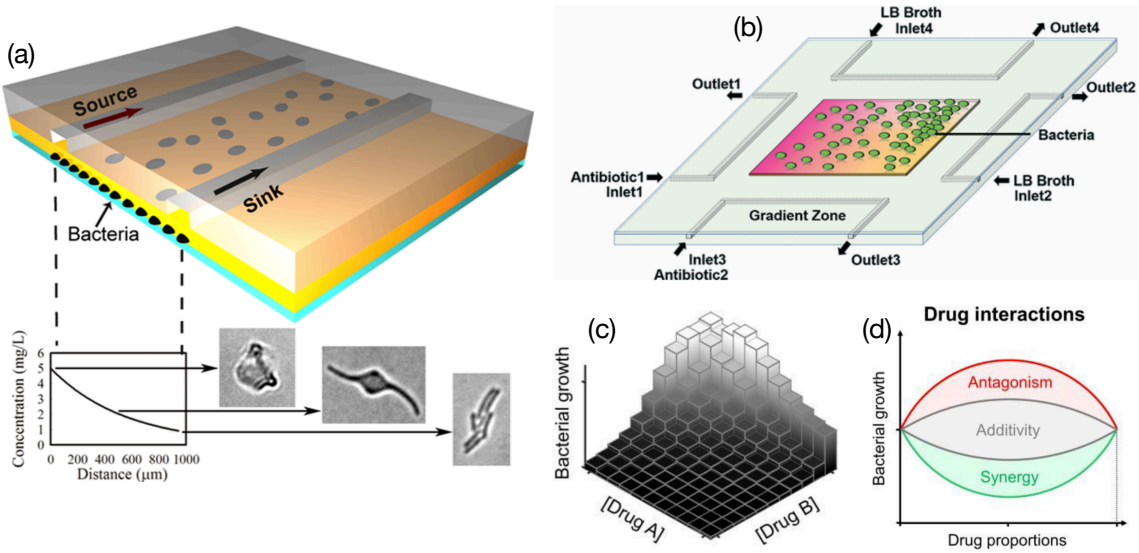

Figure 30. Examples of susceptibility tests based on gradient microfluidics. (a) Diagram of the device proposed by Li et. al [121]. Two PDMS channels act a source and a sink for antibiotics to diffuse through an underlying agarose layer. A bacteria monolayer is immobilised between the agarose and a glass slide. The established drug gradient allows one to follow morphological changes as a function of the antibiotic concentration and time. (b) Schematic of the device used for generating 2D gradients of antibiotics in [122]. Channels at opposite edges of a square agar-alginate pad are paired to generate a gradient in each direction. (c) Representation of the ideal behaviour of bacterial growth as a function of the concentration for two synergistic drugs. (d) Illustration of possible responses of bacterial growth as function of the concentration of two drugs in a combinatorial treatment approach [123].

In the context of susceptibility testing, the exposure of cells to linear gradients of antibiotics allows one to acquire MIC values in a single experiment, which is very elegant. In addition, information about the morphological dynamic of the growth inhibition process can be obtained, as shown by Li *et al*. [121]. The authors realised a platform that consisted of two PDMS channels placed above a semi-permeable agarose pad. While the first channel acted as a source by being flushed with an antibiotic-rich medium, the second functioned as a sink driving the diffusion of the antibiotic through the underlying agarose, as illustrated in Figure 30(a).

A monolayer of bacteria was sandwiched between the agarose layer and a glass substrate, so that immobilised organisms were exposed to a linear decaying gradient of antibiotic (see again Figure 30(a)). Time lapse imaging at different locations along the gradient enabled the authors to follow the morphological evolution of single bacteria over time and for different drug concentrations simultaneously. By examining the resulting changes in shape, the device afforded the determination of MIC values for amoxicillin that were comparable to the values determined by established methods.

A further possibility is to stack multiple gradients in order to gather richer information and more complex results, such as the effects of combinatory antibiotic therapy [122,123]. A schematic of such a device is shown in Figure 30(b), where two sources and two drains are placed along the opposite edges of a square agarose pad, thereby resulting in two overlapping linear gradients. In this fashion, every combination of drug concentration is generated, a possible effect of which is illustrated in Figure 30(c). Such a combination allows one to probe the outcomes of combining drugs in different proportions, as illustrated in Figure 30(d). Pharmacodynamic models were also proposed to explain the interaction between different drugs and were used to fit experimental data obtained with such platforms [122,124].

4.4. Droplet microfluidics

The need for controlling the local environment of single cells is elegantly addressed by a simple yet powerful technique: droplet microfluidics. The main idea is to rely on multiple immiscible flow phases and their interaction. In the common configuration of passive droplet generation, immiscible fluids are made to meet at a junction (see Figure 31(a)). Careful design of the junction along with a suitable flow rate causes one of the fluid phases to pinch off and create droplets. The stability of the droplets within the other fluid is then guaranteed by surface tension [125]. The size, number and generation frequency of the droplets depend on the fluid density and shear as well as on the flow rate; these parameters can be controlled with remarkably high precision and repeatability. Comprehensive reviews are provided in [126,127].

By encapsulating fluids in droplets within a microfluidic channel, one can compartmentalise different compounds, fluorescent tags and even cells or bacteria. The advantages are twofold: the effective cell/bacteria concentration is drastically increased because of the extremely small droplet volume, and the concentrations of analytes within the drops can be controlled very precisely.

As discussed previously in section 4.1, where Baltekin *et al*. analysed the growth of single bacteria, droplet microfluidics typically employs the growth of a few encapsulated bacteria as a signature of susceptibility. Unlike the mother machine-inspired device, however, growth and viability are quantified by fluorescent dyes indicative of bacteria metabolism. Statistical significance and high throughput are achieved by analysing several thousands of droplets per experiment. Figure 31(a) shows a typical configuration of such an assay, whereby two different solutions containing bacteria (yellow stream) and the antibiotic

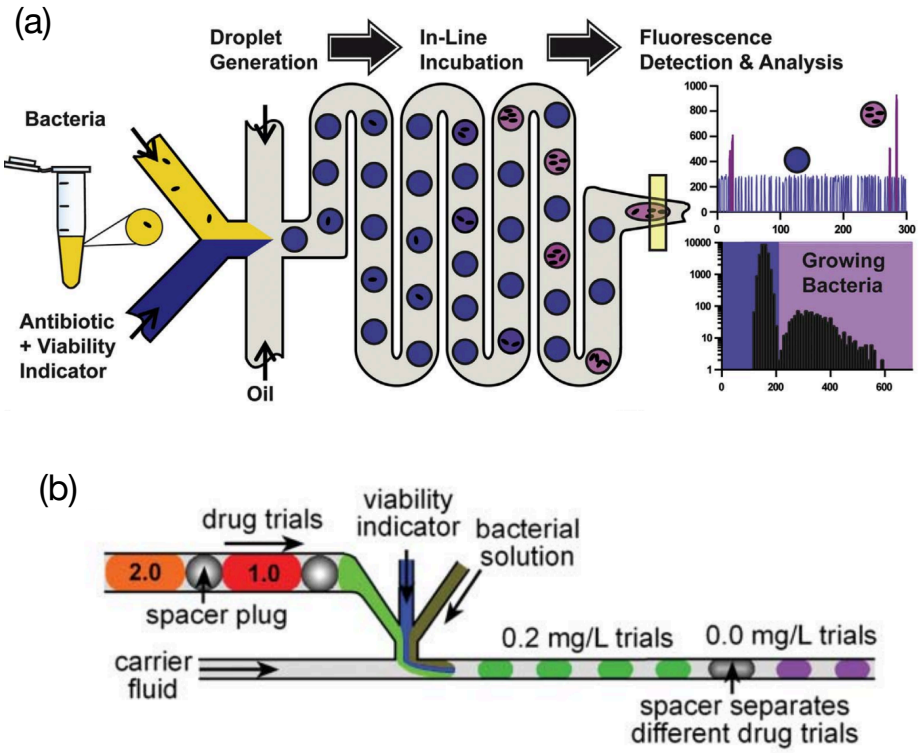

Figure 31. Typical diagrams of droplet-based susceptibility assessment. (a) Microfluidic approach employed in [128] to generate droplets that embed bacteria, antibiotics and a viability reporter dye. Formed droplets are incubated along a serpentine before reaching the detection zone on the left-hand side, where the fluorescence of the viability indicator is detected and employed as a signature of the antibiotic action. (b) Geometry adopted by Boedicker et al. [129] to test multiple drugs in the same experiment. Droplets with different drugs and at different concentrations are preformed and separated by spacer plugs. Subsequently, bacteria and a viability indicator are embedded with the different classes of droplet and fluorescence of the dye is later detected.

(plus the viability dye, blue stream) are injected through separate inlets [128]. The two streams flow laminarly towards a T-junction, where an orthogonal channel containing oil induces the droplet formation, thereby encapsulating a few bacteria and the antibiotic with the fluorescent dye. Droplets subsequently travel through a short incubation path, then viability is measured sequentially via the level of fluorescence emitted by the reporter dye in each droplet. The dye (resazurin) fluoresces in the presence of viable bacteria, as I will explain in more detail in section 12.4 of this chapter. The assay affords to correctly detect the susceptibility of *E. coli* to gentamicin in 1 hour as suggested by the low levels of observed fluorescence, unlike the higher signal measured for a resistant strain (blue and pink portions of the graph in Figure 31(a)).

Interestingly, similar platforms were employed to screen single bacteria against a variety of antibiotics in the same experiment. This was achieved in [129,130] by pre-forming arrays of droplets with different drugs separated by spacer plugs, as shown in Figure 31(b). Bacteria culture with the viability indicator was sequentially encapsulated with different

antibiotics in different droplets. Similarly to the previous approaches, fluorescence of the viability indicator was later detected and correlated to the efficacy of each drug separately.

More recently, Lyu *et al.* [131] exploited the high throughput ability to examine heteroresistance, i.e. the different levels of resistance within the same bacterial population induced by sub-lethal treatments of antibiotics. The aim was to induce the formation of a minority of resistant-subpopulations to be subsequently detected and analysed. The study revealed that a single MIC value is not sufficient to describe the response of a population to an antibiotic. Indeed, the authors found several subpopulations with a distribution of levels of resistance to three distinct drugs. These findings emphasise the importance of heterogeneity previously discussed in the response of bacteria to antibiotics.

However, while the generation of a large number of droplets allows maximising the throughput of the technique, it also makes it rather demanding in terms of detection equipment. Since most of the assays are based on fluorescence, fast and sensitive equipment is required to excite and reveal fluorescence of thousands of droplets per second. Hence, in terms of ease of implementation, mother machine designs and agarose immobilisation perform better. However, droplet microfluidics offers a higher degree of control over the bacterial environment in each droplet, as well as a remarkable reduction in the volume of reagents used.

4.5. Motility as a signature

In all techniques discussed so far, bacteria are either spatially constricted to a degree that does not allow them to move or swim, or their movement is not even considered. The reason being that prolonged observation is required to assess the action of a drug over time on the same individuals, such as in the mother-like machine described in section 4.3 or in the agarose immobilisation assays described thereafter. However, a total immobilisation of bacteria precludes the possibility of studying another interesting bacterial property, namely motility. Motility is a fundamental characteristic of many types of bacteria which plays a crucial role in the early stages of infection, chemotaxis and in the growth and proliferation of biofilms [132,133].

Motility has only emerged recently as a promising phenotypic reporter of susceptibility. We believe that it holds great promise for rapidly assessing the response to an antibiotic challenge. The first investigation of such effects was reported by Longo *et al.* [134], who

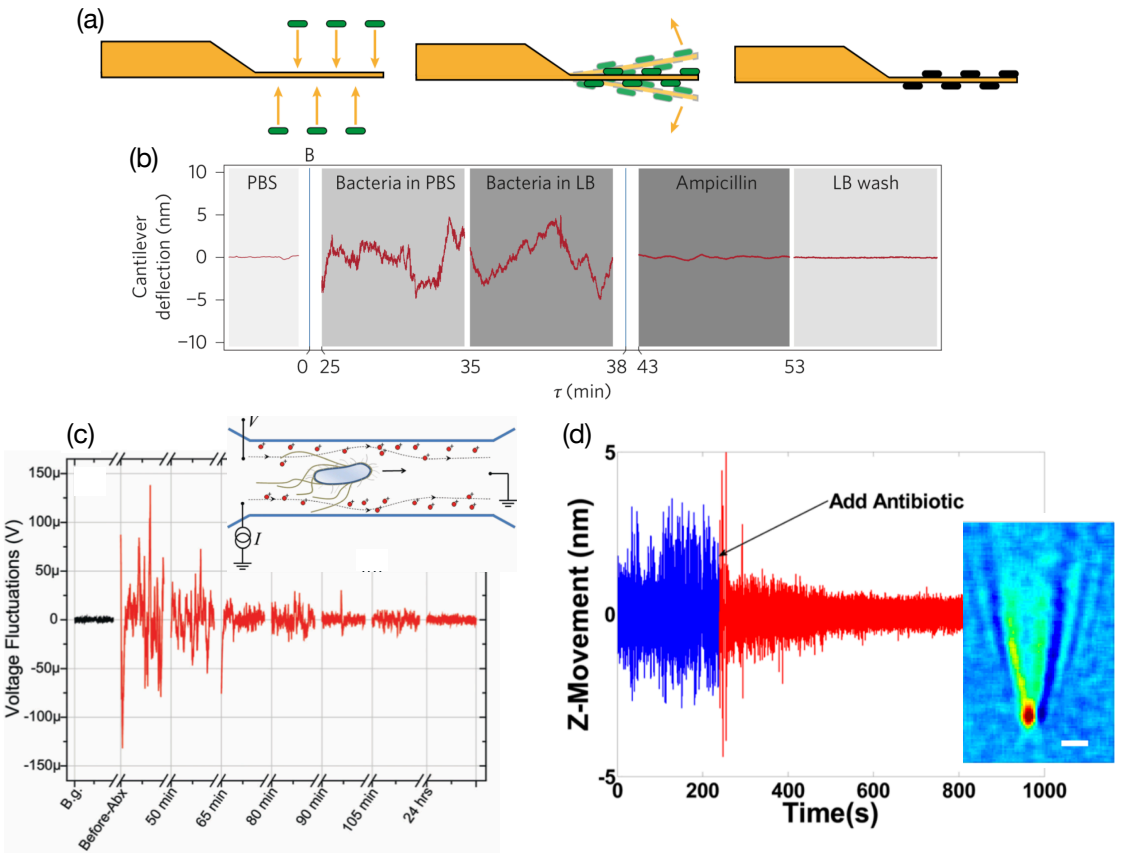

Figure 32. Examples of recent motility assays for measuring the effects of antibiotics on motility. (a) Nanomotion sensor developed by Longo et al. [134] for detecting the motion of microorganisms tethered to an AFM tip. Viable bacteria (in green, mid panel) cause increased deflections compared to dead organisms (in black, panel on the right). (b) Cantilever deflection as a function of time for E. coli attached onto the tip and exposed to different solutions. While oscillations are significant in PBS and LB media, exposure of ampicillin and subsequent wash with LB resulted in decreased amplitudes because bacteria were rendered inviable by the drug. (c) Electrical readout method of motility employed by Kara et al. [139]. Exposure to antibiotics caused voltage fluctuations across the channel to decrease because of bacteria motility being impaired. (d) Plasmonic imaging of a single E. coli tethered onto gold via antibody binding [71]. Changes in the reflected intensity are converted into z-distance of the bacterium, whose amplitude was reduced by the action of the antibiotic. Scale bar: 2μm.

indirectly measured the motility of *E. coli* exposed to ampicillin and kanamycin in 2013. A few hundred bacteria were tethered on the tip of an AFM and the cantilever deflections were picked up through the reflected laser signal, like an AFM would normally operate. The exposure to drugs caused a significant decrease of the recorded oscillations as a consequence of the antibiotic impairing the bacterial viability and reduced micromotion, as depicted in Figure 32(a) and (b). In order to prove the connection to susceptibility, the revealed MIC value was compared to standard measures, showing good agreement. The results were further corroborated by testing bacterial strains that were genetically engineered to confer resistance to ampicillin. This latter test revealed that the tip displacement featured an initial decrease upon exposure to the drug followed by recovery within approximately 30 minutes, due to the bacteria surviving the treatment (not shown

here). Additionally, the same authors showed the same assay to be able to investigate the activity of fungal, eukaryotic and plant cells [135]. More recently, they applied the nanomotion cantilever to detect susceptibility of the slowly growing *Mycobacterium tuberculosis*, for which traditional growth-bases techniques can require several weeks or even months [136].

The AFM readout method was later combined with infrared spectroscopy [137], as a mean of enhancing deflections when the illumination radiation resonates with the absorption spectra of tethered bacteria. Moreover, the integration of IR radiation provided the authors with the ability to selectively identify bacterial strains due to their characteristic spectral IR fingerprints [138] as well as to discriminate between intact and dead *E. coli* in response to ampicillin treatment.

Another method for measuring motility was recently proposed by Kara *et al.* [139], who measured the voltage drop across a microfluidic channel containing swimming *E. coli*. Following the administration of antibiotics, the fluctuations of the voltage signal decreased because of the loss of motility induced by the drug. A typical result over time and a diagram of the channel used in the experiments are shown in Figure 32(c).

A further interesting motility assay was proposed by Syal *et al*. [71] and was based on a surface plasmon resonance (SPR) sensor. The lateral confinement of the plasmonic wave conferred high spatial resolution imaging to the system, as discussed in the conclusions of chapter II. In their configuration, the authors used a constant angle of excitation, so that any change in refractive index above the surface caused the resonance to be detuned, thereby resulting in a change of the reflected light intensity. A plot of the spatial distribution of intensities produces a contrast image where single bacteria tethered via antibodies were distinguishable (see inset of Figure 32(d)). Furthermore, since the functional form of the field decay into the cover medium is known (an exponential tail), the intensity values in different time frames were converted to coordinates along z. In other words, the distance of the bacterium from the sensor surface was retrieved as a function of time, as shown by a typical trace in Figure 32(d). Administration of ampicillin caused a dramatic decrease of fluctuations, which indicated cell death. This technique is one of the few that assessed motility in response to drugs at the single cell level.

However, it should be noted that the motility assays described so far lack practicality. Complex equipment and skilled personnel are needed to operate an AFM, measure voltage

fluctuations of the order of μV, or excite and monitor a plasmon resonance. Furthermore, in the plasmonic case, the authors used a high concentration of ampicillin to amplify the effect and to shorten the response time. Additionally, while binding via antibodies provides a high selectivity and provides robust attachment, antibodies are costly, difficult to store and might lose efficacy since bacteria mutate rapidly. Finally, a surface functionalisation is needed to tether bacteria to the AFM cantilever, which increases process time and require further consumables.

An assay that overcomes most of the previous downsides was proposed by Cheong *et al.* [140]. The method relies on 3D tracking planktonic *E. coli* in a simple microfluidic chamber, by using holographic video microscopy, which only requires a common phase microscope and a low-power laser illumination. In this technique, the scattering patterns produced by swimming bacteria are recorded over time and are used to reconstruct the distance of the scattering bacterium from the focal plane (namely the z position). Hence, x, y and z coordinates are retrieved over time, which allowed for a high-throughput analysis of hundreds of single swimmers in the field of view within a few minutes. Even though the authors only revealed an abrupt loss of motility caused by high concentrations of gentamicin, the assay represents a valuable platform for the analysis of single-bacteria motility with high statistical significance and with a relatively simple experimental setup.

5. Hydrodynamic trapping of single cells

5.1. Single eukaryotic cell trapping

Hydrodynamic trapping techniques allow separating bodies from the main fluid flow by either holding them at specific locations or forcing them along specific paths. The main methods to accomplish such a retention are outlined in Figure 33(a) [141], where I provide a classification of different modalities of hydrodynamic trapping. Two major categories are identified, i.e. contact-based and contactless approaches. The first class comprises methods that retain the trapped bodies by means of mechanical forces exerted by contact with microfabricated structures. By contrast, in contactless methods, the forces are of different nature, such as due to the fluid itself (stagnation point trapping), or external acoustic, electrical or magnetic fields.

The contact-based class is also further divided into vertical and lateral trapping techniques. In the vertical modality, cells are trapped downwards into the fluid flow into microwells or micro pit structures, as shown in Figure 33(b) [142]. In contrast, lateral approaches trap

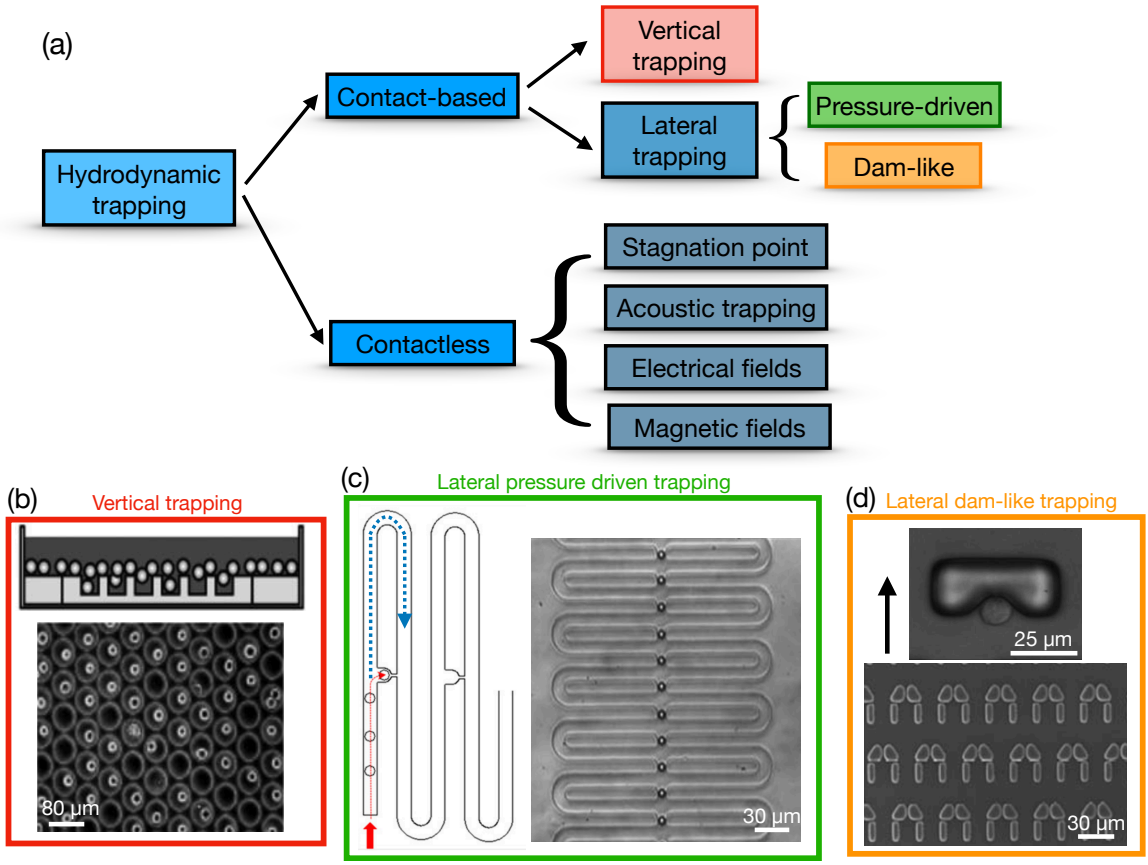

Figure 33. Classification of hydrodynamic trapping methods for single cells. (a) Diagram of the main methods employed for hydrodynamic trapping. (b) Typical vertical trapping configuration, where cells are seeded into wells vertical to the direction of the flow [142]. (c) Example of a pressure-driven trapping technique. Bodies in the fluid are more likely to move toward small openings in secondary channels, until the aperture becomes clogged and the next body moves beyond it. The same mechanism repeats in successive branches of the serpentine [143]. (d) Common examples of lateral dam-like trapping structures. U-shaped wells are integrated within a microfluidic channel to retain cells swimming in the fluid [82,150]. The black arrow indicates the direction of the fluid flow.

cell laterally or along the flow direction into microchambers or mechanical barriers. Lateral methods can be implemented either through pressure-driven designs or by using microwells as dam-like structures. An example of a pressure-driven device is shown in Figure 33(c). The main idea is to partition the flow into two separate paths of different hydraulic resistance, with the path of low-resistance featuring a narrow constriction in the end (red path in Figure 33(c)). The fluid is thus preferentially diverted along the red arrow, until the aperture is occupied by an object larger than the constriction which suddenly increases the resistance of the first track. Then, the fluid mainly flows along the blue path in Figure 33(c) and the process is repeated at the next diversion. The right side of the same figure shows such a typical device in action, where microbeads were trapped sequentially at each constriction [143].

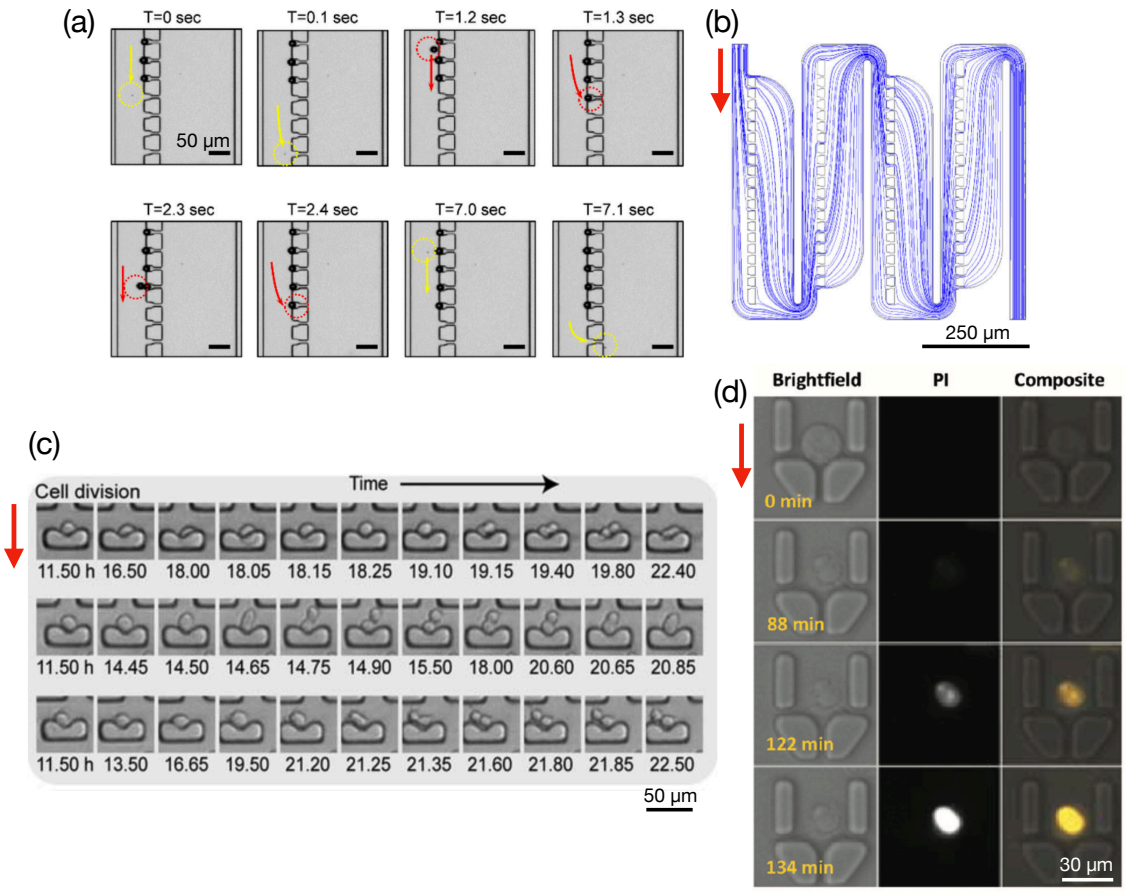

Figure 34. Examples of hydrodynamic trapping of single cells. (a) Sequential trapping of microbeads from [144]. Microbeads are drawn towards the first available opening by careful design of the fluidic resistances and streamlines, as shown by the COMSOL simulation in (b). Size-selectivity is achieved by progressively changing the width of the. (c) Time lapse monitoring of HeLa cells culturing in PDMS micro-dam traps from the work of Di Carlo et al. [82]. (d) Improved trap design employed in [150] to study hematopoietic stem cell apoptosis upon the action of anti-cancer drugs. Red arrows in each panel indicate the direction of the fluid flow.

An improved version of this design, which achieved higher throughput was proposed by Kim *et al.* [144]. The authors fabricated sieve-like structures consisting of multiple openings stacked orthogonally to the flow. The sequential openings acted as trapping apertures by preferentially diverting the streamlines, as the simulation in Figure 34(b)) illustrates. Interestingly, the assay was also size-selective due to a tapering of the size of the constrictions at different locations over the chip area. The size-dependent effect is illustrated in Figure 34(a), where large beads are sequentially immobilised (red paths) while small ones manage to go through the first set of apertures (yellow paths).

The last sub-class we describe employs micro wells or U-shaped traps for in-flow trapping, i.e. cells are held in place by mechanical barriers positioned along the fluid flow.

Even though rudimentary designs were first introduced between 2003 and 2004 [145,146], it was not until 2006 that the approach gained popularity following the works by Di Carlo

et. al. [82,147,148], who demonstrated the method to be suitable for culturing HeLa cells over extended periods of time, as illustrated in Figure 34(c) [82]. In particular, the authors followed division, adhesion and apoptosis of single trapped cells for 24 hours. The results showed that cellular dynamics were similar between the microfluidic chip and a standard slide without traps, thereby highlighting compatibility of the trapping assay with long-term cell viability. The same authors also used the assay to monitor the intracellular concentration of carboxylesterase, namely enzymes involved in important cellular pathways as well as in the deactivation of certain external drugs. The individual cell capability of the assay enabled the authors to elucidate the kinetics of enzyme production and their mechanisms of inhibition, for the first time at the single cell level.

A few years later, a similar assay was employed to study hematopoietic stem cells by Faley *et al.* [149], whose aim was to follow cell proliferation and viability upon the administration of dasatinib, a drug commonly used to treat chronic myeloid leukaemia. The experiments enabled the authors to unveil differences between stem and progenitor cells in the early phases of treatment, information that was always lost in traditional bulk experiments. Interestingly, the study was the first one to also report on the effects of dasatinib on the motility patterns of stem cells. Motility was greatly reduced by the action of the drug, as revealed by a lower fraction of treated cells being able to migrate against the fluid flow compared to untreated control cells. The same approach was applied in [150] to explore the process of cell death (through apoptosis) of hematopoietic tumor cells induced by anticancer compounds, an example of which is illustrated in Figure 34(d).

While the pressure-driven trapping method is deterministic, since it actively diverts the fluidic streamlines toward the small apertures where cells are trapped, the microwell lateral approach relies on cells actively swimming towards the trap [151,152]. The geometry of the trap still plays a role in optimising the fluid flow, as proven by the small aperture in the vertical trap block in Figure 34(d) to maximise the fluid intake. However, the degrees of freedom are more limited compared to the different-path approach. In fact, the geometry of the barriers is stringently limited by the dimension of the cell and their movements with the aim of preventing them from escaping. I will further explore these effects in the trap design and optimisation section (chapter 7).

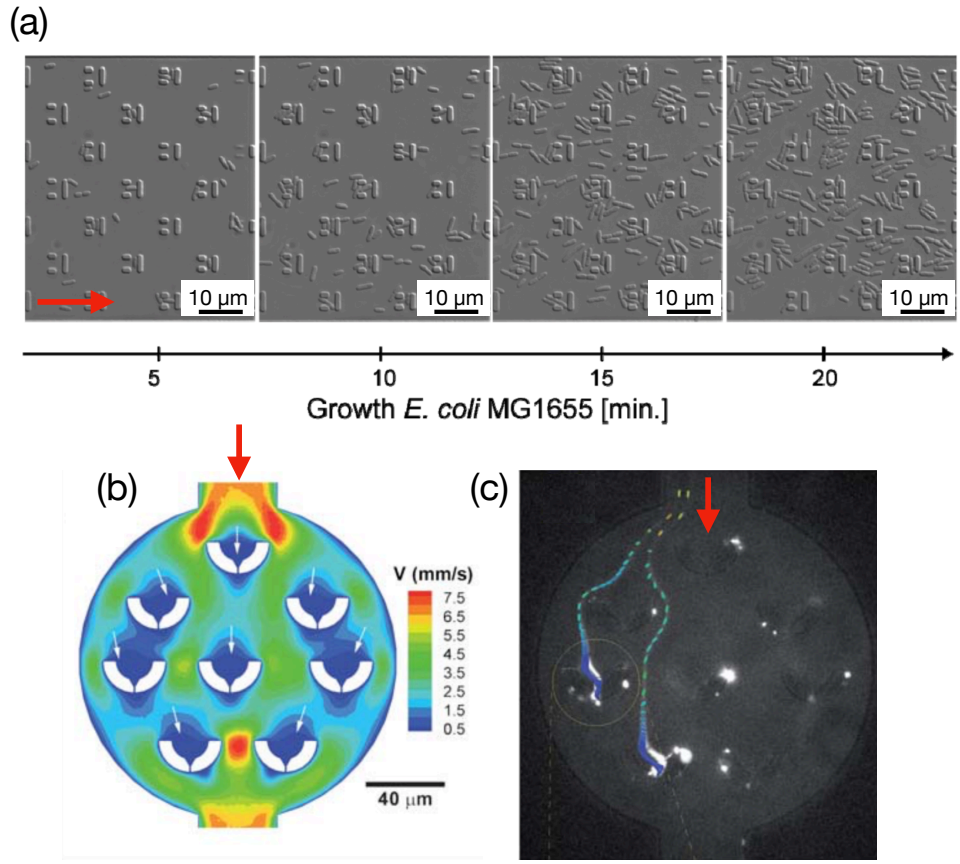

Figure 35. Examples of lateral hydrodynamic trapping of single bacteria. (a) Time lapse images of single E. coli trapped in U-shaped traps from the work of Probst et al. [153]. Growth and elongation rate of bacteria were monitored over time. (b) Fluid velocity distribution for the hydrodynamic trapping geometry proposed by Kim et al. [154]. (c) shows the remarkable agreement between measured bacterial trajectories (obtained by tracking fluorescent bacteria) and simulated ones, as indicated by the overlaid coloured paths. Red arrows in each panel indicate the direction of the fluid flow.

5.2. Single bacteria trapping

The previous arguments on the design limitation of U-shaped hydrodynamic traps suggest why this class of trapping techniques has been widely exploited for single eukaryotic cells assays, while it has been barely extended to single bacteria. Designing, fabricating and operating a micro-well able to house a single bacterium and maintain it trapped is not a trivial task. The requirements on the geometry are much more stringent, since bacteria are at least two orders of magnitude smaller than typical eukaryotic cells. Furthermore, motile bacteria are very efficient swimmers and therefore able to easily escape the trap by swimming against the flow. These arguments will be extensively detailed in the trap design section (chapters 7.2 and 8).

Hence, bacteria in microfluidic systems have been mainly studied by agarose immobilisation assays or using droplet microfluidics, as highlighted in the previous sections. Although these techniques have afforded impressive results in terms of analysis

time and robustness, they suffer from several drawbacks. For instance, droplet microfluidics often requires the use of reporter fluorescent tags, different media to form the droplets and, more importantly, external and fast optical excitation and readout systems to excite and detect fluorescence.

Contrarily, hydrodynamic trapping eliminates the need for recognition elements or fluorescent dyes as well as any external equipment other than a syringe pump. Furthermore, arraying single bacteria at regular positions facilitates automatic detection and data analysis, which is not straightforward to control with agarose immobilisation techniques. Also, as opposed to droplet techniques, hydrodynamic trapping offers the possibility of continuous medium recirculation, which ensures that trapped cells are exposed to a constant, yet controllable environment over time. Finally, daughter cells following division are removed from the trapping area, simply because they do not fit, thus ensuring a truly single cell assay. Most of these points were first demonstrated experimentally by Probst *et al*. [153], who fabricated U-shaped trapping arrays for individual *E. coli* and measured bacteria division time and length over several hours (see Figure 35(a)).

The only other example of single bacteria trapping in these class of structures was reported in [154], where the authors proposed a mathematical model to predict the bacterial trajectories in the presence of the trapping sieves shown in Figure 35(b). The particular design of the traps was optimised to maximise trapping efficiency. However, the large dimensions of the traps limited the throughput of the assay, since only 8 traps were imaged in the field of view. Furthermore, the necessity of imaging the entire chamber prevents the observation of individual organisms with sufficiently high resolution. Nevertheless, the study provided valuable insights into the bacterial motion and a theoretical framework for modelling the swimming action in the presence of obstacles. Furthermore, the model showed good agreement with the experimental trajectories recorded using fluorescent labelling (Figure 35(c)).

In conclusion, while hydrodynamic trapping has been usefully employed in several biological contexts, these have mainly been limited to eukaryotic cells. The use of hydrodynamic platforms for trapping and screening the effect of antibiotics on single bacteria has not seen much attention in the literature, in part because it is much more difficult to trap individual bacteria than trapping eukaryotic cells.

6. Theory of fluid flow

6.1. The Navier-Stokes equation

In order to understand the behaviour of moving fluids and to unravel the tight link between bacterial motility, fluid flow and trapping efficiency, it is necessary to understand the nature of fluid flow and its characteristics. The flow of an incompressible fluid is described by the Navier-Stokes equation:

$$\rho\left(\frac{\partial}{\partial t}\boldsymbol{u}(\boldsymbol{r},t) + \boldsymbol{u}(\boldsymbol{r},t)\cdot\nabla\boldsymbol{u}(\boldsymbol{r},t)\right) = -\nabla\mathrm{p}(\mathbf{r},\mathrm{t}) + \eta\nabla^2\boldsymbol{u}(\boldsymbol{r},t) + \boldsymbol{f}(\boldsymbol{r},t) \quad (24)$$

where $\boldsymbol{u}(\boldsymbol{r},t)$ and p($\mathbf{r}$,t) are the fluid velocity and pressure at any point identified by the position vector $\boldsymbol{r}$ and depending on the time t. ρ and η are the fluid density and viscosity, respectively, while $\boldsymbol{f}$ is an external force term. The non-linear differential equation, however, is notoriously difficult to solve analytically. Analytical solutions can only be obtained for a few simple cases. An important quantity that needs defining and will be useful in subsequent discussions is the shear rate $\boldsymbol{\gamma}$:

$$\boldsymbol{\gamma} = \eta\nabla\boldsymbol{u}(\boldsymbol{r},t) \quad (25)$$

$\boldsymbol{\gamma}$ describes the rate of change of velocity at which layers in the fluid move with respect to one another. In simpler words, and as the definition itself shows, $\boldsymbol{\gamma}$ is practically calculated as the first derivative of the fluid flow along the desired direction. At this point, it is also useful to introduce the Reynolds number *Re*:

$$Re = \frac{\rho u L}{\eta} \quad (26)$$

where *L* is the characteristic length of an object immersed in the fluid. Its value quantifies the ratio between inertial and viscous forces, thus dictating different regimes of motion for the fluid itself and, as a consequence, of any body in the fluid. In particular, for high values of *Re*, the flow is turbulent, while low values of *Re* result in laminar flow, namely a flow that can be imagined as an ordered ensemble of sheets of fluid neatly sliding over each other, as schematically shown in Figure 36(a). The velocity vector of each element of fluid is parallel to the channel walls and there are no transverse components causing the fluid to

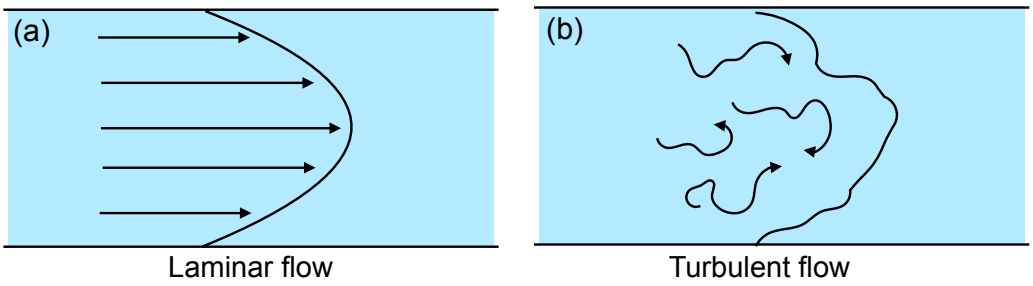

Figure 36. Schematic of a fluid profile in a laminar flow regime (panel a) and in a turbulent regime (panel b). In the laminar case, the fluid flows along the direction of the channel in an orderly manner and transversal mix happens only by diffusion, whereas in the turbulent scenario transverse velocity components cause swirled and tangled flow.

mix. Any lateral mixing can only occur by diffusion between the different layers, which is typically a rather slow process. This effect also holds when different liquids flow next to each other and it implies that two (or more fluids) hardly mix in a laminar flow regime. Contrarily, in a turbulent flow, the pressure and velocity of each fluid element chaotically change in space and time. Transversal mixing between different layers can be extremely efficient since the fluid velocity is not mainly directed along the flow direction only, as schematically depicted in Figure 36(b). As a rule of thumb, the transition between the two regimes happens for values of *Re* in the range 2000-4000 [155].

With the definition of the Reynolds number *Re*, the Navier-Stokes equation can be made dimensionless by also introducing an appropriate time (*T*) and velocity scale (*U*) [80]:

$$\frac{Re}{Sr}\frac{\partial}{\partial \tilde{t}}\,\tilde{\boldsymbol{u}}(\boldsymbol{r},t) + Re\,\tilde{\boldsymbol{u}}(\boldsymbol{r},t)\cdot\tilde{\nabla}\tilde{\boldsymbol{u}}(\boldsymbol{r},t) = -\tilde{\nabla}\,\tilde{p}(\boldsymbol{r},t) + \tilde{\nabla}^2\tilde{\boldsymbol{u}}(\boldsymbol{r},t) + \tilde{\boldsymbol{f}}(\boldsymbol{r},t) \qquad (27)$$

where the tilde indicates dimensionless quantities and the Strouhal number *Sr* has been defined to compare the characteristic time *T*, velocity *U* and length *L* scales of the system:

$$Sr = \frac{TU}{L} \qquad (28)$$

Microorganisms in microfluidic channels usually feature very low values of the *Re* number because of the flow being dominated by viscous forces, i.e. inertia does not play a significant role. For example, an estimation of the Reynolds number for a bacterium swimming in water leads to:

$$Re = \frac{\rho_{wat} u_{bac} L_{bact}}{\eta_{wat}} \sim \frac{10^3 \frac{kg}{m^3} 10^{-5} \frac{m}{s} 10^{-6} m}{10^{-3} Pa \cdot s} \sim 10^{-5} \ll 1 \quad (29)$$

A length L of 1 μm and a swimming speed of the order of 10 μm/s are assumed. Moreover, assuming a characteristic time scale T of 1/100s (which is representative of the flagellar beat period), the Strouhal number Sr is:

$$Sr = \frac{T_{bact} U_{bact}}{L_{bact}} Sr \sim \frac{10^{-2} s \; 10^{-5} \frac{m}{s}}{10^{-6} m} \sim 10^{-1} \quad (30)$$

which makes the ratio Re/Sr of the order of 10^{-4}. This regime of both $Re \ll 1$ and $Re/Sr \ll 1$ is encountered in most microfluidics devices and most swimming microorganisms. Under these assumptions, the first two terms of the dimensionless Navier-Stokes equation can then be neglected, leading to the following simplified expression:

$$\nabla \mathrm{p}(\boldsymbol{r}, t) = \mu \nabla^2 \boldsymbol{u}(\boldsymbol{r}, t) \quad (31)$$

This equation is known as the Stokes equation, which needs to be solved to determine the flow field $\boldsymbol{u}(\boldsymbol{r}, t)$ and the pressure distribution $p(\boldsymbol{r}, t)$ in the fluid.

The typical conditions described above imply that traditional effects typically encountered in macro-scale fluidics, such as inertia, buoyancy, sinking or rising and lift forces, are negligible in the micro-world, which is instead dominated by viscous damping [80,156,157]. For example, a typical bacterium swimming in a microfluidic channel would come to rest within a few tens of nanometres because of the dominance of viscous damping. In other words, it would stop moving if it were to stop beating its flagella.

6.2. Hagen-Poiseuille flow

One of the few cases in which the Navier-Stokes equation can be solved analytically is the case of pressure-driven flow between two motionless infinite parallel plates of distance $2h$. A pressure differential Δp is established between the extreme ends of the system which causes the fluid to flow, as illustrated in Figure 37(a). This problem is known as the Poiseuille or Hagen-Poiseuille flow.

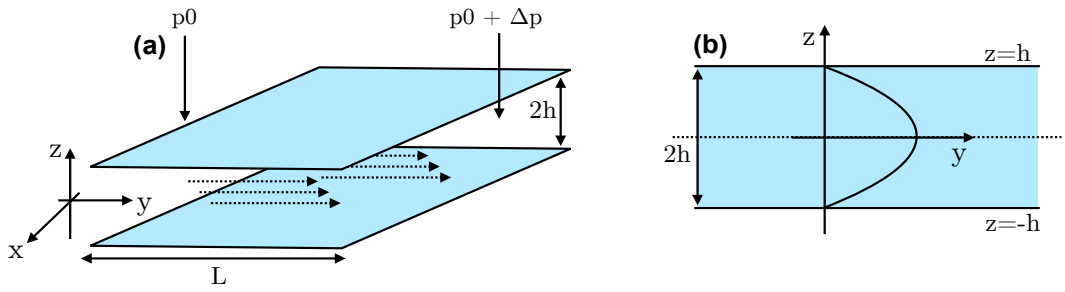

Figure 37. Geometry and relevant quantities defining a Hagen-Poiseuille flow. (a) 3D diagram of the channel. The two plates are assumed to be infinitely extended along the x direction and at a distance 2h along z. The channel length is L. A pressure differential Δp is applied between the extremes along the y direction. (b) Side view of the xz plane with the typical parabolic fluid profile flowing along y.

We assume the pressure differential to be established along the y direction and to be constant over time, namely $p(\boldsymbol{r},t) = p(y) = p(L) - p(0) = \Delta p$. Given that we are interested in the steady state solution for this geometry, the temporal dependence $\boldsymbol{u}(t)$ can be discarded. The flow can then be assumed to be unidirectional along the *y* direction as shown in Figure 37(a), so that the fluid velocity vector reduces to:

$$\boldsymbol{u}(\boldsymbol{r},t) = u_x(x,y,z,t)\hat{x} + u_y(x,y,z,t)\hat{y} + u_z(x,y,z,t)\hat{z} = u_y(z)\hat{y} \qquad (32)$$

The previous expression for $\boldsymbol{u}$ causes the first two terms of the Navier-Stokes equation to vanish, because of the lack of time dependence and because $\boldsymbol{u}$ and $\nabla\boldsymbol{u}$ will be orthogonal (because $\boldsymbol{u}$ is directed along y, while its gradient $\nabla\boldsymbol{u}$ varies along *z*) making the dot product $\boldsymbol{u}\cdot\nabla\boldsymbol{u}$ equal to zero. The equation now reads:

$$\left(\frac{\Delta p}{L} =\right)\frac{dp}{dy} = \eta\frac{d^2}{dz^2}u(z) \qquad (33)$$

The equation in this form can be easily integrated, as it simply states that the function $u(z)$ has constant concavity, i.e. $u(z)$ is a parabola with two integration constants c_1 and c_2:

$$u(z) = \frac{\Delta p}{2\eta L}z^2 + c_1 z + c_2 \qquad (34)$$

These constants can be determined by imposing the no-slip boundary conditions, namely that the fluid must be at rest at the plates ($u(z=-h) = u(z=h) = 0$). Upon simple substitution, the final solution is then obtained:

$$u(z) = \frac{\Delta p}{2\eta L}(z^2 - h^2) \tag{35}$$

This equation is indeed a parabola, as shown in Figure 37(b). This profile is known as the Poiseuille flow profile and describes the typical situation found in pressure-driven microfluidic devices.

6.3. Rectangular cross-section channel

An important assumption in the previous derivation was that the plates are infinitely extended in the x direction, meaning that the lateral dimension of the channel is not being considered. When the width (2*w*) of the channel becomes comparable to its height (*2h*), however, the aspect ratio *w/h* needs to be considered, causing the solution to deviate from the parabolic Poiseuille flow.

This case then describes the Navier-Stokes equation in a rectangular cross-sectional channel, which does not have an analytical solution [155]. The additional boundaries along the width 2*w* of the channel (illustrated in Figure 38(a)) force the fluid velocity to be zero there, which implies that ***u*** must now also depend on the transverse direction coordinate *x* too:

$$\boldsymbol{u}(\boldsymbol{r}, t) = u_x(x, y, z, t)\hat{x} + u_y(x, y, z, t)\hat{y} + u_z(x, y, z, t)\hat{z} = u_y(x, z)\hat{y} \tag{36}$$

The time-dependent term and the dot product in the Navier Stokes equation still vanish as before, so the equation reads:

$$\left(\frac{\partial^2}{\partial x^2} + \frac{\partial^2}{\partial z^2}\right) u_y(x, z) = -\frac{\Delta \mathrm{p}}{2\eta L} \tag{37}$$

with boundary conditions:

$$u_y(x = \pm w, z = \pm h) = 0 \tag{38}$$

The best method for solving this equation is to Fourier expand the solution $u_y(x, z)$ along the *x* and z direction. After a few passages [155], this expression leads to a solution of the form shown below and illustrated in Figure 38(b).

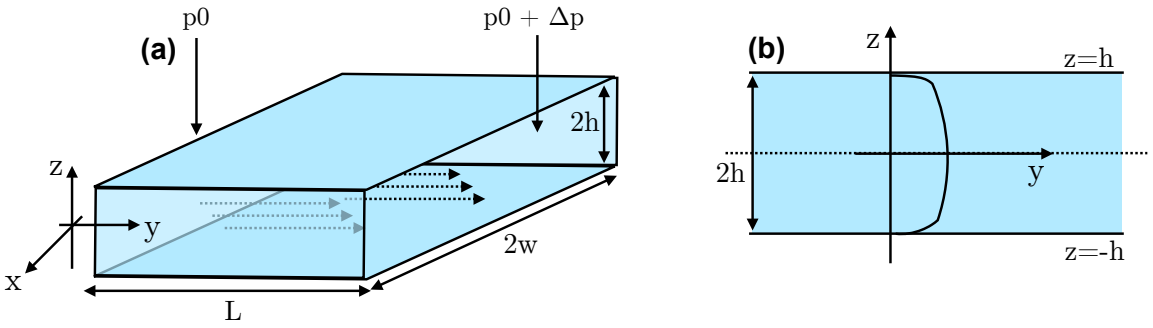

Figure 38. Geometry and relevant quantities defining a channel with a rectangular cross section. (a) 3D schematic of the channel. The two plates are placed at a vertical distance 2h, while the width and length of the channel are 2w and L, respectively. A pressure differential Δp is applied between the extremes along the y direction. (b) Side view of the xz plane with the plug-like fluid profile characteristic of a rectangular channel.

$$u_y(x,z) = \frac{4h^2\Delta p}{\eta\pi^3 L}\sum_{n,odd}^{\infty}\frac{1}{n^3}\left[1-\frac{\cosh\left(n\pi\frac{x}{h}\right)}{\cosh\left(n\pi\frac{w}{2h}\right)}\right]\sinh\left(n\pi\frac{z}{h}\right) \tag{39}$$

It is interesting to note that u_y only returns to its simple parabolic form for $w/h \to 1$ (square cross-section), as we will show next, which highlights that simple Poiseuille flow can not necessarily be assumed in practical geometries, many of which have rectangular cross-sections.

7. COMSOL simulations

The equation for u_y can be solved numerically using the commercial finite element COMSOL software. 3D simulations are performed to visualize the fluid flow inside the channel and the associated shear rate as a function of the aspect ratio. The implications of the shear on bacterial motion are also considered. An array of traps is then introduced into the channel and simulated in 2D. Finally, the fluid flow around a single trap is simulated. This last analysis is exploited for a parametric optimisation of the geometry of the trap that will then guide the fabrication.

7.1. Effects of the aspect ratio of the channel

We have seen above that the solution for a non-infinitely wide channel deviates from the ideal parabolic Poiseuille profile. In particular, the parabolic profile begins to flatten in the central area of the microchannel, resulting in a constant velocity over a section of the channel. Since the boundary condition of zero velocity at the channel walls still needs to be met, a steep slope establishes close to the boundaries. This effect is clearly visible in

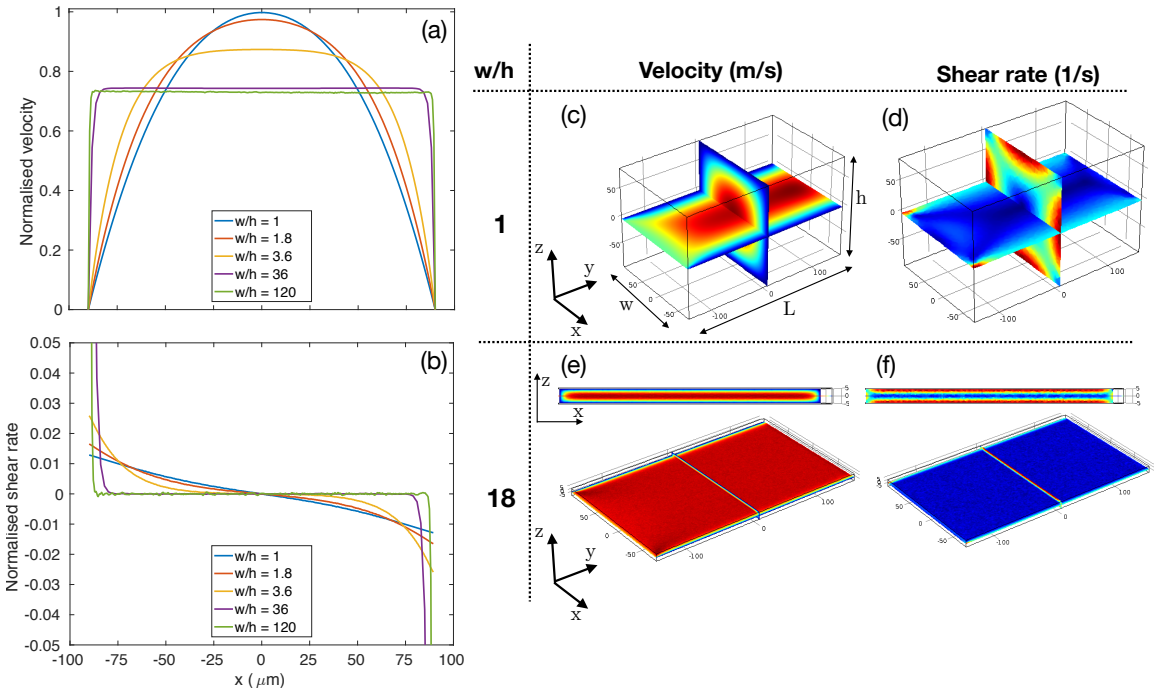

Figure 39. Results of COMSOL simulations of channels with different aspect ratio. (a) Normalised fluid velocity along the transverse direction of the channel (x) for different values of the aspect ratio w/h. As the aspect ratio increases, the standard parabolic Poiseuille profile flattens in the central regions of the channel (around x=0). (b) Normalised shear rate along x for the same set of values of the aspect ratio w/h. As w/h increases, the shear rate approaches zero over most of the breadth of the channel and rapidly increases close to the boundaries. (c-d) 2D slices of the velocity and shear rate along the two mid xy and xz planes for an aspect ratio w/h of 1. Both quantities resemble an ideal Poiseuille flow because of the width and height of the channel being comparable. (e-f) 2D slices of the velocity and shear rate for an aspect ratio of 18. The velocity is practically constant over the entire plane and the shear rate is mostly zero. The insets illustrate surface plots of the xz plane.

Figure 39(a), which was obtained by increasing the aspect ratio *w/h* (obtained by decreasing the height *h*, while fixing the width to 180 μm). The plot shows the normalised fluid velocity as a function of the x coordinate, i.e. the direction perpendicular to the channel, taken at the mid-plane y=0 (refer to the 3D simulation shown in Figure 39(c)). The shear rate, which describes the rate of change of the fluid velocity, is plotted in Figure 39(b) for the same set of aspect ratios. For small values of the aspect ratio (i.e. an almost square cross section), the shear is zero at the centre of the channel and decreases linearly to both sides, as expected for the derivative of a parabola. At larger values of *w/h*, the shear profile tends towards zero over an increasing portion of the channel width, since the velocity profile begins to flatten, as already noted in panel (a).

The right side of Figure 39 (panels (c-f)) shows the fluid velocity and shear rate across 2D slices of the COMSOL simulation domain for two different aspect ratios *w/h* (*w/h* = 1 and 18). An aspect ratio of 1 results in a rather standard situation close to the ideal Poiseuille

case, with a parabolic profile in both the x and z directions. The situation is drastically different for an aspect ratio of 18 (corresponding to a channel height of 10 μm for the width of 180 μm). The velocity is flat along much of the surface of the microchannel (Figure 39(e)), while the small inset shows the same effect across the xz plane. This leads to a zero-shear rate over most of the breadth of the microchannel (Figure 39(f)).

Building on the previous arguments, it is clear that shear is always generated in the presence of solid boundaries because of the no-slip boundary condition, which imposes the fluid to be at rest at any boundary. Turbulence can also cause shear, but this is rarely encountered in microfluidics due to the typical laminar flow regime. Because of the negligible role played by inertial forces, shear related effects start to become important and have an influence on the swimming action of microorganisms. Shear exerts torques, thereby influencing swimmers' motion in flow, especially close to walls and surfaces [157,158].

In particular, shear can cause the cell to periodically tumble and rotate because the net torque on the body is non-zero in the velocity gradient. Different points of the cell may experience different velocities, thus different torques, which induce rotation. The resulting trajectories are known as Jeffery orbits and are schematically shown in Figure 40(a) and (b) [159,160]. For a passive object in the fluid, such as a non-motile organism, the Jeffery orbit only acts on the body orientation and the centre of the object simply follows the fluidic streamlines. Conversely, the swimming direction and spatial distribution of motile organisms are affected by the Jefferey orbit phenomenon. This has been verified both theoretically [150] and experimentally [158]. The response of microorganisms to velocity gradients (i.e. shear) is known as rheotaxis [162], and any drift velocity arising as a result of shear is denoted as rheotactic velocity. This effect is particularly evident for elongated motile organisms, which represent a significant fraction of bacterial species. This class of microorganisms undergoes a shear-trapping phenomenon which tends to concentrate them in the regions of high shear, as detailed below.

Because of the body elongation, the angular velocity of the Jeffery orbit ω is higher when the cell body axis forms a large angle with the flow, while it is minimised when the body is aligned with the flow, as shown in Figure 40. In panel (a), the bacterium is oriented transversal to the flow direction, so that the extremes of the body experience two different fluid velocities $\boldsymbol{u}_1$ and $\boldsymbol{u}_2$, with $\boldsymbol{u}_2 > \boldsymbol{u}_1$. It follows that the two torques $\boldsymbol{\tau}_1$ and $\boldsymbol{\tau}_2$, calculated with respect to the centre of the cell body, have different direction and

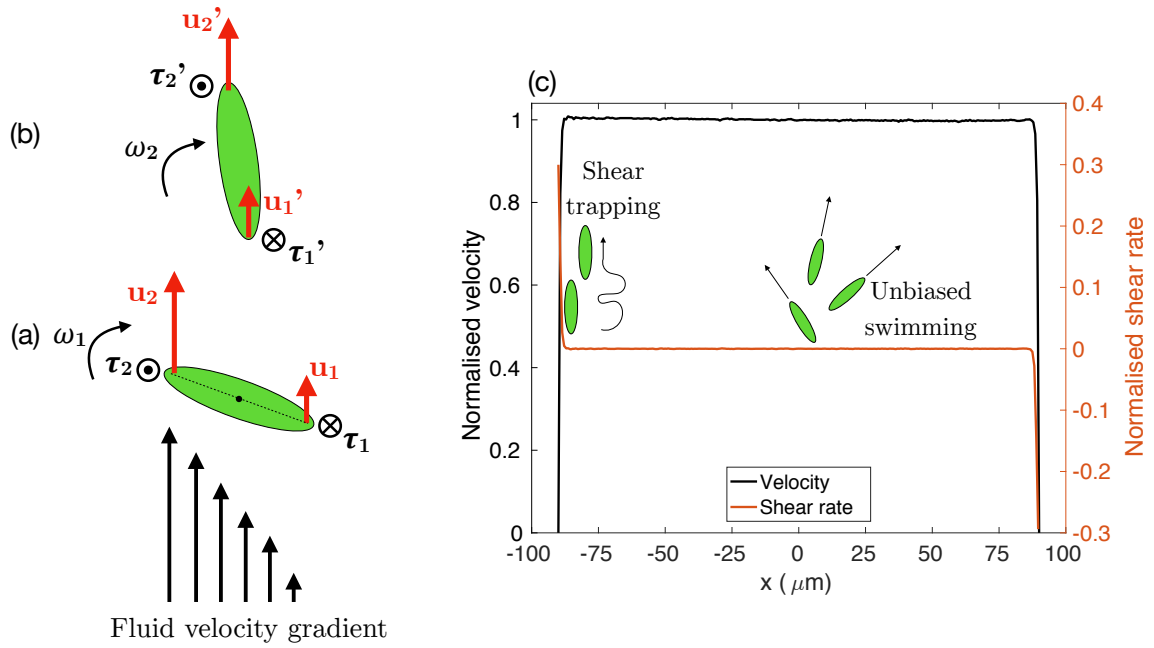

Figure 40. Effect of fluid shear on bacterial orientation. If an elongated object is subjected to a velocity gradient, as shown in (a), different parts of the body will experience different velocities ($\boldsymbol{u}_1$ and $\boldsymbol{u}_2$), thereby causing a net torque ($\boldsymbol{\tau}_1 + \boldsymbol{\tau}_2$) that induces the object's rotation at an angular velocity ω_1. ω_1 is however reduced to ω_2 when the object is aligned with the flow, as shown in (b). Hence, the body tends to stay aligned with the fluid flow. (c) The torque induces bacterial trapping close to the channel walls, where the shear is higher. Contrarily, in the central region, the swimming action is unbiased as no torques are present.

magnitude. This induces a rotation with an angular velocity ω_1 dictated by the net torque $\boldsymbol{\tau}_1 + \boldsymbol{\tau}_2$. Conversely, if the bacterium is almost oriented along the flow (situation in panel (b)) the Jefferey angular velocity ω_2 is smaller because the net torque is now decreased. This last configuration is energetically favourable and thus preferred. As a direct result, wherever shear is present, elongated bacteria spend more time aligned with the flow, thereby featuring limited migration across streamlines and remaining "trapped" in the high-shear region.

For the Poiseuille-like profile typical of low aspect ratio channels, the shear increases linearly from zero at the centre of the channel to its maximum value at the walls, as previously illustrated in Figure 39(b). Thus, the motion of bacteria will not be significantly influenced in the central regions and their swimming is almost unbiased. However, as soon as they happen to swim in a high-shear region, they will preferentially orient along the fluidic streamlines and their migratory ability will be hampered (see Figure 40(c)). Contrarily, in the extreme case of $w/h = 120$, which corresponds to the real geometry used in most of the experiments in this work, both the velocity and the shear rate flatten significantly over almost the entire breadth of the channel. The bacterial swimming is thus unbiased in most of the area of interest, as illustrated in Figure 40(c). According to this

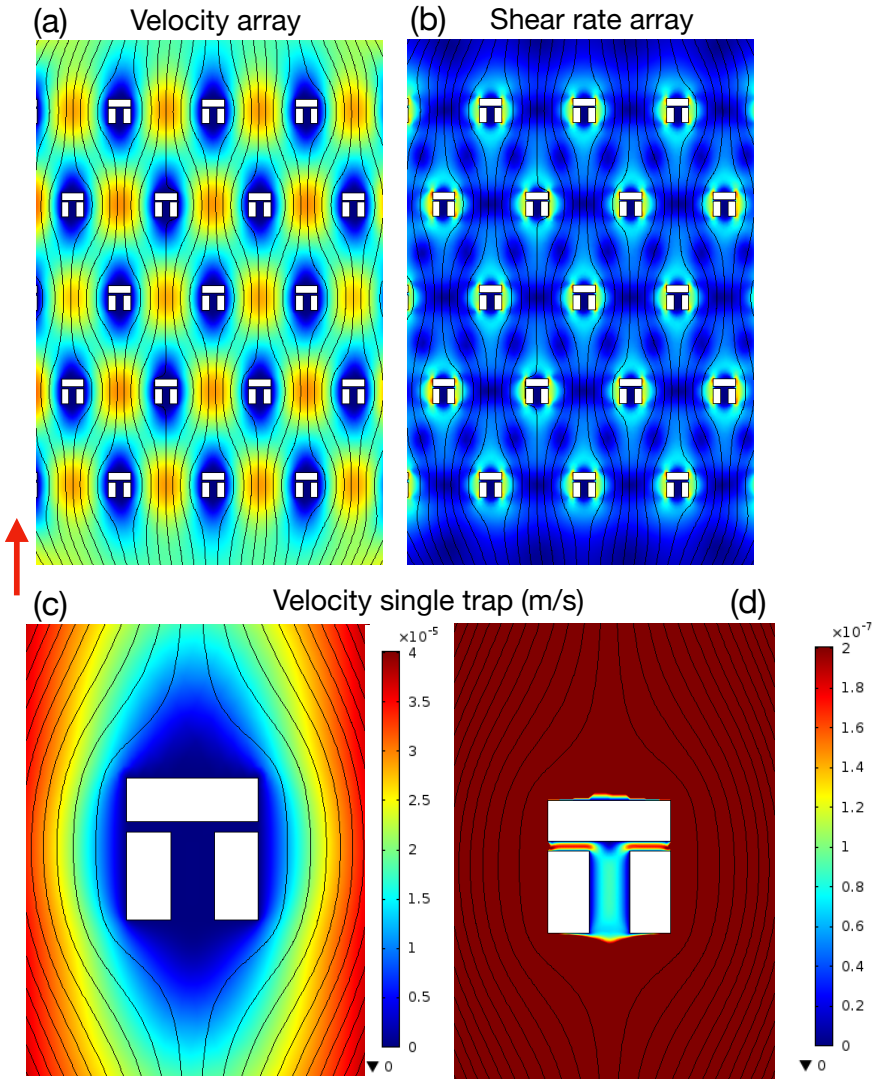

Figure 41. COMSOL simulations of the fluid flow around the traps. (a, b) Velocity and shear rate for a channel containing an array of traps. The period of the array in both x and y is 25 µm and the total width of the channel is 180 µm. The presence of the traps causes velocity gradients and enhanced shear. (c) Close-up of the fluid flow around a single trap with overlaid velocity streamlines. The streamlines avoid the inside of the trap because of the much lower fluid velocity inside, as highlighted in panel (d). Note the difference in flow scale by more than 2 orders of magnitude. The red arrow on the left indicates the direction of the fluid flow.

argument, a plug-like profile could be desirable in some situations, as it confines the high-shear regions to two extremely thin regions very close to the channel walls.

7.2. Trap design

It is clear that the above conditions do not reflect the experimental reality in most cases, yet they do provide an understanding of the baseline conditions in a microfluidic channel. For example, when traps are present aimed at capturing bacteria inside the microchannel, the ideal Poiseuille flow is disturbed; each trap represents additional boundaries, at which the fluid must be at rest. This implies that extra shear is generated around the traps (see the

shear distribution in Figure 41(b)) and that the swimming action of bacteria will be affected close to the traps' boundaries. Additionally, the no-slip condition causes the fluid velocity to reduce greatly inside the traps compared to the neighbouring regions. This effect is clearly illustrated in Figure 41(c) and (d). Note that the colour scale inside the trap in panel (d) is two orders of magnitudes lower than in panel (c), because the flow is so much lower inside the trap compared to outside. This difference causes the fluidic streamlines to avoid the trap, with most of the fluid simply flowing outside of the trapping area.

Traditionally, the design of such hydrodynamic traps, for example for eukaryotic cells, is aimed at maximizing the fluid flow through them in order to drag as much fluid as possible through them. However, in the context of bacteria, the dimensions are much more constricted; if the goal is to preserve the single-cell capability and prevent bacteria from escaping, traps must be significantly smaller than in the eukaryotic cell case. For example, the fluid flow through the trap could be enhanced by increasing the trap width or the gap between the blocks. However, enlarging these dimensions would result in multiple bacteria being able to fit into a trap or in bacteria easily escaping. Therefore, trapping individual bacteria imposes serious limitations on the fluid flow and, as a consequence, on the maximum attainable trapping efficiency.

In order to investigate these issues, COMSOL simulations were performed for different trap geometries. The geometry is shown in Figure 42(a) and is based on the work of Probst *et al*. [153]. Their design was employed as a starting point for the parametric optimisation described below (which has not been reported by Probst *et al*.) and it was chosen because of the relatively simple yet effective geometry for single bacteria trapping. The width and length of the bars forming the trap is fixed to 2 μm and 4 μm respectively, while the width of the trapping region g_v and the length of the vertical gap g_h are varied parametrically. I used the average fluid velocity over the light red shaded area as a figure of merit to assess the quality of the trap. A higher fluid velocity through the gap implies a more efficient trap since it can intake more fluid per unit time.

Figure 42(b) shows the simulated average fluid velocity through the trap as a function of g_v and g_h, as defined in the diagram in Figure 42(a); as expected, the larger the gap, the higher the flow. Given that the goal is to trap *E. coli* with a width of approx. 0.5 μm, the upper bound for g_h is constricted roughly to this value; a gap any larger than this would allow bacteria to escape. Interestingly, in this regime of $g_h \lesssim 500$ nm, the fluid velocity

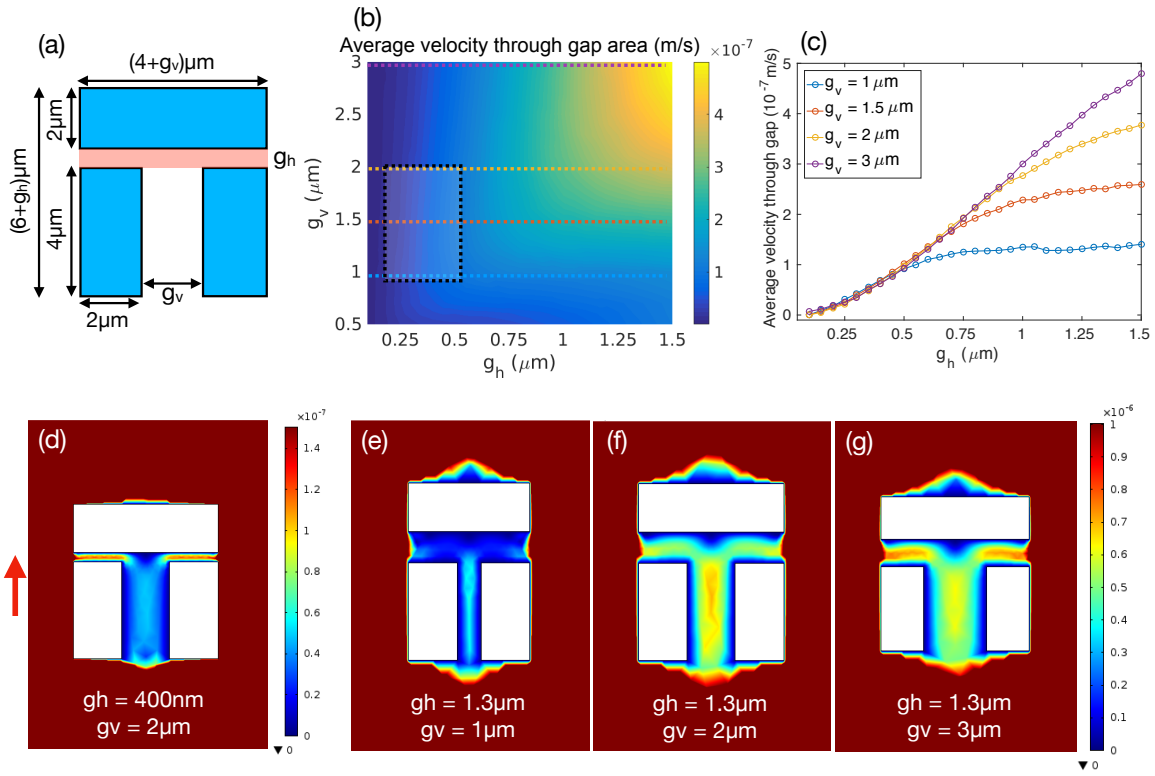

Figure 42. Results of the parametric COMSOL optimisation of the trap's shape. (a) Diagram of the trap geometry and relevant parameters used in the simulations. The average velocity through the trap is calculated over the area shaded in red. (b) Average velocity as a function of the width g_v and the gap g_h of the trap. The black dashed box highlights the optimal operational region under the constraint of maintaining the single cell capability. The four coloured dashed lines represent the slices of constant width plotted in (c). Here, the average velocity is reported as a function of the gap g_h for different widths g_v. For values of g_h smaller than about 500 nm, g_v does not have a significant influence on the performance of the trap. (d-g) Fluid velocity distributions for a selection of parameters, as indicated in each panel. The red arrow indicates the direction of the simulated fluid flow for each panel.

through the gap is independent on the width of the trap g_v, as clearly illustrated in Figure 42(c). In this graph, the average velocity is plotted as a function of g_h for four selected values of g_v corresponding to the coloured dashed lines in the previous colour plot (panel (b)). For values of the vertical gap smaller than about 500 nm, the fluid flow is limited by the gap itself since any volume of fluid flowing through the trap, must exit through the vertical gap. In other words, increasing the width of the trap does not result in any advantage because the flow is dominated by the small value of g_h.

The bounds on g_v are instead dictated by the need for preserving the single cell capability of the assay. A lower limit of 1 µm has been established in order to allow some degree of bacteria movement when trapped, while an upper limit of about 2 µm has been determined as a reasonable trade-off to accommodate a single bacterium in most cases. This optimum area is highlighted in the colour plot of Figure 42(b) by the black dashed box. The position of the box within the colour plot confirms the previous argument that the degrees of

freedom in choosing the geometry to maximise fluid flow are very limited and not able to bring significant advantages to the assay. In other words, the optimal box constrained by the small size of bacteria and fabrication limitations, lies in a region where the fluid flow as a function of the geometry is a relative flat function.

A few examples of the fluid flow distribution inside the trap are shown in Figure 42(d-g). Panel (d) illustrates one of the geometries within the optimal area highlighted by the colour plot. Panels (e-g) show instead the high-g_h region, where the width of the trap starts to play a role. Note the different color bar values between the two sets of plots, which prove how much the gap g_h influences the fluid flow (400 nm versus 1.3 μm), although these last three configurations are not suitable for trapping because of the gap being too wide.

In summary, the simulation analysis provides two major useful insights:

- It is practically impossible to recover the two orders of magnitude difference between the inside and outside of the traps highlighted by Figure 41 (c) and (d), mainly because the geometrical parameters are limited by the small dimensions of the bacteria. Therefore, most of the streamlines will always be diverted away from the interior regions of the trap.

- As a consequence, bacteria do not tend to automatically get trapped because of the fluidic action itself, but they need to actively cross streamlines. This is a clear disadvantage of such a trapping method, but at the same time it represents a way to measure motility. In fact, non-motile organisms will passively follow the streamlines. The only chance for a non-motile object to get trapped is to follow one of the (very) few streamlines going through a trap. Conversely, if the flow rate is low enough, motile organisms are able to migrate across streamlines and thus feature higher chances of entering a trap. This trapping efficiency argument is explored and detailed in the following chapter.

8. Trapping efficiency and flow rate

The flow rate at which the fluid is pumped into the microfluidic chip determines the fluid velocity, which has a critical influence on the bacteria behaviour inside the microchannel and their interaction with the trapping array. The optimisation of the flow rate is crucial to

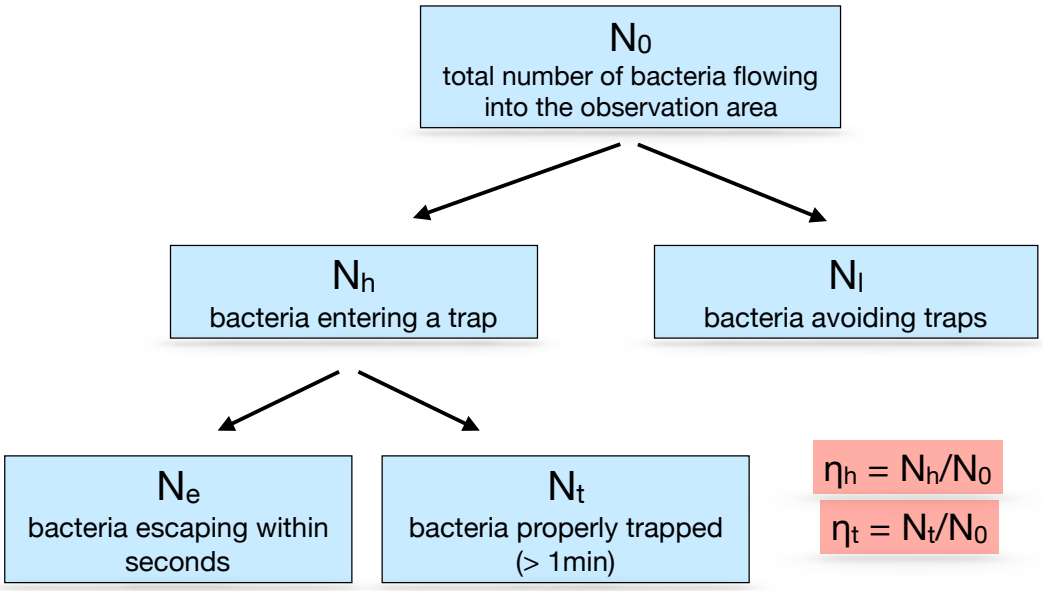

Figure 43. Diagram showing the relevant quantities used to define the hydrodynamic efficiency η_h and the trapping efficiency η_t.

avoid that the additional shear caused by the traps aligns the bacteria with the streamlines, thereby reducing the trapping efficiency. We can identify a lower and an upper bound for the flow rate: a) if it is small compared to the bacteria swimming speed, shear-trapping is negligible, and bacteria can easily migrate across streamlines. This is advantageous for trapping, but it also means that cells can easily escape from the traps; b) conversely, if the flow is too fast, the trapping efficiency drops, as the bacteria's ability to cross the streamlines is hindered by the high fluid velocity and the shear trapping effect.

In order to quantify the previous arguments, we introduce two quantities: the trapping efficiency η_T and the hydrodynamic efficiency η_H. A schematic explanation for these two efficiencies is provided in Figure 43. Let N_0 be the total number of bacteria flowing into the analysis area in a certain amount of time. Out of these, N_l will never enter any of the traps, while N_h will swim into a trap. However, not all of the N_h bacteria will stay trapped for a significant amount of time. In fact, N_e organisms will escape the traps almost immediately either through the vertical gap or because they are able to swim against the flow. N_t bacteria will instead stay trapped for a longer time, here being set to 1 minute. Clearly $N_h + N_l = N_0$ and $N_e + N_t = N_h$. The previous quantities allow us to define the trapping efficiency η_T and the hydrodynamic efficiency η_H as:

$$\eta_T = \frac{N_t}{N_0} \tag{40}$$

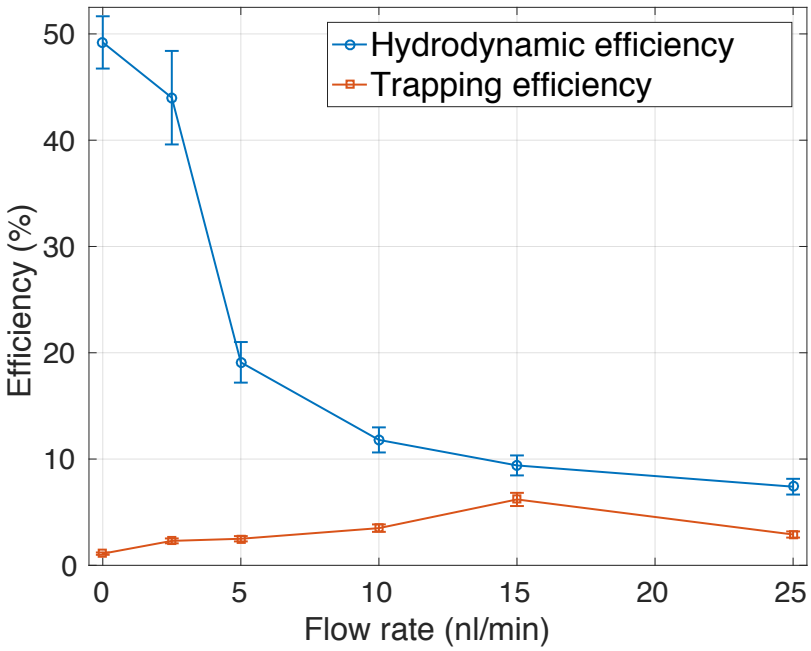

Figure 44. Hydrodynamic and trapping efficiency as a function of the flow rate. At low flow rates (and in the limiting case of no flow) approximately half the bacteria enter a trap but do not stay trapped for long as they can easily swim against the flow. As the flow rate increases, fewer swim into a trap because of a net velocity being imparted by the fluid and partly because of the shear trapping phenomenon. However, those that enter a trap are more likely to stay trapped, as shown by the growing trapping efficiency. At around 15nl/min the two efficiencies become as close as allowed by the two competing effects, reaching a value just below 10%. At higher flow rates both figures decrease as bacteria are preferentially dragged by the fluid and are not able to cross streamlines to swim into a trap. Error bars refer to the standard error over three independent replicates (N = 3) summed in quadrature with the error associated to the bacteria count (10%, as estimated in section 11.2).

$$\eta_H = \frac{N_h}{N_0} \tag{41}$$

From the definition of η_H, it can be argued that for a fixed bacterial strain and flow rate, the hydrodynamic efficiency is linked to the "quality" of the trap. An optimised trap design will convey a larger number of fluidic streamlines towards its inner region, thus increasing the chances of a bacterium flowing along one of those streamlines, regardless of whether the bacterium stays trapped for a long time. Thus, η_H can be considered a figure of merit for the shape of the trap, as well as being dependent on the flow rate. At the same time, it carries information about bacterial motility, as motile micro-organisms are more likely to migrate across streamlines. Motile bacteria are also more likely to encounter the traps because they are able to explore the environment more efficiently. On the other hand, η_T quantifies the fraction of bacteria staying trapped long enough to allow a significant assessment of their motility. The trapping efficiency will be dependent on both the flow rate and the motility too.

The dependence on the flow rate is illustrated in Figure 44, where both η_H and η_T are measured. The experiments were all conducted with the same bacterial strain (*E. coli* MG1655 at the onset of the exponential growing phase) and with the same trap geometry in order to probe only the dependence on the flow rate. The initial concentration of bacteria was chosen to be the same in all cases ($\sim 10^8$ cfu/ml, corresponding to an optical density at 600 nm of ~ 0.1) to avoid differences in the number of bacteria available for trapping, considering that the analysis time is the same across the different runs. Clearly, the absolute efficiency also depends on the analysis time. The longer the system is observed for, the more bacteria swim into a trap, especially at very low flow rate. However, this dependence on the analysis time has not been explored in detail here, and the time has simply been fixed to 5 minutes.

First of all, we note from Figure 44 that η_H (blue curve with circle markers) is always higher than η_T (orange curve with square markers) for every flow rate, simply because N_h is always larger than N_t, i.e. the number of bacteria remaining trapped is always a fraction of the total number of bacteria caught by a trap. This implies that the best theoretical case for maximising the number of trapped bacteria is $\eta_H = \eta_T$, i.e. all the bacteria that enter a trap remain trapped.

At low flow rates, bacteria are able to efficiently explore the microfluidic environment, including the inner regions of the traps, and swim almost unbiased. This is because of the fluid flow being much lower than their swimming speed and shear does not play a significant role. This results in high values of η_H, up to about 50% in the limiting case of zero flow. However, these bacteria do not remain in the traps because the fluid flow is not high enough to keep them there. Hence, the trapping efficiency (orange curve in Figure 44) is rather low. The residual non-zero trapping efficiency observed at zero flow rate (slightly less than 1%) corresponds to bacteria that become blocked in the vertical gap.

As the flow rate grows, a decrease of η_H and an increase of η_T is observed. The reason is twofold. On one hand, fewer bacteria are able to swim towards a trapping region because of the flow imparting a net velocity component along the channel direction, which tends to preferentially drag them along the channel. Furthermore, the shear starts to play a role by tending to keep bacteria aligned with the fluidic streamlines. However, those bacteria that manage to enter a trap are more likely to stay there for longer because the fluid is now

exerting sufficient force to keep them inside. On the other hand, as the trapping efficiency becomes larger, traps get occupied and it is less likely for a new bacterium to swim inside the same area. The combination of these effects causes the two curves to approach for a value of around 15 nl/min. The two quantities do not exactly match at any flow rate because some bacteria will always be able to escape immediately (i.e. N_e will never be zero) through the vertical gap, which needs to have a non-zero width in order to allow some fluid to flow, as discussed in the optimisation chapter. Above this point (i.e. at 25 nl/min), the flow rate becomes too high for bacteria to swim towards any of the traps, which results in a continuous decrease of both efficiencies.

In summary, the hydrodynamic efficiency continuously decreases as a function of the flow rate while the trapping efficiency features a maximum that represents the optimum point at which the fluid velocity is low enough to allow bacteria to migrate across streamlines and large enough to keep the maximum number of individuals trapped for a significant amount of time.

9. Bacteria tracking

Most of the features analysed so far can be visualised and confirmed by tracking bacteria inside the microfluidic channels. Three relevant examples are shown in Figure 45 for different values of the flow rate. The trajectories were obtained with the TrackMate® extension of ImageJ, which enables one to detect swimming objects in each frame and link their relative positions between different frames of the video [163]. Since videos were recorded at different flow rates, a different number of bacteria swam through the field of view per unit time. Hence, different lengths of the recorded videos were analysed in order to ensure an approximately equal number of about 150 traces in each graph. It is reasonable to assume that at a large enough distance from the trapping area, the fluid is unperturbed, and bacteria are homogenously distributed over the width of the channel.

In order to better understand the bacterial behaviour in the analysis area, one can think of the net bacteria velocity $\boldsymbol{v_T}$ as a superposition of two contributions, namely the bacterium's own velocity $\boldsymbol{v_b}$ and the fluid velocity $\boldsymbol{u}$:

$$\boldsymbol{v_T}(x,y) = \boldsymbol{v_b}(x,y) + \boldsymbol{u}(x,y) \tag{42}$$

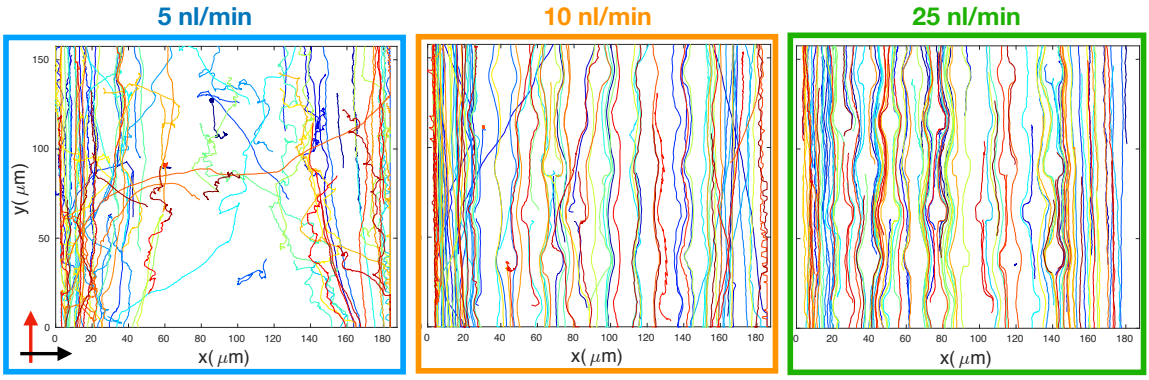

Figure 45. Bacterial trajectories extracted from videos at different flow rates. At 5 nl/min (blue-framed graph) the fluid velocity is low enough to allow bacteria to swim almost unbiased and migrate across the central area. Typical run and tumble trajectories are observed in the central regions of the channel, while the shear trapping phenomenon is observed near the walls, where the bacterial density is higher. As the flow rate increases (orange and green framed graphs), the bacterial trajectories start to gradually conform to the underlying fluid flow, thereby reducing the probability of entering a trap. The red arrow indicates the direction of the fluid flow.

The dependence on the z-coordinate is neglected, meaning that the bacterial swimming is assumed to be 2-dimensional. This assumption is motivated by the height of the channel being about 2 µm. Changes in the flow rate clearly modify $\boldsymbol{u}(x, y)$ and thus its relative contribution to the net velocity vector $\boldsymbol{v_T}(x, y)$, affecting both its magnitude and direction.

An estimation of the typical values for $|\boldsymbol{u}|$ can be easily performed by dividing the imposed volumetric flow by the cross section of the microchannel. For example, a flow rate of 5 nl/min corresponds to a volumetric rate of $5*10^6$ µm^3/min, while the cross-sectional area of the channel is ~ (200 x 2) µm^2. A simple division leads to a fluid velocity $u\sim$160 µm/s in the main section of the microfluidic device. However, the main channel directly connected to the tubes was always split into 8 different channels in order to multiplex measurements and to decrease the fluid velocity in each of them (see the microfluidic chip design B in Appendix A1). This means that for a flow rate of 5 nl/min the fluid flow is about 20 µm/s.

Hence, considering typical bacterial swimming speeds of ~30 µm/s [164], for a flow rate of 5 nl/min $\boldsymbol{v_b}$ plays an important role in determining the bacteria motion, while the flow gently drags them along the positive y direction. In fact, the trajectories appear significantly fragmented, as visible in the blue-framed graph in Figure 45, with some bacteria being able to move across the entire channel in the transverse direction. This also allows one to observe the characteristic *E. coli* run-and-tumble motion [164,165] in the central regions of the channel, where their swimming motion is mostly unbiased. However,

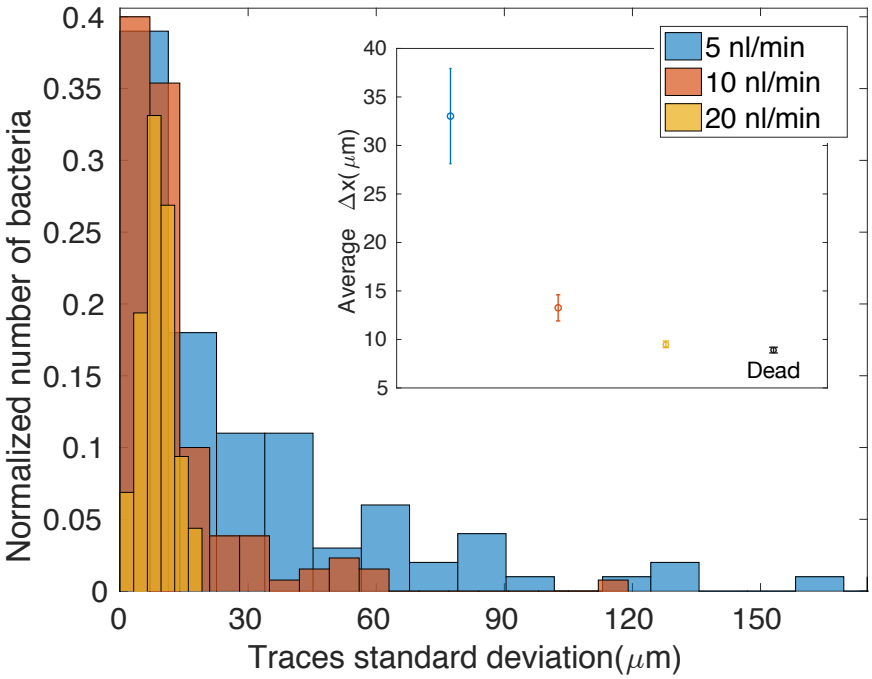

Figure 46. Distributions of the bacterial trajectories standard deviations along the direction perpendicular to the channel at different flow rates. At low flow rates (blue bars) the distribution is significantly skewed towards large values because of bacteria being able to migrate across the channel, thereby featuring large variances in their x coordinates. As the flow rate increases, the tail disappears as the x-migration ability is hampered by the fluid velocity. The inset shows how the average deviation decreases as a function of the flow rate. The dead case refers to bacteria killed by exposure to heat (60 °C for 2 hours).

in the region of high shear close to the channel walls, the Jeffery orbit and the shear trapping effect are clearly observed as trajectories showing periodic loops along the flow direction and an increased bacterial concentration in these areas.

As the rate increases to 10 nl/min and 25 nl/min (orange and green framed panels in Figure 45), the fluid velocity is about 40 and 100 µm/s respectively, which makes the velocity comparable to and larger than typical values of bacteria swimming speed, respectively. As a consequence, trajectories become more linear and start to conform to the underlying fluidic streamlines, which bacteria are not able to cross anymore. In other words, the condition $\boldsymbol{v_T}(x,y) \sim |u|\hat{y}$ is progressively met, where the total velocity of the organisms is dominated by the fluid flow along the channel.

By defining the coordinate system shown in Figure 45, a trajectory *p* can be represented as a function *p(x, y, t)*, where *t* is the time step. In particular, the dependence *p(x)* can be exploited to assess the motility-flow coupling effect and the ability to move across streamlines. In fact, for a totally passive object (or equivalently for a very high flow rate), a weak dependence *p(x)* is expected, as the trajectory follows the fluidic streamlines, which

extend mainly along *y*. This is clearly seen in the green-framed picture in Figure 45 with small deviations along *x* only due to the presence of the traps. Conversely, an object crossing streamlines modifies its *x* coordinate in time, as is the case of the 5 nl/min (blue framed panel in Figure 45). This effect can be quantified by calculating the spread of the *x* coordinates for each trajectory p_j as:

$$\Delta x_j = \sqrt{\frac{\sum_{i=1}^{t_{fj}} (x_i - \bar{x}_j)^2}{t_{fj} - 1}} \tag{43}$$

Where $\bar{x_j}$ is the average x position of the j-th trajectory over the entire analysed time range and t_{fj} is the final time step of the of the j-th trajectory. Figure 46 shows three distributions of Δx_j for different values of the flow rate, while the inset reports average values. For a low flow rate (blue histogram) the distribution of standard deviations features a slow decaying tail towards very high values since the most motile fraction of bacteria is able to migrate across the x direction. The high fraction of trajectories featuring low degree of deviations includes the shear-trapped bacteria near the walls that are not able to efficiently migrate. As the flow rate increases, the distributions tend to shrink towards lower values, as evidenced by the orange and gold histograms. The inset reports the average value for each case showing the expected decrease. Interestingly, the high flow rate case is very similar to a dead case, as shown by the black data point (corresponding histogram not shown here for clarity). Bacteria were killed by exposing them to heat (60 °C for 2 hours).

10. Fabrication

The fabrication of the devices is carried out by following a replica moulding process typically used in Polydimethylsiloxane (PDMS) microfluidics [166,167]. The procedure can be divided in two steps, namely the fabrication of the SU8 mould and of the PDMS replica.

The first step is the fabrication of the mould containing the structures to be reproduced. We use silicon as a substrate, with the SU8 being structured by UV or by electron beam lithography. An SU8 film of the desired thickness is first spun onto a silicon substrate (step 1 in Figure 47). SU8 is a polymeric negative-tone resist first developed at IBM in the early 80's. The resist is obtained by dissolving EPON® SU-8 resin in an organic solvent such as PGMEA or cyclopentanone with the addition of a specific photoinitiator. Exposure (step

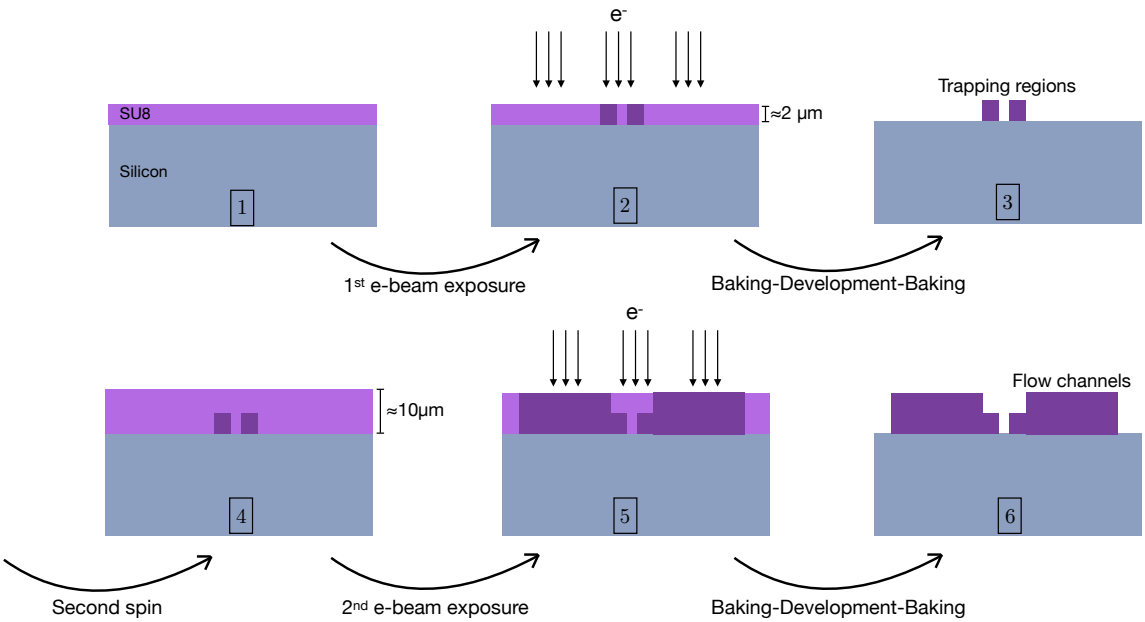

Figure 47. Schematic steps for the fabrication of a SU8 mould on silicon. The SU8 is spun onto the silicon substrate (1) and baked. Then the pattern of interest is exposed by electron beam lithography (2). The layer is baked to trigger cross-linking in the exposed areas, then developed, and finally hard-baked to cure the structures (3). The process is repeated for a potential second layer if multilayer structures with different thicknesses are needed (4-7).

2 in Figure 47) causes the photoinitiator to decompose and form an acid which is able to open some of the epoxide rings of the SU8 molecule by protonating them. Upon application of heat during the post exposure bake (PEB), the protonated rings react with the neutral ones thus starting the cross-linking process which makes the exposed film less soluble upon development. The exposed regions are then left on the substrate (step 3 in Figure 47). A final optional hard-bake step can be carried out to ensure total cross-linking, strong adhesion to the silicon surface and to remove any potential residual solvent pockets that might compromise the uniformity of the structures. The extra steps (4-6) included in Figure 47 repeat the procedure, with the aim of structuring a second layer, which is needed for the trapping geometry that I will describe later on.

Next, we make a PDMS replica of the mould. PDMS is polymeric mineral-organic (meaning its structure contains carbon and silicon atoms) compound commonly used for the fabrication of microfluidic devices. Liquid PDMS is mixed with a cross-linking agent in a variety of ratios to enable solidification upon heat exposure and allow it to turn into a transparent and soft hydrophobic elastomer. Different ratios result in different properties of the final solid mixture, such as stiffness, density and porosity. Before curing, the liquid mixture is poured onto a microfabricated mould in order to reproduce the desired structure (step 1 in Figure 48). Once solidified (step 2 in Figure 48), the PDMS is released from the

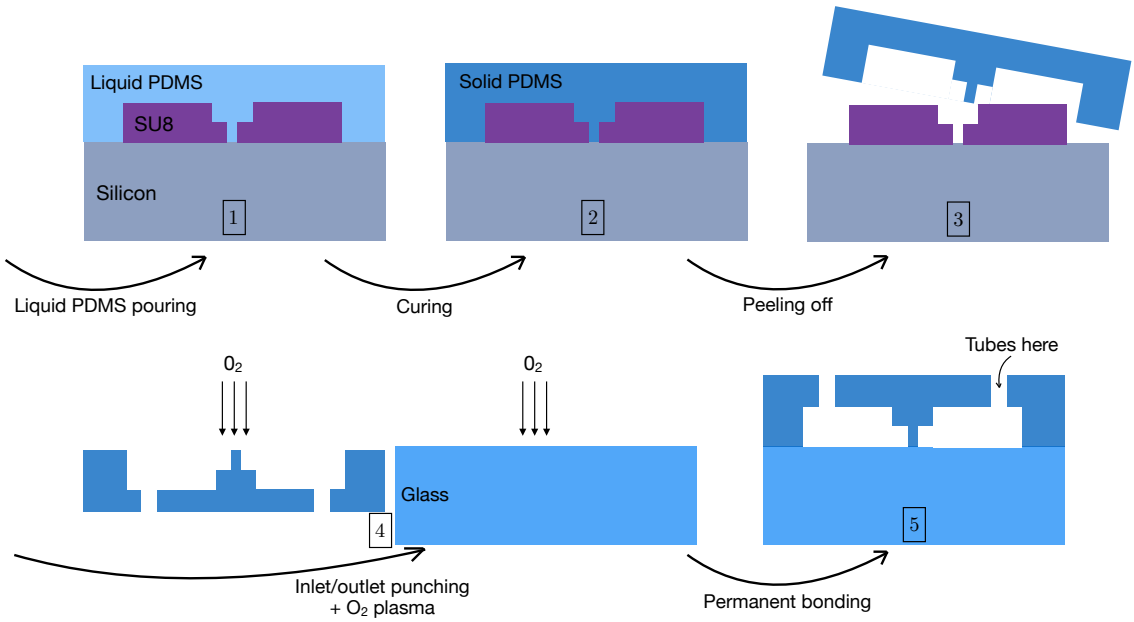

Figure 48. Steps needed for a PDMS replica moulding process. A mixture of PDMS and curing agent is poured onto a previously fabricated SU8 mould (1). The mixture solidifies upon curing thanks to polymeric cross-linking triggered by the curing agent (2). The solid PDMS is carefully peeled off the substrate (3), holes are punched, and a O_2 plasma is applied to the PDMS and the substrate of interest (glass here) (4). The plasma-activated surfaces are brought in contact and gently pressed to ensure permanent sealing thanks to the creation of covalent Si-O-Si bonds (5).

mould by peeling it off (step 3 in Figure 48), then inlet/outlet holes are punched through the elastomer (step 4 in Figure 48) before being bonded to the substrate of interest. PDMS can seal to itself or to other surfaces such as glass or silicon both reversibly (by simple contacting, based on van der Waals interactions) or irreversibly through oxidation of both surfaces to be bonded (step 4 and 5 in Figure 48). The oxidation is typically obtained by treating the surfaces with an oxygen plasma, which produces silanol (SiOH) terminations on the PDMS surface and makes it hydrophilic for a few tens of minutes. This procedure enables the formation of covalent oxygen-silicon-oxygen bonds upon contacting and slight application of pressure with the substrate surface.

The reasons why PDMS is a common choice in microfluidics are numerous. First of all, it is transparent in the visible range, hence enabling optical inspection and spectroscopy. PDMS has low autofluorescence, which makes it suitable for fluorescence measurements. Furthermore, it is biocompatible so that it allows cells to maintain viability inside the channels. It is also permeable to oxygen, which is a fundamental requirement for cell culturing. It is cheap, readily available and relatively easy to fabricate, so that it is the ideal candidate for rapid prototyping and testing of devices. Finally, being deformable, it allows for the fabrication of multilayer structures with embedded control valves. Although the deformability can represent a drawback in certain circumstances, the stiffness can be tuned

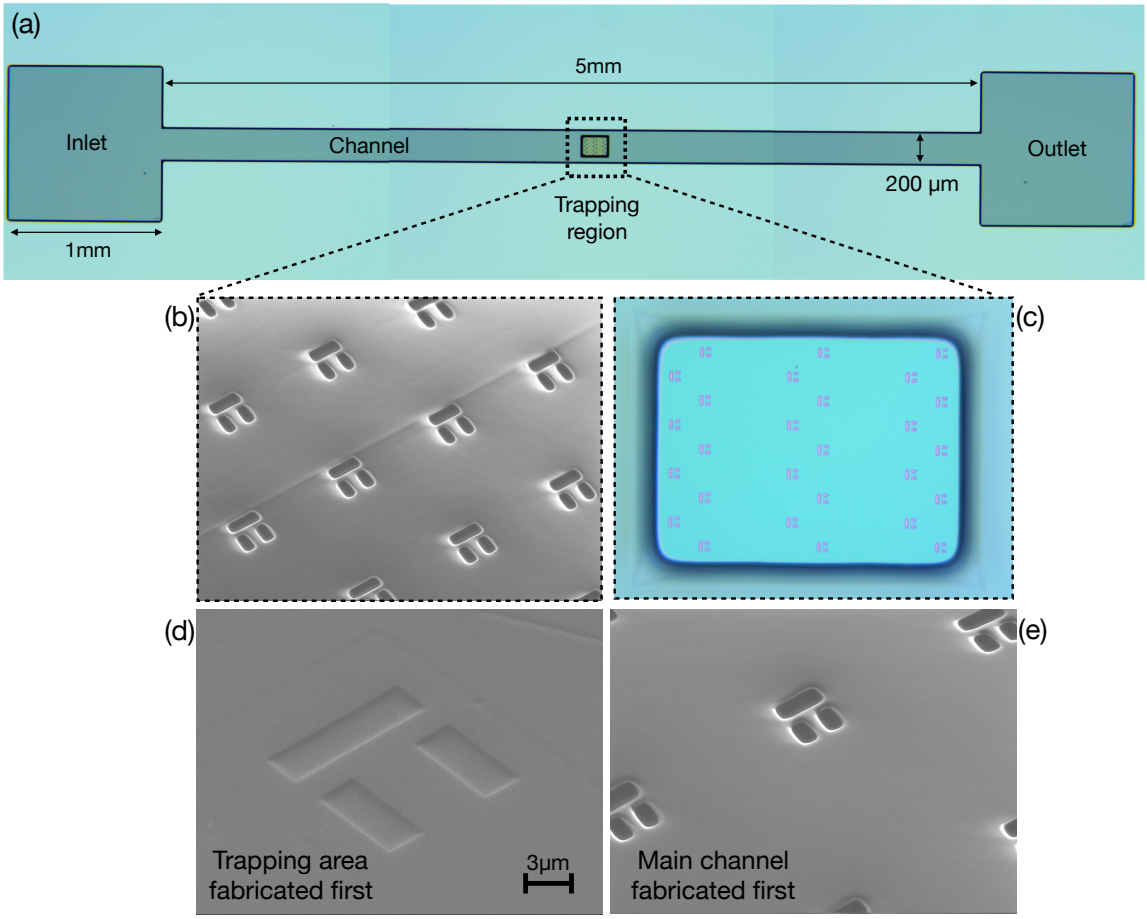

Figure 49. Pictures of SU8 moulds fabricated on silicon. (a) Mosaic of three brightfield microscopy pictures showing a two-layer SU8 mould on silicon, with the channel and the trapping area (in the middle of the picture) being fabricated separately and with different thickness. (b) SEM micrograph close-up of the trapping area featuring the hollow traps to be subsequently filled by PDMS to reproduce the positive shape. (c) Picture of the same region taken under a brightfield microscope. (d) SEM micrograph of a single trap in a SU8 mould with the traps fabricated as a first step. It shows that the SU8 spun for the second exposure of the thicker channel is not totally removed from the hollow blocks of the traps. (e) A similar trap shape in a mould with the inverted fabrication flow. The channel was fabricated first in order to avoid thick SU8 penetrating the trap. This second method clearly produces better results.

by changing the PDMS to curing agent ratio. This characteristic will be discussed in further detail in the following section.

On the other hand, using PDMS might not be always the most viable solution. Its permeability can represent a significant issue in certain circumstances, such as in cell signalling or fluorescent assays, since the molecules of interest might be absorbed by the PDMS matrix and therefore not detected. PDMS is also not very solvent-resistant, which relegates its application to water-based chemistry. Additionally, hydrophobicity could represent an issue, since proteins of interest might start adsorbing on the surface. Nevertheless, the research community continues to use it extensively, even when PDMS

is recognised as not the best material of choice. Several alternative solutions are available, as highlighted in [168–170].

10.1. Strategy 1: PDMS traps and channel

Two strategies for the fabrication of the trapping assay have been tested. The first one entails the fabrication of the trapping wells to be integrated with that of the microchannel, i.e. the trapping wells are made of PDMS and hang from the ceiling of the channel itself, as shown diagrammatically in Figure 51(a). This method has already been proven viable in the literature by Probst *et al*. [153] The fabrication steps are depicted in Figure 47 and Figure 48, and were previously described.

A brightfield microscope picture of a mould fabricated in this way is shown in Figure 49(a) with lateral dimensions specified. The 1 mm squares at each end provide sufficiently large pads to punch holes for the insertion of tubes. It is important to note that the traps' blocks are hollow in the central section in order for them to be filled up by the liquid PDMS mixture and allow replication of the negative shape, as shown in Figure 49(b) and (e).

Two electron beam exposures are needed to fabricate such a geometry because of the different thickness of the main channel and the trapping area. In particular, the exposure of the thicker main channel section was carried out first and then the traps were exposed in the second step. The reason for choosing this order is to prevent the thick SU8 layer from covering the already fabricated traps. This effect is clearly shown in panel (d) of Figure 49. If the traps are fabricated first (panel (d)), SU8 is not totally removed from the traps by the development process of the second thicker layer, thereby preventing the liquid PDMS mixture to fill the entire depth of the traps. As a consequence, upon bonding of the PDMS replica onto a glass slide, the trapping structures are not as deep the channel, hence resulting in a gap between the substrate and the basement of the wells (see Figure 51(a)).

However, even when inverting the order of the electron beam exposures (which produced the shapes shown in Figure 49(e)), a correct PDMS replica was never achieved as illustrated in Figure 50. The first column shows tilted SEM micrographs of SU8 moulds with traps of increasing dimension, in order to probe the effect of size on the reproducibility of the traps' features (see the microfluidic chip design A in appendix A1). The second column shows SEM pictures of the corresponding PDMS replicas. The surface

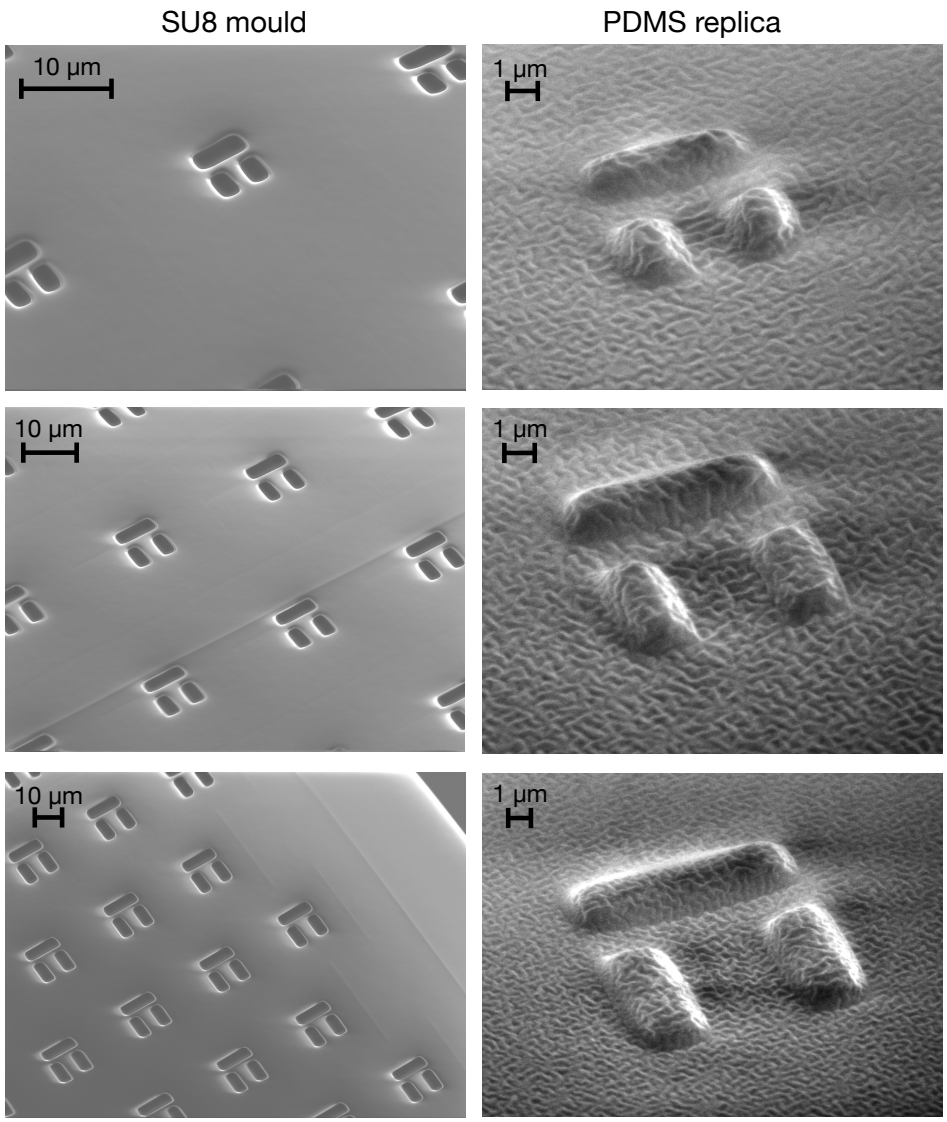

Figure 50. Direct comparison between the SU8 mould and the corresponding shape reproduced in PDMS. The first column shows SEM micrographs of SU8 moulds with traps of increasing dimension, while the second column shows scans of the corresponding structures in PDMS. It is apparent that the shapes are not faithfully reproduced. The quality appears to improve for larger sizes (bottom row). However, these dimensions are too large to preserve the single cell capabilities of the trapping.

roughness of the replicas is due to a thin layer of titanium that was necessary to sputter onto the PDMS in order to avoid charging during SEM imaging. It is clear that the shape of the blocks is not reproduced faithfully, and sizes are not maintained. The quality of the replicas increases for larger dimensions of the traps and spacings (third row). Unfortunately, these dimensions are too large to achieve reliable trapping.

It is important to note that the SU8 mould was tested both in untreated conditions and after a fluorination step with the aim of reducing the PDMS-SU8 adhesion. Both conditions yielded the same poor replicability. An imperfect reproduction of the shape, especially in terms of the height, results in the PDMS traps not being deep enough to reach the

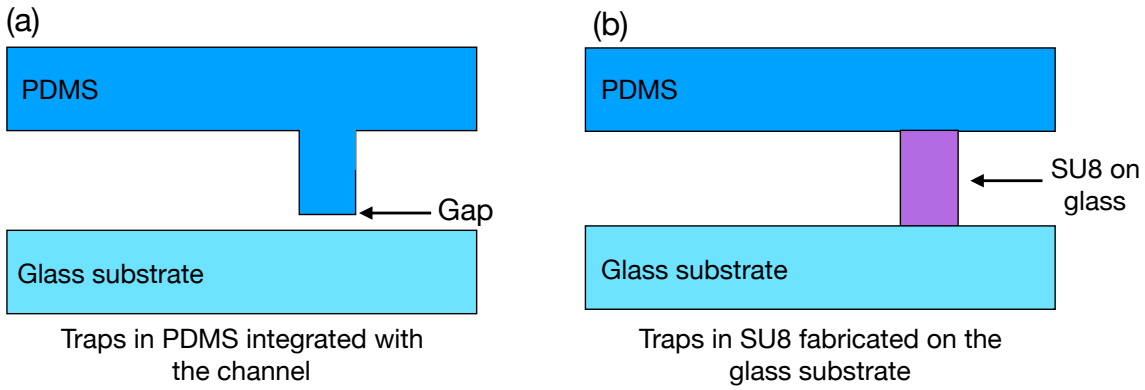

Figure 51. Schematics of the different strategies for the fabrication of the trapping assay. (a) First strategy for the fabrication of the traps. A single SU8 mould is produced in order to make traps out of PDMS and to integrate them with the channel. Shape replication was always rather poor, which resulted in th formation of a gap between the bottom of the traps and the glass substrate. (b) Alternative successful strategy. The traps are fabricated in SU8 onto the glass substrate and subsequently sealed with a simple PDMS microfluidic channel.

underlying glass substrate upon bonding, as shown in Figure 51(a). Indeed, despite several attempts, bacteria trapping was not reliably achieved with this strategy.

The main benefit of the first fabrication strategy is that the mould that includes the traps can be reused multiple times to make PDMS replicas which then need to be simply bonded onto a glass substrate. This means that the electron beam lithography step, which is time consuming, needs to be done only once. However, despite the clear practical advantage of the first method, it is not fit for purpose, because it does not produce high quality traps of the required size.

10.2. Strategy 2: SU8 traps and PDMS channel

The alternative is to fabricate the array of traps on the glass substrate in SU8 and then seal them by bonding a simple microfluidic channel (see diagram in Figure 51(b)). As a consequence, this second method requires the SU8 process flow to be carefully optimised and the traps to be fabricated on the glass substrate for each independent experiment, which is a considerable experimental overhead. The advantage, however, is that this method works and that it produces high-fidelity traps (as I will show in the next section). A side view of a trap fabricated with both methods is shown in Figure 51.

10.3. SU8 resist optimisation

One of the most important aspects of the fabrication process is to control the thickness of the SU8 layer; the mould for the microfluidic channel needs to be slightly thicker than the

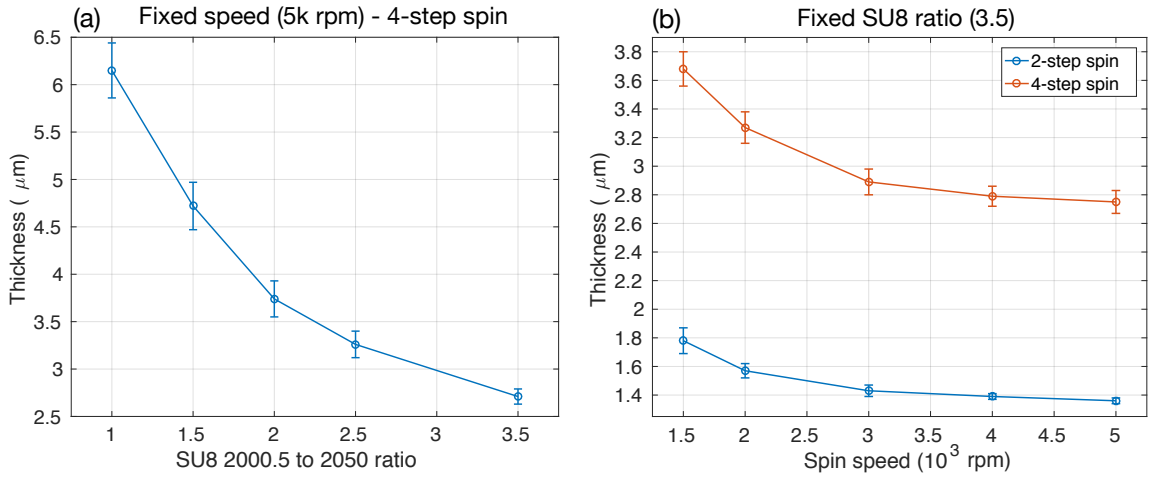

Figure 52. Spin curves of SU8 for different spin protocols and mix ratios. (a) Spin curves for SU8 at different ratios of SU8 2000.5 to SU8 2050. A fixed spin speed of 5000 rpm has been used and a 4-step employed. The higher the content of the thin SU8 (2000.5), the thinner the film because of decreased viscosity. In panel (b) the mixture ratio is maintained constant (3.5) and the spin speed is varied. The higher the spin speed, the thinner the film, as expected. The effect of the number of steps is also investigated. A 2-step process produces films half as thick as a 4-step process. Error bars refer to the standard error over five different locations (N = 5) across the sample being measured with a bespoke ellipsometer.

mould for the traps, as I will detail later on. There are two ways of controlling the resist thickness, namely via the solvent content and the spin coating speed. The solvent content controls the resist viscosity η and thus the ease of spinning it to different thicknesses, while the spin speed ω determines the centrifugal forces applied to the liquid layer during the coverage process. The final spun film thickness h_f is proportional to both of these quantities according to:

$$h_f \propto \eta^{\frac{1}{3}} \omega^{-\frac{1}{2}} \tag{44}$$

Viscous resists produce thicker films while high spin coating speed results in thin films. The dependency on these two quantities has been explored for SU8 in order to find the optimal solution for our needs. In particular, SU8 2050 and 2000.5 were used, which were the most and least viscous versions available in the lab, respectively; intermediate viscosities can be achieved by mixing. Results are shown in Figure 52, where I explore different mixing ratios at constant spin coating speed (5000 rpm, Figure 52(a)) and different spin coating speeds for a fixed mixing ratio (3.5:1 2050:2000.5, Figure 52(b)).

According to the manufacturer's guidelines, SU8 requires a multi-stage spinning procedure to ensure a gentle and even spread over the surface and avoid the formation of cracks in the final film. I used two processes. The first one is a 2-step procedure consisting

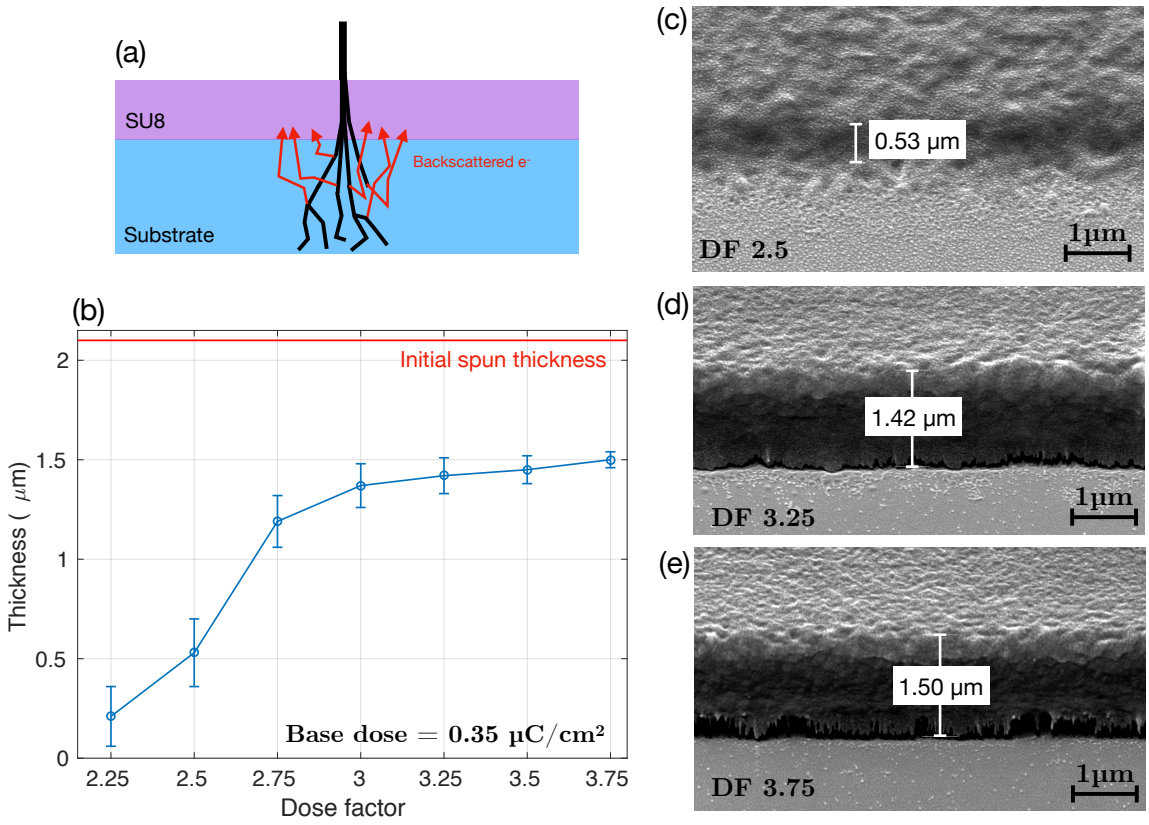

Figure 53. Exposure of an SU8 film with electron beam lithography at different exposure doses. (a) Illustration of an SU8 film on a glass substrate being exposed by an electron beam. The exposure starts from the bottom of the film because of the electrons back-scattered by the underlying substrate. This mechanism explains the curve in figure (b), where the thickness of pads exposed in SU8 is measured as a function of the exposure dose. The higher the dose, the taller the features because of more backscattered electron being generated per unit area. The initial film thickness is never recovered, as highlighted by the red horizontal line. Error bars refer to different locations along the features' edges and represent the standard error of the mean (N = 5). (c-e) Representative tilted SEM pictures used to measure the thickness of the SU8 squares. The sharpness and thickness of the structure increase for higher exposure doses.

of a 10 second spin at 500 rpm followed by 60 seconds at the target speed. The second process consists instead of a 4-step procedure, where two intermediate steps were added to the previous two before reaching the final target speed. The intermediate steps consisted of two further spins at 40% and 80% of the final target speed and lasted for 10 seconds each.

The latter method results in films twice as thick as a 2-step process, as shown in panel (b) of Figure 52. This finding is beneficial for our purpose since we will need different thicknesses for the fabrication of the traps and the mould for the microfluidic channel. The reason for adopting two different spinning process with the same resist is because of practicality. It is easier to have a certain ratio available and spin it at different speeds rather than preparing two separate batches. Furthermore, this reduces errors and reproducibility issues related to mixing liquids of very different viscosities.

It is important to note that the final thickness of the exposed structures will be different from the spun film thickness for two reasons. The first mechanism is related to the film exposure. The forward travelling electrons during electron beam exposure are too energetic; hence the resist film is practically transparent to their passage. Some of the electrons interacting with the substrate are reflected back at lower energies and are able to trigger the photoinitiator degradation described previously. This process, schematically illustrated in Figure 53(a), entails that the film exposure starts from the bottom and less energy is always deposited in the top layers. The second reason that makes the final film thinner is that SU8 shrinks and increases density upon hard baking because of pockets of solvent evaporating and cross-linking being completed. This effect is also clearly dependent on the exposure dose, that is the number of electrons per unit time and area being deposited on the resist film. Higher doses result in more electrons being backscattered and exposing the film. Typical values for a 2-μm thick SU8 layer lie in the range of a few $\mu C/cm^2$, as I will examine in detail later on.

The results are shown in Figure 53(b-e), where a dose test is performed. An initial 2.1 μm SU8 layer was spun on a silicon substrate (as indicated by the red line in panel (b)), baked, exposed, post-exposure-baked, developed and hard-baked overnight. Several squares were exposed at increasing dose factor (DF), that is a multiplicative factor for the base exposure dose (here 0.35 $\mu C/cm^2$).

In particular, the plot in Figure 53(b) illustrates how the thickness of the squares depends on the exposure dose. Error bars come from repeating measurements along the edges of the features by tilting the sample inside a SEM chamber. Three representative images are reported in panels (c), (d) and (e). For small dose factors the film is not fully exposed and the edges are quite irregular. Better definition and reliability are obtained for higher DFs, as also shown by the smaller error bars. This is the preferred operation regime because of the weak dependence of the thickness on the dose, so that the fabrication is less sensitive to dose changes and film inhomogeneities and sharper features are obtained. Clearly, the decrease in thickness compared to the initial film can be considered and compensated by adjusting the spinning speed in order to obtain the desired target thickness.

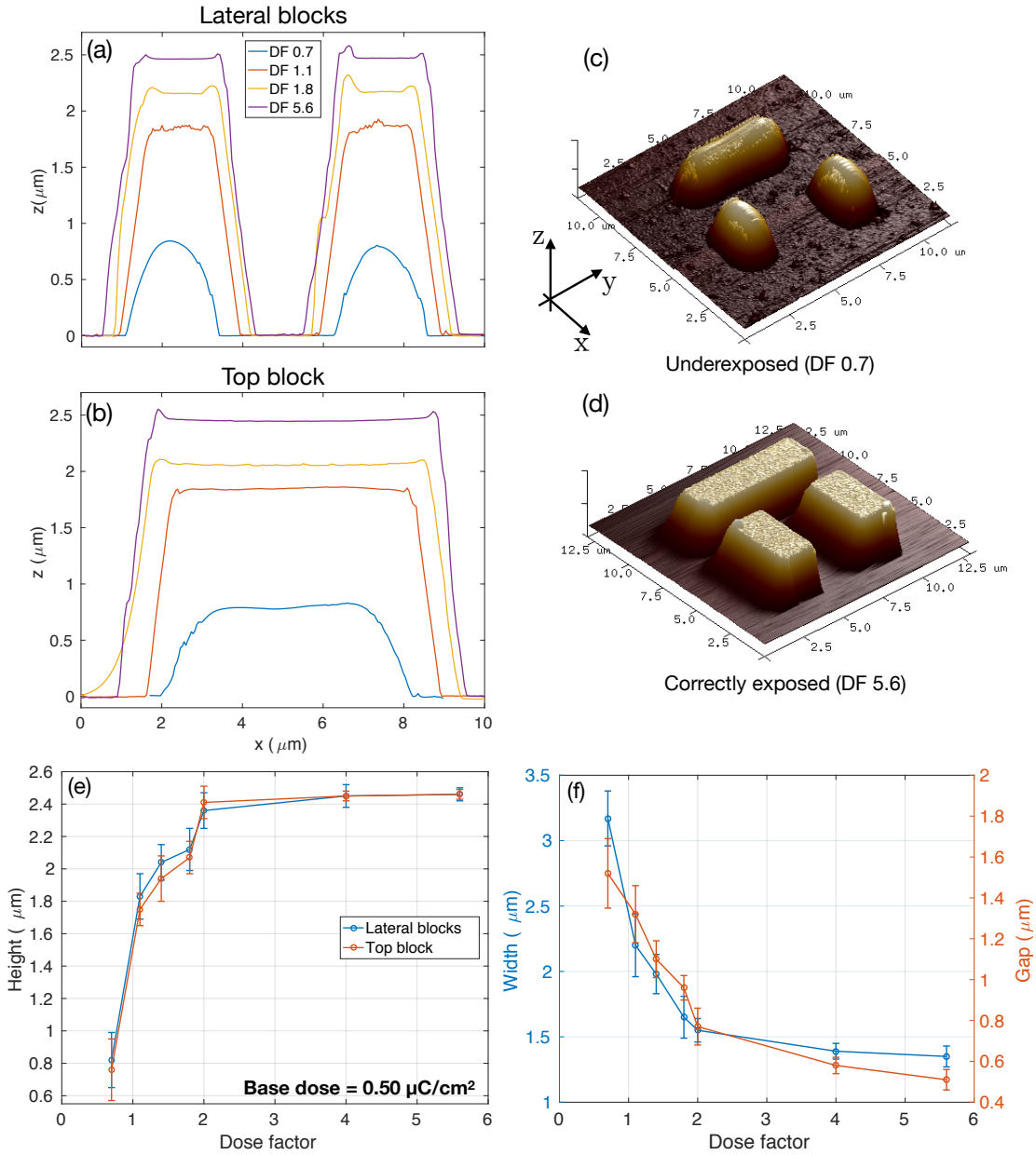

Figure 54. AFM characterisation of the fabricated traps. (a, b) Average AFM profiles of the traps across the lateral and top blocks, respectively, for increasing values of the dose factor (base dose = 0.50 μC/cm²). As the dose increases, the features become taller and better defined. (c) AFM scan of an underexposed trap featuring rounded walls and incorrect dimensions. (d) AFM of a correctly exposed trap appears better defined. (e) Height of the trap's lateral and top blocks as a function of the dose factor. Values are obtained as an average over the entire area of the blocks. For dose factors above 2, the height becomes independent of the dose factor, which defines the preferred operational regime. (f) Other dimension of interest, namely the width of the trap and the vertical gap. They both saturate at higher dose factors (approximately above 4). Error bars refer to the dimensions being measured at different locations over the trap's surface and represent the standard error of the mean (N = 50 for the height in (e) and the width in (f), N = 10 for the gap in (f)). All measured traps were fabricated on a single sample.

10.4. Trap fabrication

Because of the importance of thickness control and its dependence on the substrate material via electron backscattering, a dose test also needs to be performed for the traps fabricated on glass. Several test samples were fabricated with different exposure doses. The result is

shown in Figure 54, where AFM images were taken under the same conditions described in section 6.1 of chapter II.

The higher the DF, the taller and larger the exposed structures, as illustrated in Figure 54 (a) and (b). The sharpness and definition of the side walls are also improved at higher DFs. For instance, a DF of 0.7 produced rather short and rounded shapes, as shown by the AFM scan in panel (c). On the other hand, a DF of 5.6 (panel (d)) lies in the saturation regime where the height is almost independent of the exposure dose and the wells appear sharper and better defined. The saturation is clearly visible in panel (e), which reports the height of the blocks as a function of the dose. The values are averaged over the entire length (or width) of the corresponding block(s), so that the error bars provide an indication of the uniformity of the surface.

From the AFM scans, it is also possible to measure the other relevant dimensions of the traps, in particular the access width (previously denoted as g_v) and the size of the vertical gap (g_h, as defined in Figure 42). These quantities are critical for the hydrodynamic operation of the traps, as extensively discussed in the geometry optimisation section. The sizes as a function of the DF are plotted in panel (f) of Figure 54. The dimensions of both features clearly decrease as the DF increases. This is due to the blocks becoming larger and wider, thereby reducing the spacing between them. The broadening effect caused by the AFM tip is being neglected here. This is a reasonable assumption since we are measuring sizes of the order of a few µm, while typical dimensions of the AFM tip's radius I used (RTESPA-300 probe, Bruker) are 8 nm for the nominal radius with 15° and 25° for the front and back angle, respectively, as verified on the supplier's website.

Considering these results, an exposure DF of 5.6, corresponding to an absolute dose of 2.8 µC/cm^2, was selected as the optimum value for the subsequent fabrication of the trapping assay. Even though the height of the blocks appears to saturate at much lower doses (panel (e) of Figure 54), the other dimensions saturate at higher values, which motivates the choice of 5.6. At this value of DF, the distance between the blocks (g_v) and the vertical gap (g_h) lie within the optimum parameter region that has been studied in the simulation section

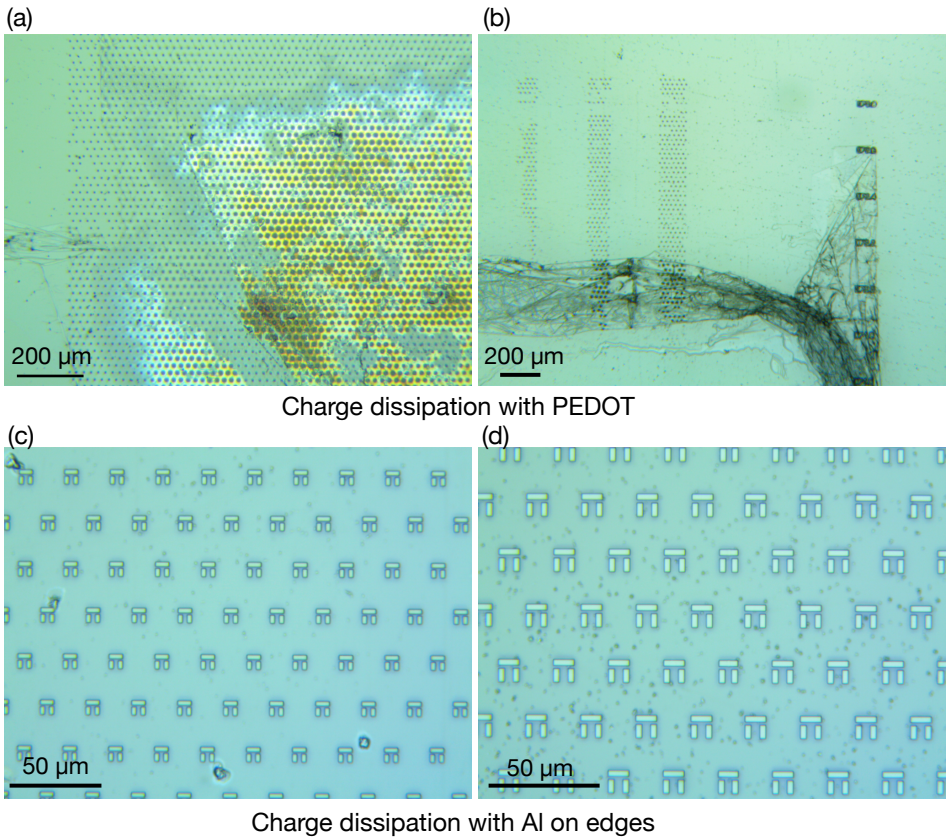

Figure 55. Different strategies for charge dissipation during the electron beam exposure. (a,b) Brightfield micrographs showing the PEDOT charge dissipation layer not being totally removed upon rinsing in DI water. The PEDOT appears to remain attached to the SU8 exposed area. Conversely, the absence of charge dissipation directly on the exposed structures does not affect the results, as shown in (c) and (d).

(section 7.2), being (1.35 ± 0.08) µm and (510 ± 50) nm, respectively. The corresponding height of (2.46 ± 0.10) µm is small enough to ensure that bacteria will approximately lie within the depth of focus of the objective during the experiments by preventing them from swimming in the z direction. At the same time, the channel is not too thin to overly constrict the bacteria and ensure the availability of sufficient nutrients to maintain them in a viable state.

In reality, the fabrication process inevitably results in uncontrollable variability that is normally larger than the error bars shown here. Sources of variability can be identified in inhomogeneities in the SU8 due to different temperature or humidity conditions, human error in baking and development, as well as in the variability of the current during the electron beam exposure. These effects are partly counteracted by operating in the saturation region, where the dependence of quantities of interest on the exposure dose is weak. However, several arrays are always exposed at different doses in every sample, so that a set of traps close to the ideal conditions is always available for optimal trapping.

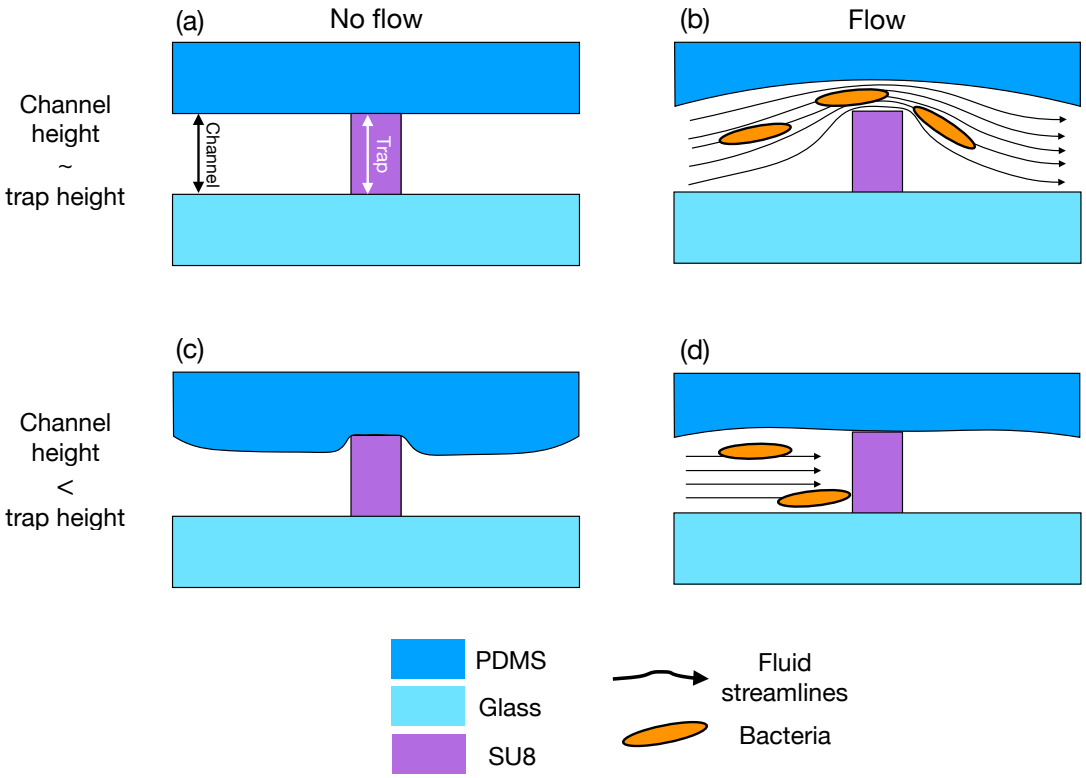

Figure 56. Schematics of a single trap operating with different relative heights of the channel and the trap itself. (a) and (b) illustrate side views of a device where the height of the PDMS channel is matched to that of the trap in the absence of flow. Upon pumping, PDMS inflates and easily detaches, thereby creating a gap that allows bacteria to flow through. In (c) and (d) the channel is fabricated thinner than the traps, in order for PDMS to exert pressure downward onto the trap. In this case, flow did not cause the creation of any gap and reliable trapping was achieved.

The use of glass as a substrate also poses the problem of charge dissipation during the electron beam fabrication step. A commonly employed solution to overcome charging is to evaporate or sputter a thin (~20 nm) layer of aluminium on top of the resist layer before the electron beam exposure and then removing it before development by rinsing in, for instance, phosphoric acid. However, it has been found that phosphoric acid somehow triggers the SU8 cross-linking, so that it was impossible to develop the film after the removal of aluminium. A second solution was based on the use of PEDOT, a conductive polymer that has been spun onto the SU8 film. However, after the exposure, removing PEDOT has proven to be rather challenging, as can be seen in panels (a) and (b) of Figure 55. Fragments of the polymer film remained attached to the surface. This might be due to a cross-linking process being triggered by the electron beam between the two polymers, considering that the PEDOT film appeared to be lifted off everywhere except for the exposed trapping arrays.

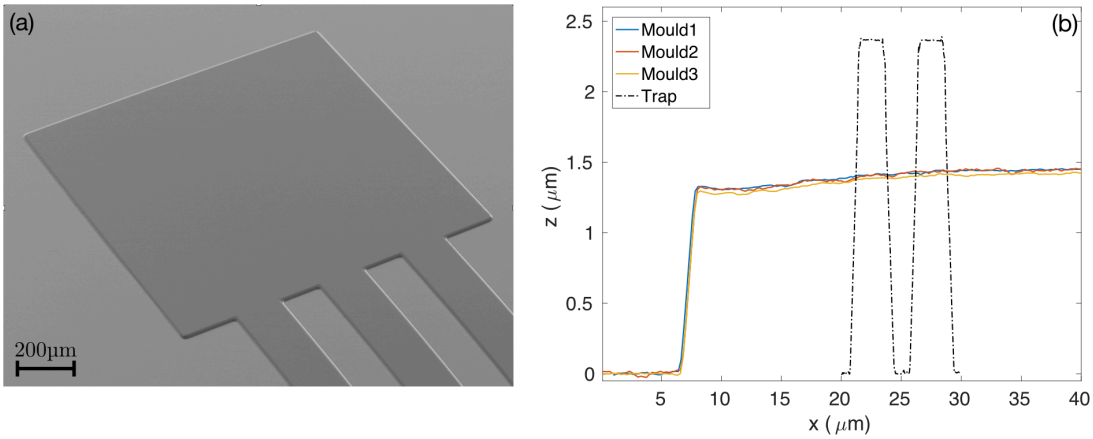

Figure 57. SEM and AFM images of a fabricated SU8 mould on silicon. (a) SEM picture of an SU8 mould on silicon featuring a large pad for placing the inlet/outlet holes and three parallel channels (microfluidic chip design A in appendix A1). (b) AFM profiles of the SU8 mould at three different locations used to measure the height of the channels. The profile of a trap is superimposed to show its relative height and highlight the need for the channel to be thinner than the trap to ensure perfect sealing.

It was later realised that, given the extremely low dose required to expose SU8, a conductive layer is not needed to dissipate the charge during the actual exposure, but only to carry out the necessary alignment steps for the electron beam lithography, which require imaging the surface of the sample. Hence, about 30 nm of aluminium was thermally evaporated only along the edges of the glass substrate before starting the fabrication. The results are superior with this second method, as clearly illustrated in panels (c) and (d) of Figure 55.

10.5. Mould and PDMS replica fabrication

The fabrication of the mould presents some critical requirements. The height of the channel should be matched to the height of the traps in order to ensure perfect sealing. However, this is a rather demanding task, partly because of the fabrication variabilities identified before. Indeed, preliminary experiments were carried out where the height of the SU8 mould (and consequently the height of the PDMS replica) was matched to the height of the trap. This solution has never produced reliable trapping either because of imperfect sealing or a mismatch in the heights which resulted in PDMS detaching from the top surfaces of the traps. This created a gap through which bacteria easily escaped, as illustrated in Figure 56(a) and (b). Since PDMS is deformable, the pressure exerted by the liquid being pumped in the channel causes it to inflate and detach. This is also due to the rather small contact area, which results in large values of pressure being exerted onto the contact area.

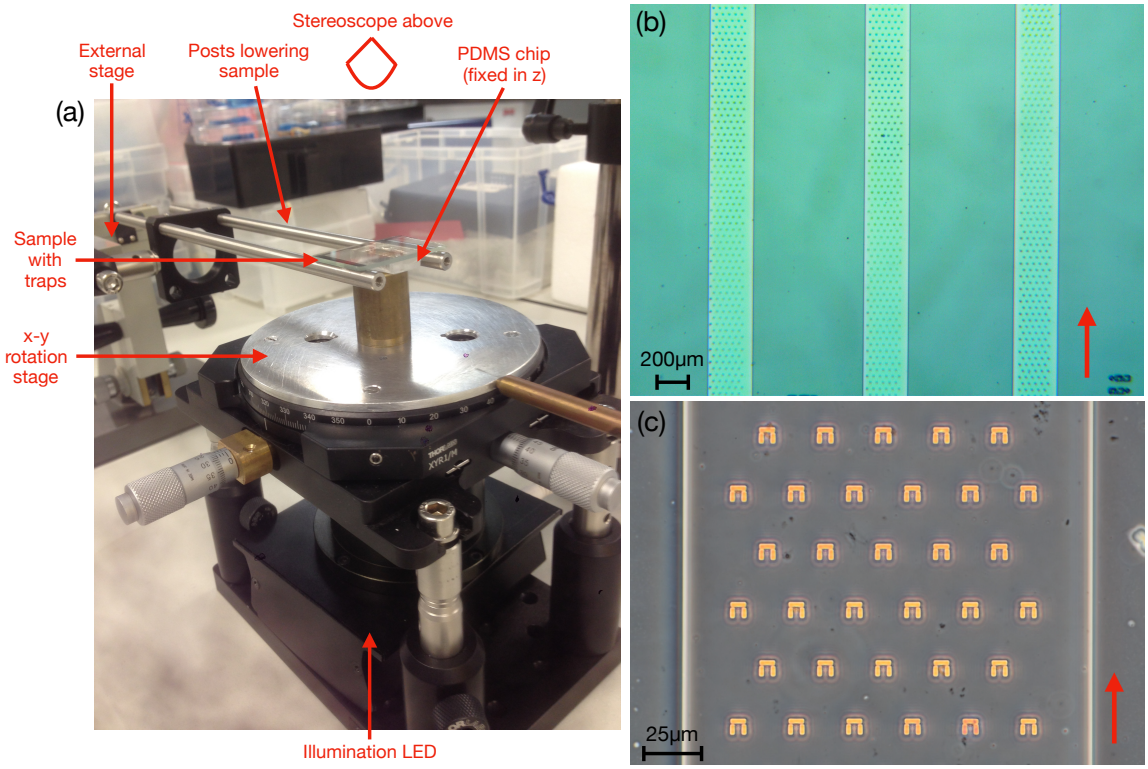

Figure 58. Alignment of the PDMS channel with the trapping arrays. (a) Custom built apparatus used for aligning the microfluidic chip to the trapping arrays. The PDMS is placed onto a rotating stage facing upwards while the sample with the traps facing downwards is carefully lowered. The alignment can be adjusted by independently moving the sample and the chip while observing with a stereoscope. The illumination is provided by an LED placed underneath the stage. (b) Brightfield micrographs of a sample aligned with the previous apparatus. (c) Close-up (60x magnification on a phase contrast microscope) of a single channel to show the high level of precision that can be achieved with this system, which can be visually estimated to be on the order of ±10 µm. The red arrows in (b) and (c) indicate the direction of the fluid flow.

Hence, two measures have been taken to prevent this scenario. Firstly, the SU8 layer for the fabrication of the mould is spun thinner than the layer used for the traps. In particular, I used a 2-step spin of a 3.5 mixture of SU8 at 1500 rpm (refer to panel (b) of Figure 52). The resulting resist thickness is (1.78 ± 0.09) µm after spin and (1.41 ± 0.01) µm after fabrication. Figure 57(a) shows a tilted SEM picture of a fabricated mould on silicon, while panel (b) reports three AFM profiles taken at different locations along the channel structures. The black dash-dot line represents one of the previously measured trap profiles superimposed onto the channels' scans. The difference in height is evident and it ensures that the PDMS channel will press downward and exert sufficient pressure onto the traps to prevent detachment when flowing solutions, as shown in Figure 56 (c) and (d).

As a second measure, the PDMS mix is altered to 7:1 (liquid PDMS:curing agent) instead of the commonly employed 10:1. The different ratio renders the final cured mixture stiffer [171] thereby decreasing its deformability and the chances of detachments while pumping

solutions inside the microfluidic channel. 30 ml of liquid PDMS are thoroughly mixed with 4.3 ml of curing agent by manual stirring and degassed for about 30 minutes before being poured onto the SU8 mould on silicon. The mixture is cured overnight in an oven at 60 °C and then carefully peeled off the substrate. The resulting chip thickness is of the order of 1cm. Holes are punched for the inlet and outlet pads and both the PDMS chip and the slide with traps are loaded into a Reactive Ion Etching (RIE) chamber. An oxygen plasma at ~280 V (pressure of approximately 0.1 mbar, O_2 flow of 22 sccm) is applied for 25 seconds in order to activate both surfaces.

The alignment of the PDMS channels with the underlying trap arrays is another critical step, given the small width of the channels (180 μm, refer to the microfluidic chip design B in appendix A1 for further details about dimensions and number of channels and traps). For this purpose, the alignment system shown in Figure 58(a) has been built. It consists of an *xy* rotating platform on which the PDMS chip is positioned on a brass hollow cylinder with the channels facing upwards. An LED is placed below the stage to provide illumination and allow observation through a stereoscope above the sample (not shown in the picture). An external *xyz* moving stage is equipped with two long posts holding the sample facing down. In this way, both the PDMS chip and the sample can be finely moved and rotated independently. The sample is thus carefully lowered while *xy* and angle corrections are made to ensure perfect alignment between the trap arrays and the channels while observing through the stereoscope. After a gentle application of pressure to trigger the PDMS adhesion over the entire surface, the sample is baked for at least 2 hours at 60 °C to secure bonding.

The result is shown in Figure 58(b). Multiple channels and trapping arrays are realised in order to decrease the effective flow velocity in each channel. Splitting the flow also allows to conduct multiple experiments in parallel. A 60x magnification picture taken with an inverted phase contrast microscope is shown in panel (c). This highlights the precision of the alignment that can be achieved with this system, which can be visually estimated to be of the order of ±10 μm by considering that the smallest feature that needs to be correctly aligned is the gap between the external columns of traps and the channel's wall.

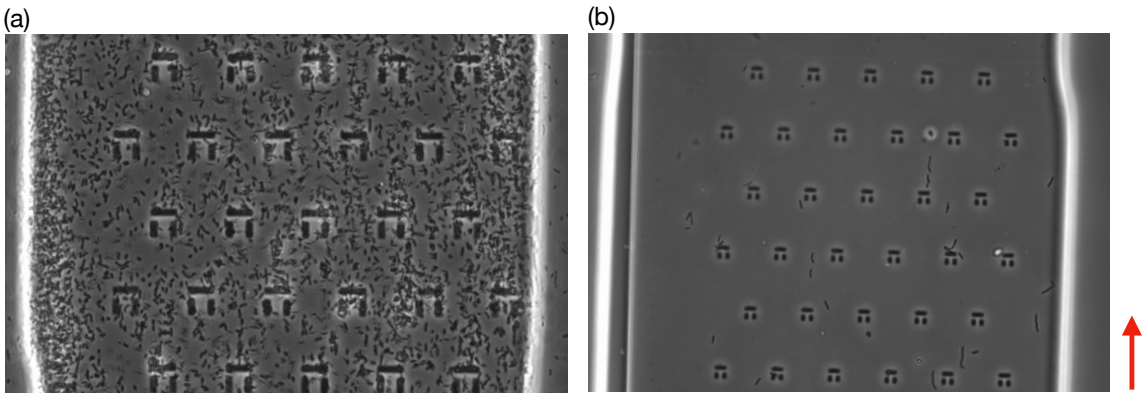

Figure 59. Effect of the BSA coverage on bacterial attachment inside the microfluidic channel. (a) Snapshot of an untreated chip after 15 minutes of exposure to 10^8 cfu/ml bacteria at 0.1 µl/min. Bacterial attachment is evident. (b) Picture taken in the same conditions, apart from the sample being treated for 30 minutes with a 1% (w/v) solution of BSA in PBS. Attachment is sensibly reduced. The red arrow indicates the direction of the fluid flow. This experiment was carried out with the microfluidic chip design A described in appendix A1.

10.6. Setting up trapping experiments

Once the sample fabrication is completed, tubes are manually inserted in the punched holes to allow the delivering of solutions into the channels. Further details on the microfluid setup are provided in appendix A1. From preliminary tests, it was found that a significant fraction of bacteria tends to attach to both the PDMS and glass surfaces resulting in almost total coverage of the analysis area within a short time. Bacterial attachment to a surface is a complicated process, with some aspects still being debated in the literature. As a general rule, surface charge and hydrophobicity are the two main factors influencing attachment. Since most bacteria are negatively charged, neutral or positive-charged surfaces tend to favour adhesion. Similarly, bacteria with a hydrophobic surface prefer to colonise hydrophobic surfaces. This is indeed the case of *E. coli* and PDMS, which is intrinsically hydrophobic. There are several ways of making PDMS hydrophilic. Here, hydrophilicity is achieved by flushing the samples with a 1% (w/v) solution of bovine serum albumin (BSA) protein in Phosphate Buffer Solution (PBS). BSA is commonly employed as a blocking agent to prevent non-specific binding in sensing assays, but it is also known to reduce surface hydrophobicity, thereby preventing bacterial attachment in the context of our experiment [172,173].

Differences in bacterial adhesion are apparent from Figure 59. Panel (a) shows a 60x magnification micrograph after flushing *E. coli* for 15 minutes into a chip with no prior BSA treatment. Panel (b) was instead passivated with BSA before starting the experiment and appears much cleaner. The BSA solution was prepared by dissolving lyophilized BSA

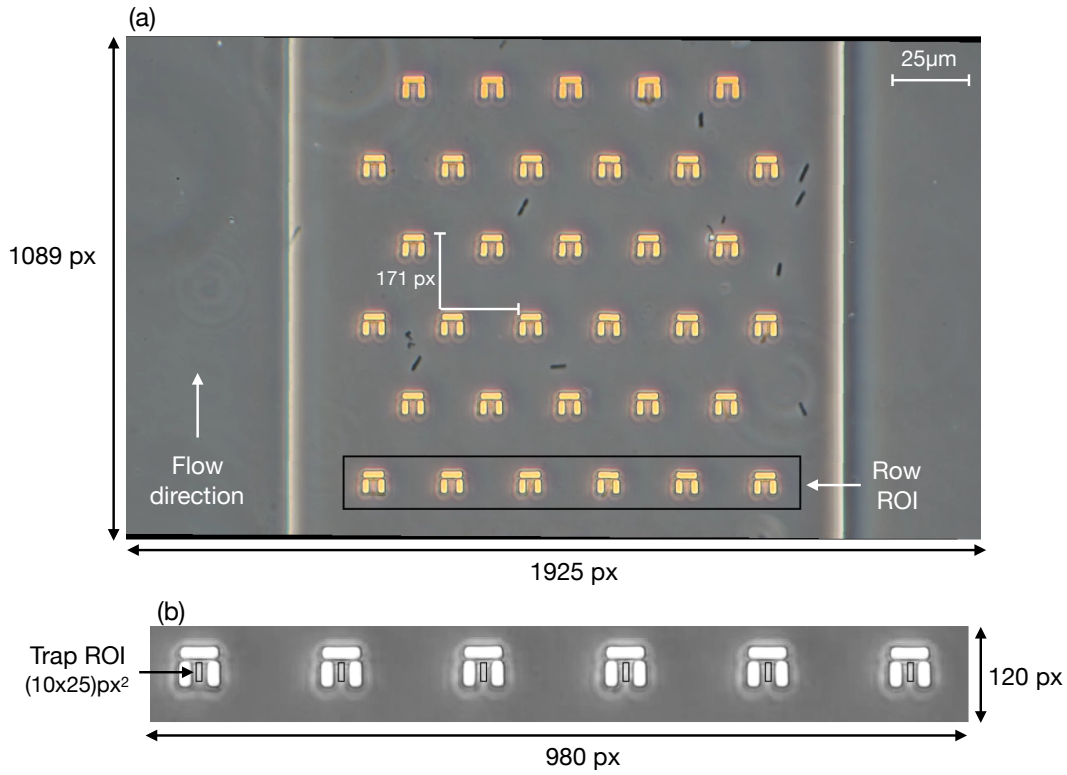

Figure 60. Example of a frame taken during a trapping experiment. (a) A frame of a video recorded during one of the experiments. Relevant dimensions are reported, and the row ROI used to crop and load the frames is superimposed. (b) Cropped row ROI converted to greyscale. The single trap ROIs are defined within each trap to highlight the areas over which the average pixel intensity is calculated. The conversion factor between real dimensions and pixels is 0.146 µm/pixel.

flakes in PBS (pH 7.4) and flushed inside the microfluidic chip for 30-40 minutes at a flow rate of 1 µl/min. It is also important to note that the two tests were run with the same starting concentration (10^8 cfu/ml) and flow rate (0.1 µl/ml). Interestingly, in the non-functionalised case (panel (a)), it is observed that bacteria are attached to both the glass substrate and the PDMS ceiling of the channel. This is evidenced by the out of focus bacteria in the figure, which have adhered to the glass substrate.

11. Signal processing and data analysis

Once the samples are fabricated and treated with BSA, the bacterial solution can be pumped inside the channel and the actual experiments can begin. In order to assess bacterial behaviour, in particular their motility and morphology, videos of swimming and trapped bacteria are recorded at regular time intervals over the course of the experiments. A DSRL camera (Nikon D3300) connected to the side port of the inverted microscope was used to record HD videos (1080p) at 50 Hz. The length of the videos is typically 5 minutes. From this point, all microfluidic chips are based on the design B in appendix A1.

The main information retrieved from the video analysis is as follows:

- $m*n$ intensity traces over time $I_{m,n}(t)$, where m indexes the row number, n the position of a trap within a specific row and t is the time step. At each time step, $I_{m,n}$ is calculated as the pixel intensity averaged over the inside area of the n-th trap in the m-th row.
- The total number of bacteria (N_t) swimming through the analysed area over the duration of the video.
- The number of bacteria that entered a trap (N_h), including both bacteria trapped for a significant amount of time and bacteria that escape immediately by either swimming against the flow or through the vertical gap of the traps.
- N_b MATLAB structure arrays containing all the geometrical properties of bacteria swimming through the entire field of view, i.e. their position, length, width, eccentricity, orientation, solidity and many others. N_b is typically smaller than the total number N_t because of the way the analysed frames are selected for the morphological analysis (see relative section below, 11.3).

The total number of bacteria and the number of trapping events is then used to calculate the hydrodynamic and the trapping efficiency (see section 8). The intensity traces are used for the assessment of motility, which is quantified by the standard deviation of $I(t)$ upon trapping, normalised to an empty trap case. The entire post process is performed with a custom MATLAB script that will be described in detail below. A further analysis step is conducted on some videos by using the *TrackMate* extension of ImageJ to perform bacterial tracking and retrieve their trajectories over the field of view in different conditions.

11.1. Intensity traces for motility

The intensity trace analysis is carried out as follows:

- The number of frames to be analysed is defined and the corresponding video section is imported in .mov format using the *VideoReader* built-in MATLAB function.
- At this stage, each frame is represented as a 1089x1925x3 matrix, where the first two dimensions represent the number of pixels in the frame and the third dimension

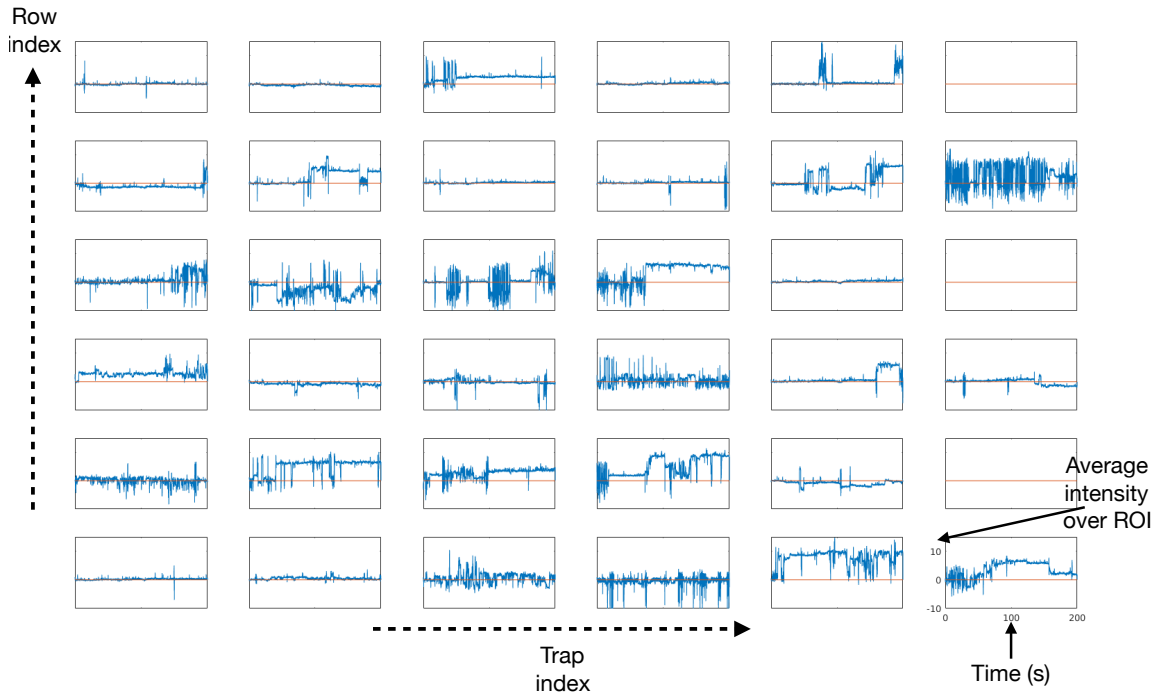

Figure 61. Example of a 6x6 matrix of intensity traces retrieved from a video analysis. Each graph refers to a specific trap, as indexed by the trap's and row's indexes. The layout reproduces the real position of the traps in the field of view. At each position, the corresponding intensity trace is plotted as a function of time. The spikes and increased noises in the traces are indicative of trapping events. These traces are then used for the assessment of the motility of trapped bacteria through the standard deviation.

contains the intensity values for the three RGB channel, respectively. An example frame is shown in Figure 60(a).

- The third dimension is collapsed by converting each RGB frame into greyscale according to the luminosity method, which takes into account the different relative power spectral density of the red (R), green (G) and blue (B) channel:

$$I_{greyscale} = 0.30I_R + 0.59I_G + 0.11I_B \tag{45}$$

- Any potential angle rotation is manually corrected by clicking the extremes of the first row of traps in order to align it.
- The position of the first row is identified by enclosing it in a manually-clicked box, as overlaid onto the frame in Figure 60(a).
- A region of interest (ROI) is drawn within the first trap of the first row to define the analysis area. The ROIs always have the same area of 10x25 px^2 across most of the experiments and are centred within the wells, as can be seen in Figure 60(b).

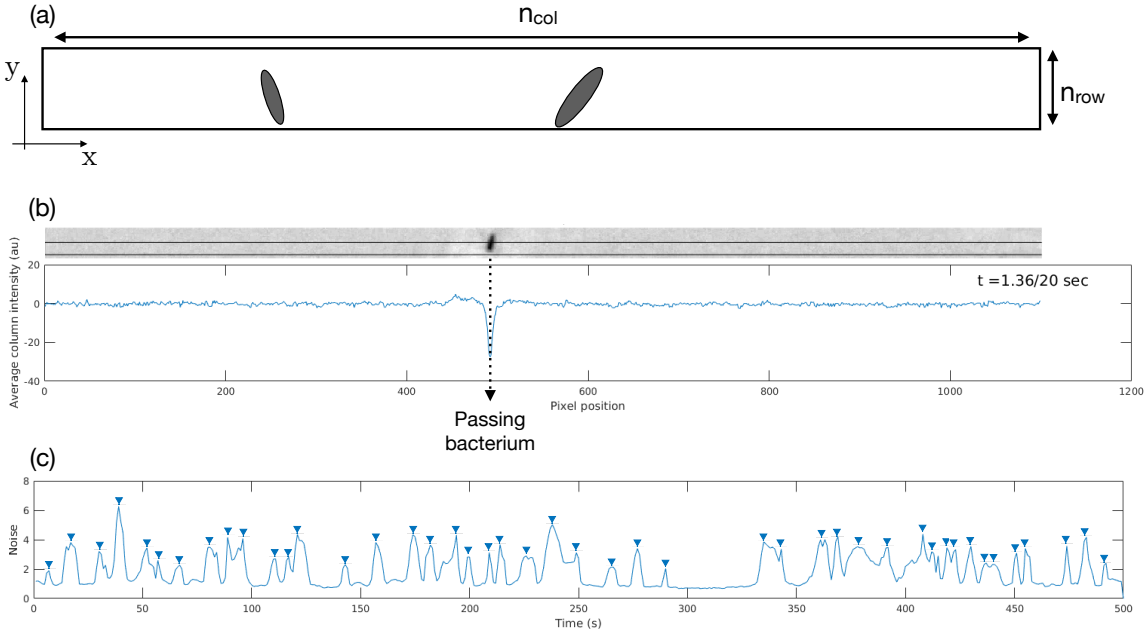

Figure 62. Working principle of the counting algorithm. (a) Diagram of the ROI defined for counting bacteria. n_{col} is typically as wide as the channel, while n_{row} is a few tens of pixels. (b) Single frame ((1100 x 23) pixel^2) showing a bacterium passing at a pixel position of around 500 and causing a dip in the intensity trace along the x direction. At this time point the standard deviation of the trace is higher compared to a no-bacterium scenario (c) Standard deviation as a function of time. Each peak corresponds to the passage of one of more bacteria.

- The position of the other ROIs is automatically calculated since the period of the array and the distance between the rows is known and constant (171 px, corresponding to a real distance of 25 µm). Typically, at the magnification of 60x, 6 rows fit in the field of view of the camera (m=6), three of which have 6 traps, and the rest have 5 traps (n = 5 or 6 depending on the row index) (see Figure 60(a)).
- Six 3D matrices are defined. Each of them is filled with the cropped video frames containing a single row. At this stage, the x and y dimensions represent the pixel dimension of the cropped row (980 x 120).
- Each pixel is filled with the value of the $I_{greyscale}$ intensity previously defined minus the temporal median over the entire duration of the video. This procedure eliminates the traps from each frame and any fixed feature that might be present in the field of view.
- The spatial average pixel intensity within each trap ROI is calculated at each time step and stored in appropriate vectors.
- At this stage, the important information is stored in a n_{rows} x n_{traps} x n_{frames} matrix, which contains the spatial average intensity values at each time step and for each trap in the field of view. An example of the retrieved intensity traces is shown in

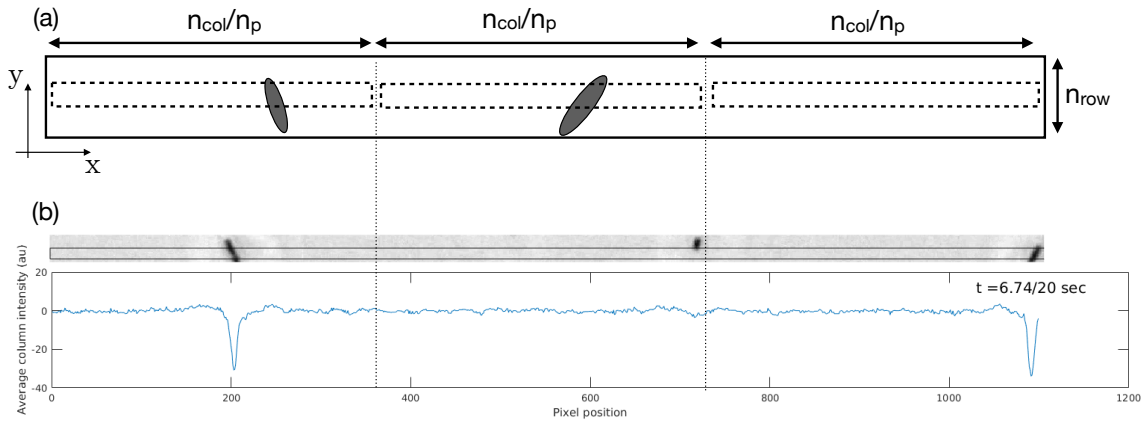

Figure 63. Counting algorithm with multiple counting sections. (a) Scheme of the ROI for counting bacteria being divided into n_p sections along the x direction. Each section is n_{col}/n_p pixel wide. (b) Single frame ((1100 x 23) pixel^2) and intensity trace relative to two bacteria passing close to each other (in time). This scenario would produce a single peak in the standard deviation trace if the ROI was not divided into multiple sections.

Figure 61. The spatial arrangement of the graphs mirrors the physical positions of the traps. Note that rows 2, 4 and 6 do not show any trace in the 6th trap position.

11.2. Bacteria count for trapping efficiency

The number of bacteria swimming through the field of view over the duration of the video is essential for both the calculation of the trapping efficiency and for assessing the bacteria multiplication over time inside the microchannel. In order to count bacteria, a custom algorithm was written:

- A single ROI of dimensions n_{row} x n_{col} is manually defined at the bottom of the frame below the first row in order to monitor the number of bacteria flowing through it, as schematically shown in Figure 62(a).
- Each column of the ROI matrix is averaged along the y direction. This leads to the definition of a n_{col}-long intensity vector for each time frame. An example is provided by Figure 62(b), where the average column intensity of the ROI is plotted along the transverse (x) direction and for a specific timestep;
- The same procedure is applied to each frame in order to retrieve the spatial intensity profile along the x direction as a function of time. If a bacterium is present within the analysed area, the intensity trace drops at the corresponding pixel position of the passing bacterium, as the example in Figure 62(b) shows.
- The dip occurring at every passage event causes the noise of the entire trace to increase. The standard deviation of the intensity traces is thus calculated at every

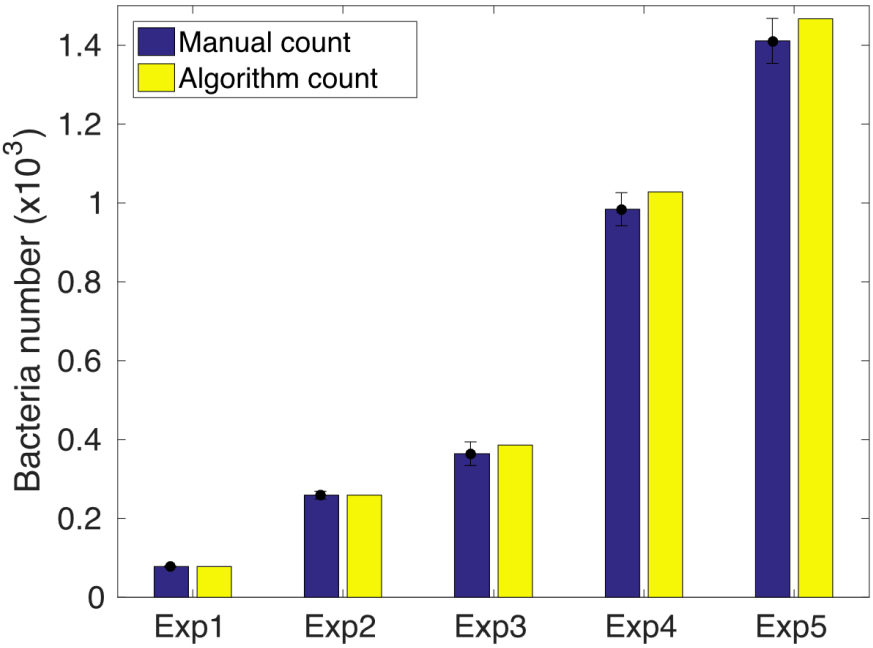

Figure 64. Comparison between a manual bacteria count method (blue bars) and the devised counting algorithm (yellow bars). Different experiments (Exp) have been conducted by varying the bacterial concentrations in order to test the algorithm in different regimes. The manual count has been repeated three times (N=3) to consider human error and the error bars report the standard error of the mean. For a relatively small number of bacteria (up to a few hundreds, Exp1 and 2) the two methods match perfectly. At higher concentrations, the algorithm tends to slightly overestimate the count compared to the visual count. Results are always compatible within the error bars.

time step and plotted as a function of the elapsed time. Each peak in this function corresponds to a sudden change of the intensity trace, indicative of one (or more) bacterium passing through the analysis area. An example over 500 seconds is shown in Figure 62(c).

- The peaks in the standard deviation traces are detected by using the *findpeak* built-in function of MATLAB with an appropriate threshold and prominence value. Assuming the flow to be sufficiently fast, or the bacterial concentration to be sufficiently low to produce clearly separated peaks in the standard deviation trace, the number of peaks corresponds to the number of swimming bacteria. However, these conditions are not always met, and the standard deviation trace can be difficult to interpret. For example, if two or more bacteria are passing through the ROI very close in time, they will produce multiple dips in the intensity trace (see Figure 63 (a) and (b)) but only a single, higher peak in the standard deviation signal. Moreover, if bacteria are too slow or too long, the peaks in the noise signature broaden significantly, thus increasing chances of superposition and odd-looking peaks. This argument implies that the width and height of the peaks should be considered to discern different scenarios. However, these quantities are influenced

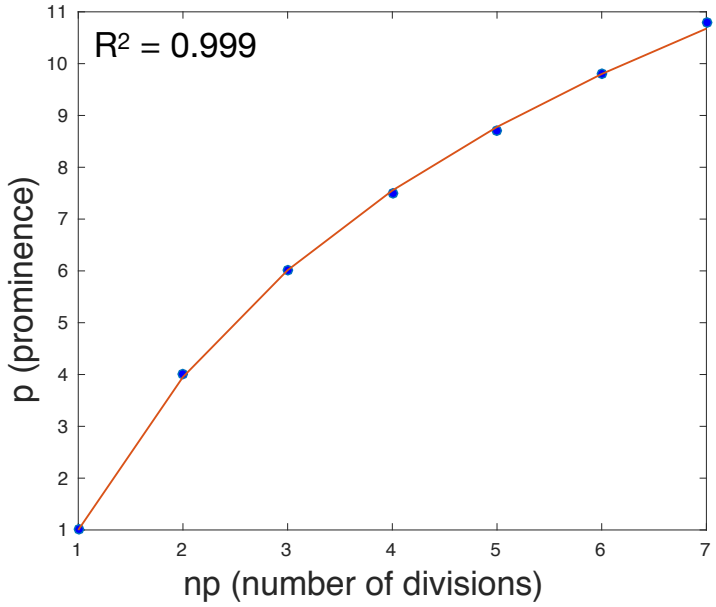

Figure 65. Dependence on the peak prominence threshold p necessary to maintain the automatic bacteria count as the number of divisions n_p is increased. The increase of the required prominence is due to the passage of a bacterium causing a higher peak in the standard deviation trace. The data points are fitted to a log function with an amplitude α and raised to a power β.

by a number of other factors, including the length, shape and motility of the bacteria, the flow rate and the dimension of the ROI, which would be extremely challenging to deconvolute.

- In order to eliminate such occurrences and to limit their influence on the count, the ROI is divided into n_p subunits in order to decrease the chance of multiple bacteria simultaneously passing through the same analysis area. An example is shown in Figure 63(b). The same procedures described above are then applied to every subunit and the peak counts from each subunit are added to retrieve the final number of bacteria.
- Given the number of variables involved in the counting algorithm and the difficulties in untangling them, the algorithm has been checked against a visual count performed by using a clicker while watching the recorded videos. This has been performed three times for five three-minute long videos recorded at different bacterial concentrations and the results are reported in Figure 64.
- The blue bars in Figure 64 report the average number of bacteria manually counted for the five independent videos. Each count has been repeated three times to consider human error. The error bars report the standard error over the three repeats. The yellow data bars show the results obtained with the counting algorithm. For the first two experiments at low bacteria number, the two methods produced exactly the same result (78 and 259 bacteria, respectively), while for

increasing number of bacteria the algorithm tends to slightly overestimate the number of bacteria passing through, with the relative error between the two methods being of the order of 5-10%. The algorithm is then considered effective and used in all the experiments to count the number of flowing bacteria. Accordingly, a relative error of 10% is attributed to all the counts obtained with the algorithm.

- We have now established that the two counting methods show good agreement for low to medium bacteria concentrations. In these conditions, the analysis ROI has been divided into three blocks ($n_p = 3$), which was sufficient for the algorithm to be reliable. Does it also work for high bacterial concentrations, however? For example, in some experiments, the number of bacteria can reach 10 000 over the course of a 5-minute video. In this case, the number of sub-matrices n_p needs to be increased in order to avoid overlaps. As n_p increases, each passing bacterium will cause a higher increase in the standard deviation signature because the number of black pixels which make up the bacterium remains constant while the number of background pixels decreases. Thus, the bacterium "weighs" more on the total trace and will increase its relative contribution in the standard deviation. In practice, this implies that the threshold value for the peak prominence *p* needs to be increased in order for a peak to be assigned to the passage of a bacterium. An empirical relation has been investigated between the number of subdivisions n_p and the value of the prominence p necessary to maintain a constant number of counted bacteria. The results are shown in Figure 65 and have been fitted to a model of the form:

$$p = p_0 + \alpha \log^{\beta}(n_p) \tag{46}$$

where p_0 is the prominence for n_p=1, typically being set to 1, while $4.1 < \alpha < 4.5$ and $1.13 < \beta < 1.22$. These values have been validated for three different counting experiments with a number of bacteria comprised between 2000 and 10000 and the previous equation has been employed to determine the optimal value of the prominence p for videos with more than 2000 bacteria swimming over the course of the video.

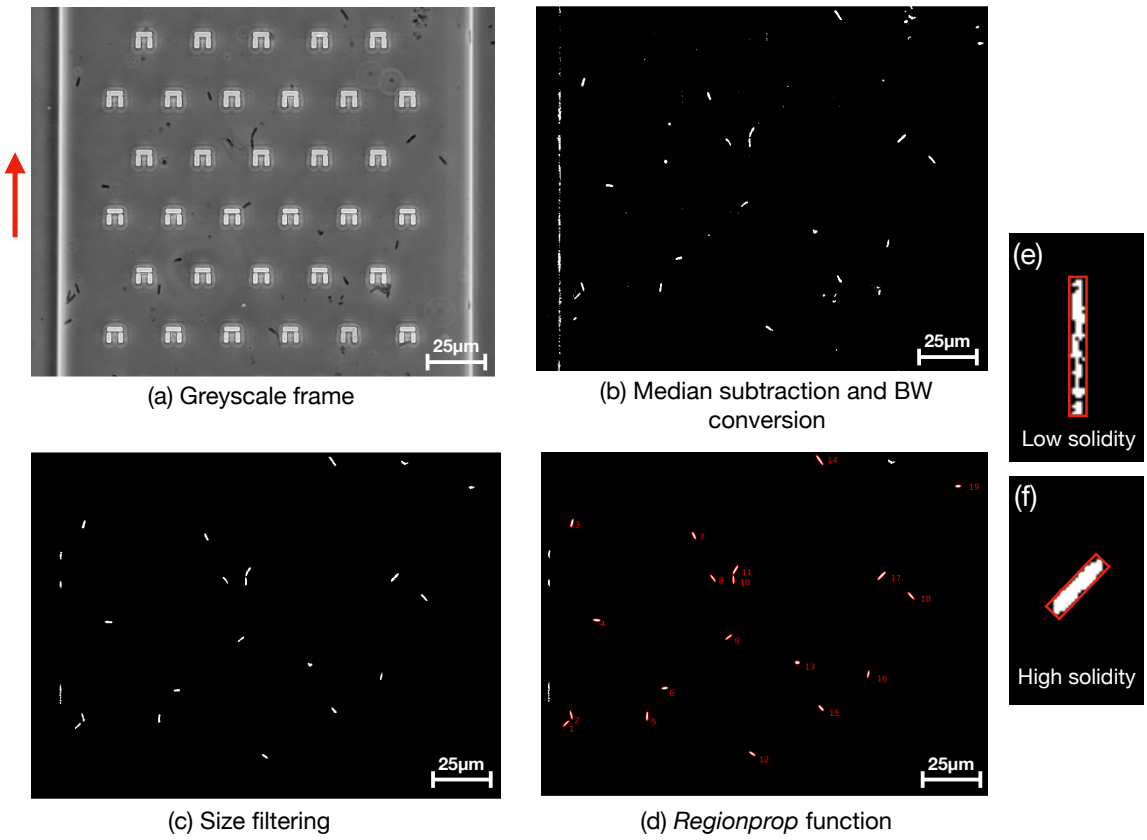

Figure 66. Post processing steps applied to detect bacteria swimming through the field of view. (a) Each frame is converted into greyscale. (b) The temporal median is subtracted to eliminate any feature fixed over time and the frame is converted to black and white according to Otsu's method. (c) A size filter is applied to remove features with an area outside of the expected range for bacteria. (d) The regionprop built-in MATLAB function is used to identify all the connected regions left in the image. (e-f) A further filtering is performed by thresholding the solidity of the detected regions. The red arrow indicates the direction of the fluid flow.

11.3. Bacteria morphology

Bacterial morphology is another parameter that is important to assess the bacteria's response to environmental challenges, such as antibiotic administration. In quantitative terms, the length of bacteria passing through the analysed area over the entire duration of the videos has been measured according to the following procedure:

- The video is loaded into MATLAB using the same procedures detailed previously.
- Each frame is converted into greyscale images according to the luminosity method used before.
- The temporal median intensity is calculated at every pixel position and subtracted from each frame before being converted into black and white images (BW, Figure 66(a)). For the BW conversion, a threshold needs to be chosen in order to assign a 0 or 1 value to each pixel. Here, the threshold values are calculated using the *greythresh* built-in MATLAB function, which uses Otsu's method [174]. A variety

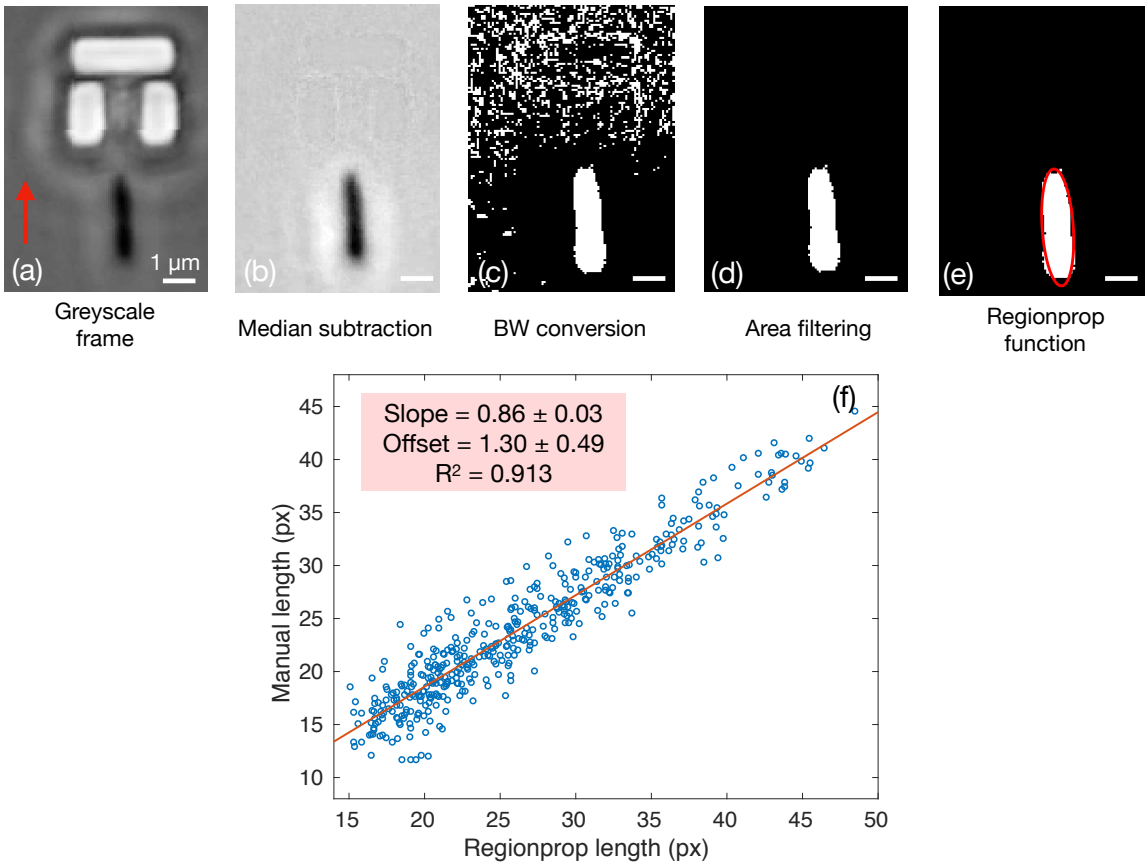

Figure 67. Procedures applied for the detection a single bacterium and measurement of its geometrical properties. (a, b) Typical halo surrounding objects imaged through a phase contrast microscope. The red arrow indicates the direction of the fluid flow. (c, d) Black and white conversion of the frame and area filtering steps. (e) Overlaid contour detected by the regionprop MATLAB function. A comparison between (a) and (e) clearly shows that the process tends to overestimate the size of the bacterium. (f) Example of a calibration curve obtained by comparing manually clicked length to the values detected by the algorithm. The relation is linear and is employed to correct all the detected dimensions.

of other thresholding methods have been tested and compared to Otsu's, which resulted in the best performance. An example frame can be seen in Figure 66(b).

- An area filter is applied to the BW frames in order to filter out features that are either too small or too large to be a bacterium. The *bwareafilt* function is employed with an area range of 100< area <700 pixel^2. These thresholding values have been optimised by visual inspection of several frames of every video. The result of the filtering procedure is shown in Figure 66(c).
- The *regionprop* built-in MATLAB function is called at this point. This function allows to identify all 8-connected components in a binary matrix, which is all the contiguous white regions in the image whose white elements consist of at least 8 white neighbouring pixels. A number of different properties of these regions can be retrieved, such as their centroid, major and minor axis length, eccentricity, area, orientation and many others. At this stage, a further filtering on the detected regions

is applied, namely a threshold for the solidity value of the region. The solidity is defined as the ratio between the area of the object and the area of the smallest polygon that can contain the connected region. This filtering allows us to discard patchy objects that might be erroneously classified as bacteria. An example is clearly visible in Figure 66(d) and in the close-ups in panels (e) and (f). The patchy areas are still present after the area filtering step, because of their dimensions being similar to those of bacteria. However, they need to be discarded from the detection as they are often remnants of the channel walls. The detected regions being classified as bacteria are highlighted in red in Figure 66(d), where an ellipse is drawn to visualise them. The properties of interest, in particular the major and minor axis are saved in a structure in the MATLAB workspace for subsequent analysis.

- The same procedure is repeated over time every 300 frames (6 seconds), which is longer than the time a single bacterium typically takes to swim along the field of view. This is to avoid the same bacterium being analysed multiple times, which could bias the final result. Furthermore, some bacteria might spend time at the same location, such as when trapped for a significant amount of time or when attached to the glass slide or the PDMS channel. These cases will not be analysed multiple times when looping over the video duration as they will be discarded by the temporal median subtraction procedure.
- Once the entire video is analysed, the geometrical properties of the swimming bacteria are stored in pixels and need to be converted into real units (i.e. μm). The conversion factor is straightforward to retrieve from the period of the trap array, which is designed to be 25 μm. This dimension corresponds to 171 pixels in the frames, making the conversion factor 0.147 μm/pixels. However, it is important to note that the automatic method employed here tends to overestimate dimensions. The reason lies in the black and white conversion procedure. Every feature in the frames is surrounded by ring halos typical of images obtained with phase contrast microscopes. These halos are mistaken for connected regions by the Otsu conversion algorithm, as clearly evidenced in the image sequence shown in Figure 67. The final detected ellipse (panel (e)) is clearly larger than the bacterium in the greyscale frame (panel (a)). In order to take this enlargement into account, the algorithm is calibrated by manually clicking a few hundred bacteria. An example calibration curve is reported in Figure 67(f).

- The relation between the manual (clicked) length and the automatically detected one (*regionprop* length) is linear, with the slope, the offset and relative errors being reported in the inset of the same panel (f). Every length value is thus corrected according to the calibration curve and then converted into μm by multiplying by the 0.147 μm/pixels conversion factor. The values are then employed in the subsequent analysis. I have verified that the correction factor is within a 5% error between four independent runs, thereby the same value was used for every experiment.

12. Results and discussion

Having established that the fabrication of the trapping assay agrees with our design rules and that the methodologies for data analysis have been tested, I now proceed to presenting and describing the main findings on the analysis of individual bacteria [175].

12.1. Characterisation of motility and trapping efficiency

I first describe a set of control experiments to prove the ability of the assay to measure motility at the single-cell level. At the same time, I show that the hydrodynamic efficiency is linked to bacterial motility, as qualitatively predicted in chapter 9. The controls were designed for strains of known but different motility in order to assess the performance of the trapping assay under different controlled conditions. The microfluid chips for all subsequent experiments were based on the design B in appendix A1.

In particular, I chose *E. coli* K12 MG1655 as a model motile peritrichous strain, which has multiple flagella (four on average) randomly distributed over the cell. In contrast, *E. coli* BW25113 was the chosen as a non-motile model micro-organism, as it is characterised by reduced expression of flagella genes, and thus it is unable to swim [176]. Additionally, the non-motile BW25113 was later killed by exposure to heat (2 hours at 60 °C) to provide a further “dead” control group.

Different replicates for each group were conducted: five independent runs for the motile MG1655 and two runs for the non-motile and dead BW25113. Each experiment consisted of five 5-minute videos from which the motility and trapping efficiency were measured according to the procedures presented in the methods section (chapter 11). Recall that post-processing the videos produced intensity traces for each trap in the field of view, whereby

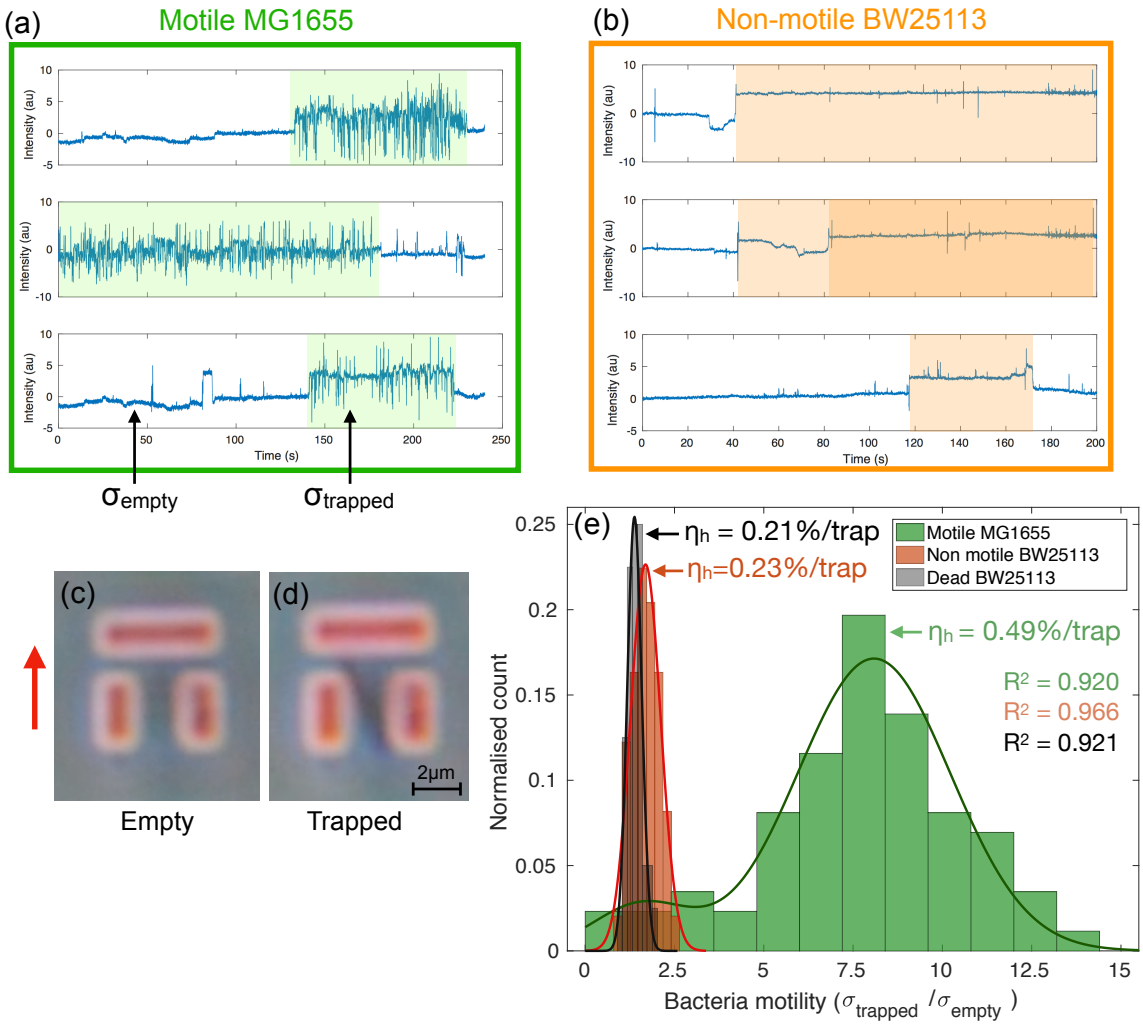

Figure 68. Control experiments for the characterisation of motility of E. coli MG1655 and BW25113. (a, b) Typical intensity traces measured upon trapping of motile E. coli MG1655 and non-motile BW25113, respectively. Light shaded areas highlight the length of time during which a bacterium is trapped. Motile bacteria produce larger fluctuations than non-motile ones. (c) Phase contrast micrograph of an empty trap. The red arrow indicates the direction of the fluid flow. (d) The same trap with a bacterium trapped inside. (e) Distribution of motility values obtained for E. coli of different motility. Histograms are fitted to Gaussian distributions for the non-motile and dead case (orange and black data) and to the sum of two Gaussians for the motile case (green data). The values of the average hydrodynamic efficiencies η_h are shown next to the corresponding distributions.

the intensity is calculated as the average pixel intensity over the trap's area, as per methods section (chapter III, section 11). Figure 68(a) and (b) show three examples of traces for the motile MG1655 and non-motile BW25113 strain, respectively. The presence of a bacterium in the trap is indicated by the changes in intensity, while bacterial motion results in increased fluctuations due to oscillations of constricted bacteria. The length of time that bacteria spent in the trap is highlighted by the overlaid shaded areas.

The link between intensity traces and motility is revealed by comparing these traces. In particular, motile *E. coli* MG1655 produced noisier traces than non-motile BW25113 and dead bacteria (traces not reported). From these traces, we quantified motility by

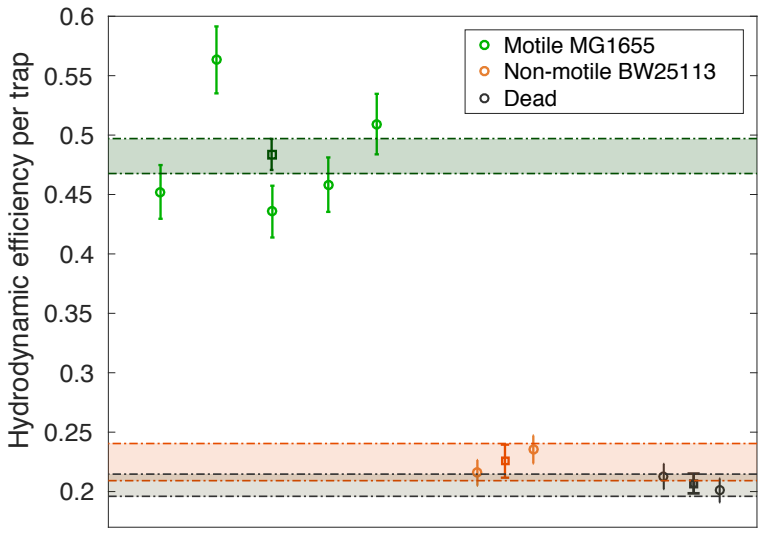

Figure 69. Hydrodynamic efficiency normalised to the number of traps for bacteria of different motility. Values from every experiment are reported separately, whereby the error bars refer to the standard error of the mean over the analysed bacteria, typically on the order of few hundreds. The average efficiency is then calculated for every group (bold square markers). The shaded rectangles indicate the standard error of the mean (N = 5 for the motile case, N = 2 for the non-motile and dead case). Motile E. coli MG1655 are approximately twice as likely to swim into a trap compared to non-motile or dead BW25113.

normalising the standard deviation of trapped bacteria to the background noise calculated for an empty trap, i.e. motility = $\sigma_{trapped}/\sigma_{empty}$. For instance, a motility of 10 means that the standard deviation produced by a constricted bacterium is ten times greater than the background noise. Occasionally, some traps were filled with more than one bacterium, as illustrated by the darker shading in the mid graph of Figure 68(b). In these cases, the two events were considered separately, and two standard deviations were measured, even though the second one was not a single bacterium trapping event. However, this was not a frequent occurrence since the traps are designed to accommodate a single bacterium. On average, only a few tens of events per experiment corresponded to double-trapping events, compared to a total number of trapping events on the order of several hundreds. Hence, these events were considered negligible and should not bias significantly the data.

Figure 68(e) shows the distribution of motility values obtained in the different conditions, along with measured values of the hydrodynamic efficiency η_h. The distributions are fitted to Gaussian curves in order to retrieve an average motility and the relative spread. Motile *E. coli* MG1655 (green distribution in Figure 68(e)) showed a mean value of 8.0 ± 0.4, while we obtained 1.7 ± 0.1 for the non-motile BW25113 (orange distribution).

Notably, the green histogram was fitted to a bimodal Gaussian distribution, which revealed the presence of a secondary peak centred at a motility value of 1.6 ± 0.2. Considering that

this value is close to the one obtained for the non-motile BW25113, we attributed the minor peak to a low-motility subpopulation, likely in a dormant state. This effect will also be observed in every subsequent experiment. We quantified the fraction of such subgroup by evaluating the area under the first component of the green Gaussian curve, i.e. up to the inflection point where the two Gaussians merge. A relative fraction of (8.0 ± 0.9) % was measured. We note that this value is likely to be underestimated since hydrodynamic trapping favours motile organisms. In other words, the measured distribution at low values of motility does not faithfully reflect the real population distribution because our sampling, i.e. the trapping process, is biased. Nevertheless, we will always be interested in relative changes of motility, as I will discuss later on.

After killing the BW25113 strain, an average motility of 1.4 ± 0.1 was measured (black distribution in Figure 68(e)). Interestingly, it is also possible to distinguish the alive, non-motile BW25113 from the same strain after the heat treatment that killed it. The non-motile strain produced a higher average signal than the dead strain, which is likely due to motility mechanisms that do not require the use of flagella, such as gliding or twitching. Additionally, unimodal distributions were recovered in the last two cases, thus suggesting that bacteria were all motility-impaired and dead, respectively. These results show that the trapping assay is able to provide a consistent measurement of motility, as well as a viable way of probing its heterogeneity.

In order to establish the connection between motility and hydrodynamic efficiency, I plotted Figure 69, which illustrates the measured values of hydrodynamic efficiency η_h for the same set of control experiments described above. Recall that η_h is defined as the fraction of the total number of bacteria that entered a trap over a defined amount of time (here five minutes), regardless of the trapping time (as established in chapter 8). The graph in Figure 69 shows the values obtained for each independent experiment consisting of five 5-minute long videos along with the average efficiency and standard error over the entire set (markers in bold). A comparison between the green (motile), orange (non-motile) and black (dead) case reveals that motile bacteria are approximately twice as likely to swim into a trap than non-motile ones. The values of η_h were normalised to the number of available traps in the field of view to provide a homogenous comparison between different experiments. This normalisation step is also useful to account for clogged traps (usually only a few traps during the entire experiment), since they are not available to accommodate bacteria, thereby artificially decreasing the measured hydrodynamic efficiency.

We obtained average values of (0.49 ± 0.02) %/trap for the motile MG1655 strain (green data points), (0.23 ± 0.01) %/trap for the non-motile BW25113 (orange data points) and (0.21 ± 0.01) %/trap for dead bacteria (black points). These numbers correspond to about (16.2 ± 0.7) %, (7.6 ± 0.3) % and (6.9 ± 0.3) % absolute hydrodynamic efficiency, respectively.

Like the motility analysis, Figure 69 also suggests that the assay is able to distinguish non-motile alive from non-motile dead bacteria. The non-zero remaining probability of trapping dead organisms is expected because of the design of the traps (i.e. a few streamlines still cross the traps) and because even inactive organisms still experience Brownian motion associated with any object suspended in a fluid. These results correlate well with the motility analysis, thereby supporting the aforementioned connection between bacteria motility, ability to cross streamlines and, consequently, hydrodynamic efficiency.

12.2. Size and shape selectivity

The physical geometry of the traps intrinsically selects bacteria according to their size and shape. In order to illustrate this point, I studied the trapping process for bacteria of different morphology by exploiting the natural length heterogeneity within the same population of *E. coli*. In particular, using the criteria for the definition of hydrodynamic and trapping efficiencies, I classified trapping events according to their duration in time. For a fixed trap geometry, I measured the length, width and eccentricity of bacteria that entered a trap and immediately escaped as well as the those of trapped bacteria.

The resulting length and eccentricity distributions are shown in Figure 70(a) and (b). Red data refers to trapped bacteria that remained trapped for at least one minute, while blue distributions represent escaped bacteria. The length distributions were fitted to a Gaussian distribution of the form:

$$n = ae^{-\left(\frac{x-b}{c}\right)^2} \tag{47}$$

In order to calculate eccentricity, *E. coli* were modelled as ellipses with major axis *a* and minor axis *b*, as illustrated in the diagram in Figure 70(c) and the eccentricities were fitted to the asymmetric beta distribution:

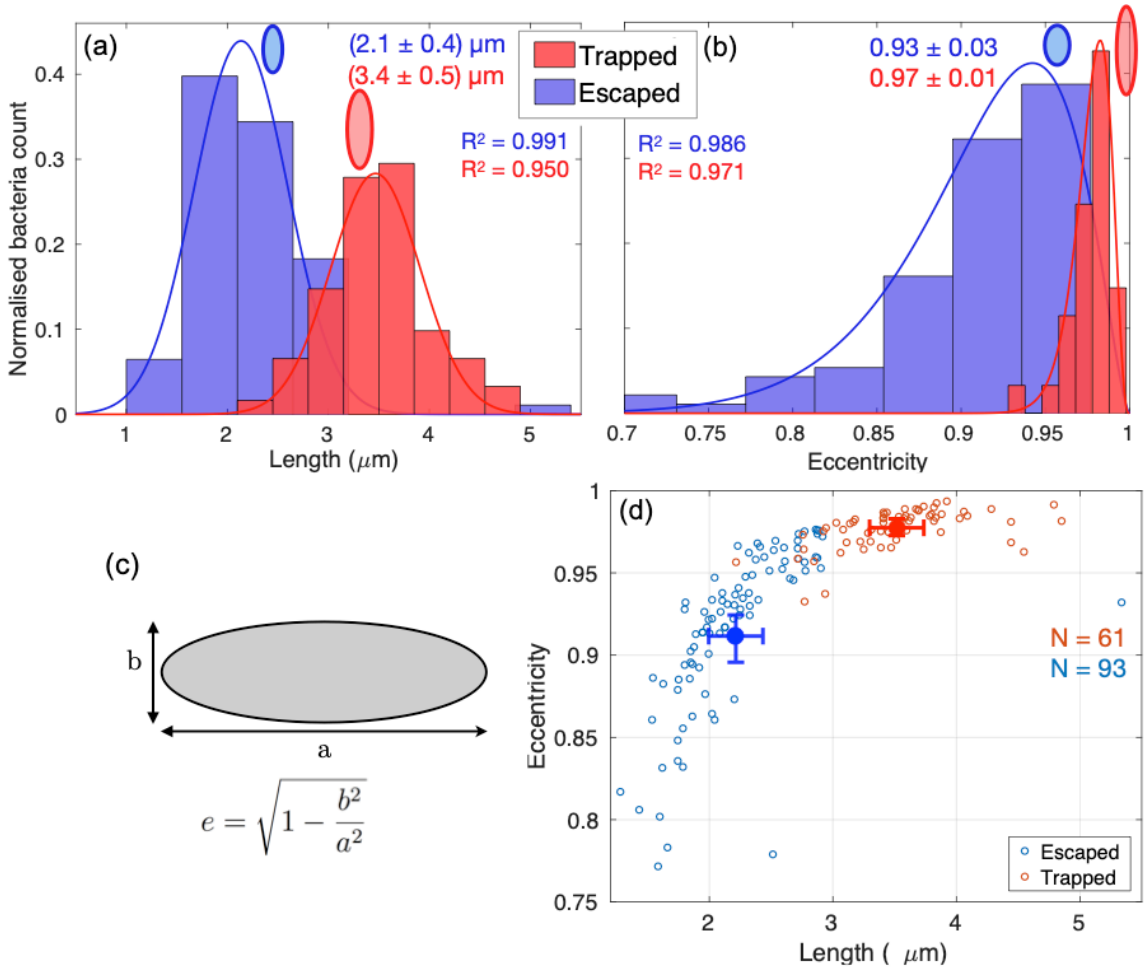

Figure 70. Characterisation of the size selectivity of the trapping assay. (a, b) Length and eccentricity distributions of bacteria that have entered a trap, respectively. The blue curves represent bacteria that have escaped within a few seconds by swimming through the vertical gap, while the red curves refer to bacteria that have been trapped for a minimum of 3 minutes. The lengths are fitted to Gaussian distributions, while the eccentricities are fitted with an asymmetric beta distribution. The eccentricity is calculated by modelling the rod-shaped E. coli as ellipses with major axis a and minor axis b, as illustrated in panel (c). (d) Scatter plot of eccentricity versus length for escaped and trapped bacteria. Centroids and relative errors (originating from the fitted distributions above as the 95% confidence bounds) are overlaid to show the achieved degree of selectivity. The number of analysed bacteria N is reported in the inset.

$$n = x^{a-1}(1-x)^{b-1}\frac{\Gamma(a+b)}{\Gamma(\mathrm{a})\Gamma(\mathrm{b})} \tag{48}$$

where Γ is the gamma function and the mean value of the distribution can be shown to be equal to $a/(a+b)$ [177].

We note a clear difference between the two cases. Elongated bacteria, characterised by a major axis $a = (3.4 \pm 0.5)$ µm and an eccentricity of 0.97 ± 0.01, exhibit extended residence

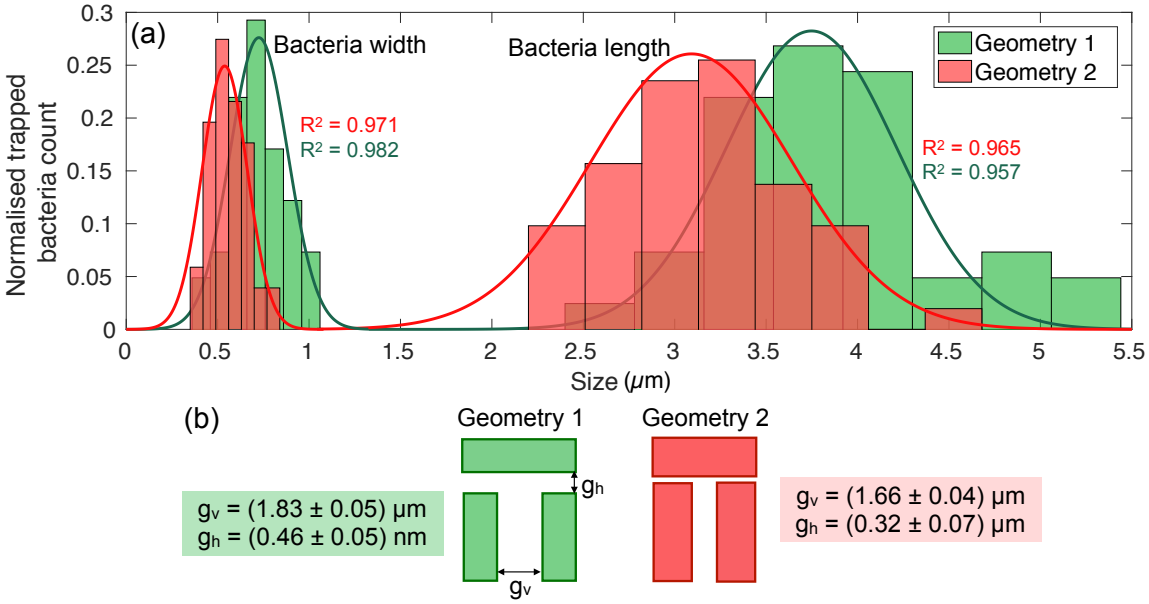

Figure 71. Size selectivity for different trap's geometries. (a) Distributions of width (minor axis) and length (major axis) of trapped bacteria for the two different geometries illustrated in (b). The distributions are fitted to Gaussian curves. The key differences are the width of the trap g_v and the size of the vertical gap g_h, whose values are specified next to the diagrams.

times within the trap. In contrast, shorter and rounded ones ((2.1 ± 0.4) µm long and with an eccentricity of 0.93 ± 0.03) escape the traps more easily. The reason for the marked selectivity is the fact that shorter and more rounded bacteria are able to rotate within the trap to gain access to the vertical gap. Conversely, the motion of elongated bacteria is physically restricted by the trap walls, so they remain trapped for longer.

In order to validate this mechanism, we repeated the same experiment with traps of different geometries, as illustrated in Figure 71(b) and colour-coded in green and red. In the interest of clarity, the figure only shows data for trapped bacteria, in particular the distributions of bacterial length and width.

The key difference between the two trap geometries is the different width of the entrance gap (g_v) and the vertical gap (g_h). As the resulting distributions in Figure 71(a) show, the larger these dimensions are, the larger the bacteria need to be to remain trapped. Indeed, the threshold cell length for efficient trapping with geometry 2 is smaller than that of geometry 1. For instance, a 3 µm long bacterium is more likely to remain trapped in geometry 2 because of the reduced trap width which prevents rotation. We observe the same effect on the width of the bacterium, although it depends on the vertical gap g_h of the trap rather than its width g_v. Therefore, g_h controls the minimum width of the bacteria that can remain trapped by preventing wider bacteria from going through the vertical gap.

Conversely, g_h determines the minimum length of bacteria able to rotate within the trapping area and thus escape.

12.3. Antimicrobial susceptibility assay

Having verified that the trapping assay is sensitive to both bacteria motility and morphology, I now proceed to show how these quantities can be employed as a signature of antibiotic action and classification of susceptibility vs. resistance of *E. coli* strains [175]. Three different antibiotics were tested: ampicillin, kanamycin and trimethoprim. They were chosen to prove the generality of the approach since they cover the three main mechanism of action of antibiotics, as I will detail below.

In general, antibiotics are molecules that interfere with the normal bacterial life cycle by either arresting bacterial division (bacteriostatic action) or by killing them (bactericidal action). However, it is not straightforward to place a drug in a well-defined category. In fact, the success of the antibiotic treatment and its mechanism of action depends on the drugs' concentration. The possible outcome is quantified by the minimum inhibitory concentration (MIC) and the minimum bactericidal concentration (MBC), namely the minimum concentration that prevents the growth of bacteria or actively kills them, respectively. Given the toxicity of the drug to the bacteria, any bacteriostatic agent shows bactericidal behaviour at sufficiently high concentrations, provided that the strain is susceptible. An agent is usually regarded as bactericidal if the MBC is no more than four times the MIC [178,179].

In practice, the adverse action of antibiotics takes place by impairing at least one of the following bacterial functions:

- **Cell wall biosynthesis**. The cell wall is crucial for the organism's viability as it defines the volume of the bacterium and provides structural integrity. Upon division, new cell walls need to be synthetized to ensure survival of the mother and daughter cells. Penicillin binding proteins (PBPs) are critical components in the final steps of cross-linking the peptidoglycan layer of the cell wall. In fact, PBPs catalyse a number of different reactions [180]. Beta-lactam antibiotics, such as ampicillin, contain a beta-lactam ring which makes them analogues of certain amino acids needed for cross-linking. In particular, the ring is able to acylate the

PBP, thereby impeding the final phases of cross-linking of the cell wall and ultimately causing cell lysis [118,181].

- **Protein synthesis.** Bacteria constantly synthetize proteins during their life cycle. Proteins regulate most bacterial functions: metabolism, motion, division, uptake and release of compounds, taxis responses to environmental stimuli and many more. The process of protein production happens via the so-called central dogma of molecular biology. Briefly, the DNA contains the instructions needed for the production of proteins. This information is transcribed into the RNA (transcription step), which acts as a template for the bacterial ribosomes. Ribosomes are the protein-making machines inside cells where the RNA is read, and single amino acids are polymerised into polypeptides that fold to form proteins (translation step). Some antibiotics act by selectively binding to the ribosomes, causing either misreading of the RNA instructions or incorrect insertion of amino acids into polypeptides chains. This results in the production of incorrect or toxic peptides which hamper the division ability of the cell or cause death. Kanamycin belongs to this class of drugs [182].

- **Nucleic acid synthesis**. Nucleic acids are the fundamental building blocks of DNA. Bacterial DNA typically consists of a single circular double stranded molecule, called the bacterial chromosome. Before cell division, the DNA needs to be replicated in order for the daughter cell to be provided with genetic material. Some classes of antibiotics interfere with the synthesis of nucleic acids that are necessary for the production of new strands of DNA, thereby impairing bacterial division or causing death. Trimethoprim broadly belongs to this class since it hinders the production of tetrahydrofolic acid (THF), a precursor molecule for the synthesis of nucleic acids [183].

Not surprisingly, bacteria have managed to develop a vast range of sophisticated and effective resistance mechanisms through evolution. These mechanisms have been triggered by the overuse of antibiotics, as extensively discussed in chapter 3. Resistance to antibiotics can be acquired either through the uptake of foreign DNA (horizontal gene transfer, see chapter 3), or by developing genetic mutations and transmitting them to daughter cells. In both cases, the alteration of the antibiotic action happens via one of the following mechanisms [184]:

- **Modification of the antibiotic target**. Resistant bacteria are able to protect the antibiotic binding site, modify its chemistry to decrease the affinity for the antibiotic molecule or totally manage to bypass the function that the antibiotic inhibits. As an example, these processes are most common in the acquisition of resistance to trimethoprim. Resistant bacteria overproduce the antimicrobial target that trimethoprim binds to (two enzymes involved in the production of THF). The objective is to overwhelm the drug by increasing the number of targets available. Alternatively, they can produce trimethoprim-insensitive enzymes, such that the drug is not able to bind to them [185,186]. These strategies ensure that the synthesis of THF and therefore of nucleic acids can still be performed.

- **Modification of the antibiotic molecule**. This action is accomplished by either altering the chemical structure of the drug molecule to decrease its efficacy or by totally destroying it. For instance, resistance to aminoglycosides (such as kanamycin) is commonly achieved by phosphorylating the antibiotic molecule, i.e. by adding a phosphate group that decreases the affinity of kanamycin to the bacteria ribosome [187]. This mechanism is also common against beta-lactam antibiotics (including ampicillin). Resistant bacteria are able to hydrolyse the beta-lactam ring in the drug molecule by producing a beta-lactamase enzyme for this purpose [188,189].

- **Decrease drug uptake and drug efflux pumps**. Bacteria can limit the uptake of antimicrobials by modifying the permeability of the cell wall. A less permeable membrane prevents the drug molecules from reaching their target sites which are commonly located inside the bacterium or in the inner membrane. Alternatively, some bacteria have also evolved molecular machines to pump the toxic agents out of the cell, called efflux pumps [190].

12.3.1. Resistant strain engineering

The aim of a susceptibility test is to detect the ability of antibiotics to impair bacteria viability, i.e. to classify bacteria as susceptible. However, in order to accomplish a correct assessment, the test should be able to discriminate between susceptible and resistant

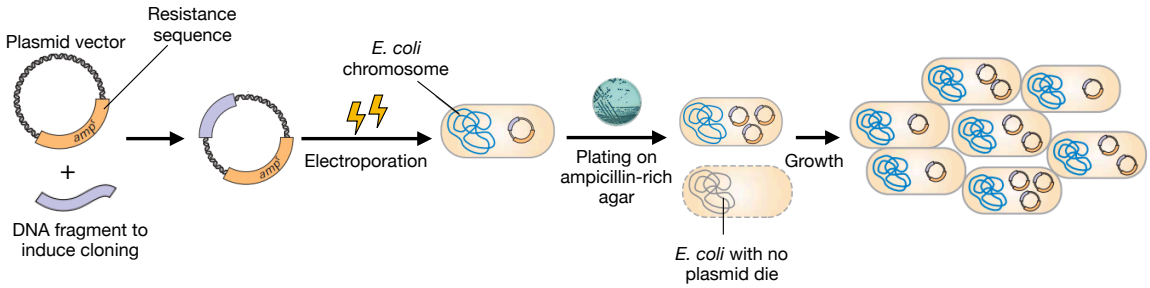

Figure 72. Diagram of the bacterial transformation process for the engineering of resistant strains. A plasmid vector contains a specific sequence to confer resistance along with a DNA fragment to induce its replication by the bacteria. Plasmids and bacteria are mixed in solution and the insertion of the plasmid is achieved by electroporation. After plating the transformed bacteria onto an antibiotic-rich medium, resistant organisms are selected and are able to multiply, while bacteria that did not take up any plasmid die.

strains. In order to provide control groups for our trapping assay, we genetically modified the wild type *E. coli* MG1655 to make it resistant to the three antibiotics we tested.

Resistance to ampicillin, kanamycin and trimethoprim was conferred by introducing plasmids into the wild type strain by artificially stimulating the mechanisms of horizontal gene transfer. A plasmid is a circular double-stranded DNA molecule which occurs naturally in bacteria and some eukaryotic cells. Plasmids can be engineered by inserting specific nucleotide sequences, for example to confer resistance, as shown in the left-hand side of Figure 72. Once plasmids are taken up by bacteria, they are expressed and, more importantly, duplicated before every cell division along with the chromosomal DNA. This procedure guarantees the transmission of resistance to daughter cells.

The process of introducing foreign DNA into host cells and inducing its replication is called transformation. An illustration is provided in Figure 72. Firstly, bacterial cells are suspended in the medium containing the plasmids of interest. Since normal cells are not efficient in taking up plasmids, the insertion needs to be induced, for instance, by electroporation. Secondly, an electrical pulse is applied to the solution in order to temporarily enhance the bacterial membrane permeability and allow the penetration of plasmids. However, not every cell will be provided with a plasmid, so that a selection procedure is needed to favour only the resistant population. This is finally accomplished by plating transformed cells onto antibiotic-rich agar plates, which causes susceptible cells to die and resistant ones to proliferate.

In our case, *E. coli* MG1655 were grown overnight in Lysogeny Broth (LB: 10 g/l tryptone, 5 g/l yeast extract, 10 g/l NaCl, pH 7.5) at 37 °C with shaking at 200 rpm. Cells were made electrocompetent by growing to an optical density (OD) of 0.6, then washing three times

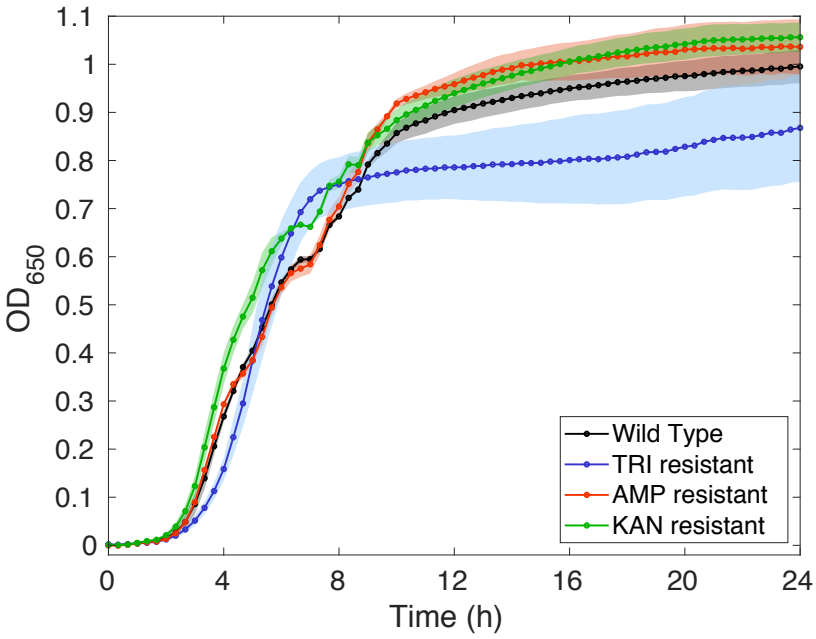

Figure 73. Growth curves over 24 hours for the wild type strain MG1655 and for the resistant engineered strains. The optical density at 650 nm was measured every 20 minutes for five independent replicates (N=5). Values are normalised to a blank medium control and the shaded areas indicate the standard error of the mean over the five replicates.

in ice-cold 10% (w/v) glycerol before resuspending in 100 µl of 10% glycerol solution. We performed electroporation with a Bio-Rad Multipulse Electroporation using 50 µl of prepared cells and 40-150 ng of plasmid DNA. A pBAD vector containing *ampR* was used for ampicillin resistance. The *kanR* gene in a pET vector encoded resistance to kanamycin, while a pT2ST vector containing *ampR* and *dfrA* was used for ampicillin and trimethoprim resistance [191].

Following the application of the electrical pulse, cells were resuspended in LB broth, warmed at 37 °C and incubated at 37 °C for 2 hours with shaking at 200 rpm to favour bacterial recovery. 10 µl of cultures were plated on ampicillin, kanamycin or trimethoprim-rich agar plates (at concentrations of 100 µg/ml, 60 µg/ml and 35 µg/ml, respectively) and incubated for 24 hours at 37 °C. At this point, the resistant colonies that survived on the plates were available for subsequent experiments. These procedures were carried out by Stephen Thorpe from the Department of Biology at the University of York.

The viability of the obtained resistant strains was verified by measuring their growth curves. We performed the assays using a Biotek Synergy plate reader at 37 °C over 24 hours, with orbital shaking at 200 rpm. OD measurements were taken at 650 nm every 20 minutes. The resulting curves are shown in Figure 73, which also includes a growth curve

for the untransformed wild type *E. coli* MG 1655 strain (black curve). Each curve is an average of five replicates, normalised to the OD of blank control LB.

12.3.2. Motility and morphology susceptibility test

I will first provide a general overview of the results obtained upon administration of antibiotics to individually trapped bacteria and later show a more detailed analysis for each drug. Figure 74 shows the main results, where 10 μg/ml of kanamycin (KAN), ampicillin (AMP) or trimethoprim (TRI) were administered to the susceptible and resistant *E. coli* strains.

Rows refer to different antibiotics (KAN in panels (a-c), AMP in panels (d–f) and TRI in panels (g–i)), while columns correspond to the three quantities being evaluated as signatures (motility, trapping efficiency and bacterial length). Red curves with circle markers refer to the susceptible wild type *E. coli* MG1655, while blue curves with square markers were obtained for the resistant strains.

Each curve reports results from a single experiment and each data point is calculated from data extracted from a 5-minute long video that is post-processed to provide measures of total cell count, number of trapped bacteria, intensity traces over the trap areas and cell morphology, as per the methods section. Motility and trapping efficiency are normalised to the maximum value in each case to provide a homogeneous measure between 0 and 1 and to facilitate comparison. Negative times serve as no-drug control baseline.

The bacterial samples were spiked with antibiotics at time t = 0 and injected into the same chip (as indicated by the vertical dashed lines). The only exception is the black dot-dash line in each graph, which refers to a no-drug control. In this case, bacterial colonies were left to proliferate inside the microfluidic channel under flow conditions with no antibiotic being flushed at any time point. We note that the three signatures are relatively constant over time. In fact, bacteria maintain motility and show only a slight decrease in length of about 10% over 6 hours (panels (c), (f) and (i)), likely due to the increased pressure in the channel compared to a normal planktonic state. This behaviour suggests that the microfluidic environment does not significantly affect our phenotypical signatures. Therefore, any subsequent change of our indicators can be ascribed to the action of the antibiotics.

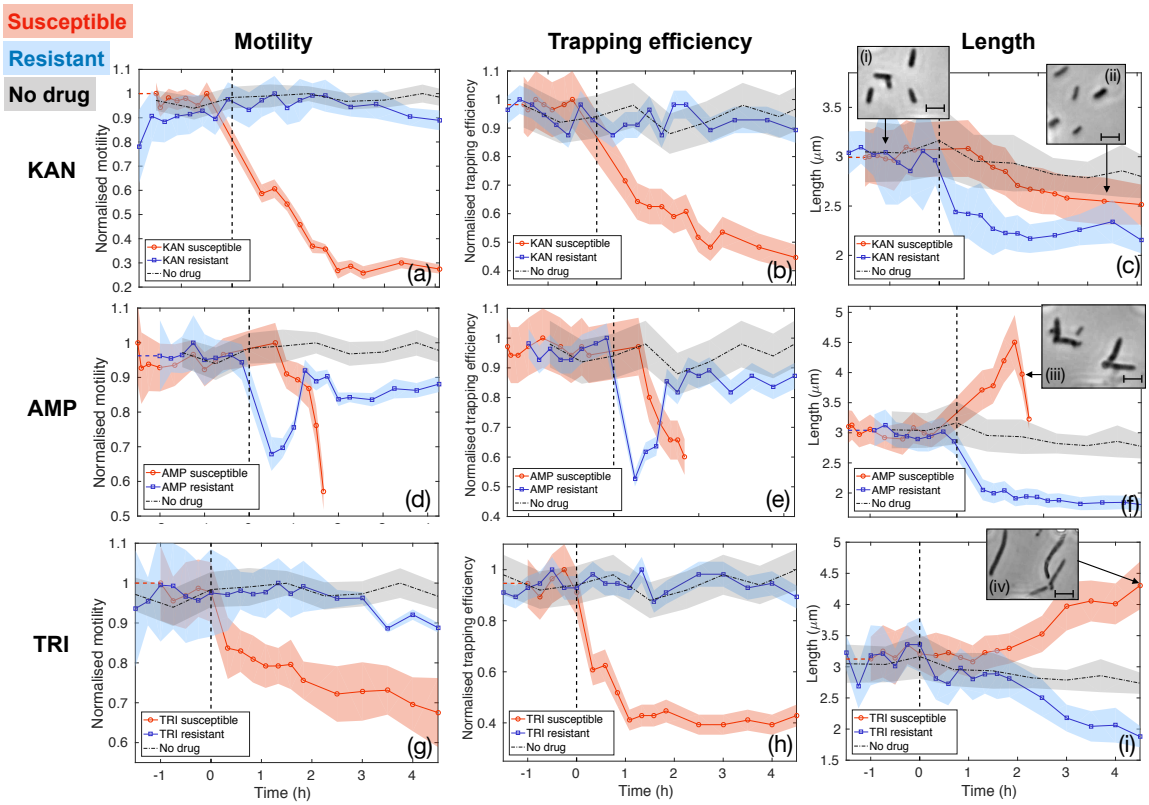

Figure 74. Motility (left column), trapping efficiency (mid column) and bacteria length (right column) over time upon the administration of 10 μg/ml of kanamycin (KAN, top row), ampicillin (AMP, mid row) or trimethoprim (TRI, bottom row) to susceptible E. coli (red curves with circle markers) and resistant ones (blue curves with square markers). Antibiotics were flushed at t=0, except for the dot-dash black line in each graph that represents a no-drug control. Motility and efficiency are normalised to their maximum values to facilitate comparison. Insets in the right column illustrate typical bacterial morphologies, where scale bars correspond to 3 μm. Shaded areas denote the standard error of the mean over the analysed bacteria. Each curve corresponds to a single biological replicate.

The first column of Figure 74 (panels (a), (d) and (g)) shows how bacterial motility varies over time following exposure of *E. coli* to each of the three antibiotics. A clear and common decreasing trend is observed for the susceptible strain (red curves with circle markers) for all three antibiotics, which directly corresponds to the similarly decreasing trapping efficiency, as illustrated in the second column (red curves in panels (b), (e) and (h)). On the other hand, resistant strains (blue curves with square markers) behave differently. Kanamycin and trimethoprim do not significantly affect the motility of resistant strains (blue curves in panels (a) and (g)) and, consequently, trapping efficiency is not influenced either (blue curves in panels (b) and (h)). In contrast, ampicillin-resistant *E. coli* show a temporary loss of motility, which is recovered after approximately 1.5 hours of exposure to the drug. This momentary loss of motility was also observed by Longo *et. al.* [134] for *E. coli* engineered with the same resistance gene user her (*ampR*, see section 12.3.1). However, the authors did not provide an explanation of the observed behaviour

and no further references could be found in the relevant literature. Thus, this behaviour remains unclear and further studies are needed to elucidate its origin. Nevertheless, the motility recovery is a clear signature that enabled detection of resistance by differentiating the two strains.

Additionally, the morphology responses (third column of Figure 74) provide further insight to aid the classification of susceptibility and resistance. The behaviour is quite diverse and includes elongation, shrinking, bending and formation of bulge structures, as illustrated in the insets of panels (c), (f) and (i). I will discuss the morphology signatures and their connection to the motility signal for each antibiotic in the next sections. The combination of information from the two domains also enabled probing the mechanism of the drugs' action, explaining the observed differences, increasing confidence and decreasing the time needed to achieve the classification of resistance and susceptibility.

12.3.2.1. Kanamycin

Kanamycin produced the most rapid and evident motility response. A significant loss of average motility (approximately 60%), and therefore of trapping efficiency, is observed only 40 minutes after administration to the susceptible strain (red curves in Figure 74(a) and (b) and plotted together in Figure 75(a)). In contrast, motility and trapping efficiency of the resistant strain are barely affected, remaining constant over time (blue curves in Figure 74(a) and (b)). This first observation already allows distinguishing the susceptible strain from the resistant one. Additionally, since the motility readout is performed for each single trapped bacterium, the data contains much richer information about the action of kanamycin and its dynamics.

The most interesting case is that of the susceptible strain. Figure 75(a) illustrates the average motility and trapping efficiency over time along with typical bacterial morphology before and after the injection of kanamycin (inset (i) and (ii), respectively). I then studied the distribution of motility values at different time points, as indicated by the coloured arrows along the motility curve. Panels (b), (c) and (d) of Figure 75 show histograms of motility at -1 hour, 0.7 hours (40 minutes) and 2.7 hours (160 minutes), respectively.

We note that before the exposure to kanamycin (panel (b), blue histogram), motility is characterised by a bimodal normal distribution. We observe a major sub-population peaked at high values of motility (approximately 10) as well as a low-motility one, similar to the first control experiment (green distribution in Figure 68(e) in section 12.1). 40 minutes of

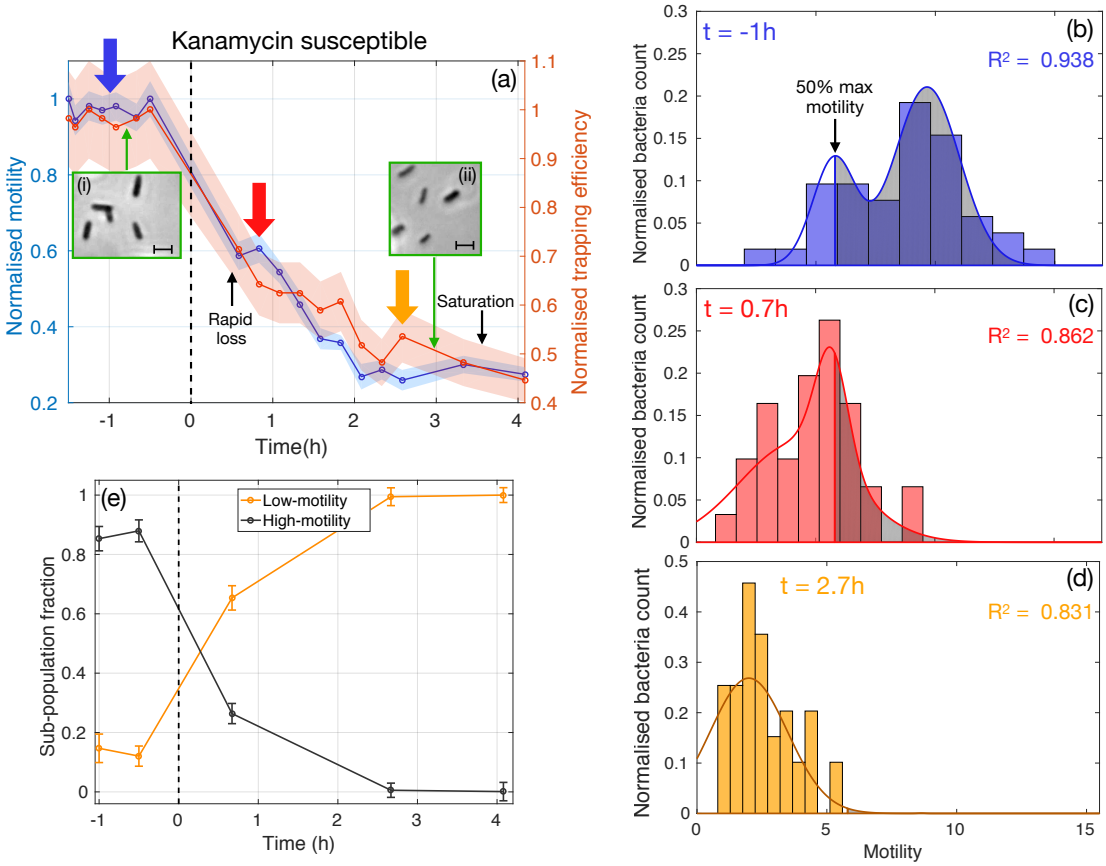

Figure 75. Motility analysis upon exposure to 10 µg/ml of kanamycin. (a) Normalised motility and trapping efficiency over time. Their behaviour is remarkably similar. Insets (i) and (ii) shows typical bacterial morphology. The scale bars correspond to 3µm. (b, c, d) Histograms of motility values at selected time points (-1h, 0.7h and 2.7h respectively). Data is fitted to bimodal Gaussian distributions, as indicated by the continuous lines. Grey-shaded areas highlight the high-motility sub-populations, defined as the fraction of bacteria with motilities larger than 50% of the no-drug maximum motility. (e) Time evolution of the two fractions calculated as the areas under the fitted curves with error bars coming from the errors on the fitting parameters (95% confidence bounds).

exposure to kanamycin significantly altered the scenario, as shown by the histogram in panel (c). Most bacteria have now lost their motility, as illustrated by the two distributions having almost merged, whereby the high-activity sub-population markedly shifted to lower values of ~6 while the low-motility fraction increased in amplitude. This stage represents the delay in the action of kanamycin, which will be analysed in more detail in section 12.3.3. and it clearly highlights the heterogeneity of the bacterial response. Finally, panel (d) refers to 160 min of exposure to the antibiotic. A high degree of homogeneity is now recovered, as illustrated by the unimodality of the distribution featuring a maximum for a motility value of approximately 2.5. This observation suggests that kanamycin has significantly affected most of the bacterial motility after 2.7 hours of exposure.

The process of motility loss can be further characterised by quantifying the fraction of bacteria belonging to the two sub-populations of different motility, approximately

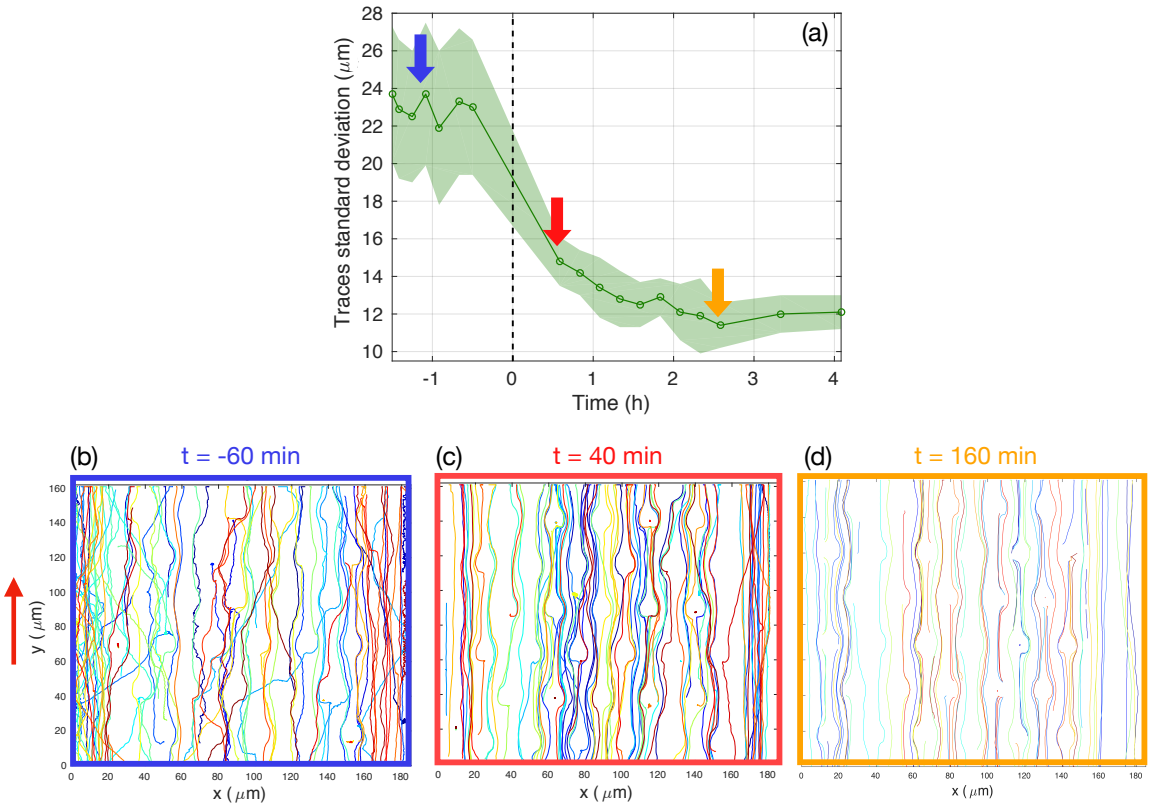

Figure 76. Results of bacteria tracking upon exposure to kanamycin. (a) Standard deviation of the x-coordinate of bacterial trajectories before and during the exposure to kanamycin. A significant decrease is observed, indicative of bacteria losing motility and conforming to the underlying fluidic streamlines. The shading denotes the standard error of the mean over the tracked bacteria (approximately 150 trajectories per video). (b, c, d) Typical bacteria swimming patterns at selected time points (-1 h, 40 min and 160 min, respectively). While trajectories appear jagged at negative times, they extend mainly along the channel after the administration of kanamycin since bacteria are not able to cross streamlines due to the loss of motility. The red arrow indicates the direction of the fluid flow.

corresponding to the two distributions we described above. In particular, we defined the low-motility group as the fraction of bacteria with a motility smaller than 50% of the maximum value measured at negative times (i.e. for viable bacteria in the absence of antibiotics). Conversely, bacteria above the 50% threshold were classified as highly motile, as indicated by the grey shaded region in each histogram (Figure 75 (b), (c) and (d)). We quantified the relative weight of each sub-population by calculating the area under the two curves defined by the threshold. Fitted curves and histograms were normalised such that the total area under the curve is equal to one. Figure 75(e) shows the time evolution of the two subpopulations. We note how this analysis confirmed the rapid action of kanamycin, which caused almost 70% of bacteria to lose half of their motility within 40 minutes. After about 2.5 hours of exposure, the entire population switched to low-motility, as evidenced by the negligible grey area in Figure 75(d) at very end of the decaying tail.

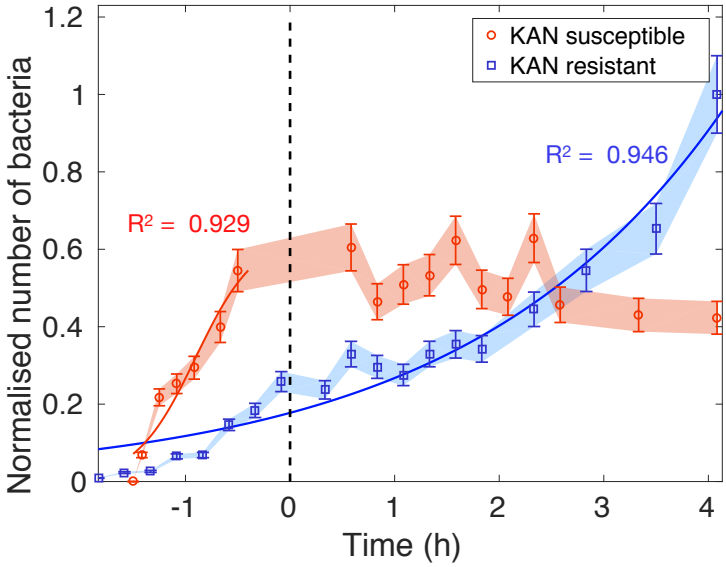

Figure 77. Bacteria count upon exposure to kanamycin. Normalised number of bacteria swimming in the microfluidic channel over time upon exposure to kanamycin to the susceptible E. coli strain (red curve with circle markers) and the resistant strain (blue curve with square markers). While the antibiotic does not influence resistant bacteria, the division of the susceptible strain is inhibited by the bacteriostatic action of kanamycin, as illustrated by the red curve remaining approximately constant at positive times. The shading denotes the error of the count algorithm (see section 11.2) and the curves refer to a single biological replicate.

Additionally, we sought to reinforce the strong link between motility, trapping efficiency and ability to cross streamlines under the influence of antibiotics by using kanamycin as a model system. We accomplished this by tracking bacteria at different time points during the exposure to kanamycin. In chapter 9, we established a useful quantity to assess the streamline crossing ability as the standard deviation of bacterial trajectories along the x direction (i.e. transverse to the flow). Figure 76(a) reports these values over time for the kanamycin experiment. A significant decrease in trapping efficiency is observed upon the action of the drug. Recall that a smaller deviation implies that bacteria motion conforms to the fluidic streamlines. This effect is evident in panels (b), (c) and (d) of Figure 76, where we plotted trajectories over one-minute long videos at the same time points previously selected and highlighted (-60, 40 and 160 min, respectively).

Finally, the morphology signature for kanamycin in Figure 74(c) showed similar behaviour for the susceptible and resistant cells, as they both shrunk upon the action of kanamycin, thus they did not provide characteristic responses.

Now, the question is whether the motility signature is indicative of susceptibility. In principle, bacteria could lose motility and shrink but still be viable. In order to verify this point, we linked the observed behaviour with the standard definition of susceptibility and resistance, i.e. by analysing bacteria division inside the microchannel. For this purpose, I

counted the number of bacteria flowing through the field of view over time. The resulting curves are shown in Figure 77, whereby kanamycin was introduced at time t=0. We observed a clear inhibition of growth for the susceptible strain by kanamycin (red curve with circle markers at positive times). Contrarily, the growth of the resistant strain (blue curve with square markers) was not affected by the drug and followed an expected logistic model of growth [192]. The normalised number of bacteria over time *n(t)* was fitted to the continuous blue line in Figure 77, which is expressed by: (49)

$$n(t) = \frac{A}{1 + e^{\frac{4\mu}{A}(\lambda - t)}}$$

This function describes a sigmoidal curve characterised by a saturation population A (not observed in Figure 77), a growth rate μ and a lag time λ. The goodness of the fit and the inhibition revealed by the red curve allowed us to establish the connection between the behaviour of motility and susceptibility to the antibiotic. Further confirmation will be provided at the end of this chapter by a microdilution experiment.

12.3.2.2. Ampicillin

The second row of Figure 74 showed how motility, trapping efficiency and bacteria length were influenced by the exposure of susceptible and resistant bacteria to 10 µg/ml of ampicillin.

In particular, this antibiotic also caused a decrease in motility for the susceptible case (red curve in Figure 74(d) and displayed again in Figure 78(a)). This reduction can be explained by two mechanisms. Firstly, ampicillin is known to interfere with the transcription of genes required for flagella synthesis and activation [118]. Secondly, ampicillin inhibits cross-linking of the peptidoglycan layer in the cell wall, which is crucial for maintaining cell morphology and balancing turgor pressure. The impeded cross-linking ultimately leads to cell lysis. Critically, the lysis process is preceded by an elongation phase and the formation of a bulged morphology [181] which make the swimming action less efficient. This significant change in morphology can be considered as an early signature of susceptibility that occurs before cell lysis, as confirmed by the morphology analysis (Figure 74(f)). This latter graph reveals the two phases: first an increase in length due to the filamentation process followed by a rapid decline caused by the two branches of the V-shaped bacteria being detected as separate objects during data analysis. (see inset (ii) of Figure 78(a)).

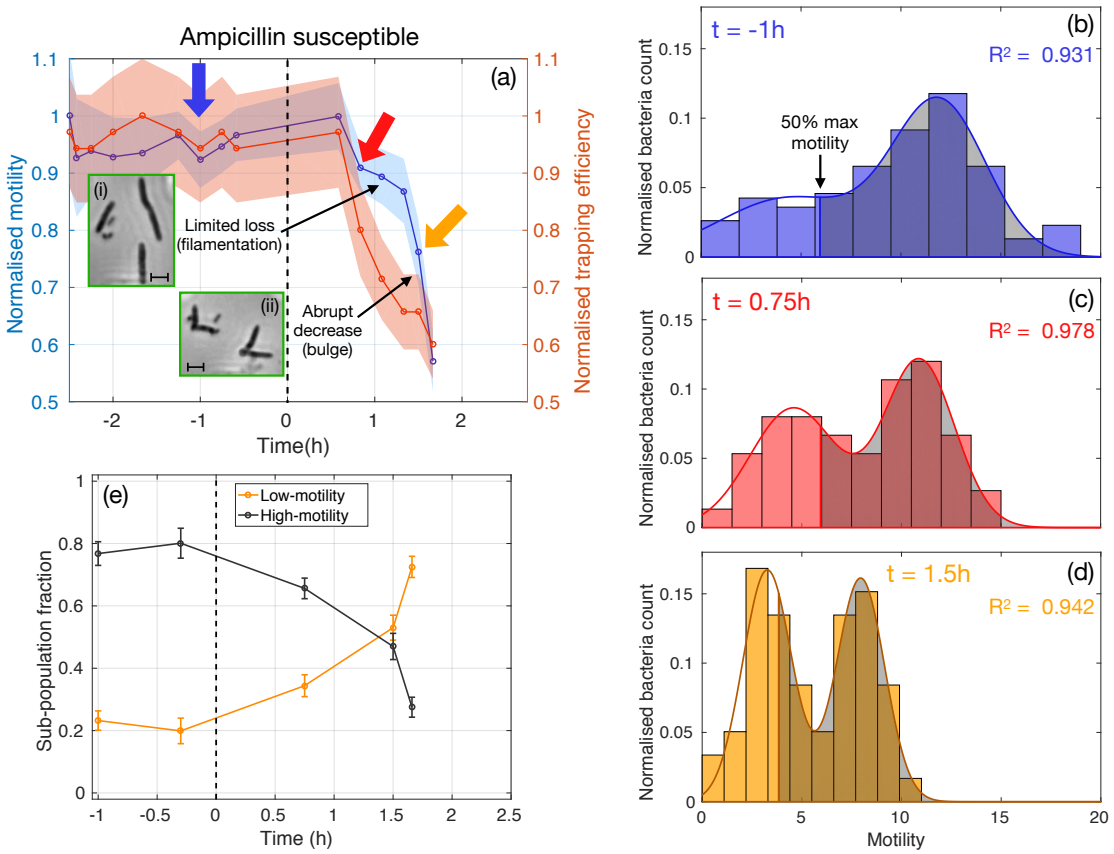

Figure 78. Motility analysis upon exposure to 10 µg/ml of ampicillin. (a) Normalised motility and trapping efficiency. Their behaviour over time is remarkably similar. Inset (i) shows elongated bacteria, while inset (ii) illustrates the typical bulge formation. The scale bars correspond to 3µm. (b, c, d) Histograms of motility values at selected time points (-1h, 0.75h and 1.5h respectively). Data is fitted to bimodal Gaussian distributions, as indicated by the continuous lines. Grey-shaded areas highlight the high-motility sub-populations, defined as the fraction of bacteria with motilities larger than 50% of the no-drug maximum motility. (e) Time evolution of the two fractions calculated as the areas under the fitted curves with error bars originating from the errors on the fitting parameters (95% confidence bounds).

Interestingly, this morphological change is reflected in the motility behaviour of the susceptible strain. We note that the loss of motility also followed a two-stage reduction (see Figure 78(a)) unlike the steep loss observed for kanamycin. Firstly, until approximately 1.3 hours of exposure to ampicillin, the decrease of motility is limited to about 85% of the maximum value, which can be ascribed to the initial filamentation process, as illustrated in the inset (i) of Figure 78(a). Indeed, elongation reduces motility, as is also observed for trimethoprim (see next sub-section 12.3.2.3). However, the formation of the bulged morphology results in a more abrupt drop to a motility of 55%, since V-shaped bacteria are severely impeded in their swimming action. Nearly total cell lysis occurred after about ~1.7 h of exposure to the antibiotic.

The morphology behaviour also explains why the trapping efficiency decreased more rapidly than the motility, as revealed by a comparison between the two curves in Figure

78(a). This happened because the ability to cross streamlines is hindered by two mechanisms: the loss of motility itself and the elongated or bulged shape of the bacteria. Indeed, this effect was also observed for trimethoprim (see next sub-section), but was less evident for kanamycin, which induced bacteria to shrink instead.

The two-phase dynamic is also revealed by the analysis of the motility distributions over time, as shown in Figure 78(b), (c) and (d). At negative times, we observed the typical bimodal distribution characterised by a primary high-motility peak and a secondary shoulder at lower values. After 45 minutes (0.75 h) of exposure to ampicillin, the filamentation process caused the position of the primary peak to decrease and the secondary one to increase in amplitude. Finally, 90 minutes of exposure (1.5 h) resulted in a large shift of both peaks to small motility values because the bulge significantly hindered the bacteria's swimming ability.

Figure 78(e) illustrates the time evolution of the two sub-populations of different motility, as defined by the 50% threshold, similar to the kanamycin case. Unlike kanamycin, the conversion between sub-populations was rather smooth until 1.5 hours, when the formation of the bulge caused the population abundance to invert. Interestingly, ampicillin caused lysis before motility was completely lost, as evidenced by about 30% of bacteria being highly motile until 20 minutes before total lysis occurred and the channel was depleted.

Finally, the previous arguments for ampicillin agree well with a bacterial count inside the microchannel over time. Results for the susceptible and resistant strains are illustrated in Figure 79. While resistant bacteria thrive and divide exponentially upon exposure to the drug, susceptible bacteria behave differently. An initial drop to 80% of the initial population is observed. Afterwards, ampicillin acted by first causing the count to plateau for approximately 1 hour and finally by lysing the cells. Two processes are taking place here: filamentation and death by lysis. The former keeps the number of bacteria constant since they only become longer without dividing, while the latter decreases the population. Filamentation dominates until about 1.5 hours where the decrease in number is less evident, while lysis dominates at later times, thereby causing the sharp decrease leading to the depletion of the channel.

Conversely, the resistant strain (blue curves with square markers) behaves differently. In terms of motility, the resistant strain also experienced a rapid loss immediately after the

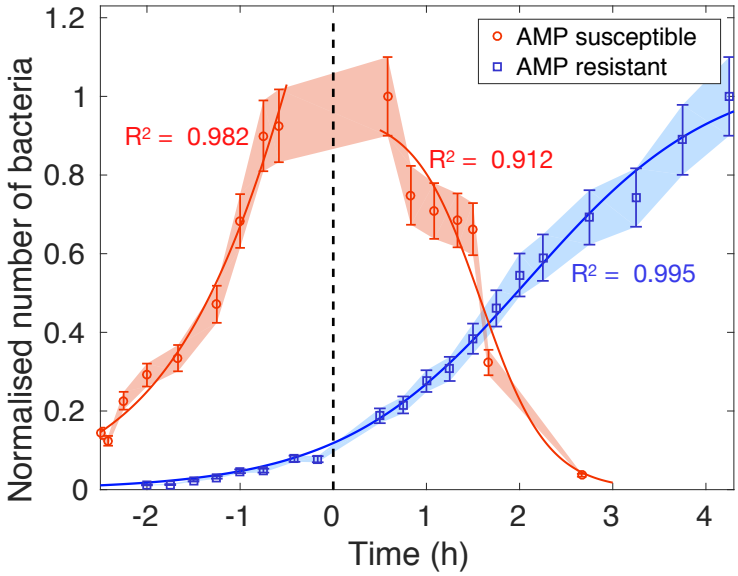

Figure 79. Bacteria count upon exposure to ampicillin. Normalised number of bacteria swimming in the microfluidic channel over time upon exposure of the susceptible E. coli (red curve with circle markers) and the resistant (blue curve with square markers) strains to 10 µg/ml of ampicillin to. The antibiotic does not prevent the resistant strain from growing, as illustrated by the logistic fit (continuous blue curve). However, in the susceptible case, the number of bacteria drastically decreases at positive times due to the bactericidal action of ampicillin, which lyses the cells. The shading denotes the error associated to the counting algorithm (see section 11.2) and the curves refer to a single biological replicate.

exposure to ampicillin (blue curve in Figure 74(d)). However, motility is almost totally recovered after 1.5h of continuous exposure to the drug. The same trend is reflected in the trapping efficiency (Figure 74(e)). The morphology signature provided the most valuable information in terms of classification, since the behaviour is significantly divergent immediately after the administration of the antibiotic.

12.3.2.3. Trimethoprim

Trimethoprim showed a smoother trend than the other two antibiotics (Figure 80(a)), likely because the lack of THF does not have a strong and direct effect on flagella activation and motion in general. The reason for the decreased motility is instead a filamentary phenotypical change, which started after around 1.5 hours of exposure to the drug and steadily increased over time (see inset (i) of Figure 80(a)).

This is also confirmed by the behaviour of the motility distributions shown in Figure 80(b), (c) and (d). The primary high-motility peak that dominates the no-drug case smoothly decreases over the course of the antibiotic action, while the secondary peak increases because of the elongation of bacteria which hampers their motility. The decreased ability of trimethoprim to suppress motility is also shown by the sub-population analysis illustrated in Figure 80(e). The population inversion does not happen until the end of the

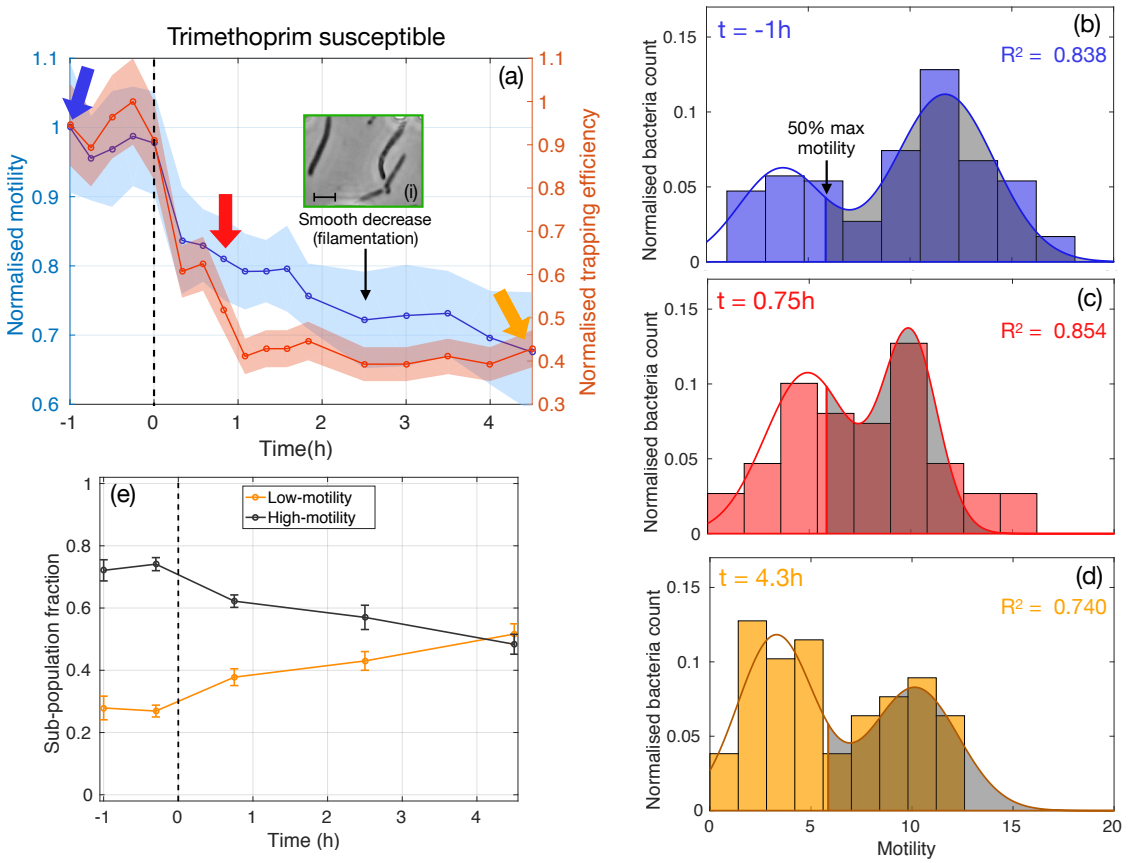

Figure 80. Motility analysis upon exposure to 10 µg/ml of trimethoprim. (a) Normalised motility and trapping efficiency. Their behaviour over time is remarkably similar. Inset (i) shows filamented bacteria during exposure to the antibiotic. The scale bar corresponds to 3 µm. (b, c, d) Histograms of motility values at selected time points (-1h, 0.75h and 4.3h respectively). Data is fitted to bimodal Gaussian distributions, as indicated by the continuous lines. Grey-shaded areas highlight the high-motility sub-populations, defined as the fraction of bacteria with motilities larger than 50% of the no-drug maximum motility. (e) Time evolution of the two fractions calculated as the areas under the fitted graphs with error bars originating from the errors on the fitting parameters (95% confidence bounds).

experiment, i.e. trimethoprim takes more than 4 hours to induce a 50% decrease in motility in half of the population. Additionally, like ampicillin, the trapping efficiency drops more rapidly than the motility (Note the difference in the y axis range of Figure 80(a)) because of the increased difficulty of elongated bacteria to cross streamlines and enter a trap.

Notably, the experiments with trimethoprim were conducted in Mueller-Hinton (MH) broth. This is because the Lysogeny Broth (LB) used elsewhere contains traces of folic acid which might be taken up by bacteria, thus partly counteracting the action of the drug. Figure 82 suggests that this might be happening. By conducting the same experiment in LB broth, we found that the motility drop is delayed in time, as shown by a comparison between the green and the red curve. Trimethoprim seems to be more effective at suppressing motility in MH broth compared to LB.

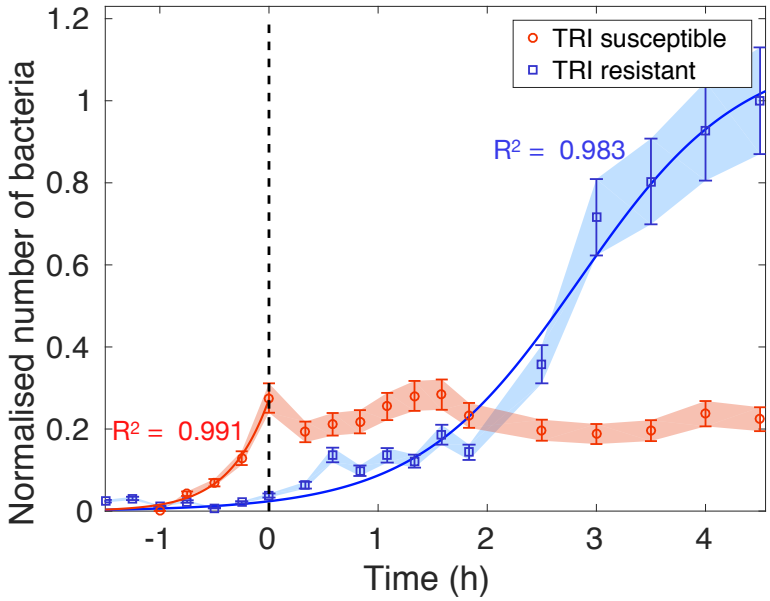

Figure 81. Bacterial count upon exposure to trimethoprim. Normalised number of bacteria swimming in the microfluidic channel over time upon edition of 10 µg/ml trimethoprim to the susceptible E. coli (red curve with circle markers) and the resistant (blue curve with square markers) strains. The division of the resistant strain is not hindered by the antibiotic, as proven by the logistic fit (continuous blue curve). However, in the susceptible case, the number of bacteria remains constant upon exposure to the drug, due to the bacteriostatic action of trimethoprim, which causes cells to elongate but not divide. The shading denotes the error of the count algorithm (see section 11.2) and the curves refer to a single biological replicate.

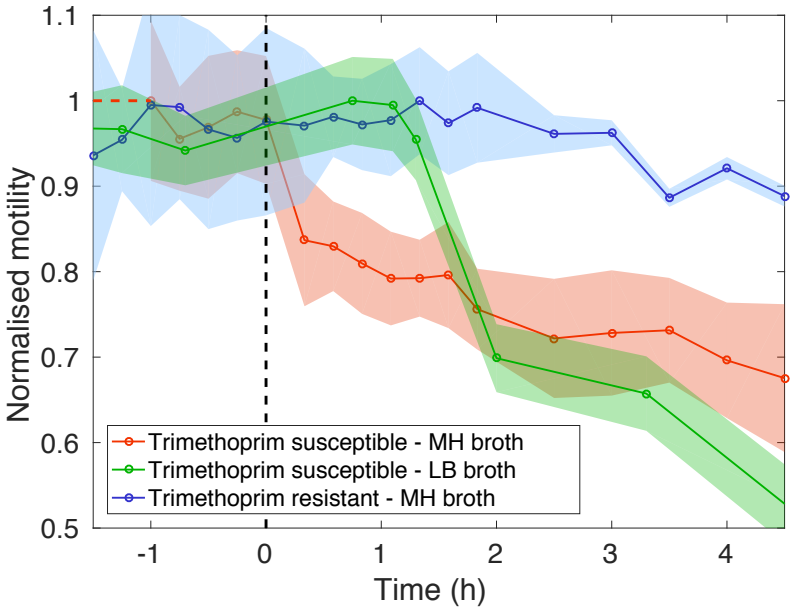

Figure 82. Motility behaviour upon exposure to trimethoprim in different media. Normalised motility upon the action of 10 µg/ml of trimethoprim in Muller-Hinton (MH, red curve) and Lysogeny Broth (LB, green curve) broth over time. The expected loss of motility is delayed in LB broth, while it occurs immediately after exposure to the drug in MH broth. The resistant case in MH broth is also reported for comparison. Shaded areas denote the standard error of the mean over the analysed bacteria. Each curve corresponds to a single biological replicate.

Finally, the correctness of the susceptible and resistant classification is further confirmed by the same bacterial count over time that was also performed for the other antibiotics. The resulting curves are shown in Figure 81. As expected, the resistant strain (blue curve with

square markers) keeps growing in the presence of trimethoprim, while the division of the susceptible *E. coli* strain (red curve with circle markers) is inhibited by the drug, as shown by the number remaining approximately constant upon exposure to the antibiotic.

12.3.3. Advantages of single-cell multiparameter analysis

The behaviour revealed by the previous analysis highlights the added value of conducting the analysis at the single cell level and the importance of assessing multiple parameters simultaneously. Examining bacteria one by one allowed us to gain relevant insight into the distributions of the quantities of interest and the killing dynamics of three different antibiotics. We have verified that bacteria populations are characterised by heterogeneity in motility and shape even before the introduction of any antibiotic.

Heterogeneity also dominated the activity of the drugs and produced a variety of bacterial responses. A rapid transient action was found for kanamycin. Ampicillin showed a similar effect, whereby the filamentation process overlapped with the formation of a bulged morphology and cell lysis. However, unlike kanamycin, this superposition produced a two-step loss of motility which we evidenced by the motility distributions increasing their bimodal nature. Trimethoprim produced instead a more monotonic behaviour, with a slow and gradual decrease in motility and a steady conversion of sub-populations from high to low motility. This process was not completed by the end of the experiment.

An alternative visualisation of the same data set is provided in Figure 83, which highlights the diverse action of the three antibiotics and directly compares them on the same graph. The curves are grouped by susceptibility and resistance, while different colours refer to the antibiotics (green, red and blue for kanamycin, ampicillin and trimethoprim, respectively). By comparing the two rows, the different behaviour of the susceptible and resistant bacteria is apparent.

Besides the insightful investigation of drug action, the combined detection of motility and morphology allowed us to select the most suitable parameter to detect differences between the susceptible and the resistant strains. While kanamycin had an immediate and marked effect on motility, it did not produce any differentiating effect in terms of morphology, since both strains shrunk upon the action of antibiotic. Similarly, the length signature of

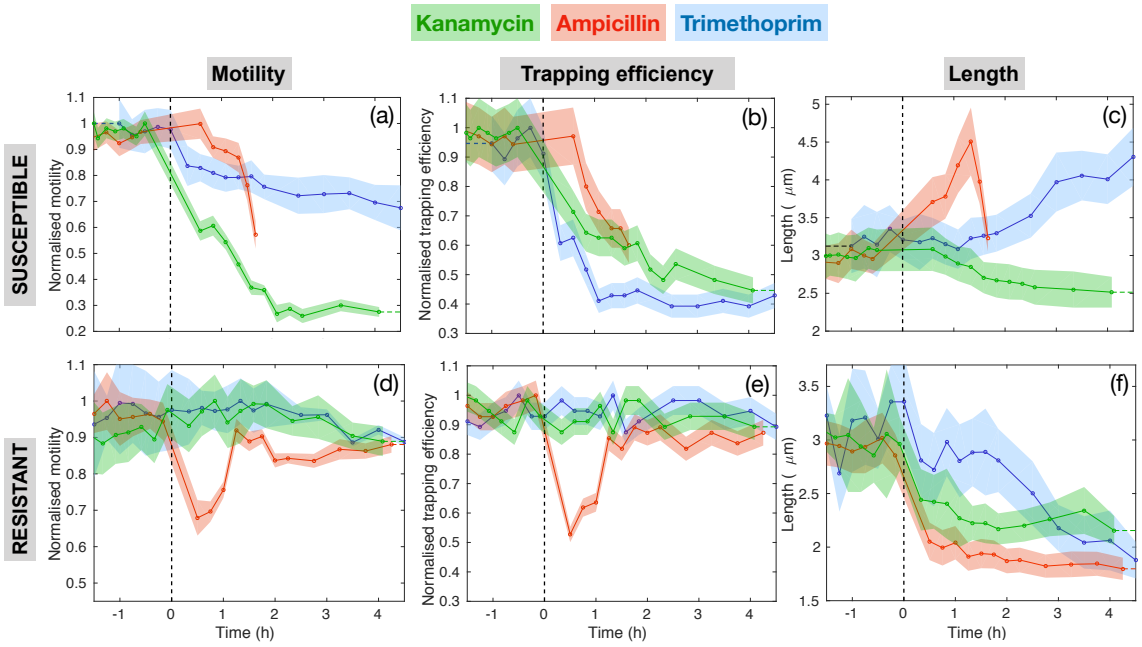

Figure 83. Motility (panels (a) and (d)), trapping efficiency (panels (d) and (e)) and length (panels (c) and (f)) for the susceptible wild type MG1655 (top row) and resistant E. coli (bottom row) exposed to 10 μg/ml of kanamycin (green curves), ampicillin (red curves) or trimethoprim (blue curves). The graphs illustrate the different effects of antibiotics on E. coli by highlighting the different temporal dynamics for suppression of motility and changes in cell length.

trimethoprim is not clearly distinguished until about 2 hours after exposure to the drugs, whereas motility provides a clearer discrimination starting immediately after exposure. Conversely, we found morphology to be the best indicator of susceptibility to ampicillin. In this case, the pronounced filamentation of the susceptible strain gave a clear distinction relative to the shrinking resistant strain. In contrast, motility could produce ambiguity until the resistant strain recovered after 1.5 hours of exposure. These considerations demonstrate how the simultaneous assessment of multiple parameters is advantageous for classification and how it provides a richness of information that would be otherwise lost in a single-parameter experiment.

The analysis also offers useful cues to probe the mode of action of the tested antibiotics. In particular, kanamycin revealed a more direct effect on the motility mechanism compared to ampicillin and trimethoprim. This suggests that kanamycin is closely involved with the biochemical pathways regulating motility in *E. coli*. Flagella are indeed very complex macromolecular machines. Their synthesis and activation are energetically costly and require the tight regulation of several biochemical pathways [193,194]. It is likely that kanamycin directly interferes with some of these regulatory mechanisms, resulting in less translation of motility genes. The results suggest that the timescale of the induced mis-regulation is of the order of 40 minutes or less.

This temporal estimate agrees satisfactorily with existing findings in the literature. More specifically, the uptake of aminoglycoside antibiotics is known to occur via three phases [195]: (i) a contact phase during which the antibiotic molecules almost immediately attach to the bacterial outer membrane via ionic binding, (ii) an energy-dependent process (EDP-I) which results in a slower lagged accumulation of drug's molecules within the cell wall, and (iii) a final enhanced accumulation phase (EDP-II) in which the concentration of the aminoglycoside molecules inside the cytoplasm becomes comparable to that in the surrounding medium. It is not until the EDP-II phase that misreading and consequent cell killing are initiated [195,196]. For instance, Bryan *et al.* [197] observed a 30-minute lag on the uptake of streptomycin (10 μg/ml) by *E. coli* K12 SA1306, while Hurwitz *et al*. [198] revealed a 60 minutes lag for 2 μg/ml of dihydrostreptomycin administered to *E. coli* B cells.

The other factor that should be considered to validate the observed lag time is the rate of motility decrease induced by the misreading of the RNA. No direct connection between the action of aminoglycosides and the flagellar motor deactivation could be found in the literature. However, the timescale of this process can be estimated from similar experiments where motility was artificially and reversibly hampered by different compounds. For example, Ridgway [199] inhibited the motility of *F. Polymorphus* ATCC 27820 by exposing cultures to carbonyl cyanide-m-chlorophenylhydrazone (CCCP) at different concentrations. A decrease of the rate of gliding was observed consistently after 3 to 15 minutes of exposure to CCCP. A similar timescale was observed for the flagellar motility of *E. coli* K12 B14 upon administration of the same compound [200].

Hence, it can be concluded that the 40-minute observation reported here is consistent with reports from the relevant literature.

In contrast, the findings for ampicillin and trimethoprim suggest that the observed motility reduction was mainly due to morphological changes. Despite ampicillin having been reported to interfere with the transcription of motility genes [118], the impact on bacteria shape appears to be more significant, since bulged bacteria were severely impaired in their swimming action. In fact, the first steady lengthening of cells resulted in a smooth decrease of motility, unlike the steep decrease with kanamycin, where cells slightly shrunk. Trimethoprim induced a similar behaviour to the susceptible case, except for the lack of a bulged morphology, which caused the smooth decrease in motility to prolong in time.

Our findings not only enabled a correct classification of susceptible and resistant *E. coli* strains, but also provided insight into the antibiotic's mode of action and rate of inhibition. More importantly, the single-cell capability afforded a more rapid detection compared to bulk experiments. The reason for this rapid detection ability is twofold:

- Any effect of drugs on motility and morphology was picked up on the biological timescale of the antibiotics' action. By examining individual bacteria, any change is detected as early as it takes place. While in a bulk experiment such a change would be masked by the averaging procedure, here the averaging is carried out after the actual readout. Furthermore, by analysing hundreds of bacteria rather than billions, the averaging procedure is less prone to concealing any changes experienced by a single bacterium, since any given individual is weighted more in the calculation of mean values.
- The two phenotypic parameters we assessed, motility and morphology, were affected by the antibiotic action on a shorter timescale compared to cell division. Additionally, for different drugs, we were able to pick the parameter that gave the most evident change in order to minimise the classification time.

12.4. Resazurin microdilution assay

In order to further validate our findings, we conducted additional control experiments that correspond to the traditional definition of susceptibility and resistance, i.e. an antibiotic administered at a certain concentration is effective if it inhibits bacterial growth.

Typically, this is achieved by the disk diffusion test, known as the Kirby-Bauer diffusion method [201], a schematic of which is shown in Figure 84. Bacterial cultures are grown uniformly over an agar plate on top of which antibiotic-impregnated paper-filter disks are placed. The antibiotics diffuse radially from the disks, thereby exposing bacteria to decreasing concentrations of the drugs. Consequently, susceptible bacteria in the proximity of the disk will not grow, up to a distance where the concentration of the antibiotic is high enough to inhibit cell growth. This defines the zones of inhibition, which appear as a clear ring surrounding the antibiotic disks, as shown by the picture on the right-hand side of Figure 84.

Bacteria are classified as susceptible, moderately susceptible or resistant by comparing the size of the inhibition zone to a database of zone standards. Hence, this method is semi-quantitative, and it does not provide an accurate value of the minimum inhibitory

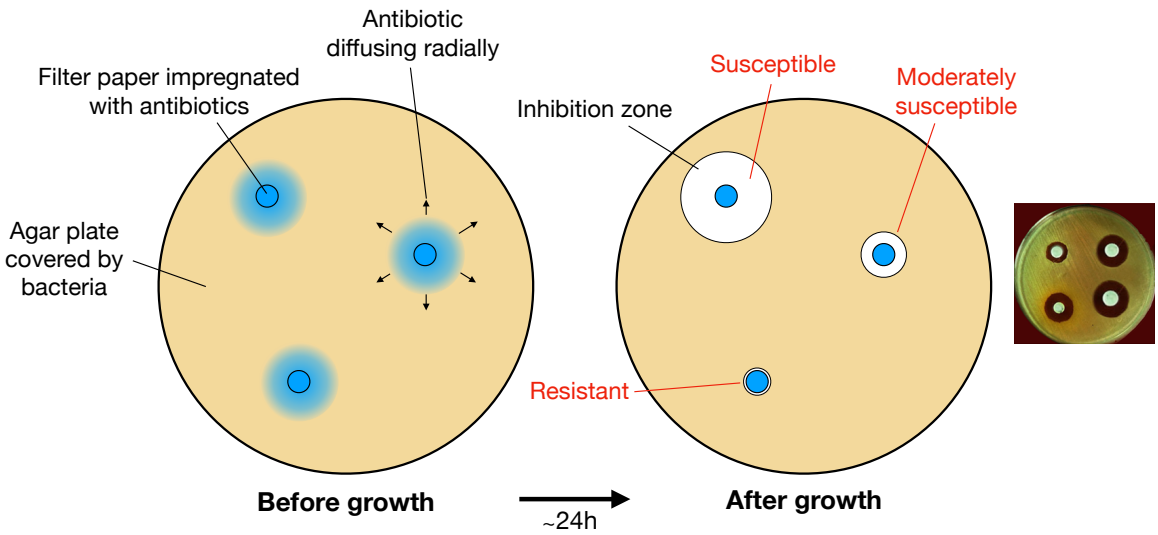

Figure 84. Schematic illustration of the Kirby-Bauer disk-diffusion antimicrobial susceptibility test. Bacterial colonies are spread uniformly onto an agar plate. Disks impregnated with different antibiotics are placed on the plate, which cause drugs to diffuse radially and expose underlying bacteria to a concentration gradient of drug. Susceptibility is determined by the size of the inhibition zones surrounding the disk, as seen in the photo on the right-hand side.

concentration (MIC) for the antibiotic, yet because it is relatively easy to perform and reasonably reliable, it is still widely used in clinical practice.

A more robust method is instead provided by microdilution assays [202]. Microdilution tests are typically conducted using 96-well plates, whereby bacterial inoculums are added to each well and incubated overnight with two-fold dilutions of antibiotics. Bacterial growth is quantified by measuring the optical density of the solution, typically at a wavelength of 650 nm, as we did to quantify the growth of the resistant-engineered *E. coli* strains (see sub-section 12.3.1). A clear solution is indicative of no growth and it results in low optical density values. Conversely, if bacteria divide, they scatter more light, thereby making the solution opaque, resulting in lower transmittance observed as higher optical density values. The lowest concentration of antibiotic that produces a clear solution is determined to be the MIC.

Traditional microdilution methods fail, however, if the antibiotic induces bacteria clumping or filamentation, which we have observed, for example, in the case of trimethoprim. In these cases, increased solution turbidity is not necessarily indicative of resistance, since filamented bacteria still increase the optical density of the solution despite cell division being inhibited. An alternative solution to address such a potential misjudgement is represented by the addition of a viability reporter dye, like resazurin.

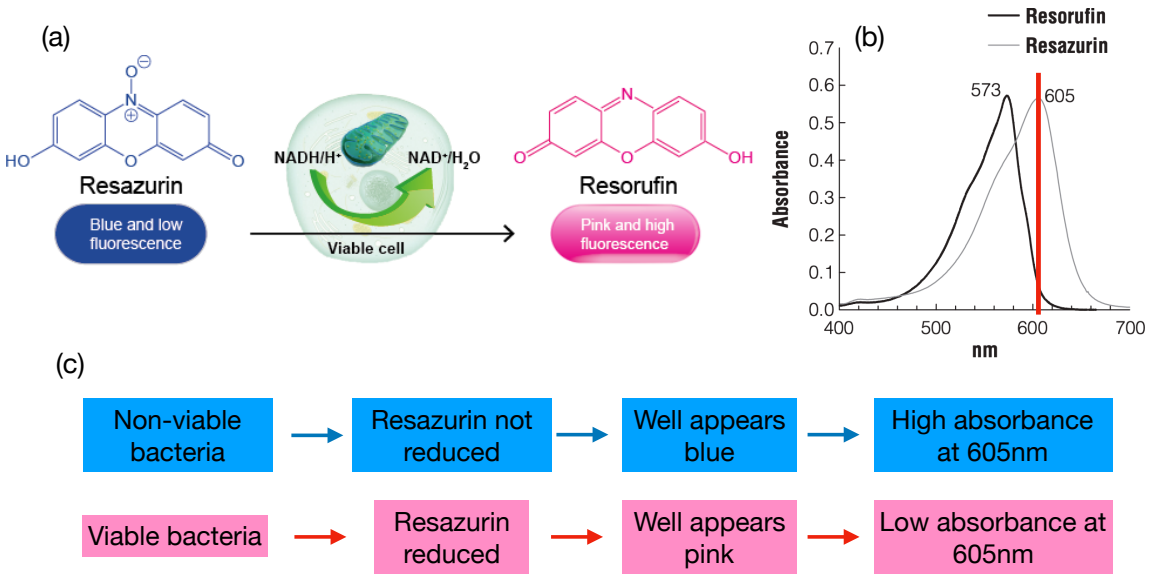

Figure 85. The use of resazurin as a viability dye. (a) Viable bacteria pick up resazurin and reduce it to resorufin. Resazurin appears blue and has low fluorescence, while resorufin becomes pink and fluoresces more efficiently. (b) Different absorption spectra of the two dyes. In particular, the resorufin absorbance peaks at 605 nm. (c) Diagram of bacterial viability and its relation to the colour and absorbance of the fluorescent dye.

Resazurin is a weakly fluorescent blue dye that can assess bacterial viability. Viable bacteria with active metabolism take up resazurin and reduce it to resorufin. Conversely, non-viable or dead organisms are not able to do so, as schematically shown in Figure 85(a) and described by the diagram in Figure 85(c). Crucially, resazurin and resorufin feature different absorbance and emission wavelengths, thereby making it possible to distinguish viability by visual inspection. In particular, resazurin emits weakly in the blue region at 605 nm, while resorufin appears pink, emitting at 573 nm, as the spectra in Figure 85(b) illustrate [203,204].

Hence, the degree of reduction to resorufin can be quantified by measuring the optical absorbance of the solution at 605 nm. Unlike a simple optical density measurement, here the degree of absorbance is directly correlated to the metabolic activity of bacteria and not just to their physical ability to scatter light.

Figure 86 shows a picture of a typical plate used to test the susceptibility of the wild type *E. coli* MG1655 to ampicillin, kanamycin and trimethoprim. The picture was taken at the end of the experiment, i.e. after the introduction of resazurin following overnight incubation with antibiotics. The concentration of the three antibiotics increases along the columns, whereas rows correspond to different antibiotics. We tested each drug in duplicate, as indicated by the labels on the left-hand side.

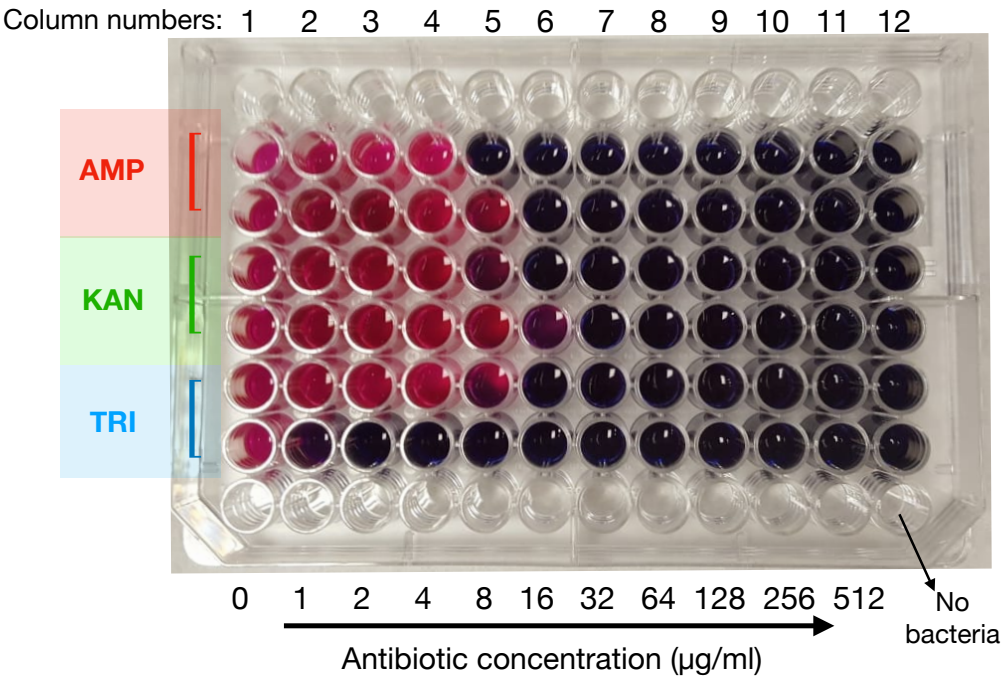

Figure 86. Picture of a 96-well plate used to quantify the susceptibility of the wild type E. coli to ampicillin (red label on the left), kanamycin (green) and trimethoprim (light blue). The concentration of antibiotics is increased in columns 2 to 11, while columns 1 and 12 represent no drug and no bacteria control wells, respectively. Pink wells are indicative of viable bacteria, while dark blue ones contain dead E. coli.

In particular, we diluted ampicillin, kanamycin and trimethoprim from stock solutions into MH broth at 1024 µg/ml. Column 1 of the plates were used as a no antibiotic control, columns 2-11 contained two-fold increase of antibiotic concentration from 1 to 512 µg/ml and column 12 was filled with blank MH broth as a sterility control. For the antibiotic serial dilution, we first added 50 µl of the 1024 µg/ml antibiotics to the 512 µg/ml column, mixed well using a multichannel pipette before transferring to the next well and repeated to give a final concentration of 1 µg/ml in column 2.

Wild type *E. coli* MG1655 and the three transformed strains were grown overnight in LB broth with appropriate antibiotics for plasmid selection. Cells were washed three times in MH then re-suspended in MH or LB before being diluted to an OD of 0.1 to give standardised suspension of 10^8 cfu/ml. We diluted the standardised suspension 1:100 and then added 50 µl to each well to give a final bacteria concentration of $5.5*10^5$ cfu/ml, as per standard conditions of microdilution assays. 50 µl of MH was added to each well in column 12 to give 100 µl of solution in all wells. After an overnight incubation at 37 °C with no shaking, we introduced 30 µl of 0.015% (w/v) solution of resazurin in MH in each well and incubated for 4 hours. These procedures were carried out by Stephen Thorpe from the Department of Biology at the University of York.

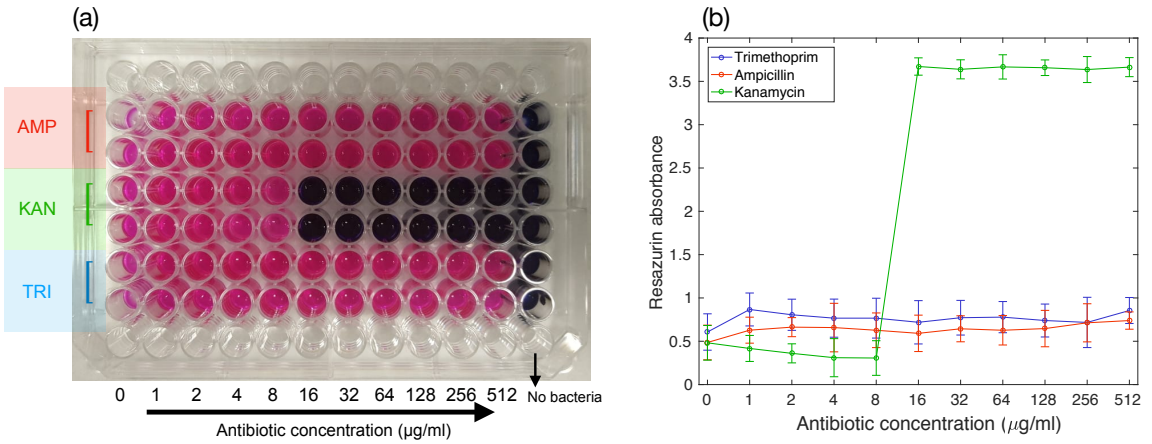

Figure 87. Resazurin microdilution assay for trimethoprim and ampicillin resistant E. coli MG1655. (a) Picture of the 96-well plate used to test trimethoprim and ampicillin resistant E. coli. Pink wells at all concentrations of trimethoprim and ampicillin (bottom and top pair of rows) indicate that resistance was successfully acquired. The two middle rows show a change in colour for values larger than 8 µg/ml, which corresponds to the MIC for kanamycin. This behaviour is reflected in the measured absorbance values at 605 nm shown in (b), whereby low absorbance corresponds to pink wells. Error bars denote the standard error over 4 replicates (2 rows for each antibiotic in 2 independent replicates).

Results were initially validated by visual inspection and then by measuring the optical absorbance of each well at 605 nm. High levels of absorbance at 605 nm imply that the resazurin was not reduced to resorufin, meaning that bacteria were not viable, and the corresponding inoculum appears dark blue/purple. Conversely, if bacteria were still viable, resazurin was reduced to resorufin, resulting in low absorbance at 605 nm and in a pink solution.

Figure 87(a) shows a picture of the plate used for testing trimethoprim resistant *E. coli*, while Figure 87(b) illustrates the measured values of absorbance from the different wells for an increasing concentration of antibiotics. Recall that for the trimethoprim-resistant experiment, we generated a strain that was also resistant to ampicillin, since the plasmid vector contained the *ampR* and *dfrA* genes. The absorbance from the trimethoprim and ampicillin rows (blue and red curves in Figure 87(b)) remained low for all concentrations, which agrees with the wells appearing pink. This observation implies that bacteria survived the exposure to antibiotics. However, the kanamycin curve shows a breakpoint at 8 µg/ml, meaning that concentrations higher than this value caused the wells to become blue. This is indicative of kanamycin making the culture non-viable.

Therefore, both visual inspection of the wells and the values of absorbance at 605 nm confirm that resistance to >512 µg/ml trimethoprim and ampicillin was successfully conferred to the stains, while they remained susceptible to >8 µg/ml of kanamycin.

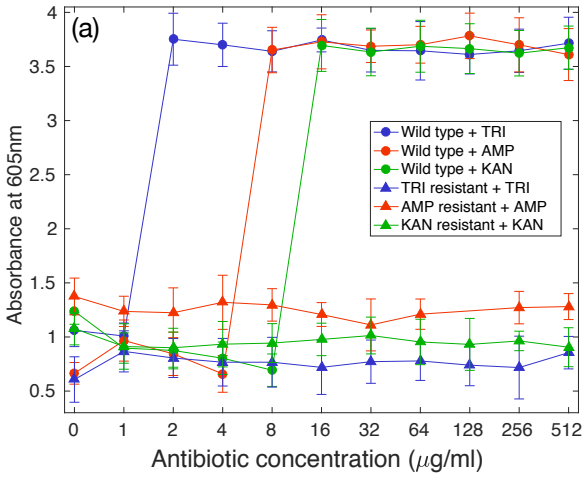

(b)

MIC values (μg/ml)

	AMP	KAN	TRI
Wild type	4-8	8-16	1-2
Resistant	> 512	> 512	>512

Figure 88. Summary of absorbance results and MIC values for susceptible and resistant E. coli exposed to the corresponding antibiotic. (a) Absorbance curves for the wild type E. coli MG1655 (circle markers) exposed to increasing concentrations of trimethoprim (blue), ampicillin (red) or kanamycin (green). These curves show breakpoints corresponding to the MIC values. Genetically engineered E. coli exposed to the corresponding antibiotic (triangular markers, same colour scheme) maintain low values of absorbance, thereby confirming that resistance was acquired. (b) Table of measured MIC ranges obtained from visual inspections of each 96-well plate and the absorbance curves in (a). Error bars in panel (a) represent the standard error over 4 replicates (2 rows for each antibiotic carried out in 2 independent replicates).

We repeated the same test for all resistant strains and the wild type *E. coli*. Figure 88(a) shows the absorbance curves measured in each case. Curves with round markers refer to the wild type *E. coli* MG1655 exposed to trimethoprim (blue curve), ampicillin (red curve) and kanamycin (green curve). The step transition to high absorbance values quantifies the MIC ranges for each drug, which are reported in the table in Figure 88(b). Triangular markers refer to the resistant strains in the corresponding antibiotic (same colour scheme as above) and revealed that bacteria transformation was successful in every case.

While the bacterial count performed inside the micro channel already suggested the inhibition of growth, the standard microdilution assay allowed us to quantify the MIC values. Specifically, we could establish that we operated at or near the MIC values for kanamycin, and at a few times the MIC range for ampicillin and trimethoprim (recall that 10 μg/ml were administered in all trapping experiments). This observation is significant because it confirms that the motility-morphology signature is sufficiently sensitive to be detected at clinically-relevant concentrations on the short timescale we have extensively discussed. More importantly, these findings allowed us to establish that the combined motility and morphology signatures are valid indicators of susceptibility and resistance of *E. coli* to the tested antibiotics.

13. Conclusions and future perspectives

In this chapter of the thesis, I have discussed all the aspects relating to the microfluidic trapping assay, starting from the theoretical background of fluid flow in a micro channel and its simulation, to its fabrication, optimisation and application to the trapping of single bacteria for susceptibility testing. The main outcomes of this chapter are outlined as follows:

- Microfluidics is powerful. Its application to microbiology has led to an unprecedented understanding of cells and bacterial behaviour. The possibility of manipulating and exposing cells to a specific micro-environment has opened up a vast set of opportunities which have been exploited to tap into fundamental biological questions as well as to tackle real problems.
- Studying single bacteria in a microfluidic device is challenging but it allows challenging biological questions to be tackled for a better understanding of the bacterial world. Single bacteria analysis is crucial to study population heterogeneity and to unveil underlying distributions of relevant biological properties. Such distributions need to be considered for an insightful understanding of the bacterial behaviour and for the success of a treatment.
- Antimicrobial resistance is a significant threat to the healthcare system as we know it, and it needs to be tackled now. The development of new drugs is not able to keep up with bacterial evolution. Hence, a more targeted use of existing antibiotic is needed. Microfluidics can help us manage the level of antibiotic resistance by combining the exquisite control over fluid handling with the quest for alternative signatures of susceptibility. Novel microfluidic diagnostic tools will be able to speed up the identification of the correct antibiotic compared to traditional bulk growth-based methods. The literature in the field is indeed very rich, which proves the significant interest of the scientific community.
- Hydrodynamic trapping is a promising technique that allows isolating individual bacteria and probing them over time. The method allows arrays of single bacteria to be created and held in place while ensuring medium recirculation and removal of daughter cells. Unlike isolation techniques such as hydrogel immobilisation, hydrodynamic trapping permits a degree of bacterial motion, which I have shown is a valuable alternative indicator of susceptibility. At the same time, external stress on the cell is minimised compared to optical or acoustic trapping. The need for

tethering agents such as antibodies is also eliminated, which simplifies device preparation and increases applicability.

- I implemented a multiparameter approach for assessing the susceptibility of trapped bacteria by analysing motility and morphology at the single bacteria level. I showed that effective antibiotics against susceptible *E. coli* affect their motility and morphology on timescales notably shorter than traditional growth-based assays. Additionally, the single cell capability afforded an insightful study of the heterogeneity typical of bacterial populations, as well as the diversity of the antibiotics action. I revealed the presence of sub-populations of different motility and studied their switching from high to low motility following exposure to different antibiotics. Combining this information with the morphology signatures provided insights into how different antibiotics affect the motility pathways of susceptible organisms.
- Finally, our findings correlated positively to the standard growth-based definition of susceptibility by counting the number of bacteria during our experiments and looking at their response to antibiotic treatments. Additionally, standard microdilution assays were conducted to quantify the MIC and verify that: a) trapping experiments were operating in the susceptibility range for the selected *E. coli* strain, and b) resistance was successfully acquired by the genetically-engineered bacteria.

The two main limitations of the hydrodynamic trapping approach stem from the very nature of the trapping mechanisms, namely the need for bacteria to cross streamlines to enter a trap.

Firstly, this mechanism restricts its applicability to motile strains because: a) they are more likely to enter a trap, thereby allowing for statistically-significant analysis and b) it is obviously not possible to exploit motility as a signature of susceptibility if viable bacteria are already non-motile. Nevertheless, motile bacteria are responsible for a large variety of infections, such as urinary tract infections (UTIs) and motility plays a fundamental role in the early-colonisation of surfaces, chemotaxis and in the growth and proliferation of biofilms. These arguments make the study of motility very relevant and applicable to a variety of susceptibility testing scenarios, especially considering the rapidity of the readout that was demonstrated here. As an addition, a more complete characterisation of the bacterial motility could be performed by examining the behaviour of flagellar knock-out strains in order to quantify the contribution of non-flagellar motility mechanisms.

Reversible inactivators of bacterial motility, such as CCCP, could also be employed as a further extension and control groups.

Secondly, even for motile organisms, the assay suffers from relatively poor trapping efficiency, as extensively discussed in the design section. This aspect would limit its extension to clinical samples, where the threshold for early identification of infections is typically much lower than the 10^7 cfu/ml that I examined in this thesis. A lower concentration of bacteria would clearly result in prolonged time needed for trapping of a significant number of individuals, thereby hindering the statistical relevance of the analysis.

Hence, future developments would involve the integration of an on-chip pre-concentration step exploiting, for instance, electrophoretic forces or deterministic lateral displacement (DLD) assays. Alternatively, a recirculation circuitry could be implemented to repeatedly flush the same bacterial solution through the trapping array. As another option, we could employ an automated system that would continuously scan across different regions of the channel looking for trapped bacteria, thereby increasing the number of analysed traps. However, this would increase complexity. Finally, as a further future addition, we could envisage a chip with several channels in order to test multiple antibiotics in parallel, potentially at different concentrations in order to also quantify the MIC on chip. Such a multi-channel device could also include tapered trap's geometries in order to exploit the size selectivity of the micro-well structure and analyse bacteria of different shapes and at different stages of growth within their life cycle.

More generally, the assay offers a unique platform for single bacterial cell analysis over time. Its applications could move beyond susceptibility testing and be applied, for instance, to evolutionary studies or bacterial communication assays. The platform can also be integrated with other techniques to probe single cell properties, such as fluorescence, electrical assays (see next chapter of the thesis) or Raman spectroscopy. Only by combining a number of different techniques and information from different domains can we really deepen our knowledge of the bacterial world and hope to win the race against antimicrobial resistance.

IV. Electrical impedance spectroscopy (EIS) for single cell analysis

This chapter of the thesis focusses on the application of electrical impedance spectroscopy (EIS) to the study of single bacteria. I will begin by giving a general introduction of EIS and its applications through a literature review and a brief summary of the theory of AC circuits. Then, I will discuss COMSOL simulations of different EIS configurations for probing the electrical properties of single Gram-negative bacteria, followed by a description of the experimental methods used to fabricate and characterise the electrical assay. Finally, I will present some preliminary experimental results to validate the fabricated devices, which provide the basis for future bacterial studies. A final summary and general remarks will be given in the last chapter. More specifically:

- Sections 1 and 2 contain an introduction to EIS and its recent applications to biologically-relevant studies in a brief literature review. I will particularly focus on assays relying on the electrical analysis of individual trapped cells over time as opposed to flow cytometry configurations, whereby only momentary properties of moving cells are measured.
- Section 3 examines the basic theory of AC circuits. I will analyse the response of individual circuit elements (i.e. resistors, capacitors and inductors) to a sinusoidal voltage signal as well as the behaviour of a Resistance-Capacitance (RC) parallel configuration, since it is a commonly used combination for modelling the electrical response of single cells.
- COMSOL simulations of increasingly complex geometries are presented in section 4. I will first simulate a three-shell single bacterium between two co-planar electrodes on a glass substrate, then place two insulating SU8 wells above the metal pads and finally move on to the real geometry of the trapping assay presented in chapter III of the thesis.
- I will detail the fabrication and measurement techniques in section 5, including a description of the metal lift-off process, SU8 coverage of the electrode tracks and the fabrication of the trapping wells above. I will also discuss issues related to electrical interfacing and the approach I adopted to solve them.
- Section 6 discusses preliminary experimental results obtained with the electrical assay. In particular, I will present measurements of salt solutions at different

concentrations and the formation of a self-assembled monolayer on the gold electrodes.

- Section 7 provides final summary, remarks and expected future development to allow the detection and analysis of individual trapped bacteria.

1. Introduction

Electrical impedance spectroscopy (EIS) is an electrical method with a number of different applications ranging from the study of surface corrosion and batteries to photovoltaic systems and biological assays [205–207]. The main aim of the technique is to study the electrical impedance of a system subjected to a sinusoidal voltage signal. A significant amount of information can be obtained by sweeping the applied frequency, since the response of electrical components in an AC circuit depends on frequency.

The aim of this chapter of the thesis is the integration of EIS measurements with the single bacteria trapping platform presented in chapter III. One of the take-home messages of chapter III was the importance of a multiparameter approach to the study of bacteria susceptibility to antibiotics. Hence the idea to include an electrical signature to the motility-morphology assay, which could complement the information retrieved from those two domains, possibly provide a faster signature of susceptibility and increase the confidence in the detection.

The choice of EIS is motivated by the fact that the technique is particularly suitable to probing the dielectric properties of cells, tissues and bacteria [208]. Microorganisms live in liquid environments and their life cycle relies heavily on interactions with the surroundings. Since the metabolic activity of bacteria entails the exchange of ions and the reduction or oxidation of compounds from the surrounding medium, EIS is a suitable candidate for probing bacteria viability [209–211]. In particular, EIS has already been shown to provide valuable indicators of cell status in a number of different contexts, as I will detail in the next chapter.

2. EIS for single cells: a brief review

The use of electrical properties to characterise biological samples dates back to 1899, when Stewart linked the presence and growth of bacteria in a solution to its conductivity by measuring the solution's freezing point [209]. Since then, a vast number of electrical assays and applications have been demonstrated and applied to the study of biological systems, as reviewed in [206,212,213]. In the context of this thesis, I will mainly focus on Electrical impedance spectroscopy (EIS) for the analysis of eukaryotic and bacterial cells.

EIS relies on including biological bodies as elements of an AC electrical circuit and on using the electrical impedance as a readout. If the circuit is designed properly, its impedance will be sensitive to the presence, shape and electrical properties of the cells. However, similarly to traditional microbiology being conducted with tubes and plates at the colony level, conventional EIS used millimetre-sized electrodes to probe entire cell populations, thereby obtaining a bulk average measurement. More recently, the field has increasingly moved towards the analysis of individual cells by leveraging on the significant advances offered by microfabrication techniques. In a typical micro-EIS (μ-EIS) assay, micron-sized electrodes are fabricated to match their size to that of a single cell. The aim is to maximise the overlap between the electric field lines and the cell, thereby increasing sensitivity.

The motivations that have fuelled these developments are the same as in the previous two chapters of this thesis. Overall, there is a significant interest in studying single cell properties in order to: a) gain deeper insight into biological mechanisms that drive a cell's behaviour, b) probe population heterogeneity in order to unveil relevant distributions and, c) speed up the analysis through the ability to detect changes on a biological timescale [83,214,215].

The development of single-cell μ-EIS was also underpinned by the rapid progress of microfluidics, which offers tools and methods to manipulate single cells, their local environment and their spatial distribution. In particular, these abilities allow us to direct or place single cells in the proximity of electrical contacts integrated within micro-channels. The aim is to expose the cell to the electric field being generated between two (or more) electrodes and to analyse the changes induced to the impedance of the circuit.

Here, I will divide EIS techniques into two main classes depending on exposure time to the electric field. Static techniques localise individuals in proximity of the contacts, hence the properties of the same cell are retrieved over time. In contrast, in flow cytometry assays, a solution is flown through the contacts, such that single cells only pass through the electric field and produce a signature during their transit which is localised in time.

2.1. Static measurements

The first category of techniques relies on analysing electrical properties of single cells over time. For this purpose, cells need to be held at the same location. In the previous chapter

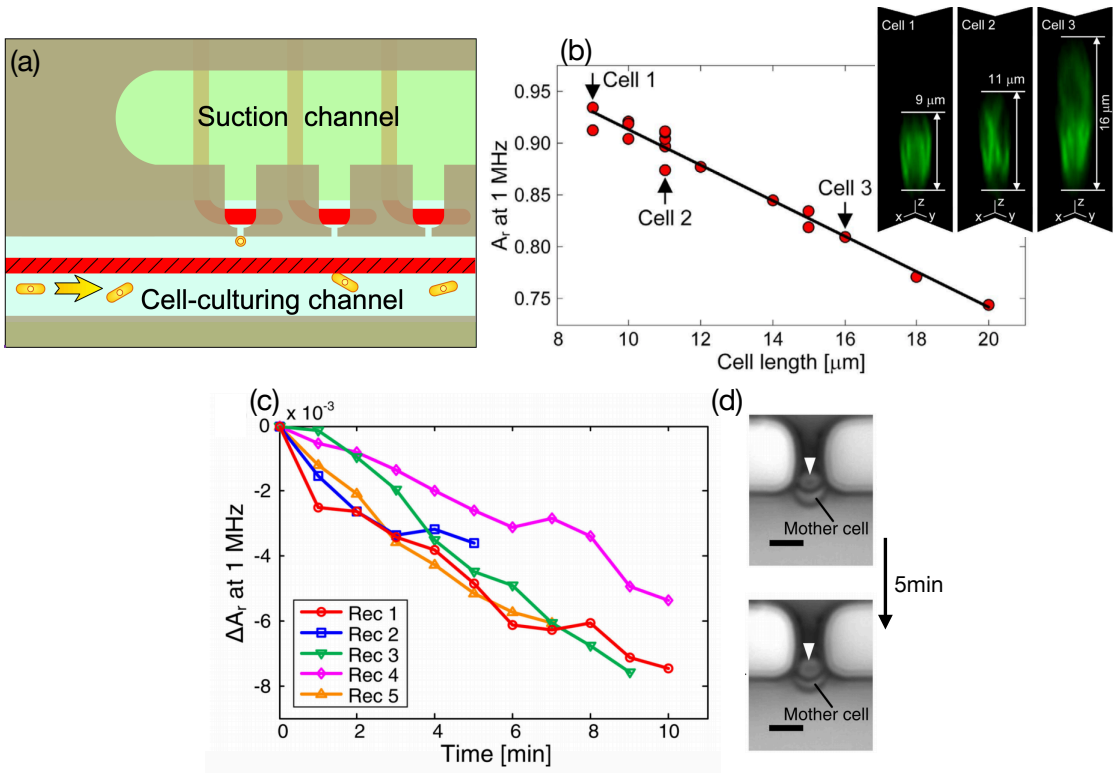

Figure 89. Examples of EIS assays for electrically monitoring single yeast cells over time. (a) Top view of the µ-EIS trapping assay proposed by Zhu et al. [216] for the impedance analysis of single S. pombe cells. Cells are driven towards small apertures by applying a negative pressure to the suction channel and their electrical properties are monitored by biasing the electrodes placed underneath the trapping locations. (b) illustrates the link between the cell length and the amplitude of the measured impedance at 1 MHz, as verified by the confocal fluorescence microscopy images shown in the inset. (c) Decrease of the impedance amplitude over time as the bud of single yeast cells increases in size. The difference in signal is high enough to detect the growing bud. (d) Optical micrographs of a single trapped yeast cell about to divide, showing that the growth of the bud is difficult to recognise and quantify [217]. Scale bar: 5µm.

of the thesis, I discussed trapping techniques for retaining single cells (chapter III, section 5). In particular, I emphasised lateral hydrodynamic trapping methods where the cells are retained either in microwells or in apertures smaller than their size. In the context of electrical measurement, these trapping assays can precisely hold the cell where the electric field is generated by the electrodes. Typically, planar electrodes are realised on a glass substrate as a first step, then the trapping structures are fabricated above the metal tracks.

An exemplary application of this approach was recently proposed by Zhu *et al.* [216], who implemented pressure-driven trapping for *Schizosaccharomyces pombe* cells (*S. pombe,* which are rod-shaped yeast cells of 7-14 µm length). Single cells were trapped in small apertures below which gold electrodes had been previously fabricated, as illustrated by the top view of the device in Figure 89(a). Trapping was achieved by designing a suction channel which actively drove single cells towards the orifices. Once captured, an AC voltage was established between the two electrodes in red. By monitoring the time

evolution of the impedance amplitude and phase, the platform provided an electrical readout of developmental changes during the cell cycle, such as elongation, division and cytokinesis. The interpretation of the electrical signatures was aided by observation through a microscope together with fluorescent labelling, which confirmed the different phases that *S. pombe* was undergoing. For instance, Figure 89(b) shows how the amplitude of the impedance was linked to the length of the cell, as confirmed by the confocal scans shown in the inset. Notably, the assay was proven able to be sensitive enough to detect length changes as small as 250 nm.

The same authors also applied the technique to monitor the bud growth in *Saccharomyces cerevisiae* yeast cells, which is often difficult to quantify with standard microscopy at sufficient temporal resolution [217]. The EIS techniques showed instead sufficiently high sensitivity to detect yeast cells of different shapes as well as the early phases of bud formation prior to cell division. For instance, while the bud growth over 5 minutes was hardly measurable from microscopy images (Figure 89(d)), the amplitude of the impedance allowed the authors to clearly detect the increased size of the bud (Figure 89(c), where Rec. refer to records performed on different trapped yeast cells.)

The integration of micro-dam structures for trapping with μ-EIS was also reported for single eukaryotic cells. Malleo *et al.* [218] proposed a design where SU8 wells were fabricated on top of gold metal tracks, which acted as recording electrodes. The device was closed with an ITO-covered glass slide to provide sealing and a stimulus electrode at the same time. Interestingly, each trap was paired to a second one facing against the flow direction, so that a reference empty trap was always present in the vicinity of every trapped cell. Figure 90(a) shows an optical micrograph of the fabricated device, while Figure 90(b) depicts a cross section of a pair of traps. Single HeLa cells were trapped, and their electrical properties monitored over time. In particular, the authors investigated the effect of different concentrations of Tween, a surfactant typically used to lyse mammalian cells. By looking at the time-dependant decrease of impedance at 300 kHz, the results revealed the dynamics of the induced membrane depolarisation, ultimately leading to cell lysis.

As a final example, I will discuss the work of Asphahani *et al*.[219] since it points out and quantifies the importance of matching the size of the electrodes to that of the cells. In this case, the immobilisation of U87MG human glioblastoma cells onto circular electrodes was achieved by functionalising the gold surface. Electrodes of different sizes were included in each device, as shown in Figure 90(c), in order to probe the difference between a large

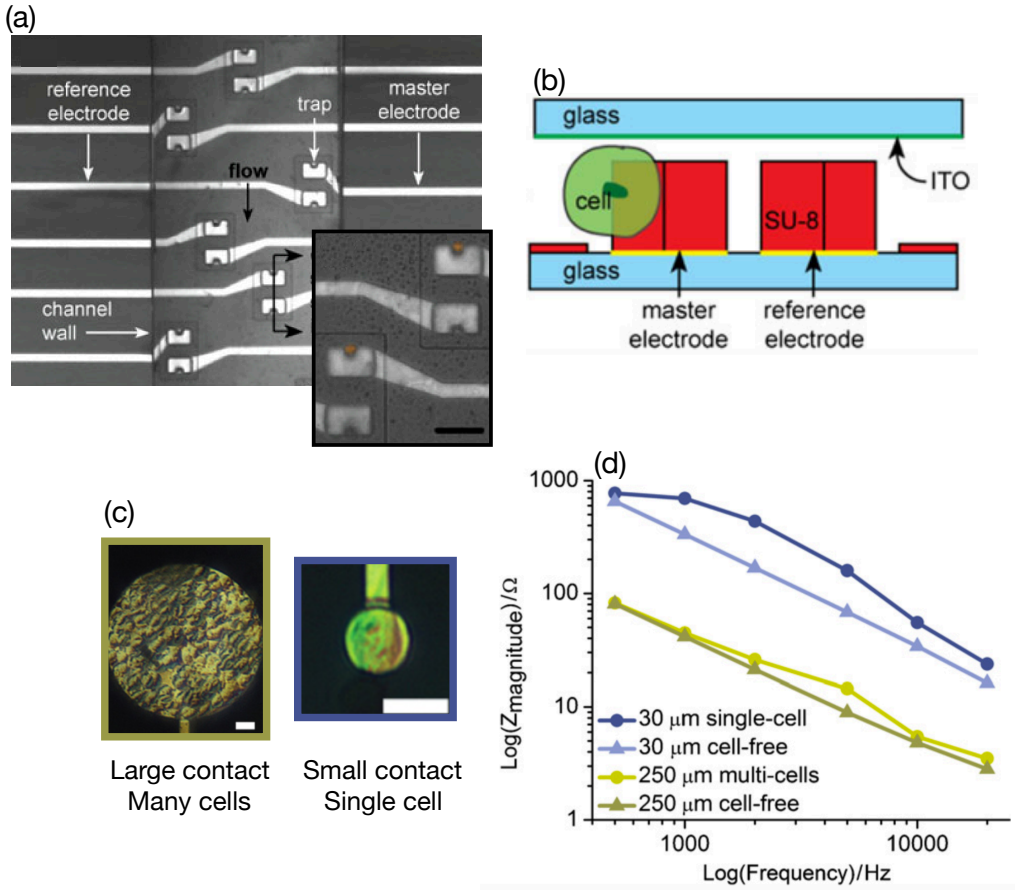

Figure 90. Examples of EIS assays integrated with lateral hydrodynamic trapping. (a) Top view of the device studied by Malleo et al. [218]. Metal electrodes are fabricated below hydrodynamic traps and enclosed in a glass microfluidic device. Each trap is paired with a second one facing against the flow. The inset illustrates two traps filled with microbeads. Scale bar is 30 µm. (b) Cross sectional view of a pair of traps, showing the electrodes below the SU8 and the ITO-covered glass seal which provides a stimulus electrode. (c) Optical micrographs of a large (250 µm) gold electrode covered by cells, as opposed to a small (30 µm) electrode covered by a single cell from the work of Asphahani et al. [219]. Both scale bars are 30 µm. (d) Impedance spectra for the two geometries. The change in impedance due to the presence of cells is more evident for the small electrode covered by a single cell (light vs dark blue curves).

contact (250 µm) entirely covered by cells and a smaller contact (30 µm) hosting instead a single cell. Figure 90(d) shows typical impedance spectra measured for both cases and for bare and covered contacts. The spectra clearly show that changes in impedance were more significant (by a factor 3) for a small contact covered by a single cell (blue curves). This finding represents a model example to show how single cell analysis with matched electrode size enhances the detected signal by enabling higher sensitivity.

2.2. EIS flow cytometry

Flow cell cytometry is a well-known and established technique for the study of single cells. The method allows one to count cells while analysing their size, morphology or the

presence of specific proteins or markers, typically achieved by fluorescent labelling. The main idea of cytometry is to rapidly flow cells across a detection area illuminated by a fixed light beam. For this purpose, a fluidic system is integrated to focus cells uniformly through the centre of the light beam, typically by hydrodynamic or acoustic focussing. The light scattered by each passing cell is detected and its characteristics are linked to the cell properties. For instance, the amount of forward-scattered light is proportional to the exposed area of the cell, while side-scattered components depend on the cell granularity and carry information about the internal structure of the cell, since lateral scattering relies on interfaces of different refractive indexes [220].

EIS flow cytometry exploits the same idea, except for the readout method being electrical instead of optical. These systems are commonly known as Coulter counters, whereby the main goal is to detect changes of electrical properties of the fluid caused by passing cells. To realise this detection method, the cell suspension is flown across electrical contacts while a voltage signal is continuously applied, as illustrated by the scheme in Figure 91(a) [207]. Every time a cell moves through the electrical probing region, a sudden change in impedance at a certain frequency is measured, both in magnitude and phase. In addition, note that the diagram includes two pairs of opposing electrodes. The first pair provides the sensing signatures caused by the passage of a particle or a cell. In the same instant, the second pair records the impedance of the bare medium and acts as a reference. The readout consists of the differential signal between the two pairs. This configuration is widely employed because of three intrinsic advantages: a) the properties of the cells or particles are measured against the suspending medium, b) any potential drift of the electrodes and the solution over time is referenced out and c) the velocity of the cells can be obtained from the transit time.

This technique (or similar designs) has been applied to a vast range of biological assays [221], such as the identification of cancer cells at different metastatic stages [222,223], the classification of differentiated and undifferentiated stem cells [224] or the recognition of red blood cells, platelets and lymphocytes in blood [225–227]. However, since most of these studies were focussed on eukaryotic cells, a thorough examination of such applications is outside the scope of this work given that our main focus is the study of single bacteria, as detailed in the next section.

2.2.1. Single bacteria assays

While time-dependent measurements of impedance for single bacteria have not been reported, EIS flow cytometry has been applied to bacteria studies in a few instances in the literature. However, EIS cytometry for bacteria is not entirely straightforward either, mainly because of the required higher sensitivity compared to eukaryotic cells due to the small size of bacteria. In μ-EIS techniques, one of the main aspects governing sensitivity is the overlap between the cell and the probed volume, namely the volume occupied by the electric field generated between the contacts. Ideally, the two volumes should be equal. The most obvious way to achieve volume matching for bacteria is to reduce the dimensions of the channel and the electrodes, even though this makes fabrication more demanding and increases the chance of channel blockage. Nevertheless, this approach was recently implemented by Clausen *et al.* [228], who managed to differentiate *E. coli* and microbeads of similar size in spiked media and, interestingly, in tap water, as shown in Figure 91(b).

As an alternative method, cells can be focussed in the central regions of the channels by hydrodynamic focussing the bacteria suspension with a sheath fluid of low conductivity. The insulating property of the focussing fluid confines most of the field within the highly conductive thin stream of cell medium, while forcing cells to move through a region of constant electric field. This approach also decreases the readout noise due to inhomogeneity of the field, as showed by Bernabini *et al.* [229], who managed to detect and differentiate *E. coli* and 1 μm polystyrene beads.

Another original solution to the problem of increasing sensitivity was proposed by Haandbæk *et al.* [230]. By adding an external discrete inductor, an RLC resonance was created in the entire measurement circuit. The value of the inductance was matched to the impedance of the bare circuit, such that the passage of a bacterium through the electrodes detuned the resonance, thereby causing the impedance of the entire circuit to drop significantly. This addition allowed the authors to detect single *E. coli* and *B. subtilis,* and to distinguish them from microbeads of similar sizes because of the opposite sign of the phase signature, as shown in Figure 91(c). The different sign of the response is due to bacteria being significantly more conductive than beads, therefore causing the resonance to shift in opposite directions.

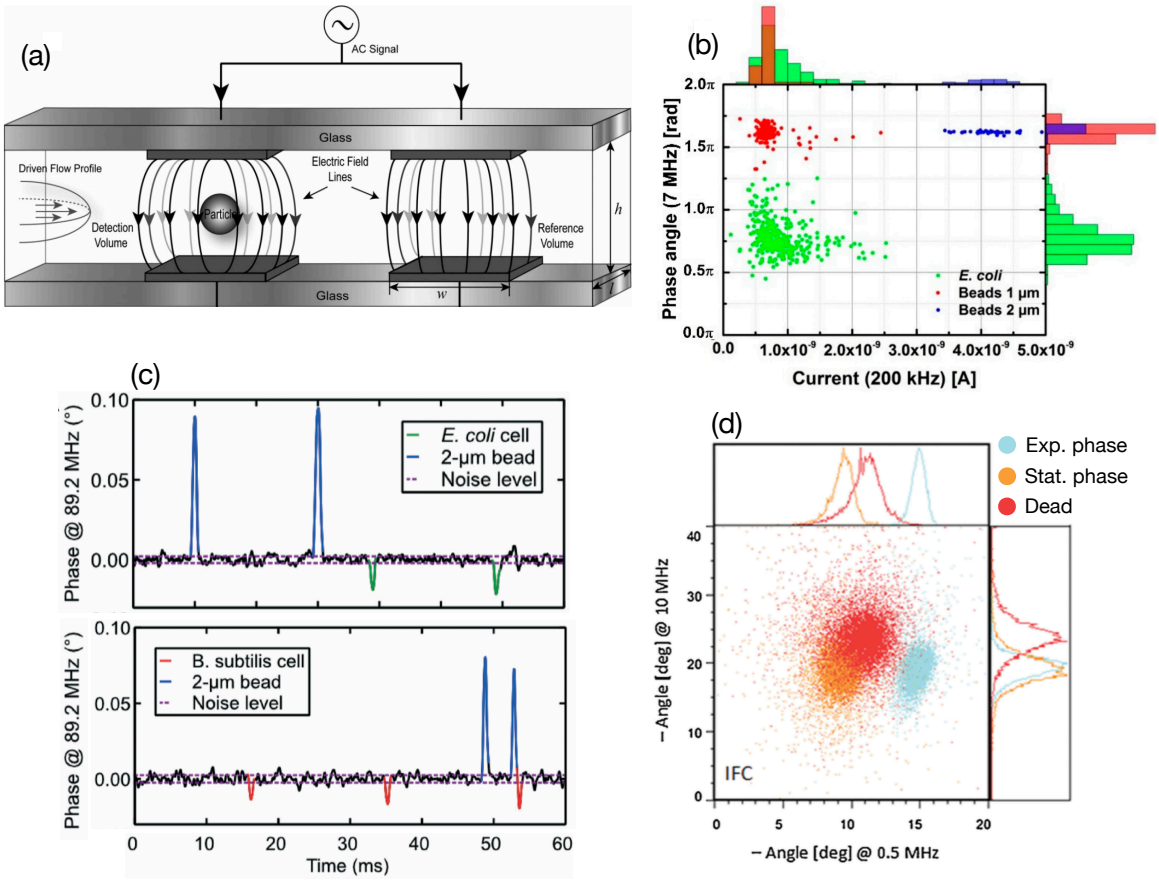

Figure 91. EIS flow cytometry for single bacteria studies. (a) 3D illustration of a typical differential impedance scheme employed in flow cytometry. A microfluidic channel is created by the two glass slides and equipped with two pairs of opposing metal electrodes. The first pair detects the passage of particles or cells, while the second one probes a reference volume at the same instant [207]. (b) Scatter plot of the measured current and phase allowing classification of E. coli (green) and microbeads of different sizes (red and blue) from the work of Clausen et al. [228]. (c) Peaks in the impedance phase caused by the transit of E. coli, B subtilis and microbeads from the work of Haandbæk et al. [230]. The differentiation was ensured by the implementation of a resonant RLC circuit, which also resulted in different signs of the phase change between inert beads and living bacterial cells. (d) Scatter plot of the measured phase at two different frequencies for B. megaterium in different conditions, namely in the exponential growth phase (light blue), stationary phase (orange) and dead (red) [231].

A final notable work I would like to mention used EIS cytometry for the analysis of *Bacillus megaterium* bacteria of different viability and at different stages of growth [231]. Figure 91(d) shows how the technique can clearly detect three groups of cells by exploiting the phase signature at two frequencies (0.5 MHz and 10 MHz). In particular, organisms in the exponential phase (light blue data points) were distinguished from bacteria in the stationary phase (orange) and those killed by heat (red). The choice of the two frequencies allowed the authors to probe different properties of the passing bacteria. The low frequency (0.5 MHz) is sensitive to the volume of the passing bacterium, while at 10 MHz the current is able to penetrate the cell body, thereby providing information about the membrane's integrity and potential.

In conclusion, compared to the trapped cell assays described in the previous section (2.1), EIS cytometry affords much higher throughput, allowing up to several thousand cells per second to be analysed. However, cytometry does not allow for time-dependent analysis of the same cell. Only momentary cellular information is retrieved, since the readout is obtained for the specific time point at which the cell passes the detection area.

3. Theory of EIS

Electrical impedance spectroscopy (EIS) is based on measuring the electrical impedance Z of a circuit as a function of the frequency of an applied AC voltage signal. Hence, Z is an extension of the concept of electrical resistance to AC circuits. In fact, its definition as the ratio between the applied voltage V and the current flowing in the circuit I is similar to the well-known Ohm's law for DC circuits:

$$Z = \frac{V(t)}{I(t)} \tag{50}$$

In contrast to Ohm's law, the previous equation includes the time dependence of V and I, i.e. contemplates the possibility of a delay between the applied voltage and the current response of the system. For these reasons, assuming that quantities have a sinusoidal time dependence, it is convenient to express them in a complex notation which includes a phase shift φ:

$$\begin{aligned} V(t) &= |V|e^{j\omega t} \\ I(t) &= |I|e^{j(\omega t+\varphi)} \end{aligned} \tag{51}$$

The previous definitions imply that the impedance takes the form:

$$Z = |Z|e^{j\varphi} \tag{52}$$

where ω is the angular frequency of the imposed voltage signal. Hence, Z is a complex number with amplitude $|Z| = |V|/|i|$ and phase φ describing any delay of the current I with respect to the applied voltage V. $|Z|$ and φ are typically employed as the readout quantities

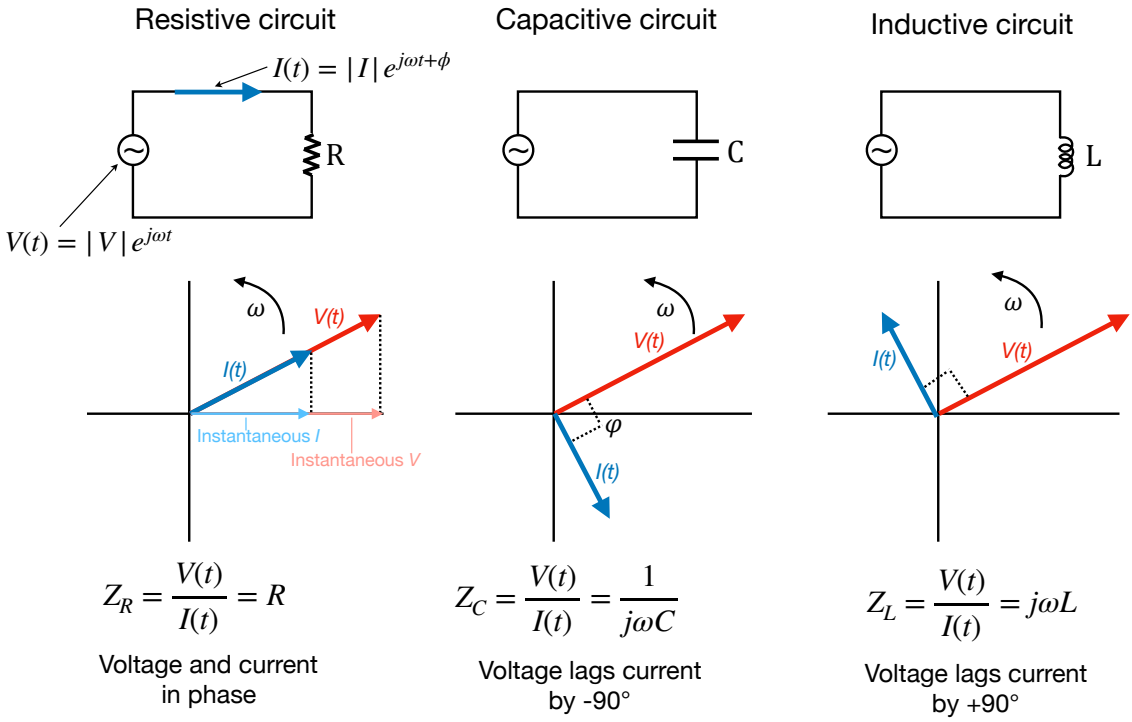

Figure 92. Diagrams of purely resistive, capacitive and inductive AC circuits. A sinusoidal voltage V(t) is applied at the terminal of a resistor (R), capacitor (C) and inductor (L). A sinusoidal current I(t) flows in the circuit with a phase delay φ. V(t) and I(t) can be depicted as phasors, i.e. vectors rotating at an angular speed ω. The two phasors are in phase for a resistive circuit and 90° out of phase for a capacitive and inductive circuit. The induced delay between current and voltage is described by the complex impedances Z_R, Z_C and Z_L, respectively.

in EIS experiments, whereby their dependence on ω carries information about the nature of the probed system, as I will show in the next section.

3.1. Brief review of AC circuits

It is well known from the theory of AC circuits that different electrical elements, namely resistors, capacitors and inductors respond differently to an applied AC voltage signal. The behaviour of each element can be associated with a complex value of the impedance that accounts for the delay induced to the current flowing in the circuit. A useful visualisation of the different effects is provided by a phasor diagram, whereby the complex current I and voltage V are depicted as rotating vectors, as shown in Figure 92. Phasors rotate at an angular speed ω, which corresponds to the frequency of the applied signal. The magnitude of the vectors is equal to the amplitudes $|I|$ and $|V|$, while the phase delay φ is represented by the angle between the phasors. Their projection onto the x-axis is the instantaneous value at time t. The behaviour of a purely resistive, capacitive and inductive circuit is schematically depicted in Figure 92, along with the value of the complex impedances (Z_R, Z_C and Z_L, respectively).

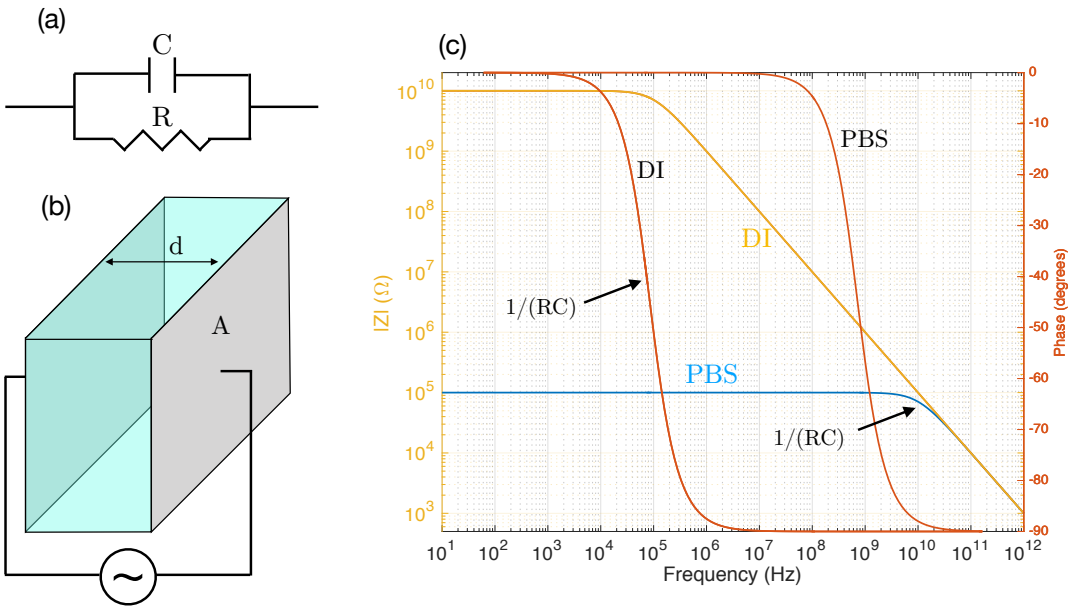

Figure 93. Behaviour of an AC parallel RC circuit. (a) Diagram of a parallel RC circuit. (b) The previous scheme can be represented as two plates of area A and of distance d containing a medium of resistance R and capacitance C. (c) Frequency response of the RC parallel in terms of the amplitude of the impedance |Z| and its phase. The curves are plotted assuming two different media between the plates (DI water and PBS solution). The spectra show a frequency transition above which the capacitor acts as a short circuit, thereby causing most of the current to flow in its branch. The transition frequency depends on the dielectric properties of the medium, as shown by a comparison between the DI water and PBS curve.

In the purely resistive case, the current and the voltage are in phase and the expression of the resistive impedance Z_R reduces to Ohm's law. If the circuit includes only a capacitance C, the current is delayed with respect to the voltage. The reason lies in the time needed to charge and discharge the capacitor for every voltage inversion at the terminal. This process is described by a capacitive impedance $Z_C = 1/j\omega C$. Finally, in the inductive case the opposite effects hold because of the delay due to the self-induced electromotive force in the inductor, as described by the inductive impedance $Z_L = j\omega L$.

Interesting effects take place when combining multiple elements in the same circuit. I will briefly analyse the simple case of a RC parallel circuit because of its relevance to the biological analysis of a single cell, in particular of the cell membrane. A diagram of the circuit is depicted in Figure 93(a). Such a configuration can be pictured as an AC voltage applied to two plates of area A and at a distance d containing a medium of conductance σ and relative dielectric permittivity ε_r, as shown in Figure 93(b). The values of the conductance and resistance of the circuit can thus be calculated as:

$$R = \frac{1}{\sigma}\frac{d}{A} \tag{53}$$

$$C = \varepsilon_0 \varepsilon_r \frac{A}{d} \tag{54}$$

and employed to calculate the total impedance $Z_T(\omega)$ of the circuit as:

$$Z_T(\omega) = \left(\frac{1}{Z_R} + \frac{1}{Z_C(\omega)}\right)^{-1} = \frac{1}{j\omega C + \frac{1}{R}} \tag{55}$$

The behaviour of the amplitude $|Z|$ and phase of Z_T as a function of ω are plotted in Figure 93(c). Curves are plotted for two different media filling the plates, i.e. DI water and PBS solution, whose conductivities are significantly different (6 orders of magnitude). A clear transition is identified in both cases, as revealed by the drop in phase from 0° to -90° and by the magnitude of the impedance changing from a stationary regime to a linearly decaying behaviour. This transition happens for a frequency of about $1/RC$, when the circuit behaviour changes from purely resistive to capacitive at high frequency.

3.2. EIS for biological studies

From the previous section, it is clear that frequency plays an important role in determining the behaviour and response of an AC circuit. Importantly, similar behaviour is observed in biological measurements, hence allowing us to understand and model the electrical response of single cells incorporated in an AC circuit.

Indeed, the AC electrical response of most biological cells and their membranes can be modelled as a parallel RC circuit. In particular, the bacterial cell envelope includes the cell membrane and the cell wall, both of which contribute to electrically isolating the inside of the cell from the outside environment. A scheme of the envelope of a Gram-negative bacterium is shown in Figure 94(a), where the presence of a periplasm sandwiched between the inner and outer membrane is highlighted. Electrical insulation is not (and should not be) perfect since microorganisms need communication channels with their surroundings for exchanging ions and acquiring nutrients. In addition, proteins and pores are embedded in the lipid bilayer, which make the membrane less than perfectly insulating. However, for practical purposes, the membrane resistance is often assumed sufficiently large to be neglected, as I will detail below. More importantly, the envelope shows a capacitive behaviour, since it also acts as an insulating spacer with a certain thickness between the two regions and allows for charges to travel across it.

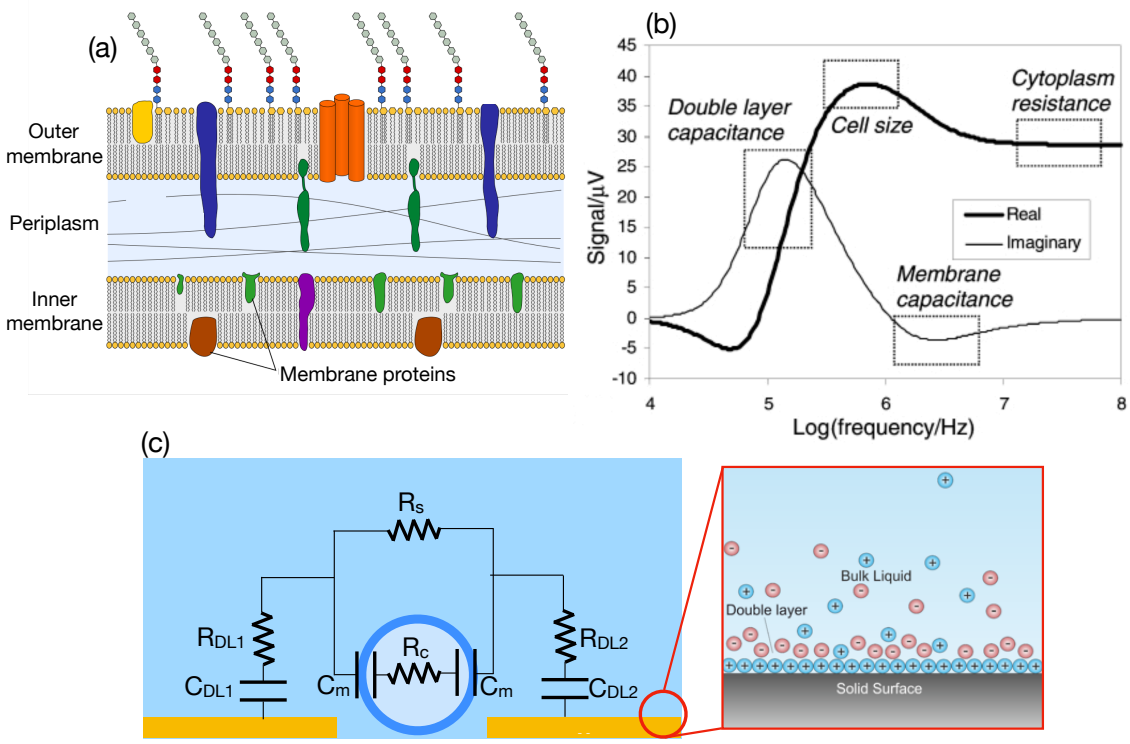

Figure 94. Diagrams of EIS for gathering relevant biological information on single cells. (a) Schematic of the cell envelope of a Gram-negative bacterium, such as E. coli. The envelope features a periplasm sandwiched between an outer and an inner membrane. Several proteins are inserted in the lipid bilayer forming the two membranes. (b) Simulated response of a single cell exposed to an AC signal at different frequencies. At low frequencies, the double layer capacitance dominates the response, while at medium values the EDL is shunted and the size of the cell is probed. As the frequency increases, the cell membrane starts to play a role, while at very high frequencies the membrane is also permeated, and the cytoplasm resistance dominates the response. (c) Equivalent circuit model of a single cell between two metal electrodes. $C_{DL1,2}$ and $R_{DL1,2}$ are the double layer capacitance and resistance of the two metal electrodes, respectively, while R_s is the resistance of the solution. The cell is typically modelled as a series of two membrane capacitances C_m and a cytoplasm resistance R_c. Inset: Magnified diagram of the electrical double layer, which consists of charges absorbed onto the electrodes and opposite ions being attracted from the solution.

Different operational regimes are observed as a function of frequency, as illustrated in Figure 94(b), which shows the typical voltage response obtained for (20x20) µm^2 coplanar gold electrodes [232]. The cells in this experiment were assumed to be spheres consisting of a uniform cytoplasm of conductivity 0.5 S/m enclosed in a thin non-conductive membrane of capacitance 1 µF/cm^2. The cells are immersed in PBS, which has a conductivity of 1.6 S/m. A diagram of the assay and the equivalent circuit model are depicted in Figure 94(c), where the subscripts *DL1* and *DL2* refer to the double layer at each electrode interface, *s* indicates the solution, while *m* and *c* represent the cell membrane and cytoplasm, respectively. The different frequency regimes can be described as follows:

- Low frequency regime – typically up to hundreds of kHz. The response of the system is dominated by the capacitance of the electrical double layer (EDL) forming at the electrode-liquid interface. The EDL consists of two parallel layers of charges covering the electrodes. The first layer is made up of charges adsorbed onto the electrodes, while the second one stems from ions attracted from the solution to screen the first layer, as schematically shown in the inset of Figure 94(c) [233,234]. Since the double layer is extremely thin (less than 1 nm), its capacitance per unit area is relatively high (typically of the order of tens of $\mu F/cm^2$), meaning that in the low-frequency regime the frequency is not sufficiently high to shunt it. Therefore, no relevant information on the biological object can be obtained in this region.

- Mid-frequency regime – low MHz range. The electric field penetrates the double layer and probes the solution, including the cell placed between the electrodes. However, only information about the cell size is retrieved in this region, since the interior of the body is still screened by the cell membrane. In other words, the cell simply acts as an obstacle impeding the flow of current proportionally to its volume in relation to that of the electric field.

- Mid-high frequency regime – high MHz range. This transition happens when the excitation frequency matches the characteristic frequency of the cell membrane $1/R_mC_m$. The membrane capacitance is now being probed as the field is able to permeate it and current starts to flow across the cell. This is often the preferred operational range if the aim is to probe a cell's properties and status.

- High frequency regime – above tens of MHz. The cell membrane and cytoplasm are shunted and act as a conductive path, which makes the cell entirely transparent to the field lines. The electric field penetrates the interior of the cell, which now behaves as a purely resistive element. Hence, this regime provides information about the cytoplasm resistance.

From the previous arguments, it is clear that gathering biologically-relevant information from an EIS experiment implies that the frequency response of the system needs to be determined in order to select the frequency that maximises sensitivity to the cell. However, given the wide variability of experimental conditions, it is essential to first conduct

simulations as a significant aid for determining the response of an EIS assay, as I will show in the next chapter.

4. COMSOL simulations

The AC/DC module of COMSOL Multiphysics 5.0 was used for all simulations in this chapter. I will first present the simulated response of an individual *E. coli* placed between two micron-sized gold electrodes (section 4.1) and then add two SU-8 trapping wells above the metal in order to show the importance of confining the electric field to enhance sensitivity (section 4.2). Finally, I will show simulations of the complete trapping device including a microfluidic channel (section 4.3).

4.1. Single *E. coli* between electrodes

A 2D diagram of the simulated geometry is shown in Figure 95(a). Two gold electrodes are defined on top of a glass substrate covered in different liquids. Unless otherwise specified, I assumed the cover medium to be the LB broth, which has a conductivity σ of 1.6 S/m and a dielectric constant ε_r of 78 [207]. The bacterium is assumed to be an *E. coli*, with a circular cross section of 1 μm width and a three-shell envelope, as illustrated by the inset of Figure 95(a). In particular, the membranes were assumed to have an electrical conductivity σ of 10^{-7} S/m and a dielectric constant ε_r of 6. The periplasm was assigned values of σ = 3 S/m and ε_r = 60, while for the cytoplasm, values of 0.22 S/m and 81 were assumed [235], respectively.

The boundaries of the domain were assumed to be perfect electric insulators and both electrodes were defined as electrical terminals. I imposed a sinusoidal AC voltage with an amplitude $|V|$ of 10 mV to the stimulus electrode and then integrated the terminal current along the edges of the recording electrode, which produced a real and an imaginary component of the current I. The complex impedance Z was then obtained by dividing the 10 mV amplitude by the complex recorded current, from which it was possible to retrieve the impedance amplitude $|Z|$ and phase.

Typical spectra are illustrated in Figure 95(b) and (c), where $|Z|$ and the phase are plotted as a function of the frequency of the AC signal. Orange curves refer to the bacterium being placed between the electrodes, while blue curves are simulated for an empty configuration to provide a reference. From the reference curves, we note that as the frequency increases,

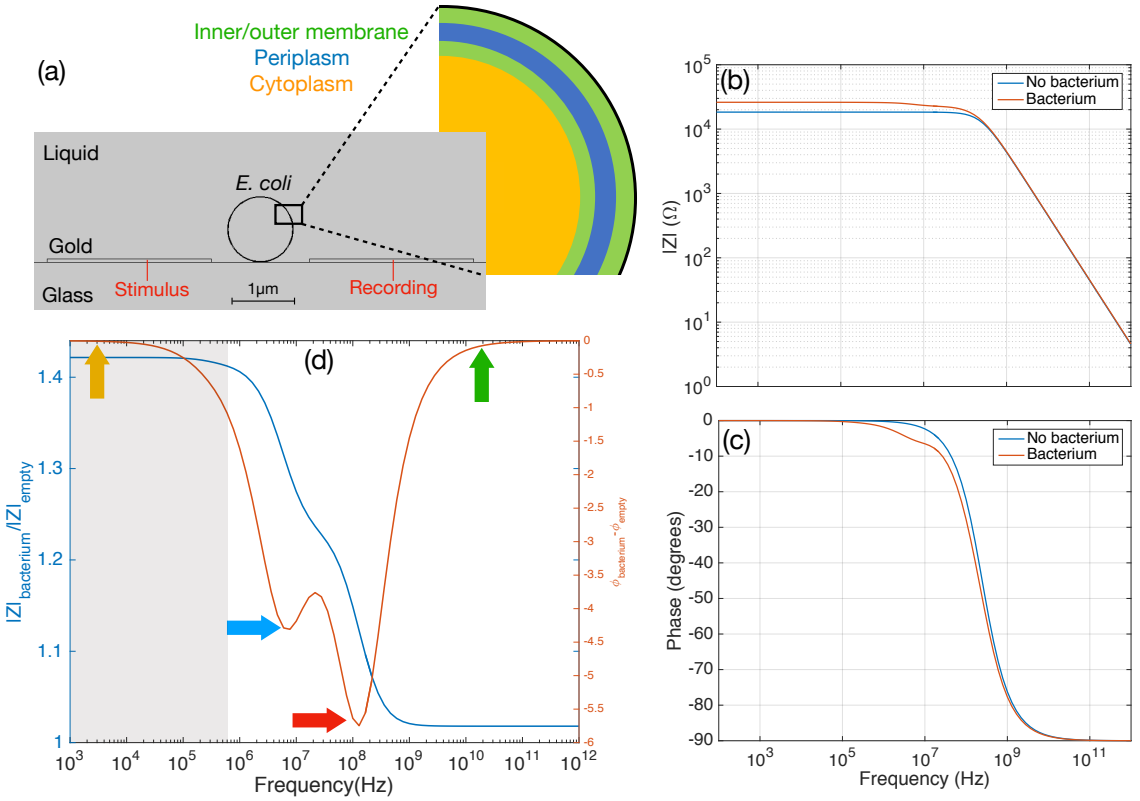

Figure 95. Impedance magnitude and phase spectra obtained from COMSOL simulations of a single three-shelled E. coli placed between two metal electrodes. (a) Illustration of the simulation domain designed in COMSOL. Two gold electrodes are placed on a glass substrate and covered in liquid. The AC voltage signal is applied to the stimulus electrode (on the left), while the current is measured at the recording electrode (on the right). A single E. coli sits between them. The bacterium cross-section is modelled as a three-shell sphere of diameter 1 µm. (b, c) Amplitude of the impedance |Z| and its phase as a function of frequency with and without the bacterium. The behaviour resembles that of an RC parallel circuit. A clear difference is observed between the two configurations. (d) Relative increase in impedance and shift in phase caused by the bacterium with respect to the empty case. A double dip resonance effect is observed. The grey shaded area represents the frequency range at which the EDL should mask the electrical readout. Coloured arrows indicate relevant data points that will be examined in Figure 96.

the phase drops from 0° to -90°, while |Z| changes from a flat behaviour to a linear decrease at high frequencies. This behaviour resembles that of an RC parallel circuit (see Figure 93 in section 3.1), which is indicative of the resistance and capacitance of the solution acting in parallel, as previously argued. The presence of the bacterium, however, modifies the spectrum, as seen from the red curves.

In order to highlight the differences, Figure 95(d) plots the amplitude of the impedance normalised to the empty configuration ($|Z|_{bacterium}/|Z|_{empty}$, blue curve) and the difference in phase between the two configurations ($\varphi_{bacterium} - \varphi_{empty}$, red curve). The *E. coli* causes an increase of impedance, which is due to its body impeding the current flow between the electrodes. However, this only holds until the frequency is high enough to penetrate the

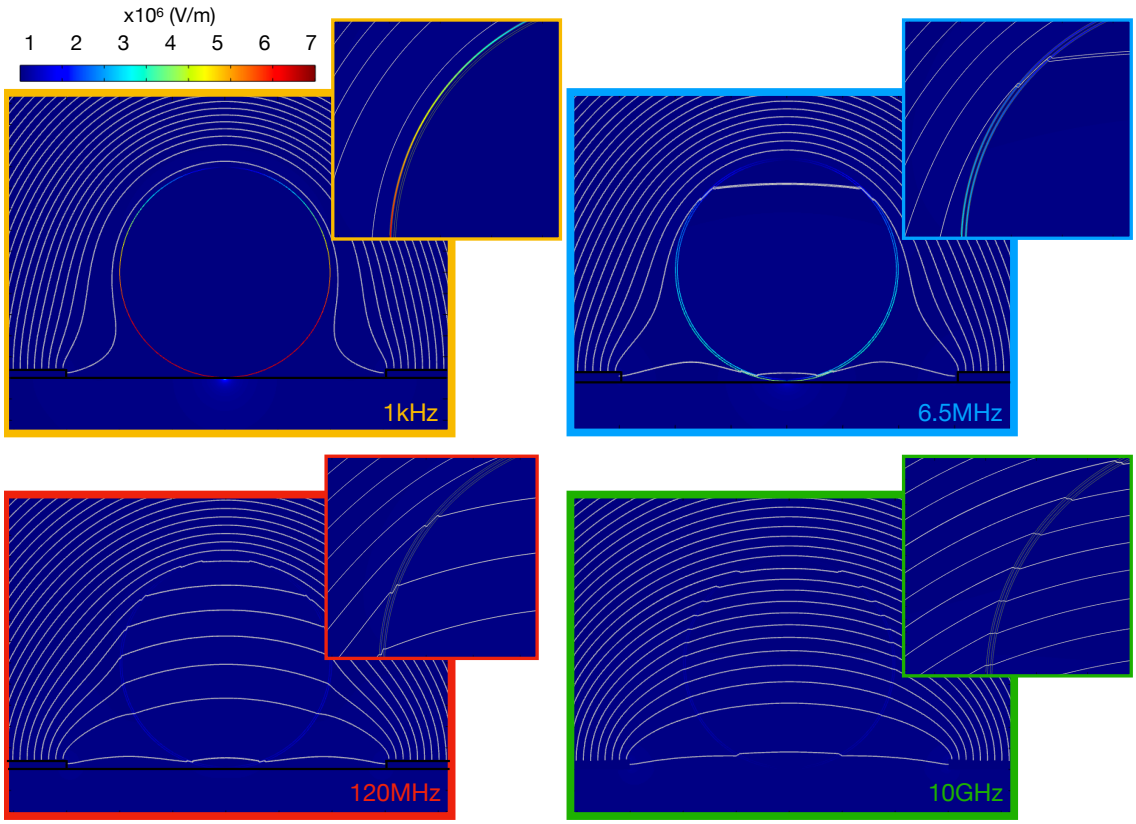

Figure 96. Electric field plot and field lines at four selected frequencies for a single E. coli between the electrodes. The four selected frequencies are indicated in Figure 95(d). Insets show close-ups of the bacterial membrane in order to highlight the progressive shunting of the inner membrane and the cytoplasm. As the frequency increases, the field lines start to penetrate the body, thereby making the bacterium entirely transparent to the field. Interestingly, the refraction of the electric field lines due to the different dielectric constants is clearly visible at high frequencies.

cell body, after which the ratio tends to 1 since the bacterium is now transparent to the field. The most interesting feature that emerges from this graph is the presence of a double dip in the relative phase response (red curve) at frequencies of approximately 6.5MHz and 120MHz.

In order to further elucidate this resonance effect, Figure 96 shows the electric field distributions and field lines at the four selected frequencies indicated by the coloured arrows in Figure 95(d). It is clear that the resonances (blue and red framed plots in Figure 96) occur when the inner membrane and the cytoplasm are sequentially shunted by the field and allow current to flow through them. In these conditions, the field lines start to penetrate the cell, while in the orange and green framed plots the field does not shunt the cell and totally penetrates it, respectively. In other words, when the frequency matches the RC constant of the membrane and cytoplasm, a shoulder and a drop appear in the relative $|Z|$ and phase, respectively (see again Figure 95(d)).

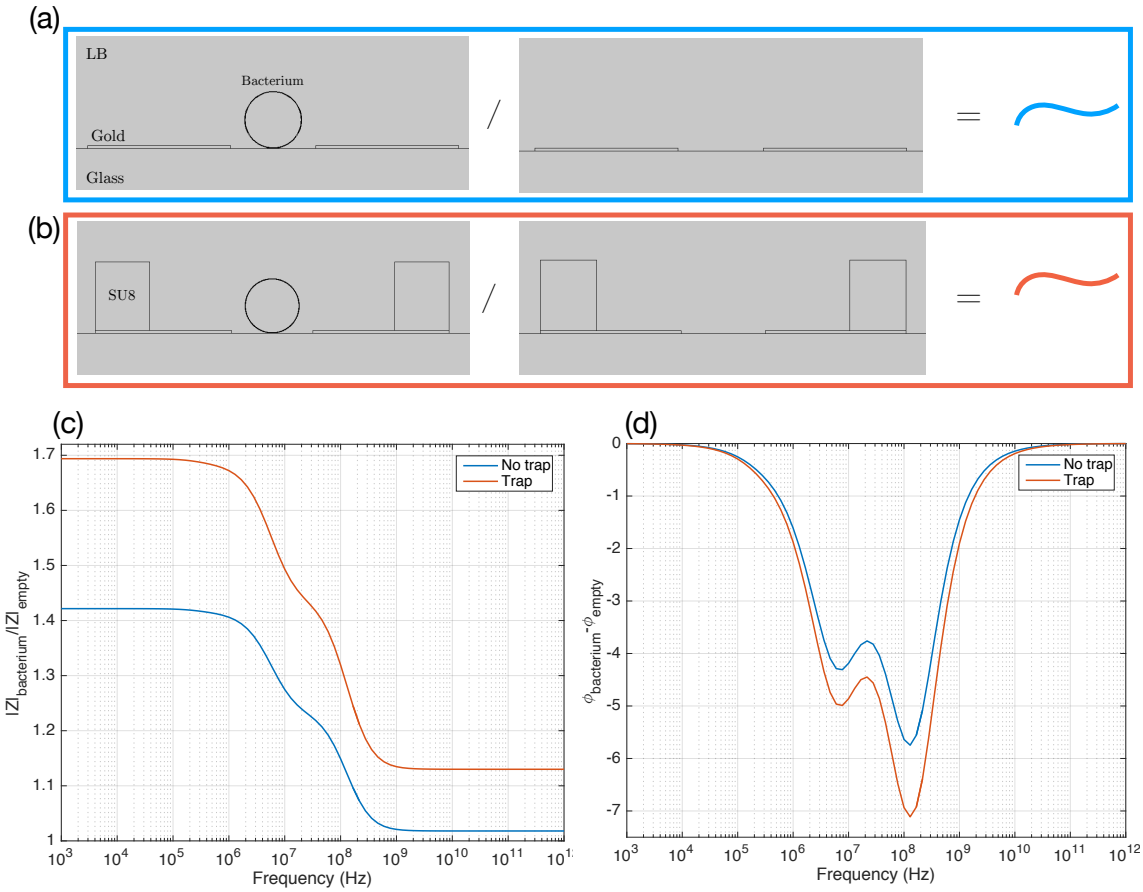

Figure 97. Simulated impedance and phase response of a single bacterium between two metal electrodes partly covered by SU8 wells. (a) Schematic of the simulation domain for a three-shell bacterium between the electrodes and the empty configuration used to normalise the results. (b) Same schematic with the addition of SU8 wells onto the electrodes to retain the bacterium in place. The empty trap configuration is illustrated on the right-hand side. (c) Normalised impedance amplitude upon trapping for both configurations. The presence of the trap (red curve) enhances the response to the presence of the bacterium. (d) Relative phase showing the double resonance behaviour. The SU8 wells increase the magnitude of the response by about 1° for both dips.

These results show that the simulated configuration is sufficiently sensitive to detect the presence of a single *E. coli* between the electrodes. However, we note that the findings reported for the low-mid frequency range are not entirely reliable since the presence of the EDL was not implemented in the model. Nevertheless, as discussed in section 3.2, the effects of the EDL are manifested up to 10-100kHz, as indicated by the grey-shaded area in Figure 95(d). Hence, the double phase resonance should not be shadowed by the EDL effect.

4.2. Single *E. coli* in SU8 wells

In this next set of simulations, I placed SU8 wells above the contacts with the twofold aim of mimicking the trapping of *E. coli* while enhancing the electrical readout signal. Since

SU8 is electrically insulating [218], field lines do not penetrate the blocks at frequencies relevant to the analysis. Hence, the effective volume probed by the field decreases and the overlap with the volume of the bacterium increases. A diagram of the simulation domain is shown in Figure 97(a), where I used the empty-well configuration to normalise the spectra. Additionally, the no-well design (Figure 97(b)) is still simulated to highlight the beneficial effect of the SU8. Indeed, a comparison between the blue and red curves in Figure 97(c) and (d) reveals that the presence of SU8 (red curves) enhances sensitivity to the bacterium by approximately 20% in terms of magnitude of impedance, while the double resonance in the phase response becomes deeper, reaching values of up to ~-7°.

4.3. Simulation of the real geometry

Building on the previous results obtained for simplified configurations, I now present simulation results obtained by modelling the real geometry of the microfluidic trapping assay. Figure 98(a) illustrates a side view of the simulation. The domain also includes the microfluidic channel, as shown by the liquid medium (LB broth, in light blue) being sandwiched between the glass substrate and a PDMS block above (both in dark blue). Metal tracks (in yellow) are placed above the substrate and covered in 200 nm of SU8 (in brown). The top block of the SU8 trap is also included with the aim of retaining an individual *E. coli*. The bacterium is modelled as a three-shell ellipsoid with a major axis of 3 μm and a minor axis of 0.7 μm. The material properties set for each domain are reported in the table in Figure 98(b), while Figure 98(c) depicts a cross-sectional view of the modelled bacterium in different conditions. The first diagram on the left represents a live bacterium, while two dead bacteria are shown in the middle and right diagrams of Figure 98(c). The aim is to investigate any significant difference in electrical readout upon bacterial death compared to the live bacterium. In particular, I used two models to simulate a dead *E. coli*:

- Dead model 1, shown in the middle of Figure 98(c). This model consists of an intact cytoplasm and inner membrane, while the outer membrane is assumed to be disrupted. This configuration models the transient action of a beta-lactam antibiotic that inhibits the cell wall synthesis and eventually causes cell lysis. This process is modelled by the lack of the outer membrane and a 1.5-fold thicker conductive periplasm, whereby the increased thickness simulates a snapshot of the diffusion of ions from the cell body upon cell death. However, some of the parameters in the

table are difficult to determine, so the corresponding results only provide a qualitative understanding of the process and need to be interpreted with caution.

(a)

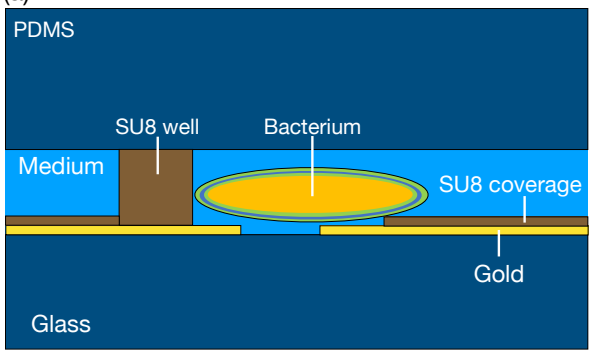

(b)

Simulation domain	σ (S/m)	ε_r	Relevant size
Glass	10^{-13}	7	/
Gold	$4.1*10^{7}$	6.7	100 nm
SU8	0	5	200 nm
LB broth	1.15	78	1.5 µm
PDMS	$2.5*10^{-14}$	2.8	/
Cytoplasm	0.22	81	3 µm x 0.7 µm
Membranes	10^{-7}	6	7 nm
Periplasm	3	60	10 nm
Periplasm - model 1	2	60	15 nm
Dead - model 2	0.09	60	1 µm

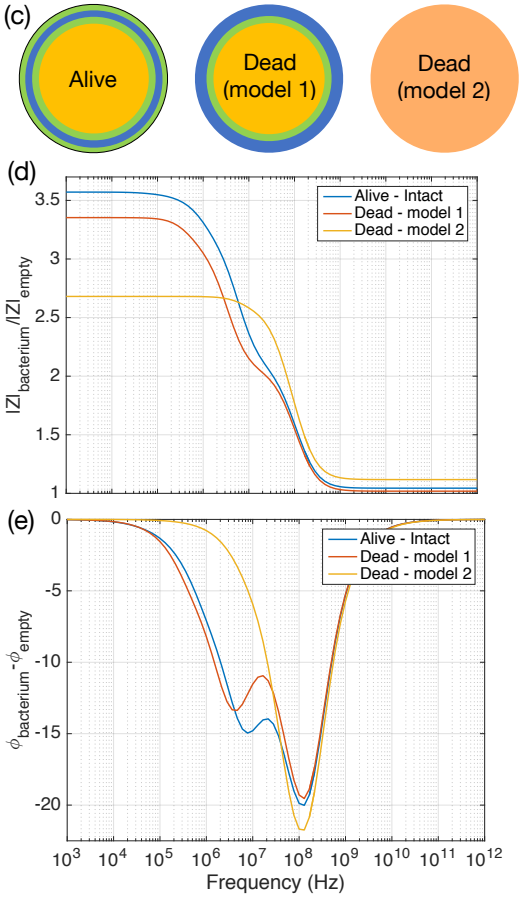

Figure 98. COMSOL parameters and results for the simulation of the real trapping geometry. (a) Side view of the modelled trapping geometry. The medium containing the bacterium is enclosed in the microfluidic channel defined by the glass substrate and the PDMS block above. Metal tracks are mostly covered by SU8 except for the 1.5 µm long tips below the bacterium. (b) Tables containing the values of conductivities, dielectric permittivities and relevant dimensions of the simulated elements. (c) Cross sectional views of a live and dead Gram-negative bacterium, according to two different models. The first model of a dead E. coli (diagram in the middle) assumes that only the external membrane is disrupted and the periplasm is thicker. The second diagram (right-hand side) models the entire body as a uniform sphere with decreased conductivity. (d) Simulated relative impedance for a live and dead bacterium according to the previous models. (e) Relative phase response for the same three cases. The double resonance is present as long as a multi shell bacterium is assumed. The uniform dead bacterium produces instead a single dip due to cytoplasm shunting.

- Dead model 2, shown on the right-hand side of Figure 98(c). The dead bacterium is modelled as a uniform sphere with about half the conductivity compared to the live bacterium (see values in Figure 98(b)). This assumption is supported by a series of electrorotation experiments performed by Holzel [235]. Briefly, electrorotation induces rotation of a polarizable object by employing a four-contact configuration. By imposing a 90° phase delay to the voltage signal at each electrode, rotation of the bacterium is induced [236]. The angular rotation speed as a function of the AC frequency signal is then measured and fitted to a dielectric

model of the rotating bacterium. Holzel studied the rotation of live and heat-killed *E. coli* and found that the dead cells could be modelled as uniform spheres. The lower conductivity is interpreted as the dead bacterium releasing ions that were previously contained in the cell body. Hence, this second model can be considered as a stationary long-term result of the previous one, after all the ions have diffused away from the cell body.

The results obtained for the three conditions are plotted in Figure 98(d) and (e). Firstly, we note that the response to the live bacterium is significantly enhanced by this configuration compared to the previous two sets of simulations (sections 4.1 and 4.2). The amplitude of the impedance is increased by a factor as high as ~3.5 at low frequencies, while it tends to 1 at high frequencies, as expected. The phase response (blue curve in Figure 98(e)) is also amplified to differences as large as ~-22°. The reason for this enhanced signal is the maximised overlap between the field and the bacterium, as previously predicted. The *E. coli* is placed exactly above the electrodes and the generated field is tightly confined between the two tips thanks to the insulating boundaries of the glass substrate and the SU8 well and coverage. In addition, the PDMS above defines a channel slightly thicker than the bacterium which prevents the electric field to spread in the upper half plane.

The red curves in Figure 98(d) and (e) refer to the first model of a dead bacterium. Even though the increase of periplasm thickness is assumed to be small (from 10 to 15 nm), the configuration is sufficiently sensitive to reveal measurable differences. The amplitude of the impedance shows a similar behaviour to the live case, while the double dip response features shallower and slightly shifted dips. A difference of approximately 2° is predicted, which should be within the experimental level of noise, and therefore measurable. Additionally, the presence of the low-frequency dip confirms that it does not originate from the outer membrane, since the external bacterial layer is now absent.

The second model of a dead bacterium, i.e. a uniform ellipse, leads to a significantly different outcome. The simulated impedance is lower than the previous two and three-shell models, as shown by the yellow curve in Figure 98(d). A comparison with the other two curves also reveals that one of the two resonances is now absent, as visible from the presence of a single shoulder in the yellow curve. This loss is also confirmed by the phase response illustrated by the yellow curve in in Figure 98(e). A single dip corresponding to

the cytoplasm being shunt is now visible, which still provides a sufficiently large change compared to the live case (~2°).

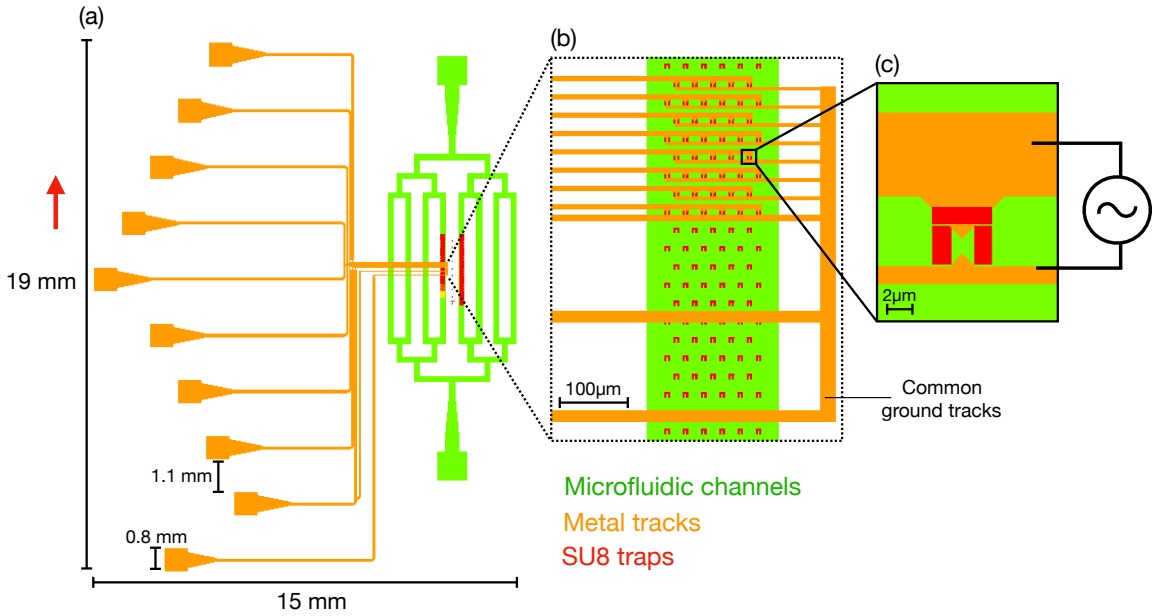

Figure 99. Schematic of the device with integrated electrical contacts. (a) Overview of the complete device including microfluidic channels (in green), trap arrays (in red, in the two middle channels) and metal tracks (in orange). 10 macroscopic pads are designed on the left-hand side to allow contacting the rows of traps. The two bottom pads contact the same ground electrode common to the 8 rows of traps to be measured. The red arrow indicates the direction of the fluid flow. (b) Close up of a single channel highlighting the 8 contacted rows and the common ground tracks. Each pair of tracks simultaneously measures an entire row containing either five or six traps. (c) Close up of a single trap showing the top and bottom micron-sized tips below the SU8 protruding inside the trapping area.

In conclusion, it is clear that the best representation of a dead Gram-negative bacterium is still an open question. Nevertheless, I have used two reasonable models that make use of realistic physical dimensions and electrical properties taken from the relevant literature. Both models predict the system to be sensitive enough to detect the presence of an individual trapped *E. coli* and distinguish a live cell from a dead cell. Model 1 most likely applies to antibiotics that disrupt the outer membrane, such as beta-lactams, while model 2 might apply to drugs that keep the bacterium intact, such as kanamycin or trimethoprim. Measuring such differences in an experiment would be very exciting and will be the subject of future work.

5. Fabrication and measurement techniques

This section presents the fabrication steps I performed to realise the complete device simulated in the previous section (4.3). Most of the workflow builds on the methods used for the fabrication of the traps in SU8 presented in chapter III of the thesis. Figure 99

illustrates a schematic of the entire device, where I integrated microfluidic channels (in green), trapping arrays (in red) and metal tracks (in orange).

5.1. Metal contacts lift off

Metal tips and tracks are fabricated first, on a microscope slide, by lift-off. In detail:

- Standard microscope slides are diced into two equal pieces (25 mm x 37.5 mm) and cleaned in piranha solution for 10 minutes, then rinsed with ACE and IPA in an ultrasonic bath for a few minutes.

- Two layers of resist are spun and baked: Lift-off resist (LOR) at 5000 rpm for 60 seconds baked at 180 °C for 10 minutes, followed by a layer of PMMA 495 spun at 5000 rpm for 60 seconds plus a final bake at 180 °C for 5 minutes. I then covered the resist with a charge dissipation layer (AR-PC from AllResist) by spinning it at 2000 rpm for 60 seconds. Finally, the sample was baked at 90 °C for 2 minutes.

- The contact tracks, tips and pads (orange areas in Figure 99) are exposed by electron beam lithography with a dose of 310 $\mu C/cm^2$ and a current of ~23 nA. The design includes a ground electrode which is common to eight rows of traps, as visible from Figure 99(b). This choice reduces the number of tracks and pads compared to a design where two tracks are used to address each row. However, any damage on this track prevents measurements to be conducted on the entire chip. I compromised these two effects by designing a bifurcation of the common ground track into two different pads (the bottom two in Figure 99(a)). Each row also includes metal tips protruding into each trap, as illustrated in Figure 99(c). Exposed areas are highlighted in red in step 1 of Figure 100(a), which shows a side view of the sample during electron beam exposure.

- After exposure, the charge dissipation layer was removed by a 2-minute rinse in DI water, the PMMA layer developed in a 3:7 mixture of DI water and IPA (see Figure 100 (b)) and the LOR undercut in MF-319 for 8 seconds (Figure 100(c)). At this stage, the side view of the sample looks like step 2 of Figure 100(a). The double layer resist takes the typical mushroom shape that makes it suitable for subsequent metal lift off.

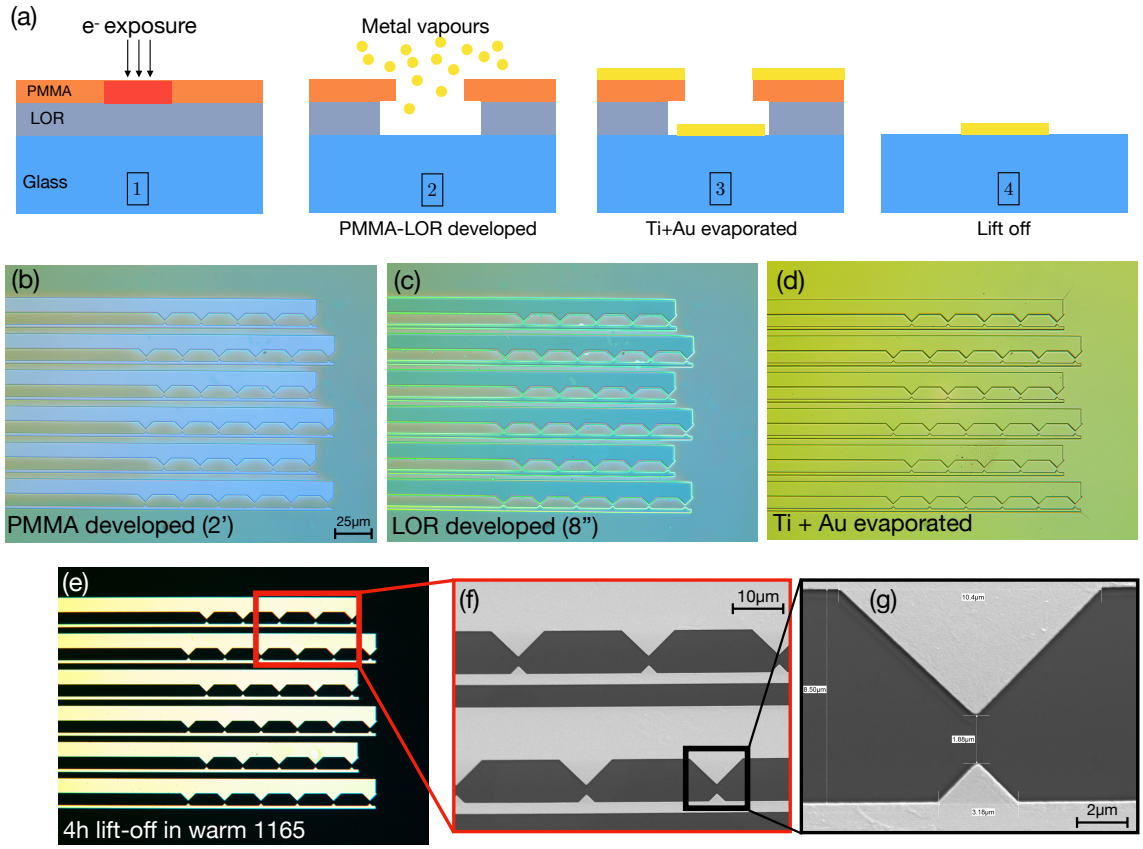

Figure 100. Schematic and pictures of the metal lift-off process. (a) Illustration of the lift-off process. PMMA is exposed by electron beam lithography (step 1). The resist is then developed, the LOR undercut, and the metal evaporated (step 2). The metal layers are formed over the entire surface of the sample (step 3) and the tracks are finally defined after lifting off the LOR and PMMA (step 4). (b-e) Sequence of optical micrographs showing the different stages of fabrication, as indicated by the label in each panel. (f) SEM image showing a portion of two rows of contacts. (g) Close-up of a single pair of gold tips.

- The next step consists of the evaporation of the contact material. This was achieved by depositing 10 nm of titanium (as an adhesion layer), followed by 100 nm of gold using an electron beam evaporator, as schematically illustrated in step 3 of Figure 100(a) and imaged in Figure 100(d) with a brightfield microscope. I subsequently carried out the lift off in warm 1165 (65 °C) agitated with a magnetic stirrer at 650 rpm for at least 3 hours. The removal of the resist was aided by manual agitation and pipetting. The final metal structures are depicted in step 4 of Figure 100(a) and imaged in Figure 100(e-g).

5.2. SU8 coverage of metal tracks and traps fabrication

As discussed in the simulation section (chapter 4) the electrical double layer forming at each electrode interface plays an important role in determining the electrical behaviour of the system. In order to screen the metal tracks from the electrolyte, it is necessary to insulate the tracks as much as possible from the solution, apart from the tips probing the

inner regions of each trap. In practice, the regions that need covering are represented by the intersection between the green areas (microfluidics channels) and the orange ones (metal tracks) in Figure 99(a).

For this purpose, I covered the metal tracks with a thin layer of insulating SU8. I spun SU8 2000.5 at 500 rpm for 10 seconds followed by 60 seconds at 5000 rpm and finally baked the sample at 65 °C, 95 °C and 65 °C for 1 minute, 2 minutes and 1 minute, respectively. Electron beam exposure was carried out with a dose of 3.5 $\mu C/cm^2$. This dose is relatively high compared to typical values used for SU8 (refer to chapter III of the thesis). The reason for this choice is to ensure lateral coverage of the tracks, which is achieved by overexposing the SU8. After post-exposure bake (2 minutes at 95 °C plus two 1-minute long ramps at 65 °C) and development for 2 minutes in EC solvent, a hard bake was carried out to harden the exposed layer for a minimum of 2 hours at 180 °C.

I verified the quality and thickness of covered and uncovered metal tracks at each stage of the fabrication process by measuring their profiles either by AFM or with a stylus surface profilometer. Figure 101(a) illustrates the height profile of seven adjacent uncovered metal tracks at different phases of the fabrication flow. They are not expected to be affected by any of the procedures. The blue curve is a scan performed after the lift-off process to verify that the target thickness had indeed been deposited (10nm Ti + 100 nm Au). The red curve was recorded after the SU8 was exposed and developed and it shows that unexposed SU8 was correctly removed from the tracks. Finally, the yellow scan refers to uncovered tracks after the sample was hard baked for 2 hours at 180 °C. This profile reveals that the quality of the gold layer is slightly affected by the baking process, as visible from the increase in thickness and non-uniformity of some of the tracks. This is likely due to impurities in the metal film being drawn to the surface by the baking process.

The same set of measurements was taken on SU8-covered metal tracks and plotted in Figure 101(b). The blue curve serves as a no-SU8 reference, while the red one shows that the exposure of SU8 was correctly carried out and coverage was achieved. The hard bake process caused the thickness to increase for some of the tracks, likely because of the same effect discussed before for uncovered tracks. In addition, the coverage features an M-shaped profile characterised by two humps at each edge of the underlying track. This inhomogeneity was consistently observed across multiple samples (not shown here). Figure 101(c) suggests that the irregularity is due to a non-uniform coverage of the metal

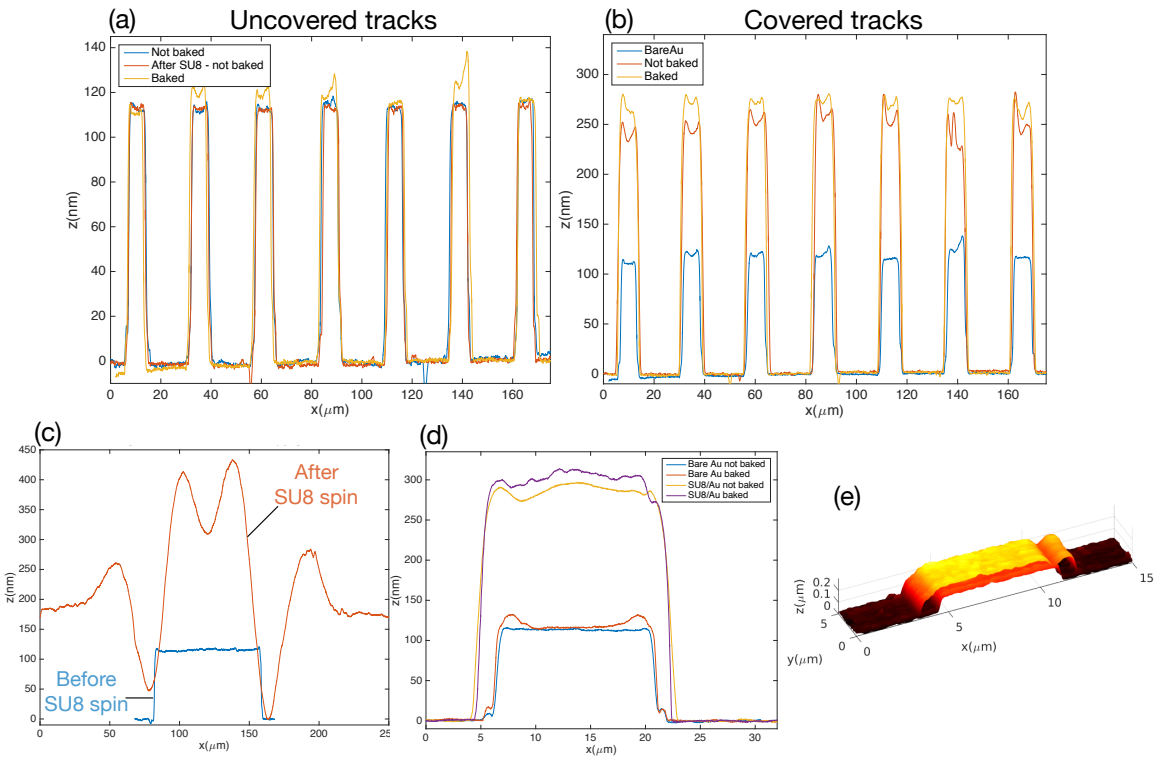

Figure 101. Characterisation of the metal tracks coverage procedure with SU8 through profilometry and AFM. (a) Height profiles obtained with a stylus profilometer for an uncovered series of gold tracks at different stages of fabrication i.e. after lift-off (blue curve), after SU8 exposure and development (orange curve) and after hard baking at 180 °C for 2 hours (yellow curve). (b) The same series of height profiles for a contact covered in SU8, showing that coverage was achieved. (c) Profile of a bare gold contact (blue curve) superimposed onto a profile of the same contact after the SU8 layer was spun (orange curve). The unevenness of the orange profile reveals that SU8 did not cover the gold uniformly because of the step in height and resulted in an M-shaped coverage. (d) Close-up of the profiles of single metal tracks at different stages of the process. Coverage was successfully achieved, both laterally (within a few microns) and vertically (approximately 200 nm). (e) Superposition of two AFM scans taken before and after a portion of a gold track was covered in SU8. These AFM scans were taken under the same conditions described previously (section 6.1 of chapter II).

structures, as illustrated by the profile of the spun SU8 (orange curve) overlaid on that of a single metal track (blue curve). However, this is not a significant issue for coverage, since the SU8 still guarantees electrical insulation of the underlying metal, even if not entirely conformed to its shape. Indeed, the close-up of a single metal track in Figure 101(d) demonstrates that both vertical and horizontal coverage of the metal was satisfactorily achieved. Finally, Figure 101(e) shows a superimposition of two AFM scans performed over a bare contact and a covered one.

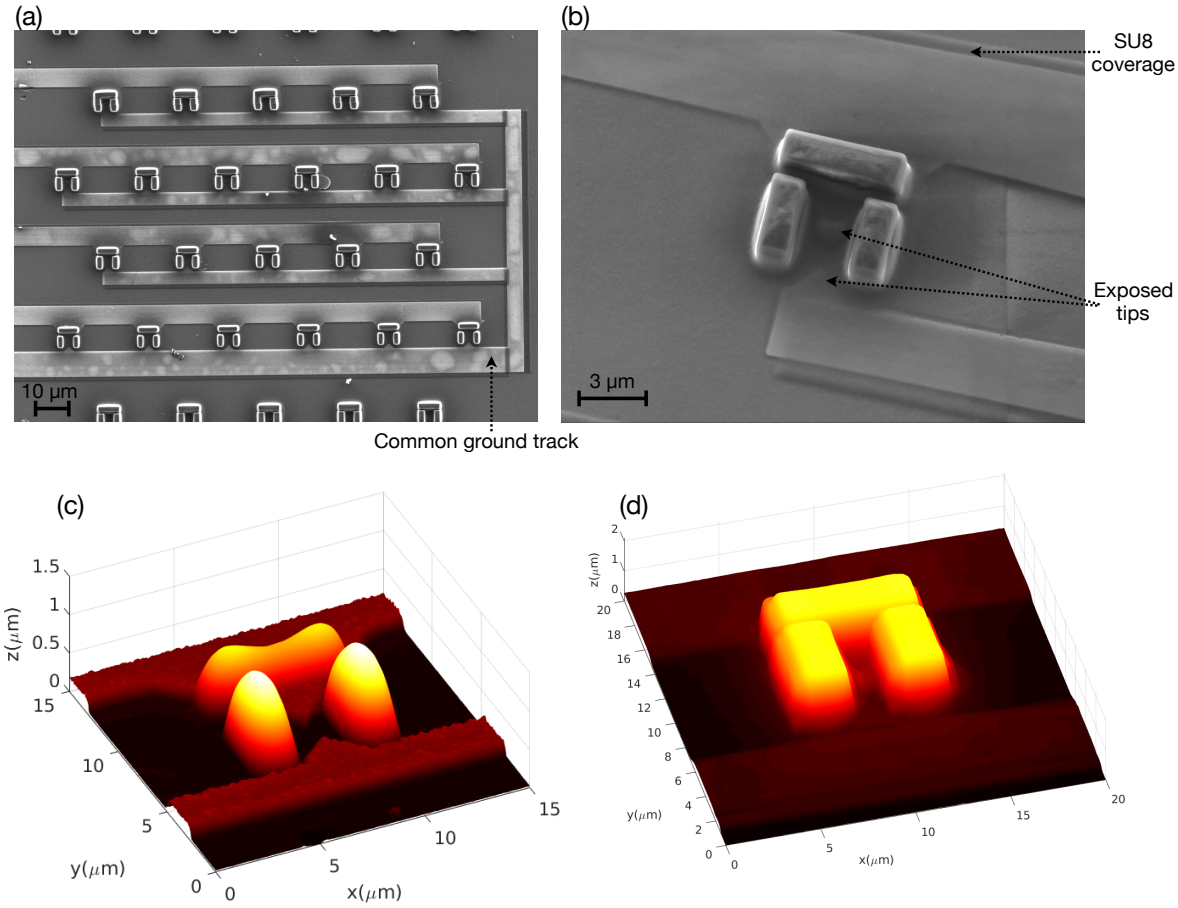

Figure 102. SEM and AFM images of a complete device including traps and metal tracks. (a) SEM image of a complete device. Four rows of traps are contacted with metal electrodes underneath. The metal tracks are entirely covered in SU8, apart from the tips inside each trap. (b) Close-up tilted SEM micrograph of a single trap. The SU8 coverage is evident, as well as the uncovered tips protruding inside the trap. (c) AFM image of an underexposed SU8 traps with contacts and tips below. (d) AFM image of a correctly-exposed trap and metal tracks. The AFM scans in (c) and (d) were taken with the same methods and AFM instrument described in section 6.1 of chapter II, here equipped with a VTESPA-300 probe (Bruker) and using a scan frequency of 0.5 Hz.

After successfully covering the portion of the metal tracks that will be exposed to solution, a third electron beam lithography was carried out to fabricate the traps in SU8 above the uncovered metal tips. The same fabrication protocols presented in chapter 10.4 of chapter III were used here. An example of a complete sample that integrates all the elements is shown in Figure 102. In particular, panels (a) and (b) are SEM micrographs of contacted traps, where relevant structures are indicated by the arrows. The image of a single trap in (b) clearly highlights the metal tips protruding inside the single trap. Figure 102(c) and Figure 102(d) show two AFM scans of a single trap at different exposure doses. In particular, the trap in panel (c) is underexposed, as revealed by the rounded SU8 blocks and the uneven height. However, it evidences the presence of the metal tips. Panel (d) is instead correctly exposed. After the exposure of the tracks, the sample is hard baked for a second time in the oven at 180 °C for at least 2 hours to harden the SU8 traps. If needed,

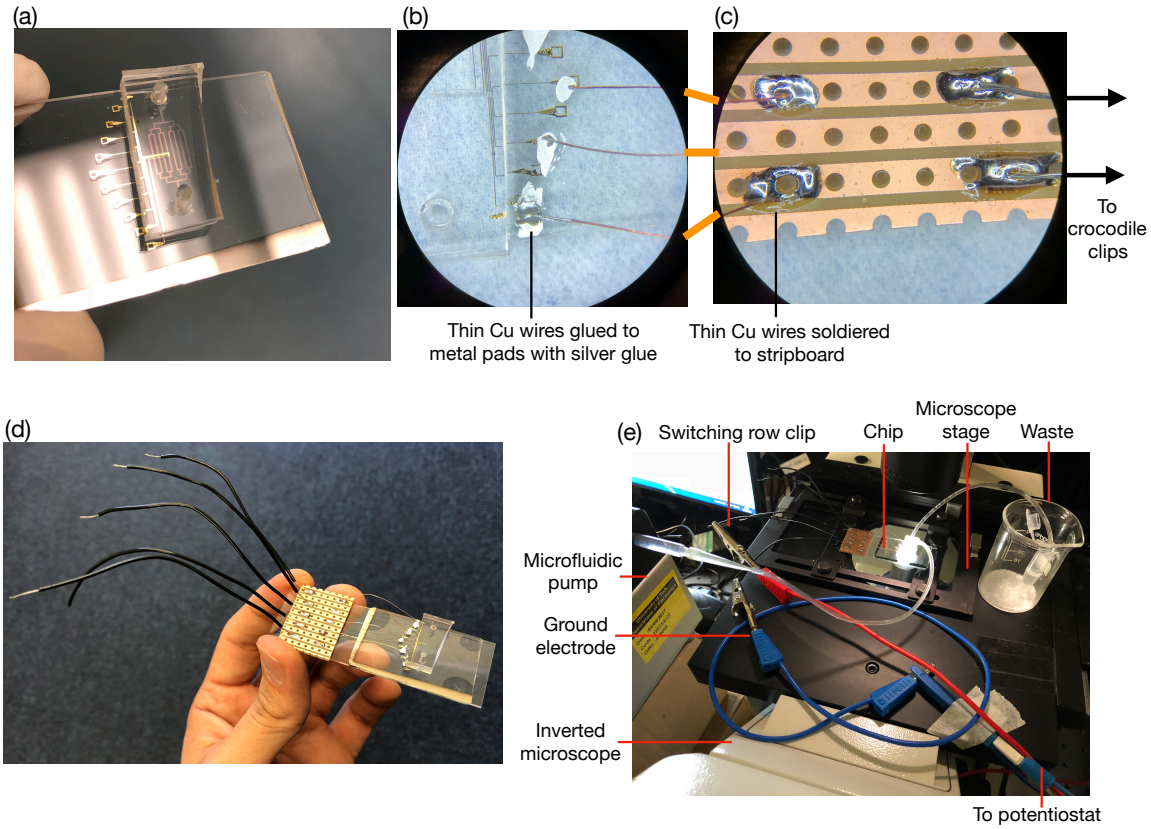

Figure 103. Pictures of the soldering and electrical measurement protocols. (a) Picture of a complete device including metal contacts, SU8 coverage, trap arrays and the microfluidic chip bonded above. (b-c) Stereoscopic images of the wire bonding steps. The left end of thin copper wires was glued onto the metal pads (b), while the right end was soldiered onto a stripboard (c). Thicker wires for crocodile clips connection were soldiered to the opposite of the stripboard. (d) Picture of a finalised sample super-glued onto a microscope slide to ensure stability. (e) Picture of the setup during an experiment under an inverted phase contrast microscope. Labels indicate key components.

an 8-channel microfluidic chip was aligned and bonded onto the chips through oxygen plasma, as per methods section of chapter III (section 10.5) Figure 103(a) shows a picture of a complete device.

5.3. Measurement techniques

Once the fabrication is completed, the sample needs external electrical probes or wires to apply the AC signal to the metal tracks and measure the electrical impedance. The electrical connection was achieved by two different methods: a) connecting and soldering wires directly onto the metal pads, or b) using spring-loaded probes integrated with a 3D printed case. I will describe these two methods next.

5.3.1. Soldering and gluing

The first configuration is illustrated in Figure 103(b-e). The complete sample (shown in Figure 103(a)) and a custom-sized stripboard were glued onto a standard microscope slide to provide stability. The sample was then placed under a stereoscope to aid the positioning of thin copper wires. I glued one end of each wire to the metal pads onto the glass chip by applying a small amount of silver glue, as shown in Figure 103(b). The other end of the wire was soldered onto one of the tracks of the stripboard (left hand side of Figure 103(c)). Thicker electrical wires were soldered onto the corresponding track of the stripboard, as visible in the right-hand side of Figure 103(c) to provide a more stable interface to attach crocodile clips. Figure 103(d) shows the final result, while Figure 103(e) is a picture of the experimental setup during one of the measurements. The chip was placed onto the stage of an inverted phase contrast microscope. Microfluidic tubes were inserted into the PDMS chip to pump solutions, while the wires were connected to a potentiostat (SP-300 from BioLogic Science Instrument, not shown in the picture). The potentiostat applies the AC voltage and records the impedance.

Even though this method is feasible, it suffered from complicated experimental procedure and poor reproducibility. The main limitation was gluing the wires onto the pads, which introduces a significant human factor. Additionally, the use of silver glue prevented every metal pad to be contacted, since it was difficult to produce drops sufficiently small while avoiding adjacent drops to merge. For these reasons, a different approach was used and is described in the next section.

5.3.2. Spring-loaded probes and 3D printed case

The use of complex wiring was circumvented by employing spring-loaded probes, which can be directly pressed onto the metal pads. Therefore, I devised a mechanism to clamp the probes reliably, which made use of a custom designed 3D printed case. The case consisted of two components, whose top views and relevant dimensions are shown in Figure 104(a) and (b). The bottom piece is designed to accommodate half a microscope slide and hold it in place, while the top piece features 10 holes to fit the spring probes and fix them with superglue. In addition, both pieces have clear windows to expose the sample to the light from the microscope, allowing access to the sample from above and accommodating the PDMS microfluidic chip. The positions of the holes in the top component were designed for the pads to be exactly below once the two pieces were

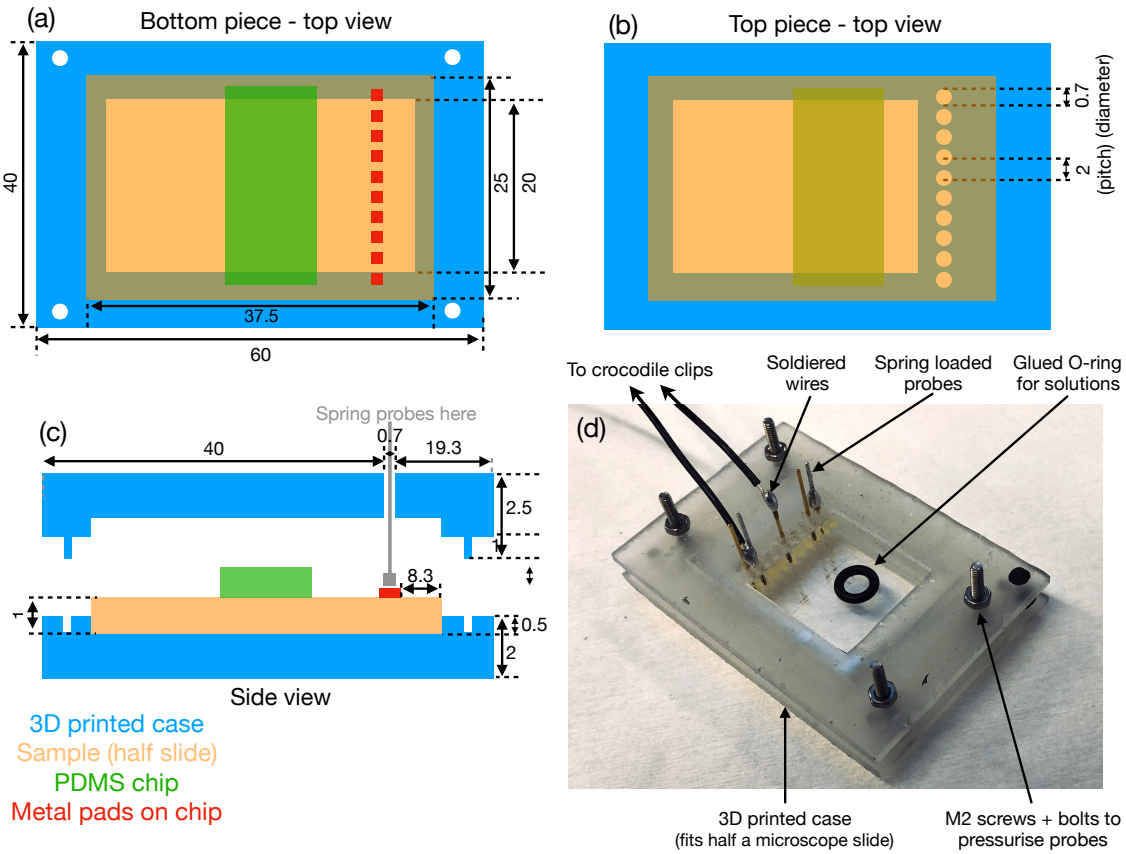

Figure 104. Schematics of the 3D printed units for housing the samples and performing electrical measurements. (a, b) Top view diagram of the bottom and top pieces of the 3D printed case. The lateral dimensions are designed to fit half a microscope slide. The top piece contains holes to match the metal pads of the sample for inserting and holding the spring-loaded probes. An opening is included in the middle to house the PDMS chip and to allow observation under a microscope. (c) Side view of the case showing how the two pieces pressurise the spring probes to ensure electrical contact. All dimensions are reported in mm. (d) Picture of the printed case including standard M2 screws and bolts to clamp the sample and pressurise the probes onto the pads. A 3mm O-ring was glued onto the measurement area to hold solutions and allow measurement when a microfluidic channel is not needed. Wires are soldered to the top end of the probes to provide connection through standard crocodile clips (not shown here).

brought together, as is clear from the side view of the case in Figure 104(c). Four standard M2 screws were fitted in the four larger holes at the corners.

Pressurisation was achieved by carefully tightening the screws at each corner. Figure 104(d) is a picture of the printed case accommodating a sample. In this case, I did not bond any PDMS chip to create microfluidic channels. Instead, I created a well by gluing a standard 3 mm diameter O-ring for holding the solution to be electrically probed by the underlying contacts. Connection to the potentiostat was ensured by soldiering wires to the upper end of the probes and attaching them to standard crocodile clips. Clearly, the case is reusable for multiple measurements, which ensures higher throughput and better reproducibility since it reduces human error incurred by manual wiring.

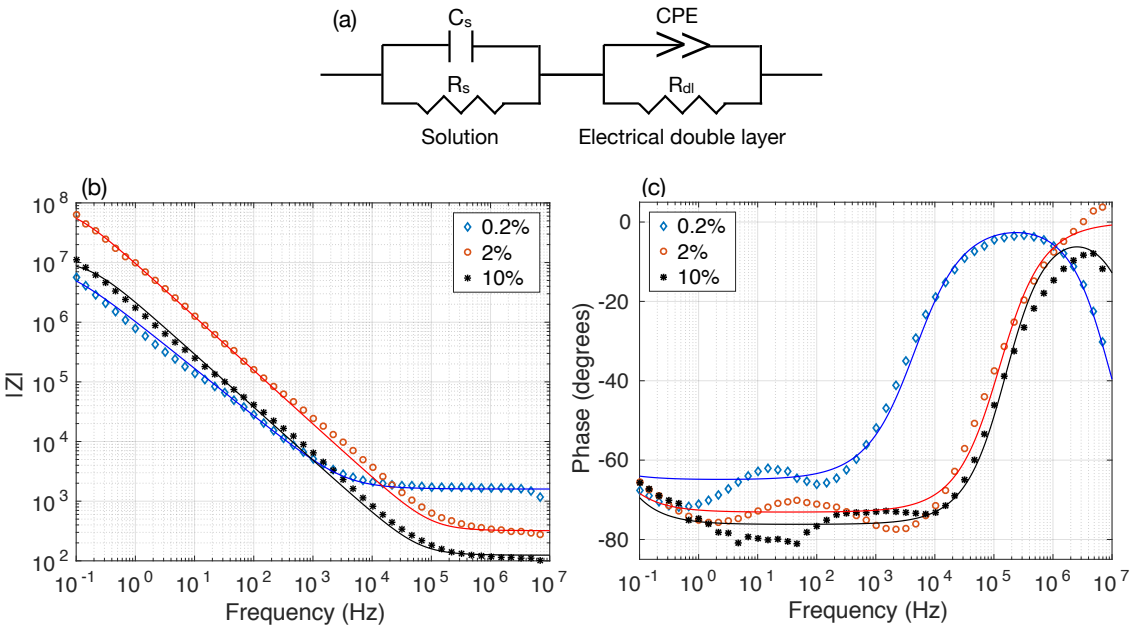

Figure 105. Experimental EIS spectra of salt solutions of different concentrations. (a) Randles equivalent circuit featuring a series of two parallel RC elements corresponding to the solution and the EDL, respectively. The capacitance of the EDL is modelled as a constant phase element (CPE) to consider deviations from the ideal capacitor behaviour. (b) Impedance amplitude spectra for the different concentrations. The saturation at high frequency is indicative of the EDL being shunted and the circuit behaving as mainly resistive. The lower saturation levels for higher concentrations derive from the increased conductivity of the solution. (c) Phase spectra for the same solutions. The increase of the phase to values close to 0° is indicative of the resistive regime at high frequency. Spectra are fitted to the Randles circuit described above, as shown by the continuous lines.

6. Preliminary results

Having optimised the fabrication of the electrical assay and established reliable measurement protocols, this section presents some preliminary EIS measurements to demonstrate the basic concept.

6.1. Salt solutions at different concentrations

A simple proof of concept measurement was carried out by exposing the contacts to salt solutions in DI water at different concentrations (0.2%, 2% and 10% (w/v)). Figure 105(b) and (c) show the measured impedance response for the three tested concentrations. Panel (b) plots a spectrum of the magnitude of the impedance $|Z|$, while panel (c) illustrates the phase behaviour.

This system can be modelled by the Randles circuit [237] illustrated in Figure 105(a), whereby the solution and the EDL are modelled as two distinct RC parallel elements. However, the EDL is known to deviate from an ideal capacitor, which is typically ascribed

to the roughness of the electrode surface [238,239]. This discrepancy is commonly accounted for by substituting the capacitance of the EDL with a constant phase element (CPE), whose impedance Z_{CPE} is assumed to be of the form:

$$Z_{CPE} = \frac{1}{(j\omega Q)^n} \tag{56}$$

where Q substitutes the standard capacitance C and n accounts for deviations. In particular, Z_{CPE} reduces to a perfect capacitor for $n = 1$, while values in the range $0<n<1$ describe deviations from the ideal conditions.

Continuous lines in Figure 105(b) and (c) represent the curves of best fit to the Randles circuit described above. The non ideality of the EDL is confirmed by the obtained values of n, which are 0.86, 0.88 and 0.85 for the different concentrations. Note that $|Z|$ saturates at high frequencies, corresponding to the RC parallel of the EDL being shunted by the electric field. In this regime, the impedance reduces to the resistance of the solution. Indeed, the saturation levels decrease for increasing salt concentration, confirming that solutions at high salt concentrations have lower resistance. A further breakdown and linear decrease are expected above the observed saturation level, as suggested by the blue curve. However, since the capacitance of the solution is typically negligible, the transition frequency is too high to be measured with standard equipment.

These arguments are also confirmed by the phase spectra in Figure 105(c). The low frequency behaviour is capacitive, as revealed by the phase approaching values close to -90°. As the frequency increases, so does the phase, until values close to 0° are obtained in the MHz range, which is indicative of the resistive behaviour of the circuit. Similarly to the case of $|Z|$, a subsequent drop is expected at higher frequencies due to the capacitance of the solution. A decreasing trend is indeed observed for the 0.2% (w/v) solution (blue curve) which has the lowest solution breakdown frequency due to the high electrical resistance compared to the other two cases.

As a final remark, no traps were fabricated above the electrodes in this experiment to avoid the addition of further circuit elements. The aim of this test was to show the quality of the contacts and the ability to produce reliable results for a relatively simple scenario.

Furthermore, all the measurements were acquired in a static configuration, i.e. no flow was applied to the solution to remove the influence of moving charges on the measurements.

6.2. 6-Mercapto-1-hexanol (MCH) self-assembled monolayer (SAM)

As a further proof of concept experiment, I decided to probe the formation of a self-assembled monolayer (SAM) on the exposed tips of the electrodes. A SAM is formed by the surface assembly of molecules containing a head and a tail group connected by a hydrocarbon chain of variable length, as schematically shown in Figure 106(a). Once the heads are bound onto the surface, a self-organisation process leads to a tight packing of the tails driven by the minimisation of the free energy and mainly regulated by van der Waals interactions. Typically, the head group is chosen to be highly reactive to the surface of interest and to ensure strong binding. Here, I selected 6-mercapto-1-hexanol (MCH) since the head contains a thiol group (-SH), which readily and strongly binds to gold, as shown by the rightmost molecule in Figure 106(a). The tail has a hydroxyl group (-OH). Part of the experiment was conducted in flow and consisted of three main steps: flushing of PBS solution to establish a baseline and verify stability, exposure of the electrodes to a solution of MCH in PBS and a final washing step with PBS.

Typical impedance and phase spectra at different stages are illustrated in Figure 106(b), while Figure 106(c) shows the variation of the impedance amplitude and phase at a fixed frequency (176 Hz). The reason for choosing this frequency is twofold: a) from Figure 106(b), it is clear that differences between the spectra are maximised in the hundreds of Hz frequency region, as highlighted by the significant steepness of the phase response; b) in the 10^2-10^3 Hz range, the electric field typically drops within the EDL, which makes the detection very sensitive to the surface and therefore ideal to probe the formation of the thin SAM.

After flushing the microfluidic chip with PBS solution, a 0.14 mg/ml MCH solution in PBS was introduced for several hours. The formation of the SAM is confirmed by the significant decrease in phase, which suggests that the surface layer is introducing an extra capacitance. An increase in impedance is also expected due to the SAM restricting the current flow. The self-arrangement of the SAM layer was allowed to happen overnight (with zero flow), as shown by the middle section of Figure 106(c).

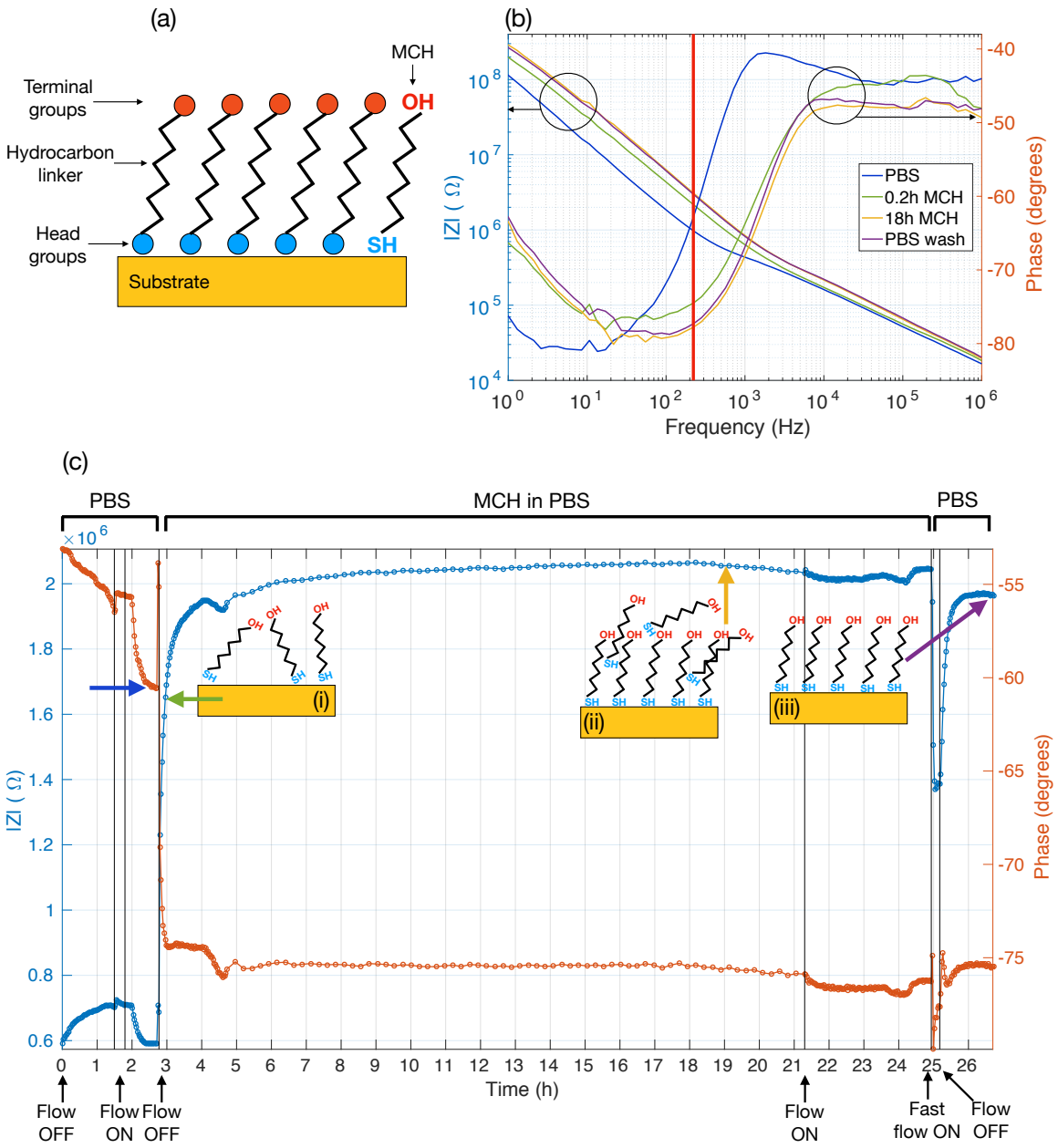

Figure 106. Experimental EIS study of the formation of a MCH SAM onto the electrodes. (a) Schematic of a SAM assembled on a surface. Head groups bind to the substrate, while the tail groups rearrange to minimise the energy of the layer. The last molecule on the right-hand side is an MCH molecule, featuring a thiol (-SH) as a head group and a hydroxyl group (-OH) in the tail. (b) Impedance (left axis) and phase (right axis) spectra at different stages of the SAM formation. The first PBS spectrum establishes a starting condition (blue curve). MCH at different time points modify the spectra to the green and orange one, while a final PBS wash produces the purple spectrum. (c) Impedance and phase over time at 222Hz, as indicated by the red vertical line in panel (b). Differently coloured arrows refer to the time point at which the spectra in panel (b) were plotted. The insets in (c) show different stages of the SAM formation: (i) molecules start to bind to gold; (ii) the tails are fully arranged; unbound and misoriented molecules are also present; (iii) fully formed SAM after the PBS washing step. Flow conditions are indicated below the x axis and all curves in panel (b) and (c) are obtained from a single experiment.

It is worth noting that the flow rate influences the electrical readout, as indicated by the labels below the x-axis. For instance, the flow was terminated at time zero, when the PBS

reached the contacts and measurements started. A drift of both |Z| and phase is clearly visible, which is due to the flow in the channel gradually decreasing over time. Similarly, the behaviour upon the introduction of the MCH solution (at t~3h) is a convolution of the flow rate slowly decreasing and the MCH molecule beginning to bind. Finally, the application of a 0.05 µl/min flow (at t~21h) resulted in slight decrease of |*Z*| and phase.

Therefore, in order to exclude any artefact of the flow rate, I performed a final washing step with PBS and allowed the flow to stabilise (as visible from the flatness of the curves at the end of the experiment). This final step removed unbound molecules and ensured that the SAM was indeed stable on the surface. The different final values of both impedance and phase as compared to the PBS starting point confirm that the SAM was formed.

7. Conclusions and future perspectives

In this final chapter of the thesis I have explored the possibility of using electrical impedance spectroscopy (EIS) to study single bacteria. A survey of the existing literature revealed that while single eukaryotic and bacterial cell resolution has been achieved with flow cytometry assays, electrical observation of an individual bacterium over time is more challenging and has not yet been reported. Therefore, we sought to integrate the hydrodynamic trapping assay with co-planar electrodes to probe the small volume of a single trap. The main outcomes of this work can be summarised as follows:

- Hydrodynamic trapping is a promising platform to hold a single bacterium in place over time and continuously expose it to an electric field. However, while the small volume of the trapping area maximises the overlap between the field and the bacterium, it also brings the disadvantage of being extremely sensitive to bacterial motility, as I will detail below along with potential solutions.

- COMSOL simulations of a single trap showed that the strong field confinement affords sufficient sensitivity to produce significant changes of the electrical readout upon trapping of a single bacterium. In addition, the simulations highlighted an interesting double resonance effect manifested as two dips in the relative phase of the impedance. An analysis of the field distributions and the homogeneous model of a dead bacterium suggested that the dips occur when the inner membrane and cytoplasm of the bacterium are sequentially shunted by the field. Finally, the two

simulated models of a dead micro-organism showed that the assay should be sensitive enough to electrically detect the disruption of the outer membrane and the eventual cell death.

- The fabrication of the device was optimised, which included a metal lift-off process, the coverage of the metal tracks with an insulating layer of SU8, and the fabrication of the trapping wells in SU8. Moreover, I carefully designed the interfacing to electrical wires and instruments to ensure reliability of the measurement apparatus. In fact, any inhomogeneity and variability in the copper wires as well as human error in the gluing and soldiering process would impact negatively the reproducibility of the experiments. The size and the geometry of the electrodes were standardised to fit a custom designed 3D printed unit equipped with spring-loaded probes in order to connect the device to a potentiostat.

- Finally, I presented some preliminary results that showed the ability of the device to sense different electrical properties. In particular, I first examined salt solutions at different concentrations, for which the Randles equivalent circuit model provided satisfactory fits. Secondly, I studied the formation of an MCH SAM onto the gold electrodes. These experiments confirmed the surface sensitivity of the assay, which was able to detect the different stages of the formation of the SAM.

There are, however, a few limitations. Two drawbacks concern the validity of the COMSOL simulations, a third one is related to the motility of the bacterium.

Firstly, the electrical double layer (EDL) was not included in the COMSOL model because of the added complexity of implementing it. The effects of the EDL should be negligible since the bacterial resonances occur in the 10^6-10^8 Hz frequency region, which are above the typical threshold for shunting the EDL (10^4-10^5 Hz). On the other hand, 10^6-10^8 Hz could be challenging to probe experimentally with standard equipment. Therefore, the bacterial dips should occur at frequencies large enough to bypass the EDL, but low enough to be measurable experimentally. To this purpose, their spectral position can be tuned experimentally by changing the conductivity of the medium. In particular, a lower conductivity would shift the observed dips towards lower, measurable frequencies. However, a trade-off needs to be made in this case, because long-term bacterial viability might be compromised in low conductivity media.

Secondly, I implemented two electrical models of a dead bacterium which rely on significant assumptions. The enlargement of the bacteria periplasm upon membrane rupture was chosen arbitrarily and the uniform sphere model does not consider the three-shell cell envelope. While both models are based on educated guesses and published data obtained with an electrorotation experiment, further experimental investigations are needed to refine these models.

Finally, regarding the motility, we note that bacteria can move inside each trap. This ability can be counterproductive for the electrical assay, since it introduces significant noise into the electrical measurement which may screen the subtle changes predicted in simulation. However, measurements are needed to confirm this, and solutions may be found. For instance, CCCP might be employed to reversibly inhibit motility in order to minimise the noise due to bacterial oscillations inside the trap. Alternatively, the trap could be designed to limit the bacterium oscillations upon trapping, even though this would decrease the trapping efficiency of the assay (as discussed extensively in sections 7 and 8 of chapter III). A more viable solution might be to use a different capture method, such as optical tweezing or antibody binding. An external laser would allow us to trap a single bacterium and to place it onto the electrode sensing areas. Similarly, functionalising the gold surface with antibodies selective to a specific bacteria strain would result in the bacterium being more strongly tethered in the vicinity of the field.

In conclusion, electrical impedance spectroscopy (EIS) appears to be a valuable tool for the detection and study of micro-organisms. Microorganisms live in a liquid world where they constantly exchange compounds and ions in order to maintain their transmembrane potential. Hence, it is sensible to assume that an electrical method might probe bacterial interactions with their environment, and their reaction to external challenges. In particular, EIS could represent a valuable addition to a susceptibility assay by providing sufficient sensitivity to the changes induced by antibiotics on a short timescale, as suggested by the simulation results presented here.

V. Conclusions and future outlook

Studying the effects of antibiotics on individual bacteria is of paramount importance for the fight against antimicrobial resistance. Following the smallest unit of a bacterial infection should provide detailed information on the shortest possible timescale. Additionally, any bulk averaging effect is avoided. Rapid detection and quantification of susceptibility are urgently needed to replace traditional tests based on bacterial growth because of their intrinsic slowness. The aim of this thesis was to highlight technological means of addressing these needs and to provide potential systems to measure them.

The major outcomes arising from this work are as follows:

- **Single cell analysis**. There is a steadily growing interest in single cell analysis, and my work perfectly fits this trend. Indeed, the motility-morphology analysis of individual *E. coli* cells revealed a significant heterogeneity of the bacterial response that enabled us to investigate the time-dependent action of different antibiotics. Additionally, the single cell analysis afforded the ability to record phenotypical changes as soon as they took place, instead of being masked by bulk averaging effects. This aspect, in combination with the rapidity of the biological response itself, resulted in a short detection time of 1 hour from spiking the culture with antibiotics. Similar performance was obtained with three antibiotics with different mechanisms of action, thereby proving a degree of generality for the approach.

- **Multiparameter analysis**. Bacteria are extremely complex and variable entities. Even though the reductionist mindset of a physicist would like to do so, it would be a gross underestimation to state that a single parameter could explain bacterial behaviour in the diverse circumstances encountered in cultures. Hence, multiparametric analysis is needed. This is yet another key aspect of my work, as particularly shown by the susceptibility results discussed in section 12 of chapter III. The combined motility-morphology approach not only led to a reduction in detection time, but also allowed us to assess the different modes of action for the antibiotics. In the last chapter (IV), I explored the use of EIS for profiling antibiotic susceptibility. While I was unable to conduct experiments on single bacteria due to

time constraints, simulations predict the approach to be feasible and sufficiently sensitive to detect signatures of bacterial death.

- **Microfluidics**. Controlling the flow of fluids on the microscale is crucial to directing and sorting bacteria in chip-based diagnostic. In this work, the initial detection was envisaged to rely on a photonic resonant surface. However, this first route was unable to provide sufficient spatial resolution to examine individual *E. coli*, as compared to a standard phase contrast microscope, so was not pursued in the end. Nevertheless, microfluidic trapping combined with phase contrast microscopy was sufficient to gain considerable insights, which highlights the power of microfluidics. Microfluidic assays will also be crucial for future developments of the proposed EIS approach, whereby single bacteria need to be localised in the volume probed by the electric field over time.

- **Initial hypotheses do not always work** and do not necessarily conform to expectations. The photonic platform was not able to deliver the expected performance, hence the need to change strategy. This process has been a valuable lesson of my scientific development, which pushed me to modify my original research plan.

- **Interdisciplinarity**. This thesis is inherently multidisciplinary, which fits the ever-increasing need for acquiring diverse competences in order to tackle important biological questions. Traditional microbiology alone is not able to address antimicrobial resistance. There needs to be cooperation between different disciplines to identify such biological problems and appropriate strategies to address them. Indeed, this thesis has drawn inspiration and borrowed knowledge from physics, microbiology, mathematics, electrical engineering and medicine. Physicists and engineers might be very ingenious at solving problems and developing new technologies. However, technology should not be developed for its own sake and it is only through the synergistic interaction with other disciplines that biomedical problems can be successfully addressed.

Looking forward, an immediate further study would involve the determination of the minimum inhibitory concentration of different antibiotics. The motility loss and morphological changes could be studied for different drug concentrations in order to

identify a threshold value that is able to establish the MIC. This feature would add the advantage of making the assay more quantitative instead of providing a simple binary susceptible/resistant outcome.

The EIS assessment of the individual trapped bacteria is another short-term future development. The design, simulations and fabrication are already optimised. Experiments would provide evidence to support (or disprove) the theoretical modelling, while adding a potential third system to profile antibiotic susceptibility. Even though the hydrodynamic trapping might not be the most suitable platform, other retention mechanisms could be used, such as optical tweezers or antibody binding. However, regardless of the mechanism, electrically probing a single bacterium is novel and exciting, and therefore worth pursuing.

In the long term, applications of the assay could extend beyond antibiotic susceptibility testing to *in-vitro* evolution or bacterial communication studies, where the platform could also benefit from other analysis techniques like fluorescence or Raman spectroscopy. This would extend the set of examined biological parameters. Finally, the multiparameter capability could make the platform suitable for antibiotic screening and for testing new antimicrobial agents by providing much richer data compared to simply testing the agents on solid or liquid media.

In conclusion, despite the significant advances I have reported in this thesis, numerous challenges are yet to be addressed and they still pose exciting research questions for the future. Answers to these questions will shape our future understanding of the bacterial realm and may eventually enable us to tackle antimicrobial resistance. It is our obligation to preserve the power of antibiotics for future generations. While it might sound a bit presumptuous for us humans to attempt slowing down the natural course of evolution towards universal resistance, this is what it takes if we want to have a chance to win the race against antimicrobial resistance.

A1. Appendix 1. Microfluidic chips designs and setup

A1.1. Microfluidic chips designs

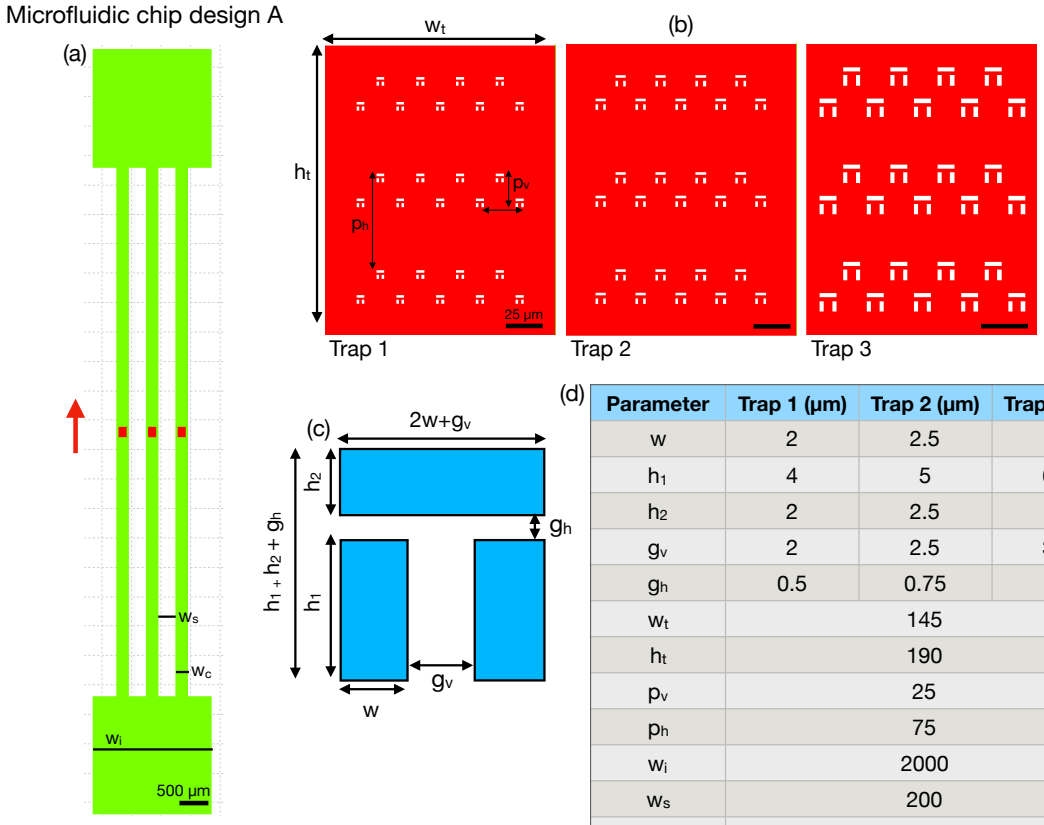

Parameter	Trap 1 (µm)	Trap 2 (µm)	Trap 3 (µm)
w	2	2.5	3
h_1	4	5	6.5
h_2	2	2.5	3
g_v	2	2.5	3.5
g_h	0.5	0.75	1
w_t	145		
h_t	190		
p_v	25		
p_h	75		
w_i	2000		
w_s	200		
w_c	250		

Figure A1.1. Microfluidic chip design A. (a) Diagram of the whole chip consisting of 3 parallel channels. The red arrow indicates the direction of the fluid flow. Different colours (green and red) refer to different thicknesses of the SU8 mould (10 µm and 2 µm, respectively), hence different electron beam exposures. (b) Different trap geometries fabricated in each channel (from left to right in (a)). (c) Diagram of a single trap highlighting relevant dimensions. (d) Relevant dimensions of the design.

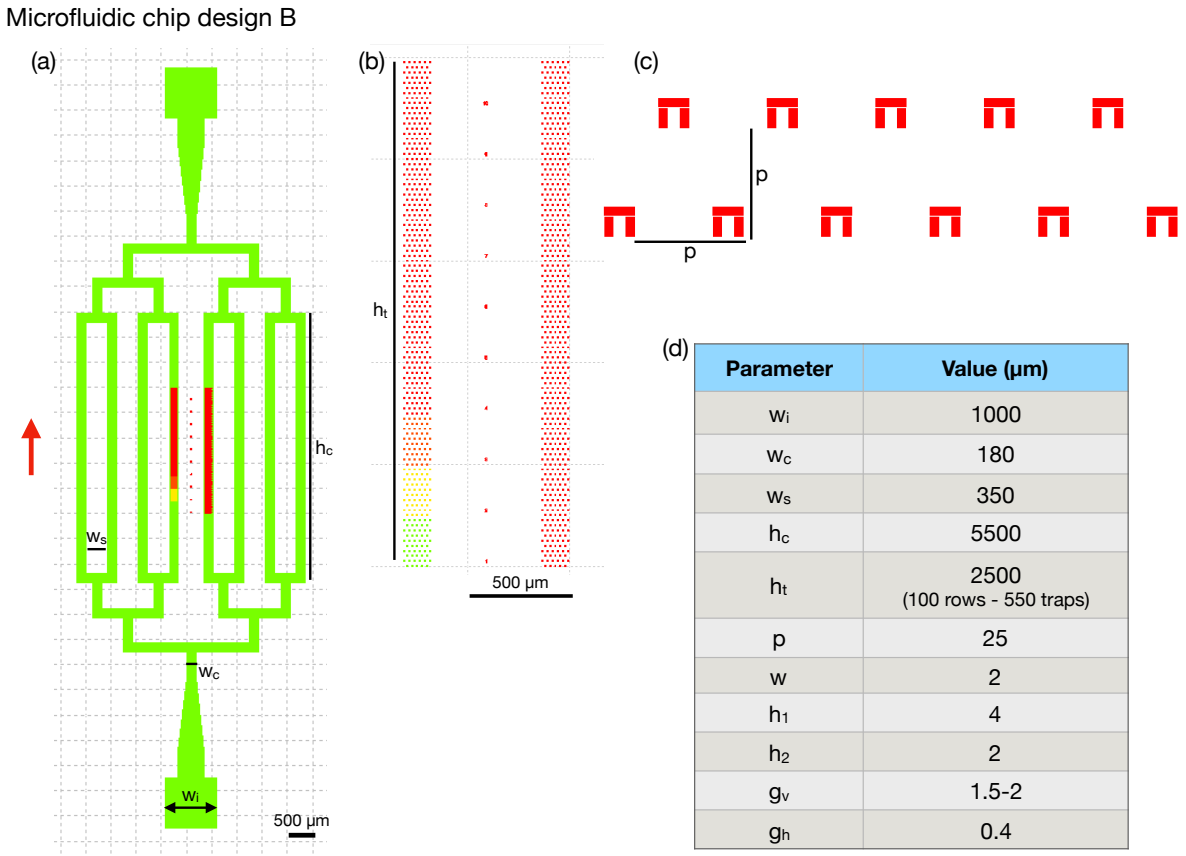

Parameter	Value (µm)
w_i	1000
w_c	180
w_s	350
h_c	5500
h_t	2500 (100 rows - 550 traps)
p	25
w	2
h_1	4
h_2	2
g_v	1.5-2
g_h	0.4

Figure A1.2. Microfluidic chip design B. (a) Diagram of the whole chip consisting of 8 parallel channels. The red arrow indicates the direction of the fluid flow. Channels in green are exposed with electron beam in SU8 for the mould. The columns of traps in the central channels are exposed onto a glass substrate. (b) Close-up of the trap arrays. Different colours indicate different electron beam dose factors. A total of 100 rows of traps, corresponding to 550 traps, are fabricated in each channel. (c) A pair of rows of traps showing the alternation of 5 and 6 traps per row. (d) Relevant dimensions of the design.

A1.2. Microfluidic setup

After bonding the PDMS chips onto the glass substrates with traps (as per methods sections 10.1 and 10.2 of chapter III), microfluidic tubes were manually inserted in the holes punched through the PDMS chip with the aid of round-tip tweezers. 1 ml plastic syringes from Terumo were employed to load and flush solutions. Tygon tubes E-3603 (inner diameter 0.8mm, outer diameter 2.4 mm and wall thickness of 0.8 mm) were used to connect the syringe to the microfluidic chip. Tubes were connected to the syringes with 1-100 µl standard Eppendorf pipette tips. Tubes were cut to a length of approximately 10 cm. The flow rate was initially set to 10 µl/ml and subsequently decreased to 10-15 nl/min and the solution was allowed to stabilise for 15 to 20 minutes before starting to record videos. 10 µl/ml was chosen to allow the solution to reach the microfluidic chip in a

reasonable time (approximately 5 to 6 minutes) while preventing excessive pressure from building up and creating leaks. 10 or 15 nl/min was chosen for most of the experiments (unless stated otherwise throughout the thesis) as a result of the optimisation described in sections 7 and 8 of chapter III. It was found that pulling solutions from an external reservoir consistently resulted in the channel collapsing, thereby stopping the fluid flow and preventing any data acquisition. Pushing liquids from the syringe was determined to be a better approach and the microfluidic chip was able to withstand flow rates of up to 25-30 µl/min before tubes came out of the PDMS holes due to the increased pressure. The same microfluidic syringe pump was used throughout the thesis research (Legato 180 from kdScientific).

Bibliography

1. G. Pitruzzello and T. F. Krauss, "Photonic crystal resonances for sensing and imaging," J. Opt. **20**(7), 073004 (2018).
2. D. Threm, Y. Nazirizadeh, and M. Gerken, "Photonic crystal biosensors towards on-chip integration," J. Biophotonics **5**(8–9), 601–616 (2012).
3. H. Inan, M. Poyraz, F. Inci, M. A. Lifson, M. Baday, B. T. Cunningham, and U. Demirci, "Photonic crystals: Emerging biosensors and their promise for point-of-care applications," Chem. Soc. Rev. **46**(2), 366–388 (2017).
4. B. Troia, A. Paolicelli, F. De Leonardis, and V. M. N. Passaro, "Photonic Crystals for Optical Sensing : A Review," Adv. Photonic Cryst. 241–295 (2013).
5. A. Manz, N. Graber, and H. M. Widmer, "Miniaturized Total Chemical Analysis System: a Novel Concept for Chemical Sensing," Sensors Actuators, B Chem. **1**, 244–248 (1990).
6. *Photonic Sensor Market by Type, Technology, Application— Global Opportunity Analysis and Industry Forecast, 2014- 2021 (Allied Market Research)* (2014).
7. L. Bornmann and R. Mutz, "Growth Rates of Modern Science: A Bibliometric Analysis Based on the Number of Publications and Cited References," J. Assoc. Inf. SCIIENCE Technol. **60**(11), 2215–2222 (2015).
8. "Web of Science Service for UK Education, Jisc, Digital Resources," (n.d.).
9. X. Fan, I. M. White, S. I. Shopova, H. Zhu, J. D. Suter, and Y. Sun, "Sensitive optical biosensors for unlabeled targets: A review," Anal. Chim. Acta **620**(1–2), 8–26 (2008).
10. J. D. Joannopoulos, S. G. Johnson, J. Winn, and R. D. Meade, *Photonic Crystals: Molding the Flow of Light*, Second Edi (Princeton University Press, 2007).
11. T. F. Krauss, R. M. D. La Rue, and S. Brandt, "Two-dimensional photonic- bandgap structures operating at near-infrared wavelengths," Nature **383**, 399–402 (1996).
12. H. Sekoguchi, Y. Takahashi, T. Asano, and S. Noda, "Photonic crystal nanocavity with a Q-factor of ~9 million," Opt. Express **22**(1), 916 (2014).
13. S. S. Wang and R. Magnusson, "Theory and applications of guided-mode resonance filters," Appl. Opt. **32**(14), 2606 (1993).
14. S. Fan and J. D. Joannopoulos, "Analysis of guided resonances in photonic crystal slabs," Phys. Rev. B **65**(23), 1–8 (2002).
15. D. A. Armbruster and T. Pry, "Limit of blank, limit of detection and limit of quantitation.," Clin. Biochem. Rev. **29**, 49–52 (2008).
16. M. Moretti, D. Sisti, M. B. Rocchi, and E. Delprete, "CLSI EP17-A protocol: A useful tool for better understanding the low end performance of total prostate-specific antigen assays," Clin. Chim. Acta **412**(11–12), 1143–1145 (2011).
17. I. M. White and X. Fan, "On the performance quantification of resonant refractive index sensors," Opt. Express **16**(2), 1020–1028 (2008).
18. T. Claes, J. G. Molera, K. De Vos, E. Schacht, R. Baets, and P. Bienstman, "Label-free biosensing with a slot-waveguide-based ring resonator in silicon on insulator," IEEE Photonics J. **1**(3), 197–204 (2009).
19. J. Hu, X. Sun, A. Agarwal, and L. C. Kimerling, "Design guidelines for optical resonator biochemical sensors," J. Opt. Soc. Am. B **26**(5), 1032 (2009).
20. H. Zhu, I. M. White, J. D. Suter, P. S. Dale, and X. Fan, "Analysis of biomolecule detection with optofluidic ring resonator sensors," Opt. Express **15**(15), 9139–9146 (2007).
21. M. El Beheiry, V. Liu, S. Fan, and O. Levi, "Sensitivity enhancement in photonic crystal slab biosensors.," Opt. Express **18**(22), 22702–14 (2010).
22. I. D. Block, P. C. Mathias, S. I. Jones, L. O. Vodkin, and B. T. Cunningham, "Optimizing the spatial resolution of photonic crystal label-free imaging.," Appl.

Opt. **48**(34), 6567–74 (2009).
23. I. D. Block, N. Ganesh, M. Lu, and B. T. Cunningham, "A Sensitivity Model for Predicting Photonic Crystal Biosensor Performance," IEEE Sens. J. **8**(3), 274–280 (2008).
24. A. Ricciardi, M. Pisco, I. Gallina, S. Campopiano, V. Galdi, L. O' Faolain, T. F. Krauss, and A. Cusano, "Experimental evidence of guided-resonances in photonic crystals with aperiodically ordered supercells," Opt. Lett. **35**(23), 3946 (2010).
25. A. Ricciardi, M. Pisco, A. Cutolo, A. Cusano, L. O'Faolain, T. F. Krauss, G. Castaldi, and V. Galdi, "Evidence of guided resonances in photonic quasicrystal slabs," Phys. Rev. B - Condens. Matter Mater. Phys. **84**(8), 1–4 (2011).
26. B. Cunningham, P. Li, B. Lin, and J. Pepper, "Colorimetric resonant reflection as a direct biochemical assay technique," Sensors Actuators, B Chem. **81**(2–3), 316–328 (2002).
27. I. D. Block, L. L. Chan, and B. T. Cunningham, "Photonic crystal optical biosensor incorporating structured low-index porous dielectric," Sensors Actuators B Chem. **120**(1), 187–193 (2006).
28. L. Chan, M. Pineda, J. Heeres, P. Hergenrother, and B. Cunningham, "A General Method for Discovering Inhibitors of Protein-DNA Interactions Using Photonic Crystal Biosensors," ACS Chem. Biol. **3**(7), 437–448 (2008).
29. M. C. Estevez, M. Alvarez, and L. M. Lechuga, "Integrated optical devices for lab-on-a-chip biosensing applications," Laser Photon. Rev. **6**(4), 463–487 (2012).
30. M. C. Estevez, M. A. Otte, B. Sepulveda, and L. M. Lechuga, "Trends and challenges of refractometric nanoplasmonic biosensors: A review," Anal. Chim. Acta **806**, 55–73 (2014).
31. J. Homola, "Surface plasmon resonance sensors for detection of chemical and biological species," Chem. Rev. **108**(2), 462–493 (2008).
32. M. Huang, A. A. Yanik, T.-Y. Chang, and H. Altug, "Sub-wavelength nanofluidics in photonic crystal sensors," Opt. Express **17**(26), 24224 (2009).
33. J. Juan-Colás, S. Johnson, and T. Krauss, "Dual-Mode Electro-Optical Techniques for Biosensing Applications: A Review," Sensors **17**(9), 2047 (2017).
34. W. Zhang, N. Ganesh, I. D. Block, and B. T. Cunningham, "High sensitivity photonic crystal biosensor incorporating nanorod structures for enhanced surface area," Sensors Actuators, B Chem. **131**(1), 279–284 (2008).
35. R. Magnusson, D. Wawro, S. Zimmerman, and Y. Ding, "Resonant photonic biosensors with polarization-based multiparametric discrimination in each channel," Sensors **11**(2), 1476–1488 (2011).
36. J. Juan-Colás, S. Johnson, and T. Krauss, "Dual-Mode Electro-Optical Techniques for Biosensing Applications: A Review," Sensors **17**(9), 2047 (2017).
37. J. Juan-Colás, T. F. Krauss, and S. D. Johnson, "Real-Time Analysis of Molecular Conformation Using Silicon Electrophotonic Biosensors," ACS Photonics **4**(9), 2320–2326 (2017).
38. J. Juan-Colás, A. Parkin, K. E. Dunn, M. G. Scullion, T. F. Krauss, and S. D. Johnson, "The electrophotonic silicon biosensor," Nat. Commun. **7**, 1–7 (2016).
39. C. Ge, M. Lu, S. George, T. A. Flood, C. Wagner, J. Zheng, A. Pokhriyal, J. G. Eden, P. J. Hergenrother, and B. T. Cunningham, "External cavity laser biosensor," Lab Chip **13**(7), 1247–1256 (2013).
40. M. Zhang, J. Peh, P. J. Hergenrother, and B. T. Cunningham, "Detection of Protein–Small Molecule Binding Using a Self-Referencing External Cavity Laser Biosensor," J. Am. Chem. Soc. **136**(16), 5840–5843 (2014).
41. M. Zhang, C. Ge, M. Lu, Z. Zhang, and B. T. Cunningham, "A self-referencing biosensor based upon a dual-mode external cavity laser," Appl. Phys. Lett. **102**(21), (2013).

42. D. Wawro, P. Koulen, Y. Ding, S. Zimmerman, and R. Magnusson, "Guided-mode resonance sensor system for early detection of ovarian cancer," in *Proceeding of SPIE*, G. L. Coté, ed. (2010), **7572**, p. 75720D.
43. W.-K. Kuo, N.-C. Huang, H.-P. Weng, and H.-H. Yu, "Tunable phase detection sensitivity of transmitted-type guided-mode resonance sensor in a heterodyne interferometer," Opt. Express **22**(19), 22968 (2014).
44. W.-K. Kuo, S.-H. Syu, P.-Z. Lin, and H. H. Yu, "Tunable sensitivity phase detection of transmitted-type dual-channel guided-mode resonance sensor based on phase-shift interferometry," Appl. Opt. **55**(4), 903 (2016).
45. P. K. Sahoo, S. Sarkar, and J. Joseph, "High sensitivity guided-mode-resonance optical sensor employing phase detection," Sci. Rep. **7**(1), 1–7 (2017).
46. G. J. Triggs, Y. Wang, C. P. Reardon, M. Fischer, G. J. O. Evans, and T. F. Krauss, "Chirped guided-mode resonance biosensor," Optica **4**(2), 229–233 (2017).
47. Y. Nazirizadeh, U. Bog, S. Sekula, T. Mappes, U. Lemmer, and M. Gerken, "Low-cost label-free biosensors using photonic crystals embedded between crossed polarizers," Opt. Express **18**(18), 19120–19128 (2010).
48. Y. Nazirizadeh, V. Behrends, A. Prósz, N. Orgovan, R. Horvath, A. M. Ferrie, Y. Fang, C. Selhuber-Unkel, and M. Gerken, "Intensity interrogation near cutoff resonance for label-free cellular profiling," Sci. Rep. **6**, 1–6 (2016).
49. Y. C. Lin, W. H. Hsieh, L. K. Chau, and G. E. Chang, "Intensity-detection-based guided-mode-resonance optofluidic biosensing system for rapid, low-cost, label-free detection," Sensors Actuators, B Chem. **250**, 659–666 (2017).
50. S. Jahns, M. Bräu, B.-O. Meyer, T. Karrock, S. B. Gutekunst, L. Blohm, C. Selhuber-Unkel, R. Buhmann, Y. Nazirizadeh, and M. Gerken, "Handheld imaging photonic crystal biosensor for multiplexed, label-free protein detection," Biomed. Opt. Express **6**(10), 3724 (2015).
51. M. Fischer, G. J. Triggs, and T. F. Krauss, "Optical sensing microbial life on surfaces," Appl. Environ. Microbiol. **84**(1), 1362–1371 (2016).
52. A. A. Khalili and M. R. Ahmad, "A Review of cell adhesion studies for biomedical and biological applications," Int. J. Mol. Sci. **16**(8), 18149–18184 (2015).
53. W. Chen, K. D. Long, M. Lu, V. Chaudhery, H. Yu, J. S. Choi, J. Polans, Y. Zhuo, B. A. C. Harley, and B. T. Cunningham, "Photonic crystal enhanced microscopy for imaging of live cell adhesion," Analyst **138**(20), 5886–5894 (2013).
54. Y. Zhuo, H. Hu, W. Chen, M. Lu, L. Tian, H. Yu, K. D. Long, E. Chow, W. P. King, S. Singamaneni, and B. T. Cunningham, "Single nanoparticle detection using photonic crystal enhanced microscopy," Analyst **139**(5), 1007–1015 (2014).
55. E. A. Lidstone, V. Chaudhery, A. Kohl, V. Chan, T. Wolf-Jensen, L. B. Schook, R. Bashir, and B. T. Cunningham, "Label-free imaging of cell attachment with photonic crystal enhanced microscopy," Analyst **136**(18), 3608–3615 (2011).
56. J. Juan-Colás, I. S. Hitchcock, M. Coles, S. Johnson, and T. F. Krauss, "Quantifying single-cell secretion in real time using resonant hyperspectral imaging," Proc. Natl. Acad. Sci. **115**(52), 13204–13209 (2018).
57. Y. Zhuo and B. Cunningham, "Label-Free Biosensor Imaging on Photonic Crystal Surfaces," Sensors **15**(9), 21613–21635 (2015).
58. G. J. Triggs, M. Fischer, D. Stellinga, M. G. Scullion, G. J. O. Evans, and T. F. Krauss, "Spatial Resolution and Refractive Index Contrast of Resonant Photonic Crystal Surfaces for Biosensing," IEEE Photonics J. **7**(3), 1–10 (2015).
59. E. Yablonovitch, T. J. Gmitter, R. D. Meade, A. M. Rappe, K. D. Brommer, and J. D. Joannopoulos, "Donor and acceptor modes in photonic band structure," Phys. Rev. Lett. **67**(24), 3380–3383 (1991).
60. V. Liu and S. Fan, "S4: A free electromagnetic solver for layered periodic structures," Comput. Phys. Commun. **183**(10), 2233–2244 (2012).

61. M. G. Moharam and T. K. Gaylord, "Rigorous coupled-wave analysis of planar-grating diffraction," J. Opt. Soc. Am. **71**(7), 811–818 (1981).
62. V. Liu, "Introduction to S4," https://web.stanford.edu/group/fan/S4/.
63. R. Rumpf, "EE 5337 - Computational Electromagnetics," http://emlab.utep.edu/ee5390cem.htm.
64. B. Saleh and M. C. Teich, *Fundamentals of Photonics* (Wiley, 1991).
65. "Postivite Ebeam Resists AR-P6200 (CSAR 62)," ALLRESIST Prod. Infos 22–23 (2014).
66. M. Polyanskiy, "Refractiveindex.info - refractive index database," https://refractiveindex.info/.
67. U. Fano, "Effects of Configuration Interaction on Intensities and Phase Shifts," Phys. Rev. **124**(6), 1866–1878 (1961).
68. M. Galli, S. L. Portalupi, M. Belotti, L. C. Andreani, L. O'Faolain, and T. F. Krauss, "Light scattering and Fano resonances in high-Q photonic crystal nanocavities," Appl. Phys. Lett. **94**(7), 071101 (2009).
69. G. Reshes, S. Vanounou, I. Fishov, and M. Feingold, "Cell shape dynamics in Escherichia coli," Biophys. J. **94**(1), 251–264 (2008).
70. C. E. H. Berger, R. P. H. Kooyman, and J. Greve, "Resolution in surface plasmon microscopy," Rev. Sci. Instrum. **65**(9), 2829–2836 (1994).
71. K. Syal, R. Iriya, Y. Yang, H. Yu, S. Wang, S. E. Haydel, H. Y. Chen, and N. Tao, "Antimicrobial susceptibility test with plasmonic imaging and tracking of single bacterial motions on nanometer scale," ACS Nano **10**(1), 845–852 (2016).
72. S. Wang, X. Shan, U. Patel, X. Huang, J. Lu, J. Li, and N. Tao, "Label-free imaging, detection, and mass measurement of single viruses by surface plasmon resonance," Proc. Natl. Acad. Sci. **107**(37), 16028–16032 (2010).
73. W. Wang, Y. Yang, S. Wang, V. J. Nagaraj, Q. Liu, J. Wu, and N. Tao, "Label-free measuring and mapping of binding kinetics of membrane proteins in single living cells," Nat. Chem. **4**(10), 846–853 (2012).
74. Y. Yang, H. Yu, X. Shan, W. Wang, X. Liu, S. Wang, and N. Tao, "Label-Free Tracking of Single Organelle Transportation in Cells with Nanometer Precision Using a Plasmonic Imaging Technique," Small **11**(24), 2878–2884 (2015).
75. G. M. Whitesides, "The origins and the future of microfluidics," Nature **442**(7101), 368–373 (2006).
76. D. Di Carlo, "Inertial microfluidics," Lab Chip **9**(21), 3038–3046 (2009).
77. N. Pamme, "Continuous flow separations in microfluidic devices," Lab Chip **7**(12), 1644–1659 (2007).
78. D. R. Reyes, D. Iossifidis, P.-A. Auroux, and A. Manz, "Micro Total Analysis Systems. 1. Introduction, Theory, and Technology," Anal. Chem. **74**(12), 2623–2636 (2002).
79. P.-A. Auroux, D. Iossifidis, D. R. Reyes, and A. Manz, "Micro Total Analysis Systems. 2. Analytical Standard Operations and Applications," Anal. Chem. **74**(12), 2637–2652 (2002).
80. J. S. Guasto, R. Rusconi, and R. Stocker, "Fluid Mechanics of Planktonic Microorganisms," Annu. Rev. Fluid Mech. **44**(1), 373–400 (2012).
81. F. J. H. Hol and C. Dekker, "Zooming in to see the bigger picture: Microfluidic and nanofabrication tools to study bacteria," Science (80-.). **346**(6208), 1251821 (2014).
82. D. Di Carlo, L. Y. Wu, and L. P. Lee, "Dynamic single cell culture array.," Lab Chip **6**(11), 1445–1449 (2006).
83. K. Kogermann, M. Putrinš, and T. Tenson, "Single-cell level methods for studying the effect of antibiotics on bacteria during infection," Eur. J. Pharm. Sci. **95**, 2–16 (2016).

84. L. Armbrecht and P. S. Dittrich, "Recent Advances in the Analysis of Single Cells," Anal. Chem. **89**(1), 2–21 (2017).
85. P. Wang, L. Robert, J. Pelletier, W. L. Dang, F. Taddei, A. Wright, and S. Jun, "Robust growth of escherichia coli," Curr. Biol. **20**(12), 1099–1103 (2010).
86. J. W. Bigger, "Treatment of staphylococcal infections with penicillin," Lancet **244**(294), 497–500 (1944).
87. R. A. Fisher, B. Gollan, and S. Helaine, "Persistent bacterial infections and persister cells," Nat. Rev. Microbiol. **15**(8), 453–464 (2017).
88. N. Q. Balaban, "Bacterial Persistence as a Phenotypic Switch," Science (80-.). **305**(5690), 1622–1625 (2004).
89. O. Gefen, C. Gabay, M. Mumcuoglu, G. Engel, and N. Q. Balaban, "Single-cell protein induction dynamics reveals a period of vulnerability to antibiotics in persister bacteria," Proc. Natl. Acad. Sci. **105**(16), 6145–6149 (2008).
90. J. Mannik, R. Driessen, P. Galajda, J. E. Keymer, and C. Dekker, "Bacterial growth and motility in sub-micron constrictions," Proc. Natl. Acad. Sci. **106**(35), 14861–14866 (2009).
91. J. Mannik, F. Wu, F. J. H. Hol, P. Bisicchia, D. J. Sherratt, J. E. Keymer, and C. Dekker, "Robustness and accuracy of cell division in Escherichia coli in diverse cell shapes," Proc. Natl. Acad. Sci. **109**(18), 6957–6962 (2012).
92. R. Sender, S. Fuchs, and R. Milo, "Revised Estimates for the Number of Human and Bacteria Cells in the Body," PLOS Biol. **14**(8), e1002533 (2016).
93. F. Alexander, "Penicillin - Nobel Lecture," https://www.nobelprize.org/uploads/2018/06/fleming-lecture.pdf.
94. A. Panáček, L. Kvítek, M. Smékalová, R. Večeřová, M. Kolář, M. Röderová, F. Dyčka, M. Šebela, R. Prucek, O. Tomanec, and R. Zbořil, "Bacterial resistance to silver nanoparticles and how to overcome it," Nat. Nanotechnol. **13**(1), 65–71 (2018).
95. H. Goossens, M. Ferech, R. Vander Stichele, and M. Elseviers, "Outpatient antibiotic use in Europe and association with resistance: A cross-national database study," Lancet **365**(9459), 579–587 (2005).
96. J. O'Neill, "Review on Antimicrobial Resistance. Tackling a Global Health Crisis: Rapid Diagnostics : Stopping Unnecessary Use of Antibiotics," Indep. Rev. AMR (October), 1–36 (2015).
97. A. Cassini, L. D. Högberg, D. Plachouras, A. Quattrocchi, A. Hoxha, G. S. Simonsen, M. Colomb-Cotinat, M. E. Kretzschmar, B. Devleesschauwer, M. Cecchini, D. A. Ouakrim, T. C. Oliveira, M. J. Struelens, C. Suetens, and D. L. Monnet, "Attributable deaths and disability-adjusted life-years caused by infections with antibiotic-resistant bacteria in the EU and the European Economic Area in 2015: a population-level modelling analysis," Lancet Infect. Dis. **19**(1), 56–66 (2019).
98. L. L. Silver, "Challenges of Antibacterial Discovery," Clin. Microbiol. Rev. **24**(1), 71–109 (2011).
99. R. J. Fair and Y. Tor, "Antibiotics and Bacterial Resistance in the 21st Century," Perspect. Medicin. Chem. **6**, 25–64 (2014).
100. J. A. Douglas Friedman, *Technological Challenges in Antibiotic Discovery and Development* (National Academies Press, 2014).
101. L. Ling, T. Schneider, A. Peoples, A. Spoering, I. Engels, B. Conlon, A. Mueller, T. Schaberle, D. Hughes, S. Epstein, M. Jones, L. Lazarides, V. Steaman, D. Cohen, C. Felix, A. Fettermann, W. Millett, A. Nitti, A. Zullo, C. Chen, and K. Lewis, "A new antibiotic kills pathogens without detectable resistance," Nature **517**(7535), 455–459 (2015).
102. L. Pantel, T. Florin, M. Dobosz-Bartoszek, E. Racine, M. Sarciaux, M. Serri, J.

Houard, J. M. Campagne, R. M. de Figueiredo, C. Midrier, S. Gaudriault, A. Givaudan, A. Lanois, S. Forst, A. Aumelas, C. Cotteaux-Lautard, J. M. Bolla, C. Vingsbo Lundberg, D. L. Huseby, D. Hughes, P. Villain-Guillot, A. S. Mankin, Y. S. Polikanov, and M. Gualtieri, "Odilorhabdins, Antibacterial Agents that Cause Miscoding by Binding at a New Ribosomal Site," Mol. Cell **70**(1), 83–94.e7 (2018).
103. N. S. McClure and T. Day, "A theoretical examination of the relative importance of evolution management and drug development for managing resistance," Proc. R. Soc. B Biol. Sci. **281**(1797), 1–8 (2014).
104. D. J. Shapiro, L. A. Hicks, A. T. Pavia, and A. L. Hersh, "Antibiotic prescribing for adults in ambulatory care in the USA, 2007-09," J. Antimicrob. Chemother. **69**(1), 234–240 (2014).
105. A. Köchling, C. Löffler, S. Reinsch, A. Hornung, F. Böhmer, A. Altiner, and J. F. Chenot, "Reduction of antibiotic prescriptions for acute respiratory tract infections in primary care: A systematic review," Implement. Sci. **13**(1), (2018).
106. T. Smieszek, K. B. Pouwels, F. C. K. Dolk, D. R. M. Smith, S. Hopkins, M. Sharland, A. D. Hay, M. V. Moore, and J. V. Robotham, "Potential for reducing inappropriate antibiotic prescribing in English primary care," J. Antimicrob. Chemother. **73**(suppl_2), ii36-ii43 (2018).
107. S. G. Jenkins and A. N. Schuetz, "Current concepts in laboratory testing to guide antimicrobial therapy," Mayo Clin. Proc. **87**(3), 290–308 (2012).
108. K. Syal, M. Mo, H. Yu, R. Iriya, W. Jing, S. Guodong, S. Wang, T. E. Grys, S. E. Haydel, and N. Tao, "Current and emerging techniques for antibiotic susceptibility tests," Theranostics **7**(7), 1795–1805 (2017).
109. A. Aroonnual, T. Janvilisri, P. Ounjai, and S. Chankhamhaengdecha, "Microfluidics: innovative approaches for rapid diagnosis of antibiotic-resistant bacteria," Essays Biochem. **61**(1), 91–101 (2017).
110. Z. Liu, N. Banaei, and K. Ren, "Microfluidics for Combating Antimicrobial Resistance," Trends Biotechnol. **35**(12), 1129–1139 (2017).
111. E. Zankari, H. Hasman, S. Cosentino, M. Vestergaard, S. Rasmussen, O. Lund, F. M. Aarestrup, and M. V. Larsen, "Identification of acquired antimicrobial resistance genes," J. Antimicrob. Chemother. **67**(11), 2640–2644 (2012).
112. J. Choi, J. Yoo, M. Lee, E.-G. Kim, J. S. Lee, S. Lee, S. Joo, S. H. Song, E.-C. Kim, J. C. Lee, H. C. Kim, Y.-G. Jung, and S. Kwon, "A rapid antimicrobial susceptibility test based on single-cell morphological analysis," Sci. Transl. Med. **6**(267), 267ra174-267ra174 (2014).
113. A. D. Hay, K. Birnie, J. Busby, B. Delaney, H. Downing, J. Dudley, S. Durbaba, M. Fletcher, K. Harman, W. Hollingworth, K. Hood, R. Howe, M. Lawton, C. Lisles, P. Little, A. MacGowan, K. O'Brien, T. Pickles, K. Rumsby, J. A. C. Sterne, E. Thomas-Jones, J. van der Voort, C. A. Waldron, P. Whiting, M. Wootton, and C. C. Butler, "The Diagnosis of Urinary Tract infection in Young children (DUTY): A diagnostic prospective observational study to derive and validate a clinical algorithm for the diagnosis of urinary tract infection in children presenting to primary care with an acute i," Health Technol. Assess. (Rockv). **20**(51), 1–197 (2016).
114. Ö. Baltekin, A. Boucharin, E. Tano, D. I. Andersson, and J. Elf, "Antibiotic susceptibility testing in less than 30 min using direct single-cell imaging," Proc. Natl. Acad. Sci. **114**(34), 9170–9175 (2017).
115. T. P. T. Cushnie, N. H. O'Driscoll, and A. J. Lamb, "Morphological and ultrastructural changes in bacterial cells as an indicator of antibacterial mechanism of action," Cell. Mol. Life Sci. **73**(23), 4471–4492 (2016).
116. N. A. C. Curtis, D. Orr, G. W. Ross, and M. G. Boulton, "Affinities of penicillins and cephalosporins for the penicillin-binding proteins of Escherichia coli K-12 and

their antibacterial activity," Antimicrob. Agents Chemother. **16**(5), 533–539 (1979).
117. T. S. J. Elliott and D. Greenwood, "The response od Pseudomonas Aeruginosa to azlocillin, ticarcillin and cefsulodin," J. Med. Microbiol. **16**, 351–362 (1983).
118. N. Kaldalu, R. Mei, and K. Lewis, "Killing by Ampicillin and Ofloxacin Induces Overlapping Changes in Escherichia coli Transcription Profile," Antimicrob. Agents Chemother. **48**(3), 890–896 (2004).
119. Y. Matsumoto, S. Sakakihara, A. Grushnikov, K. Kikuchi, H. Noji, A. Yamaguchi, R. Iino, Y. Yagi, and K. Nishino, "A microfluidic channel method for rapid drug-susceptibility testing of Pseudomonas aeruginosa," PLoS One **11**(2), 1–17 (2016).
120. S. Kim, H. J. Kim, and N. L. Jeon, "Biological applications of microfluidic gradient devices," Integr. Biol. **2**(11–12), 584–603 (2010).
121. B. Li, Y. Qiu, A. Glidle, D. McIlvenna, Q. Luo, J. Cooper, H. C. Shi, and H. Yin, "Gradient microfluidics enables rapid bacterial growth inhibition testing," Anal. Chem. **86**(6), 3131–3137 (2014).
122. Z. Hou, Y. An, K. Hjort, K. Hjort, L. Sandegren, and Z. Wu, "Time lapse investigation of antibiotic susceptibility using a microfluidic linear gradient 3D culture device.," Lab Chip **14**(17), 3409–18 (2014).
123. H. Sun, Z. Liu, C. Hu, and K. Ren, "Cell-on-hydrogel platform made of agar and alginate for rapid, low-cost, multidimensional test of antimicrobial susceptibility," Lab Chip **16**(16), 3130–3138 (2016).
124. S. Kim, F. Masum, J. Kim, H. J. Chung, and J. S. Jeon, "On-chip phenotypic investigation of combinatory antibiotic effects by generating orthogonal concentration gradients," Lab Chip **19**(6), 959–973 (2019).
125. C. N. Baroud, F. Gallaire, and R. Dangla, "Dynamics of microfluidic droplets," Lab Chip **10**(16), 2032–2045 (2010).
126. M. T. Guo, A. Rotem, J. A. Heyman, and D. A. Weitz, "Droplet microfluidics for high-throughput biological assays," Lab Chip **12**(12), 2146–2155 (2012).
127. L. Shang, Y. Cheng, and Y. Zhao, "Emerging Droplet Microfluidics," Chem. Rev. **117**(12), 7964–8040 (2017).
128. A. M. Kaushik, K. Hsieh, L. Chen, D. J. Shin, J. C. Liao, and T.-H. Wang, "Accelerating bacterial growth detection and antimicrobial susceptibility assessment in integrated picoliter droplet platform," Biosens. Bioelectron. **97**(June), 260–266 (2017).
129. J. Q. Boedicker, L. Li, T. R. Kline, and R. F. Ismagilov, "Detecting bacteria and determining their susceptibility to antibiotics by stochastic confinement in nanoliter droplets using plug-based microfluidics," **8**(8), 1265–1272 (2008).
130. K. Churski, T. S. Kaminski, S. Jakiela, W. Kamysz, W. Baranska-Rybak, D. B. Weibel, and P. Garstecki, "Rapid screening of antibiotic toxicity in an automated microdroplet system," Lab Chip **12**(9), 1629–1637 (2012).
131. F. Lyu, M. Pan, S. Patil, J. H. Wang, A. C. Matin, J. R. Andrews, and S. K. Y. Tang, "Phenotyping antibiotic resistance with single-cell resolution for the detection of heteroresistance," Sensors Actuators, B Chem. **270**(February), 396–404 (2018).
132. C. Josenhans and S. Suerbaum, "The role of motility as a virulence factor in bacteria," Int. J. Med. Microbiol. **291**(8), 605–614 (2002).
133. Q. Duan, M. Zhou, L. Zhu, and G. Zhu, "Flagella and bacterial pathogenicity," J. Basic Microbiol. **53**(1), 1–8 (2013).
134. G. Longo, L. Alonso-Sarduy, L. M. Rio, A. Bizzini, A. Trampuz, J. Notz, G. Dietler, and S. Kasas, "Rapid detection of bacterial resistance to antibiotics using AFM cantilevers as nanomechanical sensors," Nat. Nanotechnol. **8**(7), 522–526 (2013).
135. S. Kasas, F. S. Ruggeri, C. Benadiba, C. Maillard, P. Stupar, H. Tournu, G. Dietler, and G. Longo, "Detecting nanoscale vibrations as signature of life," Proc. Natl. Acad. Sci. **112**(2), 378–381 (2015).

136. A. Mustazzolu, L. Venturelli, S. Dinarelli, K. Brown, R. A. Floto, G. Dietler, L. Fattorini, S. Kasas, M. Girasole, and G. Longo, "A Rapid Unraveling of the Activity and Antibiotic Susceptibility of Mycobacteria," Antimicrob. Agents Chemother. **63**(3), 1–13 (2019).
137. H. Etayash, M. F. Khan, K. Kaur, and T. Thundat, "Microfluidic cantilever detects bacteria and measures their susceptibility to antibiotics in small confined volumes," Nat. Commun. **7**, 12947 (2016).
138. W. Jiang, A. Saxena, B. Song, B. B. Ward, T. J. Beveridge, and S. C. B. Myneni, "Elucidation of Functional Groups on Gram-Positive and Gram-Negative Bacterial Surfaces Using Infrared Spectroscopy," Langmuir **20**(26), 11433–11442 (2004).
139. V. Kara, C. Duan, K. Gupta, S. Kurosawa, D. J. Stearns-Kurosawa, and K. Ekinci, "Microfluidic Detection of Movements of Escherichia coli for Rapid Antibiotic Susceptibility Testing," Lab Chip **18**(5), 743–753 (2018).
140. F. C. Cheong, C. C. Wong, Y. Gao, M. H. Nai, Y. Cui, S. Park, L. J. Kenney, and C. T. Lim, "Rapid, High-Throughput Tracking of Bacterial Motility in 3D via Phase-Contrast Holographic Video Microscopy," Biophys. J. **108**(5), 1248–1256 (2015).
141. V. Narayanamurthy, S. Nagarajan, A. Y. Firus Khan, F. Samsuri, and T. M. Sridhar, "Microfluidic hydrodynamic trapping for single cell analysis: Mechanisms, methods and applications," Anal. Methods **9**(25), 3751–3772 (2017).
142. J. R. Rettig and A. Folch, "Large-scale single-cell trapping and imaging using microwell arrays," Anal. Chem. **77**(17), 5628–5634 (2005).
143. A. Lawrenz, F. Nason, and J. J. Cooper-White, "Geometrical effects in microfluidic-based microarrays for rapid, efficient single-cell capture of mammalian stem cells and plant cells," Biomicrofluidics **6**(2), 1–17 (2012).
144. J. Kim, J. Erath, A. Rodriguez, and C. Yang, "A high-efficiency microfluidic device for size-selective trapping and sorting," Lab Chip **14**(14), 2480–2490 (2014).
145. A. Prokop, Z. Prokop, D. Schaffer, E. Kozlov, J. Wikswo, D. Cliffel, and F. Baudenbacher, "NanoLiterBioReactor: Long-term mammalian cell culture at nanofabricated scale," Biomed. Microdevices **6**(4), 325–339 (2004).
146. A. R. Wheeler, W. R. Throndset, R. J. Whelan, A. M. Leach, R. N. Zare, Y. H. Liao, K. Farrell, I. D. Manger, and A. Daridon, "Microfluidic Device for Single-Cell Analysis," Anal. Chem. **75**(14), 3581–3586 (2003).
147. D. Di Carlo, N. Aghdam, and L. P. Lee, "Single-Cell Enzyme Concentrations , Kinetics and Inhibition Analysis Using High-Density Hydrodynamic Cell Isolation Arrays," Anal. Chem. **78**(14), 4925–4930 (2006).
148. D. Di Carlo and L. P. Lee, "Dynamic Single-Cell Analysis for Quantitative Biology," Anal. Chem. **78**(23), 7918–7925 (2006).
149. S. L. Faley, M. Copland, D. Wlodkowic, W. Kolch, K. T. Seale, J. P. Wikswo, and J. M. Cooper, "Microfluidic single cell arrays to interrogate signalling dynamics of individual, patient-derived hematopoietic stem cellsY," Lab Chip **9**(18), 2659–2664 (2009).
150. D. Wlodkowic, S. Faley, M. Zagnoni, J. P. Wikswo, and J. M. Cooper, "Microfluidic single-cell array cytometry for the analysis of tumor apoptosis," Anal. Chem. **81**(13), 5517–5523 (2009).
151. W.-H. Tan and S. Takeuchi, "A trap-and-release integrated microfluidic system for dynamic microarray applications," Proc. Natl. Acad. Sci. **104**(4), 1146–1151 (2007).
152. J. Nilsson, M. Evander, B. Hammarström, and T. Laurell, "Review of cell and particle trapping in microfluidic systems," Anal. Chim. Acta **649**(2), 141–157 (2009).
153. C. Probst, A. Grünberger, W. Wiechert, and D. Kohlheyer, "Polydimethylsiloxane

(PDMS) sub-micron traps for single-cell analysis of bacteria," Micromachines **4**(4), 357–369 (2013).
154. M.-C. Kim, B. C. Isenberg, J. Sutin, A. Meller, J. Y. Wong, and C. M. Klapperich, "Programmed trapping of individual bacteria using micrometre-size sieves," Lab Chip **11**(6), 1089 (2011).
155. H. Bruus, *Theoretical Microfluidics* (2007).
156. R. Rusconi and R. Stocker, "Microbes in flow," Curr. Opin. Microbiol. **25**, 1–8 (2015).
157. K. Son, D. R. Brumley, and R. Stocker, "Live from under the lens: exploring microbial motility with dynamic imaging and microfluidics," Nat. Rev. Microbiol. **13**(12), 761–775 (2015).
158. R. Rusconi, J. S. Guasto, and R. Stocker, "Bacterial transport suppressed by fluid shear," Nat. Phys. **10**(3), 212–217 (2014).
159. G. I. Taylor, "The Motion of Ellipsoidal Particles in a Viscous Fluid," Proc. R. Soc. A Math. Phys. Eng. Sci. **102**, 58–61 (1923).
160. E. J. Hinch and L. G. Leal, "Rotation of small non-axisymmetric particles in a simple shear flow," J. Fluid Mech. **92**(3), 591–607 (1979).
161. A. Zöttl and H. Stark, "Periodic and quasiperiodic motion of an elongated microswimmer in Poiseuille flow," Eur. Phys. J. E **36**(1), (2013).
162. Marcos, H. C. Fu, T. R. Powers, and R. Stocker, "Bacterial rheotaxis," Proc. Natl. Acad. Sci. **109**(13), 4780–4785 (2012).
163. J. Y. Tinevez, N. Perry, J. Schindelin, G. M. Hoopes, G. D. Reynolds, E. Laplantine, S. Y. Bednarek, S. L. Shorte, and K. W. Eliceiri, "TrackMate: An open and extensible platform for single-particle tracking," Methods **115**, 80–90 (2017).
164. N. C. Darnton, L. Turner, S. Rojevsky, and H. C. Berg, "On torque and tumbling in swimming Escherichia coli," J. Bacteriol. **189**(5), 1756–1764 (2007).
165. A. Wang, R. F. Garmann, and V. N. Manoharan, "Tracking E coli runs and tumbles with scattering solutions and digital holographic microscopy," Opt. Express **24**(21), 23719 (2016).
166. P. Kim, K. Woo Kwon, M. C. Park, S. H. Lee, S. M. Kim, & Kahp, and Y. Suh, "Soft Litography for Microfluidics: a Review," Biochip **2**(1), 11 (2008).
167. B. Gale, A. Jafek, C. Lambert, B. Goenner, H. Moghimifam, U. Nze, and S. Kamarapu, "A Review of Current Methods in Microfluidic Device Fabrication and Future Commercialization Prospects," Inventions **3**(3), 60 (2018).
168. R. Mukhopadhyay, "When PDMS isn't the best," Anal. Chem. **79**(9), 3248–3253 (2007).
169. X. Hou, Y. S. Zhang, G. T. De Santiago, M. M. Alvarez, J. Ribas, S. J. Jonas, P. S. Weiss, A. M. Andrews, J. Aizenberg, and A. Khademhosseini, "Interplay between materials and microfluidics," Nat. Rev. Mater. **2**(5), (2017).
170. K. Ren, J. Zhou, and H. Wu, "Materials for microfluidic chip fabrication," Acc. Chem. Res. **46**(11), 2396–2406 (2013).
171. Z. Wang, A. A. Volinsky, and N. D. Gallant, "Crosslinking effect on polydimethylsiloxane elastic modulus measured by custom-built compression instrument," J. Appl. Polym. Sci. **131**(22), 41050 (2014).
172. D. Cunliffe, C. A. Smart, C. Alexander, and E. N. Vulfson, "Bacterial adhesion at synthetic surfaces," Appl. Environ. Microbiol. **65**(11), 4995–5002 (1999).
173. P. Moazzam, A. Razmjou, M. Golabi, D. Shokri, and A. Landarani-Isfahani, "Investigating the BSA protein adsorption and bacterial adhesion of Al-alloy surfaces after creating a hierarchical (micro/nano) superhydrophobic structure," J. Biomed. Mater. Res. Part A **104**(9), 2220–2233 (2016).
174. N. Otsu, "A Threshold Selection Method from Gray-Level Histograms," IEEE Trans. Syst. Man. Cybern. **9**(1), 62–66 (1979).

175. G. Pitruzzello, S. Thorpe, S. Johnson, A. Evans, H. Gadêlha, and T. F. Krauss, "Multiparameter antibiotic resistance detection based on hydrodynamic trapping of individual E. coli," Lab Chip (2019).
176. T. K. Wood, A. F. González Barrios, M. Herzberg, and J. Lee, "Motility influences biofilm architecture in Escherichia coli," Appl. Microbiol. Biotechnol. **72**(2), 361–367 (2006).
177. P. Johnson and M. Beverlin, "Beta Distribution," Univ. Kansas 1–10 (2013).
178. G. A. Pankey and L. D. Sabath, "Clinical Relevance of Bacteriostatic versus Bactericidal Activity in the Treatment of Gram-Positive Bacterial Infections," Clin. Infect. Dis. **39**(5), 864–870 (2004).
179. G. L. French, "Bactericidal agents in the treatment of MRSA infections - The potential role of daptomycin," J. Antimicrob. Chemother. **58**(6), 1107–1117 (2006).
180. P. Macheboeuf, C. Contreras-Martel, V. Job, O. Dideberg, and A. Dessen, "Penicillin Binding Proteins: key players in bacterial cell cycle and drug resistance processes," FEMS Microbiol. Rev. **30**(5), 673–691 (2006).
181. Z. Yao, D. Kahne, and R. Kishony, "Distinct Single-Cell Morphological Dynamics under Beta-Lactam Antibiotics," Mol. Cell **48**(5), 705–712 (2012).
182. L. P. Kotra, J. Haddad, and S. Mobashery, "Aminoglycosides: Perspectives on mechanisms of action and resistance and strategies to counter resistance," Antimicrob. Agents Chemother. **44**(12), 3249–3256 (2000).
183. R. N. Brogden, A. A. Carmine, R. C. Heel, T. M. Speight, and G. S. Avery, "Trimethoprim: A Review of its Antibacterial Activity, Pharmacokinetics and Therapeutic Use in Urinary Tract Infections," Drugs **23**(6), 405–430 (1982).
184. J. M. Munita, C. A. Arias, A. R. Unit, and A. De Santiago, "Mechanisms of Antibiotic Resistance," Microbiol. Spectr. **4**(2), 1–37 (2016).
185. G. M. Eliopoulos and P. Huovinen, "Resistance to trimethoprim-sulfamethoxazole," Clin. Infect. Dis. **32**(11), 1608–1614 (2001).
186. J. Flensburg and O. Skold, "Massive overproduction of dihydrofolate reductase in bacteria as a response to the use of trimethoprim," Eur. J. Biochem. **162**(3), 473–476 (1987).
187. M. S. M. S. Ramirez and M. E. Tolmasky, "Aminoglycoside Modifying Enzymes," Drug Resist. Updat **13**(6), 151–171 (2010).
188. E. P. Abraham, "An enzyme from Bacteria able to Destroy Penicillin," Nature **42**, 2202–2205 (1940).
189. K. Bush, "Proliferation and significance of clinically relevant β-lactamases," Ann. N. Y. Acad. Sci. **1277**(1), 84–90 (2013).
190. J. Sun, Z. Deng, and A. Yan, "Bacterial multidrug efflux pumps: Mechanisms, physiology and pharmacological exploitations," Biochem. Biophys. Res. Commun. **453**(2), 254–267 (2014).
191. J. Kim, A. M. Webb, J. P. Kershner, S. Blaskowski, and S. D. Copley, "A versatile and highly efficient method for scarless genome editing in Escherichia coli and Salmonella enterica," BMC Biotechnol. **14**(1), 1–13 (2014).
192. M. Peleg and M. G. Corradini, "Microbial Growth Curves: What the Models Tell Us and What They Cannot," Crit. Rev. Food Sci. Nutr. **51**, 917–945 (2011).
193. D. M. Fitzgerald, R. P. Bonocora, and J. T. Wade, "Comprehensive Mapping of the Escherichia coli Flagellar Regulatory Network," PLoS Genet. **10**(10), (2014).
194. H. S. Girgis, Y. Liu, W. S. Ryu, and S. Tavazoie, "A comprehensive genetic characterization of bacterial motility," PLoS Genet. **3**(9), 1644–1660 (2007).
195. H. W. Taber, J. P. Mueller, P. F. Miller, and A. S. Arrow, "Bacterial uptake of aminoglycoside antibiotics," Microbiol. Rev. **51**(4), 439–457 (1987).
196. B. D. Davis, "Mechanism of bactericidal action of aminoglycosides.," Microbiol. Rev. **51**(3), 341–350 (1987).

197. L. E. Bryan and H. M. Van den Elzen, "Streptomycin accumulation in susceptible and resistant strains of Escherichia coli and Pseudomonas aeruginosa.," Antimicrob. Agents Chemother. **9**(6), 928–938 (1976).
198. C. Hurwitz, C. B. Braun, and C. L. Rosano, "Role of ribosome recycling in uptake of dihydrostreptomycin by sensitive and resistant Escherichia coli," Biochim. Biophys. Acta - Nucleic Acids Protein Synth. **652**(1), 168–176 (1981).
199. H. F. Ridgway, "Source of energy for gliding motility in Flexibacter polymorphus: effects of metabolic and respiratory inhibitors on gliding movement.," J. Bacteriol. **131**(2), 544–556 (1977).
200. S. H. Larsen, J. Adler, J. J. Gargus, and R. W. Hogg, "Chemomechanical Coupling without ATP: The Source of Energy for Motility and Chemotaxis in Bacteria," Proc. Natl. Acad. Sci. **71**(4), 1239–1243 (1974).
201. W. L. Drew, A. L. Barry, R. O'Toole, and J. C. Sherris, "Reliability of the Kirby-Bauer disc diffusion method for detecting methicillin-resistant strains of Staphylococcus aureus.," Appl. Microbiol. **24**(2), 240–7 (1972).
202. C. A. Rotilie, R. J. Fass, R. B. Prior, and R. L. Perkins, "Microdilution Technique for Antimicrobial Susceptibility Testing of Anaerobic Bacteria," Antimicrob. Agents Chemother. **7**(3), 311–315 (2012).
203. S. D. Sarker, L. Nahar, and Y. Kumarasamy, "Microtitre plate-based antibacterial assay incorporating resazurin as an indicator of cell growth, and its application in the in vitro antibacterial screening of phytochemicals," Methods **42**(4), 321–324 (2007).
204. A. J. Drummond and R. D. Waigh, "The development of microbiological methods for phytochemical screening.," Recent Res. Dev. Phytochem. **4**, 143–152 (2000).
205. E. P. Randviir and C. E. Banks, "Electrochemical impedance spectroscopy: An overview of bioanalytical applications," Anal. Methods **5**(5), 1098–1115 (2013).
206. M. Grossi and B. Riccò, "Electrical impedance spectroscopy (EIS) for biological analysis and food characterization: A review," J. Sensors Sens. Syst. **6**(2), 303–325 (2017).
207. T. Sun, D. Holmes, S. Gawad, N. G. Green, and H. Morgan, "High speed multi-frequency impedance analysis of single particles in a microfluidic cytometer using maximum length sequences," Lab Chip **7**(8), 1034–1040 (2007).
208. N. G. Green, D. Holmes, T. Sun, S. Gawad, and H. Morgan, "Single cell dielectric spectroscopy," J. Phys. D. Appl. Phys. **40**(1), 61–70 (2006).
209. G. N. Stewart, "the Charges Produced By the Growth of Bacteria in the Molecular Concentration and Electrical Conductivity of Culture Media," J. Exp. Med. **4**(2), 235–243 (2004).
210. P. Cady, S. W. Dufour, J. Shaw, and S. J. Kraeger, "Electrical impedance measurements: rapid method for detecting and monitoring microorganisms," J. Clin. Microbiol. **7**(3), 265–272 (1978).
211. M. Grossi, M. Lanzoni, A. Pompei, R. Lazzarini, D. Matteuzzi, and B. Riccò, "An embedded portable biosensor system for bacterial concentration detection," Biosens. Bioelectron. **26**(3), 983–990 (2010).
212. K. F. Lei, "Review on impedance detection of cellular responses in micro/nano environment," Micromachines **5**(1), 1–12 (2014).
213. T. Sun and H. Morgan, "Single-cell microfluidic Impedance cytometry: A review," Microfluid. Nanofluidics **8**(4), 423–443 (2010).
214. T. S. Santra, L. Angeles, and F. Tseng, "Essentials of Single-Cell Analysis," (March 2018), (2016).
215. M. A. Mansor and M. R. Ahmad, "Single cell electrical characterization techniques," Int. J. Mol. Sci. **16**(6), 12686–12712 (2015).
216. Z. Zhu, O. Frey, N. Haandbaek, F. Franke, F. Rudolf, and A. Hierlemann, "Time-

lapse electrical impedance spectroscopy for monitoring the cell cycle of single immobilized S. pombe cells," Sci. Rep. **5**(October), 1–14 (2015).
217. Z. Zhu, O. Frey, F. Franke, N. Haandbæk, and A. Hierlemann, "Real-time monitoring of immobilized single yeast cells through multifrequency electrical impedance spectroscopy," Anal. Bioanal. Chem. **406**(27), 7015–7025 (2014).
218. D. Malleo, J. T. Nevill, L. P. Lee, and H. Morgan, "Continuous differential impedance spectroscopy of single cells," Microfluid. Nanofluidics **9**(2–3), 191–198 (2010).
219. F. Asphahani, K. Wang, M. Thein, O. Veiseh, S. Yung, J. Xu, and M. Zhang, "Single-cell bioelectrical impedance platform for monitoring cellular response to drug treatment," Phys. Biol. **8**(1), (2011).
220. A. Adan, G. Alizada, Y. Kiraz, Y. Baran, and A. Nalbant, "Flow cytometry: basic principles and applications.," Crit. Rev. Biotechnol. **37**(2), 163–176 (2017).
221. J. Chen, C. Xue, Y. Zhao, D. Chen, M. H. Wu, and J. Wang, "Microfluidic impedance flow cytometry enabling high-throughput single-cell electrical property characterization," Int. J. Mol. Sci. **16**(5), 9804–9830 (2015).
222. H. L. Gou, X. B. Zhang, N. Bao, J. J. Xu, X. H. Xia, and H. Y. Chen, "Label-free electrical discrimination of cells at normal, apoptotic and necrotic status with a microfluidic device," J. Chromatogr. A **1218**(33), 5725–5729 (2011).
223. J. Chen, C. Wei, Y. Zhao, X. T. Zhao, J. B. Wang, W. T. Yue, R. Long, M. Jiang, Y. N. Luo, and D. Y. Chen, "Tumor cell characterization and classification based on cellular specific membrane capacitance and cytoplasm conductivity," Biosens. Bioelectron. **57**, 245–253 (2014).
224. H. Song, B. Prabhakarpandian, Y. Wang, C. Garson, K. Pant, E. Lai, and J. M. Rosano, "A microfluidic impedance flow cytometer for identification of differentiation state of stem cells," Lab Chip **13**(12), 2300 (2013).
225. C. Van Berkel, J. D. Gwyer, S. Deane, N. Green, J. Holloway, V. Hollis, and H. Morgan, "Integrated systems for rapid point of care (PoC) blood cell analysis," Lab Chip **11**(7), 1249–1255 (2011).
226. R. Bashir, G. Damhorst, N. N. Watkins, U. Hassan, A. Vaid, H. Ni, and W. Rodriguez, "Microfluidic CD4+ and CD8+ T Lymphocyte Counters for Point-of-Care HIV Diagnostics Using Whole Blood," Sci. Transl. Med. **5**(214), 214ra170-214ra170 (2013).
227. K. Cheung, S. Gawad, and P. Renaud, "Impedance spectroscopy flow cytometry: On-chip label-free cell differentiation," Cytom. Part A **65**(2), 124–132 (2005).
228. C. Clausen, M. Dimaki, C. Bertelsen, G. Skands, R. Rodriguez-Trujillo, J. Thomsen, and W. Svendsen, "Bacteria Detection and Differentiation Using Impedance Flow Cytometry," Sensors **18**(10), 3496 (2018).
229. C. Bernabini, D. Holmes, and H. Morgan, "Micro-impedance cytometry for detection and analysis of micron-sized particles and bacteria," Lab Chip **11**(3), 407–412 (2011).
230. N. Haandbæk, O. With, S. C. Bürgel, F. Heer, and A. Hierlemann, "Resonance-enhanced microfluidic impedance cytometer for detection of single bacteria," Lab Chip **14**(17), 3313–3324 (2014).
231. F. David, M. Hebeisen, G. Schade, E. Franco-Lara, and M. Di Berardino, "Viability and membrane potential analysis of Bacillus megaterium cells by impedance flow cytometry," Biotechnol. Bioeng. **109**(2), 483–492 (2012).
232. S. Gawad, L. Schild, and P. Renaud, "Micromachined impedance spectroscopy flow cytometer for cell analysis and particle sizing," Lab Chip **1**(1), 76–82 (2001).
233. R. Payne, "The electrical double layer: Problems and recent progress," J. Electroanal. Chem. **41**(2), 277–309 (1973).
234. Y. Hou, "Controlling Variables of electric double layer capacitance," University of

Fukui (2014).
235. R. Hölzel, "Non-invasive determination of bacterial single cell properties by electrorotation," Biochim. Biophys. Acta - Mol. Cell Res. **1450**(1), 53–60 (1999).
236. A. Rohani, J. H. Moore, Y.-H. Su, V. Stagnaro, C. Warren, and N. S. Swami, "Single-cell electro-phenotyping for rapid assessment of Clostridium difficile heterogeneity under vancomycin treatment at sub-MIC (minimum inhibitory concentration) levels," Sensors Actuators B Chem. **276**, 472–480 (2018).
237. J. E. . Randles, "Kinetics of Rapid Electrode Reactions," Discuss. Faraday Soc. **1**, 11–19 (1947).
238. P. Córdoba-Torres, T. J. Mesquita, and R. P. Nogueira, "Relationship between the origin of constant-phase element behavior in electrochemical impedance spectroscopy and electrode surface structure," J. Phys. Chem. C **119**(8), 4136–4147 (2015).
239. J. B. Jorcin, M. E. Orazem, N. Pébère, and B. Tribollet, "CPE analysis by local electrochemical impedance spectroscopy," Electrochim. Acta **51**(8–9), 1473–1479 (2006).